

University of Warwick institutional repository: <http://go.warwick.ac.uk/wrap>

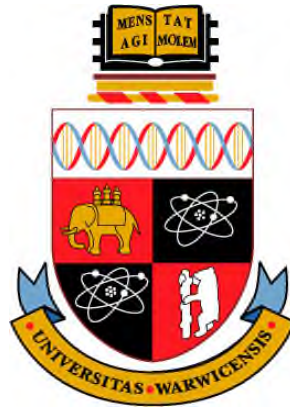
A Thesis Submitted for the Degree of PhD at the University of Warwick

<http://go.warwick.ac.uk/wrap/78058>

This thesis is made available online and is protected by original copyright.

Please scroll down to view the document itself.

Please refer to the repository record for this item for information to help you to cite it. Our policy information is available from the repository home page.



**Effect of Surface Adhesion in Contact: Application of
Johnson-Kendall-Roberts model on Nanoindentation**

by

Xinyao Zhu

A thesis submitted in partial fulfilment of the requirements for the
degree of Doctor of Philosophy in Engineering

School of Engineering, University of Warwick

September 2015

THE UNIVERSITY OF
WARWICK

Table of Contents

TABLE OF FIGURES	v
TABLE OF TABLES	xi
ACKNOWLEDGEMENTS	xii
DECLARATION.....	xiii
PUBLICATIONS	xiv
ABSTRACT	xv
NOMENCLATURE.....	xviii
ABBREVIATION	xxii
1 Introduction	1
1.1 General Background	1
1.1.1 Application of Nanoindentation	1
1.1.2 Atomic force microscope.....	2
1.2 Existing Challenges.....	5
1.3 Objective and outlines of the Thesis.....	9
1.3.1 Objectives	9
1.3.2 Outlines of this thesis	10
2 Literature Review	13
2.1 Brief History of Macroscopic Indentation.....	13
2.1.1 Brinell Testing: Spherical indenter	13
2.1.2 Shore testing: Dynamic measurement of hardness	14
2.1.3 Other indentation techniques	14
2.2 Characterization of mechanical properties by nanoindentation.....	15
2.2.1 Young’s modulus and hardness	16
2.2.2 Fracture toughness	20
2.2.3 Creep parameters	22
2.2.4 Strain-Hardening exponent.....	24
2.3 Adhesive contact in nanoindentation: surface and scale effect	26
2.3.1 Elastic adhesive contact between two bodies	26

2.3.2	Elastoplastic adhesive contact between two bodies.....	29
2.3.3	Solutions of Micro/Nano contact by molecular dynamics.....	32
2.4	Application of AFM on biological materials	34
2.4.1	Application of AFM indentation on probing cell elasticity.....	35
2.4.2	Investigation of cell adhesion by AFM indentation.....	36
2.5	Summary	37
3	Theoretical Background	39
3.1	Intermolecular and Surface Forces.....	39
3.1.1	Forces between two molecular (atoms).....	39
3.1.2	Force between two surfaces.....	43
3.1.2.1	<i>Van der Waals</i> force between two semi-infinite planes	43
3.1.2.2	<i>Lennard-Jones forces</i> between two semi-infinite planes.....	45
3.2	Classical Contact Models	48
3.2.1	Hertz model: a non-adhesive contact model.....	48
3.2.2	Bradley Model: Adhesive contact between two rigid bodies	51
3.2.3	JKR model: reference to fracture mechanics.....	53
3.2.4	DMT model: the profile outside the contact area remains Hertzian.....	55
3.2.5	Maugis–Dugdale (M-D) model: a transition from DMT to JKR model.....	57
3.2.6	Comparison of five contact models and subsequent studies.....	60
4	Quantification of Mechanical Properties by Nanoindentation: a carrier for surface force study.....	63
4.1	Introduction	63
4.2	Experiment-based Methods	63
4.2.1	Oliver and Pharr Method	63
4.2.1.1	Cylindrical indenter.....	65
4.2.1.2	Berkovich indenter	66
4.2.1.3	Spherical indenter.....	69
4.2.2	Fracture toughness.....	71
4.2.3	Viscosity parameter	76
4.3	Experiment Process and Instrument Introduction.....	82
4.3.1	Instrumentation.....	82
4.3.2	Nanoindentation Tester NHT ²	83

4.3.3	Sample Preparation.....	86
4.3.4	Experimental Procedure.....	87
4.3.4.1	Copper and fused silica	87
4.3.4.2	Silicon wafer	87
4.3.4.3	Polystyrene	87
4.4	Finite Element Analysis.....	88
4.5	Results and Discussion	89
4.5.1	Copper and Fused Silica	89
4.5.1.1	Indentation Impression.....	89
4.5.1.2	Force-displacement curve.....	90
4.5.1.3	Comparison of Simulative and Experimental Results.....	95
4.5.2	Silicon Wafer.....	97
4.5.3	Polystyrene	98
4.6	Chapter Summary	99
5	Effects of adhesion on shakedown behavior of microcontacting bodies.....	101
5.1	Introduction	101
5.2	Propaedeutics	104
5.2.1	Yield criteria.....	104
5.2.1.1	Tresca criterion.....	105
5.2.1.2	Von Mises criterion	106
5.2.2	Work hardening	106
5.2.2.1	<i>Isotropic hardening</i>	107
5.2.2.2	<i>Kinematic hardening</i>	108
5.2.2.3	Mixed hardening rules.....	110
5.2.3	Flow curve	110
5.3	Finite element model	112
5.4	Results and discussions	115
5.4.1	Pure elastic adhesive contact	115
5.4.2	Power law isotropic hardening	118
5.4.2.1	Von Mises Plastic Fields.....	118
5.4.2.2	Multiple loading-unloading cycles	123
5.4.3	Bilinear Kinematic Hardening Model	129
5.4.3.1	Von Mises Strain Fields.....	129
5.4.3.2	Multiple loading-unloading cycles	133
5.5	Summary	137

6	Determination of Work of Adhesion of Pancreatic MIN6 cells under AFM indentation (Spherical probe)	140
6.1	Introduction	140
6.2	Methodology	143
6.2.1	Data preparation	143
6.2.2	Theoretical model	143
6.3	Results and Discussions	146
6.3.1	Verification of Cellular Viscous Properties.....	147
6.3.2	Fitting results by using JKR model of bead on spherical cell	151
6.3.3	Fitting results by JKR model of bead on flattened cell.....	154
6.3.4	Finite element simulation	165
6.4	Summary	167
7	Determination of Work of Adhesion of human hepatocellular carcinoma by AFM indentation (Vickers probe)	169
7.1	Introduction	169
7.2	Methodology	170
7.2.1	Cell Preparation	170
7.2.2	Atomic force microscope.....	171
7.3	Theoretical model	172
7.4	Results and discussion	175
7.4.1	Post-processing of indentation data	175
7.4.2	Original experimental data	177
7.4.3	Control cells and cells exposed to fulleranol for 24 hours (Non-adhesion case) 186	
7.4.4	Cells exposed to fulleranol for 48 and 72 hours (Adhesion case)	188
7.5	Summary	197
8	Conclusions and Future work	198
8.1	Research Highlights and Conclusions	198
8.2	Future work	202
	References	204

TABLE OF FIGURES

Fig 1.1 Schematic diagram of an atomic force microscope (AFM)	4
Fig 1.2 Adhesion-induced phenomenon in AFM indentation: (a) negative force in biological cells (b) jump instability in hard materials. For the soft material, pull off is manifested by stepwise unbinding events as circled by the black oval in Fig 1.2 (a), and it thus called “ductile” separation in this work. For hard materials, a sudden jump off manifests itself by the vertical line circled by black ellipse as shown in Fig 1.2 (b), and hence is called “brittle” separation in this work.....	6
Fig 1.3 Example of adhesion failure in MEMS: (a) Stiction of micro-cantilevers to substrate. (b) Adhesion between fingers of a comb structure in a micro-accelerometer.	9
Fig 2.1 Approximate equivalent hardness translation chart for different standard hardness test with respect to Berkovich hardness.	15
Fig 2.2 Plastic zone developed during indentation by conical indenter with different values of E_{eff}/σ_y . The solid lines and dash lines denote elastic-perfect plastic and work hardening materials respectively.	17
Fig 2.3 Crack systems for Vickers indenter: (a) radial cracks, (b) lateral cracks, (c) median cracks and (d) half-penny cracks.....	20
Fig 2.4 Schematic of radial crack from side view after removal of indenter.	21
Fig 2.5 Different kinds of mechanical models: (a) Kelvin model (b) Maxwell model (c) three element model.	23
Fig 2.6 Stress-strain curve for elastic-plastic materials under uniaxial loading. Y denotes the initial yield stress beyond material begins to exhibit hardening with strain-hardening exponent n	24
Fig 2.7 Scanning electron microscope (SEM) images of an aurum contact bump cycled at force of $200 \mu\text{N}$. (a) The original bump before cycling; (b) the bump after several cycles and (c) its zoom in tilted at 85° . The difference of surface topographies corresponding to (a) and (b) is due to adhesion forces.	32
Fig 2.8 Atomic configurations of indentation between nickel indenter and aurum substrate.	34
Fig 3.1 <i>Lennard-Jones</i> potential versus distance between two molecules (atoms) in reduced coordinates.	42
Fig 3.2 <i>Lennard-Jones</i> force versus distance between two molecules (atoms) in reduced coordinates.	42
Fig 3.3 Schematic of the <i>van der Waals</i> force between a single molecule (atom) and a semi-infinite space	44
Fig 3.4 <i>Lennard-Jones</i> force corresponding to two parallel surfaces as a function of separation.	47
Fig 3.5 Schematic of (a) contact of two elastic spheres subjected to normal force F and (b)	

the distribution of compressive pressure in contact area.....	49
Fig 3.6 Schematic of non-contact adhesion between two rigid spheres.....	51
Fig 3.7 Distribution of contact stress predicted by different contact models. The positive pressure denotes compressive force whilst the negative pressure denotes attractive force.	53
Fig 3.8 (a) Relation between force F and mutual approach δ , in reduced coordinates. (b) The interaction forces in JKR (bold line) in comparison with realistic interaction (thin line), and positive and negative value represent repulsive and attractive interaction forces, respectively.....	55
Fig 3.9 Schematic of the interaction forces in DMT model (bold line) compared with realistic interaction (thin line).....	56
Fig 3.10 Schematic of the interaction force used in M-D (bold solid line) in comparison with realistic interaction (thin line). The area enclosed by the bold solid line with respect to abscissa is the same as that of the thin line, implying the interaction force used in M-D model gives the same work of adhesion as that of the real one.....	58
Fig 3.11 Dependence of reduced force on reduced penetration corresponding to Hertz, JKR, M-D and DMT models.....	60
Fig 3.12 Adhesive map. The vertical coordinates denotes external load reduced by $\pi\Delta\gamma R$, i.e. $F^*=F_{ext}/\pi\Delta\gamma R$	61
Fig 4.1 A typical force-indentation depth (displacement) curve obtained from nanoindentation.	64
Fig 4.2 (a) Schematic of substrate material indented by cylinder punch. (b) The corresponding $F-d$ curve. h_i and h_r denote the maximum indentation depth and depth of residual impression respectively. h_a is the depth of the contact periphery.	66
Fig 4.3 Schematic of Berkovich. α denotes the half-angle to face. (b) Schematic of substrate material indented by conic indenter. (c) The corresponding $F-d$ curve.....	67
Fig 4.4 (a) Schematic of substrate material indented by spherical indenter. (b) The corresponding $F-d$ curve. R_i denotes the radius of the sphere, and R_r denotes the radius of curvature at the center of the residual impression.....	69
Fig 4.5 Schematic of median crack: (a) elastic-plastic configuration at full load (b) residual configuration of complete unloading (c) radial crack	72
Fig 4.6 Illustration of Force-displacement curves for PMMA (Poly Methyl Methacrylate)...77	
Fig 4.7 Schematic of elastic component of viscoelastic materials	78
Fig 4.8 Schematic of viscous component of viscoelastic materials	79
Fig 4.9 Three common mechanical models: (a) Kelvin–Voigt model (b) Maxwell model (c) Three element model.....	80
Fig 4.10 Schematic illustration of an instrumented indentation system.....	83
Fig 4.11 The Nano Indentation Tester NHT ² manufactured by CSM instruments.....	83
Fig 4.12 Schematic of profile map of the NHT ² head.....	84
Fig 4.13 (a) Microscope of the Berkovich diamond indenter (b) Typical residual impression induced by Berkovich indenter on ductile materials	85
Fig 4.14 (a) Copper and (b) Fused silica (c) Silicon Wafer (d) polystyrene	86

Fig 4.15 Finite element model of a rigid conic in close proximity with a deformable half-space.	89
Fig 4.16 (a) A single indentation impression on copper substrate; (b) Cross sectional view of pile-up during indentation; (c) A matrix of indentation impressions where the distance between two adjacent spots is $25 \mu\text{m}$	90
Fig 4.17 Force-displacement curve for Berkovich indenter on (a) copper and (b) fused silica. Both the loading and unloading rate is 100mN/min with a pause of 10s at the maximum force. The displacement origin is set where the indentation depth is zero such that they are identical. The corresponding maximum indentation depth h_i , depth of residual impression h_r and depth beneath the contact periphery h_p are marked in the plot.	91
Fig 4.18 Force-displacement curves corresponding to 100 repeated indentations for (a) copper and (b) fused silica.	93
Fig 4.19 Distribution of density of (a) Young's modulus and (b) hardness for copper.....	93
Fig 4.20 Distribution of density of (a) Young's modulus and (b) hardness for fused silica....	93
Fig 4.21 Dependence of hardness on indentation depth corresponding to several materials ..	94
Fig 4.22 Comparison between FEM results and experimental data corresponding to (a) copper and (b) fused silica	95
Fig 4.23 Typical Force-displacement curve for silicon wafer.	97
Fig 4.24 Optical microscope of an indentation impression at 400 mN force in silicon wafer.	97
Fig 4.25 Displacement-time curve and its best fitting by using three element model.....	99
Fig 5.1 Schematic of stress-strain curve for (a) pure elastic (b) elastic shakedown (c) plastic shakedown and (d) ratchetting	102
Fig 5.2 Stress-strain curve showing typical yield behavior for nonferrous alloys in uniaxial loading.....	105
Fig 5.3 Schematic for the expanding of yield surface in isotropic hardening	107
Fig 5.4 Schematic for the translation of yield surface in kinematic hardening. Although point E is within the initial yield surface, it is no longer contained by subsequent yield surface, and thus plasticity occurs during the path from D to E.	109
Fig 5.5 Comparison between isotropic and kinematic hardening in terms of stress-strain curve	109
Fig 5.6 The flow curve for (a) uniaxial stress-plastic strain and (b) effective stress-effective plastic strain	111
Fig 5.7 Schematic of dependence of effective stress on effective plastic strain for (a) power law isotropic hardening and (b) bilinear kinematic hardening.	112
Fig 5.8 Schematic of (a) non-adhesive contact and (b) adhesive contact between a rigid spherical indenter and a deformable half-space	113
Fig 5.9 Schematic of FE model of adhesive contact between a rigid sphere and a deformable half-space for (a) overview and (b) its amplification at contact region.	114
Fig 5.10 Schematic of a pure elastic half-space indented by a rigid spherical indenter. The interaction force obeys Lennard-Jones potential, where the dotted line represents zero force space.....	115
Fig 5.11 Dependence of normalized force $F/\pi R \Delta \gamma$ on normalized penetration $-\alpha/z_0$ for (a)	

$\mu=0.5$, (b) $\mu = 0.75$, (c) $\mu = 1.0$ and (d) $\mu = 2.0$. The blue line and red asterisk represent results by using our FE simulation and self-consistent method, respectively.	116
Fig 5.12 Dependence of jump-in and jump-out position (in terms of normalized penetration – α/z_0) on Tabor parameter μ	117
Fig 5.13 Von Mises plastic strain fields during loading for different penetrations whose $\mu = 1$, $S = 1.35$	120
Fig 5.14 Von Mises plastic strain fields during loading for different penetrations whose $\mu = 1$, $S = 2.7$: (a) first plastic deformation (b) maximum indentation position	121
Fig 5.15 Normalized force versus normalized displacement for four consecutive loading-unloading cycles with $\mu = 0.45$, $Y = 0.5\text{GPa}$, $\delta_{max}/z_0 = -8.82$, $S=2.7$ for (a) $n = 0.75$, (b) $n = 0.15$ and (c) $n = 0.1$	124
Fig 5.16 Normalized force versus normalized displacement for four consecutive loading-unloading cycles corresponding to non-adhesive contact. $Y = 0.5\text{GPa}$, $\delta_{max}/z_0 = -8.82$, $n = 0.15$	125
Fig 5.17 Normalized force versus displacement for four consecutive loading-unloading cycles with $\mu = 1$, $Y = 0.5\text{GPa}$, $\delta_{max}/z_0 = -8.82$, $S=2.7$, $n = 0.1$	127
Fig 5.18 Normalized force versus displacement for four consecutive loading-unloading cycles with $\mu = 1$, $Y = 1\text{GPa}$, $\delta_{max}/z_0 = -8.82$, $S=1.35$, $n = 0.1$	128
Fig 5.19 Von Mises plastic strain fields for different penetration where $\mu = 0.5$, $Y = 0.5\text{GPa}$, $S=2.7$, $E_T/E = 0.5$	132
Fig 5.20 Normalized force versus displacement for four consecutive loading-unloading cycles with $\mu = 1$, $Y = 0.5\text{GPa}$, $S=2.7$, $E_T/E = 0.5$	133
Fig 5.21 Normalized force versus displacement for four consecutive loading-unloading cycles corresponding to non-adhesive contact.	134
Fig 5.22 Normalized force versus displacement for four consecutive loading-unloading cycles with $\mu = 1$, $Y = 1\text{GPa}$, $S=1.35$, $E_T/E = 0.5$	135
Fig 5.23 Normalized force versus displacement for four consecutive loading-unloading cycles with $\mu = 0.5$, $Y = 1\text{GPa}$, $S=1.35$, $E_T/E = 0.5$	136
Fig 5.24 Normalized force versus displacement for four consecutive loading-unloading cycles with $\mu = 0.5$, $Y = 1\text{GPa}$, $S=1.35$, $E_T/E = 0.1$	137
Fig 6.1 Schematic of the retraction part of force-displacement curve from cell AFM indentation. The green area enclosed by the curve and horizontal axis denotes work of detachment (W_D) whilst the minimum (negative) value of indentation force denotes maximum unbinding force (F_{max}).	142
Fig 6.2 Schematic diagrams of the AFM bead tip in contact with cells of (a) spherical shape and (b) flattened shape.	144
Fig 6.3 Example of force-versus-displacement curves obtained by AFM indentation on (a) sample A and (b) sample B cells.	147
Fig 6.4 Schematic diagram of Kelvin model where a dashpot is in parallel with a spring undergoing the same deformation.	149
Fig 6.5 Typical force-versus-time curves during loading part and the best fitting curves by using Kelvin model for (a) sample A and (b) sample B.	150

Fig 6.6 Viscous relaxation time of the two type cells. The data are presented as average values with standard deviations.....	151
Fig 6.7 Typical force-displacement curves and the best fitting curves by using JKR model for (a) Sample A and (b) Sample B cells.	153
Fig 6.8 Statistics of (a) Young's modulus and (b) work of adhesion respectively.	153
Fig 6.9 (a) Schematic diagram of the non-adhesive contact between a rigid bead and an elastic layer with finite thickness h . (b) Scheme of the adhesive contact between a rigid bead and an elastic layer.....	156
Fig 6.10 Typical force-displacement curves and the best fitting curves by using "generalized" JKR model for (a) normal and (b) treated cells corresponding to case 1.....	158
Fig 6.11 Typical force-displacement curves and the best fitting curves by using "generalized" JKR model for (a) normal and (b) treated cells corresponding to case 2.....	159
Fig 6.12 Typical force-displacement curves and the best fitting curves by using "generalized" JKR model for (a) normal and (b) treated cells corresponding to case 3.....	160
Fig 6.13 Typical force-displacement curves and the best fitting curves by using "generalized" JKR model for (a) normal and (b) treated cells corresponding to case 4.....	161
Fig 6.14 The statistics of (a) Young's modulus and (b) work of adhesion for both sample cells determined by all the models in this chapter.....	162
Fig 6.15 Typical force-indentation depth curve (loading part) and the best fitting curves by Hertz contact model	163
Fig 6.16 Statistics of Young's modulus (bold solid lines) and work of adhesion (thin solid lines) for Sample A (blue lines) and Sample B (red lines) with four thickness cases. ..	164
Fig 6.17 Typical force-displacement curves and the best fitting curves by using FEM ($\mu = 5$) for (a) Sample A and (b) Sample B cells (in reduced coordinates). The red bold and thin blue lines denote experimental data and <i>FEM</i> simulation results, respectively.	166
Fig 6.18 Results of extracted Young's modulus and work of adhesion respectively. The data are presented as average values with standard deviations.....	167
Fig 7.1 Microscope of (a) top of cantilever and (b) the silicon nitride indenter.	172
Fig 7.2 Scheme of principle of force-displacement measurement by <i>AFM</i>	172
Fig 7.3 Schematic of (a) non-adhesive and (b) adhesive contact between a Vickers indenter and a compliant semi-infinite space. α denotes the half-angle to face. The neck area is ascribed to adhesion force.....	173
Fig 7.4 Processing of raw force-displacement curve obtained from <i>AFM</i> indentation.	176
Fig 7.5 Typical <i>F-d</i> curves corresponding to (a) repeated indentations at the same point and (b) different indentation positions within the same cell.	178
Fig 7.6 Example of force-displacement curves obtained by <i>AFM</i> indentation on (a) control cells, cells exposed to fulleranol for (b) 24 hours, (c) 48 hours and (d) 72hours respectively.....	181
Fig 7.7 Top view of microscope of <i>AFM</i> of (a) control cells, cells exposed to fulleranol for (b) 24 hours, (c) 48 hours and (d) 72hours respectively. The triangle is the <i>AFM</i> cantilever.	181
Fig 7.8 <i>AFM</i> deflection imaging of (a) control cells, cells exposed to fulleranol for (b) 24	

hours, (c) 48 hours and (d) 72hours.	182
Fig 7.9 Tether rupture events during unloading stage for (a) control cells, cells exposed to fulleranol for (b) 24 hours, (c) 48 hours and (d) 72hours. The vertical solid line indicates the unbinding event.	185
Fig 7.10 The retraction part of $F-d$ curve obtained from cell A and B is fitted by Hertz model.	186
Fig 7.11 The determined Young's modulus for (a) control cell and (b) cells exposed to fullerenols for 24 hours. The data are presented as average values with standard deviations.	188
Fig 7.12 The comparison of determined Young's modulus between cell A and B.	188
Fig 7.13 Typical force-displacement curves and the best fitting curves by using JKR model. The zoom box denotes the "local fitting"	190
Fig 7.14 Scheme of cyclic tethering and detachment during unloading.	191
Fig 7.15 $F-d$ curve with considerable force discontinuity during the retraction fraction was discarded for statistics	192
Fig 7.16 Histograms showing the determined (a) Young's modulus and (b) work of adhesion for each cell C subject.	194
Fig 7.17 Results of the determined (a) Young's modulus and (b) work of adhesion for each cell D subject.	194
Fig 7.18 The comparison of determined (a) Young's modulus and (b) work of adhesion between cell C and D.	195
Fig 7.19 Results of Young's moduli of the four group cells by using JKR model.	196
Fig 7.20 Results of Young's moduli of the four group cells, by Using Hertzian contact model to fit the loading parts of $F-d$ curves.	196

TABLE OF TABLES

Table 2.1 Parameters for common indenters	17
Table 3.1 Solution for non-adhesive contact of cylindrical and conical indenter	50
Table 3.2 Comparison of the different assumptions and limitations for the five contact models	61
Table 4.1 Creep Compliance for the three common models	81
Table 4.2 Dependence of indentation depth on time for different indenters corresponding to Heaviside step load	82
Table 4.3 Material properties of copper, fused silica and silicon wafer.	87
Table 4.4 Viscoelastic properties of polymeric materials	87
Table 4.5 List of the statistics results for the two determined parameters.....	93
Table 5.1 Details of the two hardening models used in this chapter	112
Table 5.2 Parameters studied in the adhesive contact	116
Table 6.1 Values of Young's modulus determined by the two JKR models and Hertz model.	162
Table 6.2 Values of work of adhesion determined by the two JKR models.	162
Table 7.1 Young's modulus from cell <i>A2</i> (Unit: kPa).....	186
Table 7.2 Young's modulus from cell <i>B1</i> (Unit: kPa).....	187
Table 7.3 Extracted parameters from one cell <i>C2</i>	193
Table 7.4 Extracted parameters from one cell <i>D2</i>	193

ACKNOWLEDGEMENTS

The author would like to express his extreme gratitude towards his supervisor Dr Xianping Liu, for her guidance, support, encouragement, enlightenment, and also her endeavor to correct this thesis.

Many thanks to the financial support from China Scholarship Council and School of Engineering, University of Warwick.

The author appreciates his friends Hui Niu, Zhongnan Wang, Lei Wang, Yuan Xue, Zedong Hu, Yemi Jegede, for their support.

Special appreciation is given to Zuobin Wang, Nan Zhang, of Changchun University of Science and Technology, with whose support the author could conduct atomic force microscope experiment.

Much thanks to Prof. Greenwood (University of Cambridge, UK) and Prof. Gao (University of Brown, US) for their meaningful discussion.

Finally, the author would like to express his deepest gratitude to his parents, Ziming Zhu and Chunhua Zhang for their grace of birth, parental care and selfless love.

DECLARATION

This thesis is submitted in accordance with the regulations for the degree of Doctor of Philosophy by the High Degree Committee at the University of Warwick.

It is declared that the presented work was conducted by the candidate Xinyao Zhu and it has not been submitted for any degree of any other university.

Candidate's signature and date:

PUBLICATIONS

Publications arose from this work

Zhu, X.Y., Zhang, N., Wang, Z.B., Liu, X.P., 2015. Determination of Work of Adhesion of biological cell (human hepatocellular carcinoma) under AFM bead indentation. *Manipulation, Manufacturing and Measurement on the Nanoscale (3M-NANO), 2015 International Conference on*. Accepted.

Zhu, X.Y., Siamantouras, E., Liu, K.K., Liu, X.P., 2016, Determination of Work of Adhesion of biological cell under AFM bead indentation. *Journal of the Mechanical Behavior of Biomedical Materials*. 56, 77–86.

Publications arose from the other works involved

Zhu, X.Y., Liu, X.P., Tian, Y.L., 2014. Mathematical Modelling of a Droplet Sitting on Superhydrophobic Surface with Hertz Model. *Manipulation, Manufacturing and Measurement on the Nanoscale (3M-NANO), 2014 International Conference on*.

Mohamad, A.J., **Zhu, X.Y.**, Tian, Y.L., Wellington, E.M.H., Pfleging, W., Liu, X.P., 2014. Investigating the effect of surface topography on hydrophobicity and bacterial attachment on polystyrene. *Surface Topography: Metrology and Properties*, Volume 2, Number 2.

ABSTRACT

The aim of this PhD work is to investigate the effect of surface adhesion on the mechanical behavior of material subjected to nanoindentation. Nanoindentation is an effective technique to quantify the mechanical properties of various materials. However, surface adhesion becomes significant due to the increasing ratio of surface area to volume in nanoindentation environment, and thus it is appropriate to consider the effect of surface forces and adhesion in nanoindentation testing.

First, nanoindentation, as a “carrier” for surface adhesion, was deduced to quantify the mechanical properties of calibration materials. The calculated values of these objective mechanical parameters were compared to their typical values to justify nanoindentation.

Afterwards, this work employed a 2-D finite element method to investigate the effect of surface adhesion on hard elastoplastic materials subjected to cyclic loading-unloading. The elastoplastic material took two hardening manners, i.e. isotropic hardening and kinematic hardening. The surface force obeys the Lennard-Jones potential, which is incorporated into ANSYS as a user defined subroutine. The results demonstrated that surface adhesion can induce plastic shakedown in repetitive contact, regardless of the material hardening manner compared to its non-adhesive counterpart. This indicates the significance of the study on surface adhesion in miniaturized devices subjected to repetitive contact, e.g. micro-electronical-mechanical systems (MEMS) or nano-electronical-mechanical systems (NEMS).

Finally this work studied the effect of surface adhesion on the mechanical behavior of two soft materials (two kinds of biological cells) subjected to atomic force microscope (AFM) indentation, i.e. pancreatic MIN6 cell and hepatocellular carcinoma which were treated by calcimimetic R568 and fullerenol respectively. They were also indented by different AFM probes: MIN6 cell by spherical indenter, and cancer cell by Vickers indenter. First of all, surface adhesion was manifested by the negative value of indentation force. For MIN6 cells, both JKR and finite element method are used to fit the force-displacement curve obtained by AFM indentation. For hepatocellular carcinoma, the JKR model is adapted for the Vickers indenter, and the “adapted” JKR model is used to fit the force-displacement curve. The results showed that JKR model can best describe the unloading force-displacement behaviors of the indentation curves, where a new parameter, termed work of adhesion in addition to Young’s modulus was extracted. Moreover, the difference between two biological cells and their treated counterparts were detected in terms of the magnitudes of the extracted parameters, i.e. Young’s modulus and work of adhesion. This implies that the study on the surface adhesion has potential significance in terms of medical diagnostics.

The main contributions from the present research could be summarized as follows:

- i. For hard materials, this study presents a systematic investigation on the effect of surface adhesion on the shakedown behavior of two hardening materials, i.e. isotropic and kinematic hardening. The simulative results show that surface adhesion alone can initiate plastic deformation. In non-adhesive repeated contact, only elastic shakedown can occur while in adhesive repeated contact, plastic shakedown can occur, which indicate that surface adhesion force can alter the mechanical response of substrate

material subjected to repetitive indentation.

- ii. For soft materials, this work uses JKR model to fit the force-displacement curve, yielding a new parameter, i.e. *work of adhesion*, in addition to Young's modulus. In comparison to the Hertzian contact model, the JKR model provides obviously better fitting to the experimental results, indicating that the adhesion is significant in the cell interaction. Moreover, the difference between various biological cells could be characterized by the magnitude of *work of adhesion*, which implies that this parameter may also serve medical diagnostics.

NOMENCLATURE

- a contact radius, m
- a_c contact radius corresponding to occurrence of plasticity, m
- A contact area, m^2
- A_H Hamaker constant, J
- c length of radial crack, m
- C empirical ratio of hardness to yield stress
- D diameter of Brinell sphere, m
- E Young's modulus, Pa
- E_T Tangential modulus, Pa
- F applied force, N
- G shear modulus, Pa
- F_{off} pull off force
- F_c applied force corresponding to occurrence of plasticity, N
- F_{cap} meniscus or capillary force, N
- F_{chem} forces due to chemical bonds or acid–base interactions, N
- F_{el} electrostatic force, N
- F_{max} maximum indentation force
- F_{vdW} van der Waals potential, N
- E^* effective Young's modulus, Pa
- H hardness, Pa

$H(t)$ unit step function

J_2 second deviatoric stress invariant, Pa^2

$J(t)$ creep compliance, Pa^{-1}

K_e elastic component of stress intensity factor, $Pa \cdot m^{1/2}$

K_c fracture toughness, $Pa \cdot m^{1/2}$

K_i hardening parameters

K_r residual stress intensity factor, $Pa \cdot m^{1/2}$

k Boltzmann constant

h indentation depth, m

h_a depth of contact periphery, m

h_e elastic displacement of indenter during unloading, m

h_{ep} elastic displacement for an equivalent punch, m

h_p depth beneath the contact periphery, m

h_r depth of residual impression

h_{rp} depth of the residual impression for an equivalent punch, m

h_t maximum indentation depth, m

l length from center of impression to end of radial crack, m

n strain-hardening exponent, $0 \sim 1$

P indentation force, N

P_e elastic field component of applied

P_r plastic field component of applied

p contact pressure, Pa

- R radius of spherical indenter, m
- R_c radius of cell, m
- R_i radius of the spherical indenter, m
- R_p radius of probe, m
- R_r radius of curvature at the center of the residual impression, m
- r_0 radius of the *van der Waals* bond, m
- r intermolecular distance, m
- S plasticity parameter
- s_{ij} deviatoric stress, Pa
- T absolute temperature, $^{\circ}C$
- U_D *Debye* potential, J
- U_K *Keesom* potential, J
- U_L *London* potential, J
- U_p plastic energy, J
- U_{vdW} *van der Waals* potential, J
- x_V material constant
- Y first yield stress, Pa
- z_0 atomic equilibrium distance, m
- α half-face angle of indenter, $^{\circ}$
- $\Delta\gamma$ work of adhesion, J/m^2
- γ shear strain

δ indentation depth, m

ε strain tensor

ε_0 vacuum permittivity, F/m

ε_{eff}^p effective plastic strain

η viscosity, $Pa \cdot s$

λ transition parameter

μ Tabor parameter

ν Poisson's ratio

σ stress tensor, Pa

σ_{eff} effective stress, Pa

τ shear stress, Pa

ABBREVIATION

DMT Derjaguin-Muller-Toporov

JKR Johnson-Kendall-Roberts

M-D Maugis-Dugdale

MEMS Micro-Electronic-Mechanical-System

NEMS Nano-Electronic-Mechanical-System

1 Introduction

1.1 General Background

1.1.1 Application of Nanoindentation

It has been known for a long time that materials exhibit mechanical properties, e.g. elasticity, plasticity and hardness. The quantitative understanding of mechanical properties of materials is of significance of guiding for their application and precaution of failure, and they always involve some measurement techniques. For macroscopic materials, there are a number of methods to evaluate their mechanical properties of interest. For example, material hardness is measured by macroscopic indentation tests. In these tests, materials of interest are indented by an indenter of certain shape (e.g. Brinell sphere), resulting in residual indent. Hardness is calculated by dividing indentation force by area of the indent, which is measured by optical method in advance. In another instance, material of cylindrical shape is subjected to uniaxial loading to determine its elastic modulus and yield stress. However, for miniaturized materials or devices, e.g. MEMS, NEMS and biological cells, evaluation of mechanical properties by these methods may not always seem feasible enough in practice. Hence, the method for characterization of mechanical properties in nanoscale is critical for small scale materials.

In the last two decades, nanoindentation has proved an important technique to study mechanical properties of small materials volumes at nano and micrometer range. The general principle of nanoindentation is to indent the material of interest by a very small tip. The probe is applied with a pre-set force and the concurrent indentation depth is monitored. The

resulting force-displacement curve contains massive information from which many mechanical properties could be calculated, based on relevant theoretical models, such as elastic modulus, hardness, plastic or viscous parameter and fracture toughness. The indentation force used in nanoindentation usually ranges from micronewton to milinewton, and the indentation depth is in the order of nanometers. Different indenters can be used with different circumstances.

Compared to its macroscopic counterpart, the main advantage of nanoindentation is that it can access a very small material volume whose characteristic length can even be in the order of tens of nanometers. In this regard, nanoindentation is a useful technology to evaluate the mechanical properties of emerging small scale materials, e.g. nanotubes, nanoparticles and biological cells, etc.

1.1.2 Atomic force microscope

Atomic force microscope originally belongs to a series of scanning probe microscopes, and its initial function aims to image surfaces of materials and provide topographic characterization. These series start with scanning tunneling microscope (STM), which could be used to image surfaces of hard and soft synthetic materials as well as biological structures (tissues, cells, biomolecules), irrespective of opaqueness or conductivity^[1]. With STM, AFM can even image atoms on a flat surface and provide *in situ* imaging ability without moving the sample for scanning and imaging the sample^[2]. There are some extra functions in AFM derived from its imaging function. The Force modulation microscopy (FMM) is used widely for imaging composition changes in a composite material, analyzing polymer homogeneity and contaminants detection in manufacturing processes^[2]. Besides, two major dynamic AFM

modes are being developed to measure the topography of a sample surface, i.e. amplitude modulation atomic force microscope (AM-AFM) and frequency modulation atomic force microscope (FM-AFM)^[3]. The former is used in air or liquid environments while the latter is commonly used in ultra-high vacuum situation.

Besides maintaining its topography imaging function, AFM has evolved into a powerful tool for direct measurement of intermolecular force with atomic-resolution characterization, which makes AFM one of effective realizations for nanoindentation of biological cells (why AFM). Fig 1.1 shows diagram of AFM. The main components of AFM are laser, light meter, probe and scanner. The scanner is controlled by piezo electric elements. A laser light is positioned on the top of the cantilever and reflected to a position-sensitive photodetector (see the 4 quadrant photo detectors in Fig 1.1). By determining the reflected spot on it, this photo detector can calculate the bending and torsion deformation of the cantilever. Originally, the spot is in the center of the detector, and it will move as the cantilever deforms. As can be seen, signal $(A + C) - (B + D)$ on the detector represents the deflection of the cantilever whilst signal $(A + B) - (C + D)$ represents the torsion of the cantilever. While scanning, a topographic image of the sample is obtained by plotting the deflection of the cantilever against its position on the sample. On the other hand, the force between the tip and substrate is proportional to the deformation of cantilever (i.e. Hooke theory) which is related to the shift of the spot on the detector, i.e. the force F is function of the shift. Therefore, by recording the shift and transforming it to force by the function, one could obtain a force-displacement curve.

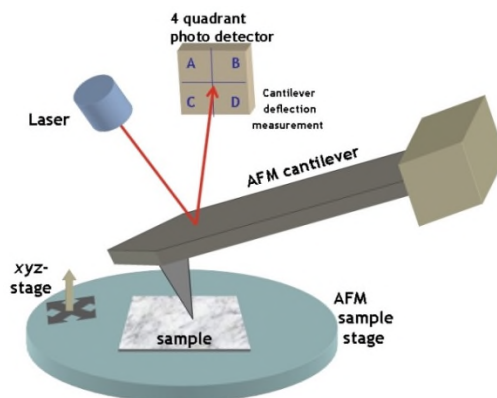


Fig 1.1 Schematic diagram of an atomic force microscope (AFM)^[4]

Owing to these factors, AFM proves an effective means to investigate the mechanical properties of soft biological cells due to its capability to measure intermolecular force with atomic-resolution characterization^{[5][6]}. The AFM tip of certain shape indents a fixed cell by pre-set force, and the concurrent displacement of tip is monitored. Usually the elastic modulus is obtained by fitting the force-displacement curve with an appropriate theoretical model. A mechanical model commonly used for extraction of elastic modulus is the Hertzian contact model, although one cannot expect that living cells do actually meet the assumptions of Hertz contact model. The extracted elastic modulus is not only an index of cell mechanical property, but has diagnostic significance. For example, comparison of the elastic modulus of normal human epithelial cell and their cancerous counterparts indicates that healthy cells have a Young's modulus of about one order of magnitude higher than their cancerous counterparts^[7]. After being treated by chitosan, the stiffness of the cancer cells increase, whereas normal cells are not influenced by chitosan in terms of elastic modulus^[8].

Moreover, AFM technique can be used to investigate adhesion forces in biological applications, such as cell-cell, cell-protein or protein-protein interactions^[2]. A quantitative investigation of these interactions plays a significant role not only in revealing the

mechanism of endocytosis^[9], but also in medical applications such as gene/drug delivery and medical diagnostics^{[10][11]}.

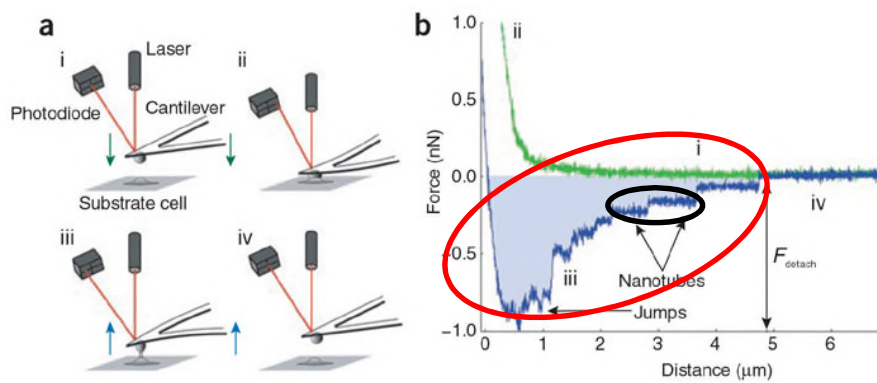
It should be borne in mind that AFM can not only be used in soft biological cells, but also in hard materials. The microelectromechanical (MEMS) system is the technology of miniaturized devices; it merges at the nano-scale into nanoelectromechanical systems (NEMS) and nanotechnology. The scale effect is one basic issue in designing MEMS. As its components dimension decreases, surface adhesion forces begin to emerge, due to the surface-to-volume ratio increase. Adhesion forces are associated with strong stiction and friction, rapid wear in MEMS which will reduce its life time^[12]. AFM is a valuable tool to study adhesion force and friction at the micro-and nano-level, and is widely used in testing anti-stiction coatings for MEMS^[13]. A typical application of AFM in MEMS should be ascribed to a direct test of the forces necessary to move single components of a MEMS device. Digital mirror devices used in digital projection displays (DMDs) are a typical MEMS device. AFM is employed to test the frictional and mechanical properties of DMD hinge and the force necessary to tile the mirrors^[14].

1.2 Existing Challenges

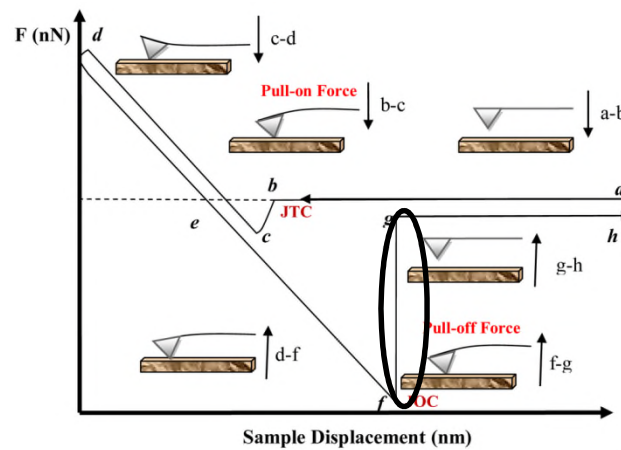
As mentioned above, in nanoindentation, the length scale may extend to micrometer or even nanometer range, and at this scale, surface adhesion force, which seldom manifests itself at macroscale, is likely to dominate other macroscopic forces, and plays a significant role in the determination of mechanical behaviors of materials. For one thing, the traditional mechanics, based on continuous medium hypothesis, does not take real surface morphology of material and surface forces between two bodies into consideration, and thus cannot provide

reasonable interpretations on surface effect. What is more, the successful application of chemical bond theory, which is based on quantum mechanics controlled by Schrödinger equations, has greatly developed nanomechanics, which is a challenge not only to traditional continuum mechanics but also to the basis of Newtonian mechanics. However, there are numerous mathematical difficulties in this quantitative investigation, e.g. it is always shrieved by massive calculations. Therefore, under the existing conditions the “from-macrocosm-to-microcosmic” method remains attractive. With endeavor by mechanics pioneers, the combination of traditional continuum mechanics and scale effect and surface effect has been greatly developed, making it probable to realize the establishment of micro/nano mechanics based on Newtonian mechanics. The relevant literature will be presented in the next chapter.

There are commonly two academic scopes which can manifest surface adhesion in contact: one is the negative detected force by AFM indentation on soft biological cells, and the other is to jump into and off contact in AFM indentation on hard materials, as shown by Fig 1.2 (a) and (b) respectively.



(a)



(b)

Fig 1.2 Adhesion-induced phenomenon in AFM indentation: (a) negative force in biological cells^[15] (b) jump instability in hard materials^[16]. For the soft material, pull off is manifested by stepwise unbinding events as circled by the black oval in Fig 1.2 (a), and it thus called “ductile” separation in this work. For hard materials, a sudden jump off manifests itself by the vertical line circled by black ellipse as shown in Fig 1.2 (b), and hence is called “brittle” separation in this work.

i. Atomic force microscope indentation on soft materials

As mentioned by Sec. 1.1.2, the Hertzian contact model is widely used to determine elastic property of soft biological cells by means of AFM indentation. However, this method is still very challenging, since no proper theoretical model accurately accounts for the complication of biological cells. At nanoscale, the effects of adhesion force on tip begin to emerge, which is manifested by the negative indentation force and cannot be interpreted by the non-adhesive Hertz contact model. Although AFM is used to measure the adhesion forces between adhesive cells, or cell/protein, these kinds of measurements always remain in the level where magnitude of explicit adhesion force is measured. For example, adhesion is

always characterized by maximum unbinding force (F_{max}) and work of detachment (W_D) (i.e. the shade area circled by red ellipse in Fig 1.2 (a)) obtained from force-versus-displacement curve (retraction part) by AFM indentation as illustrated in Fig 1.2 (a)^[17]. However, these two parameters may not be sufficiently intrinsic to characterize cell adhesion since both of them are dependent of some measurement means, e.g. the size and shape of the indenter. Therefore, it is essential to account for adhesion phenomenon in terms of a contact mechanics model analogous to the Hertzian contact model where some other parameter should be proposed to characterize adhesion rather than maximum unbinding force or work of detachment.

ii. Instability jump in AFM indentation on hard materials

For MEMS (or NEMS), adhesive contact between its components may initiate stiction which will lead to permanent failure of the devices as shown by Fig 1.3. There are some studies that investigate the adhesion-induced friction effects on MEMS devices by means of AFM as mentioned above. On the other hand, plasticity caused by surface adhesion can also occur in these systems, even without externally applied force^[18]. Since the components of MEMS are very likely to be subject to cyclic loading-unloading during service, the adhesion-induced plasticity may incur plastic shakedown, which can also lead to failure, and hence the investigation of the adhesion-induced plasticity behavior is of significant importance for these devices. To the best of our knowledge, there is little work that focuses on these two aspects in terms of contact mechanics.

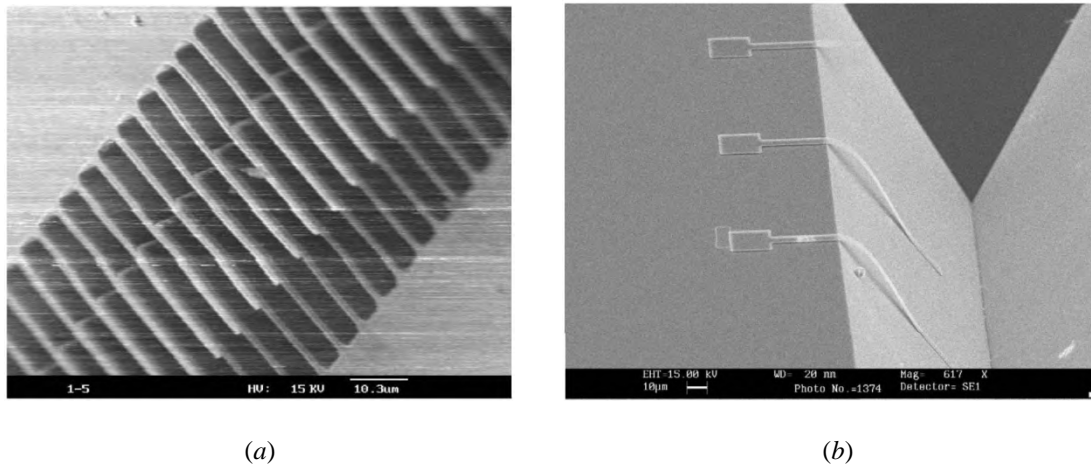


Fig 1.3 Example of adhesion failure in MEMS^[13]: (a) Stiction of micro-cantilevers to substrate. (b)

Adhesion between fingers of a comb structure in a micro-accelerometer.

From the above context, it may be seen that although the nanoindentation technique has been drawing attention from engineers and researchers, investigations on the effect of surface adhesion on small scale contact are rare or incomplete. In this regard, the present work endeavors to investigate the manifestation of surface adhesion at nanoindentation on soft biological materials and hard materials.

1.3 Objective and outlines of the Thesis

1.3.1 Objectives

The objective of this thesis is to interpret the following two issues.

- For hard materials, what is the exclusive effect that surface adhesion can exert on single and repetitive contacts in terms of mechanical behavior in small scale, compared to its non-adhesive counterpart.
- For AFM indentation on soft biological cells, can one utilize a theoretical mechanics procedure to quantitatively characterize adhesion between indenter and cell in terms of a

specific parameter, and what the form of this model will be if the AFM indenter changes its shape (e.g. from sphere to a pyramid) or the cell changes its shape (e.g. from sphere to a flat plate). Will this procedure have some potential benefits in terms of biomedical purpose?

1.3.2 Outlines of this thesis

The remainder of this work is arranged as follows.

In Chapter 2, a literature review is presented to introduce the development of macroscopic indentation. For nanoindentation technology, therelevant literature on how to extract mechanical parameters is reviewed. Then the highlights are given to several classic adhesive contact models, current computational methods to deal with adhesive contact and AFM indentation on biological cells.

Chapter 3 provides theoretical knowledge for adhesive contact. First, some fundamental concepts of intermolecular forces are introduced, and these forces are the foundation of adhesion between two contacting bodies. Afterwards, a system of contact models, i.e. Hertz model^[19], Bradley model^[20], JKR (Johnson-Kendall-Roberts) model^[21], DMT (Derjaguin-Muller-Toporov) model^[22] and M-D (Maugis-Dugdale) model^[23] is introduced in detail.

To fulfill the instrumentation part of research framework, in Chapter 4, deduction of quasi-static nanoindentation on several calibration materials, i.e. copper, fused silica, silicon wafer and polystyrene is presented, from which some mechanical parameters of interest are calculated. The determined parameters are compared with their typical values for

justification. A finite element method is used to simulate materials of interest subjected to quasi-static nanoindentation. The resulted force-displacement is compared with its experimental to identify some hypotheses in material constitutive relations.

In chapter 5, contact between a rigid sphere and an elastoplastic half-space is modeled to simulate contact between MEMS components. The adhesion force obeys Lennard-Jones force potential^[24]. Two basic strain hardening manners of substrate material, i.e. isotropic and kinematic hardening, are taken into consideration. Both single and cyclic loading-unloading are applied to adhesive contact, and the resulted mechanical responses are compared with its non-adhesive counterpart.

In the following two chapters, attention is given to the investigation of adhesion in AFM indentation on soft biological cells. In chapter 6, pancreatic MIN 6 cell is treated by calciummimetic *R568*, and both control (untreated) and treated cells are indented by spherical probe. Both JKR and “generalized” JKR model^{[25][26]} (with consideration of substrate thickness) are used to describe the unloading force-displacement behaviors of the indentation curves. A new parameter termed *work of adhesion* is employed to quantitatively characterize adhesion. The difference between control and treated cells is identified in terms of this new parameter, together with elastic modulus. Moreover, the unloading part of $F-d$ curve is fitted with that developed by finite element simulation in Chapter 5 for a further discussion.

In Chapter 7, human hepatocellular carcinoma cells are treated with fulleranol for 24, 48 and 72 hours. These four types of cells (including the untreated cells) are routinely indented by AFM whose cantilever tip is Vickers. A “transformed” JKR theory adapted to Vickers

indenter is introduced in advance. The adapted JKR model is adopted to fit the obtained force-displacement curves, resulting elastic modulus and work of adhesion. The difference between the four kinds of cells is also verified in terms of Young's modulus and work of adhesion. Although biological cells are involved, it should be borne in mind that this work treats biological cells as one material where adhesion is significant and thus no biological investigation is involved in this work.

Chapter 8 summarizes the conclusions of this thesis, as well as recommendations concerning future research in this area.

2 Literature Review

In this chapter, a literature review on the advent and development of indentation tests and nanoindentation technology is presented. Then, the classical theories of contact mechanics, i.e. Hertz model^[19], *Bradkey* model^[20], JKR model^[21], DMT model^[22] and M-D model^[23] will be introduced. Afterwards, simulative methods dealing with adhesive contact are reviewed. Finally, a review on AFM indentation on biological cells is given.

2.1 Brief History of Macroscopic Indentation

Indentation test has long been used for measurement of the mechanical properties of materials due to its ease and speedy implementation. Traditional indentation tests employ different shapes of indenters and loading methods, resulting in different standards of hardness. In this section, some common indentations tests are reviewed, and an approximate equivalent hardness conversion chart for different indentation tests is presented.

2.1.1 Brinell Testing: Spherical indenter

At the beginning of 20th century, indentation tests were widely performed by Brinell ball test^[27] to measure hardness of material. Concretely speaking, the material of interest is indented by a hard steel ball under a known load P , which is held for a predetermined time period and then removed. The Brinell hardness H_c is then calculated by dividing the load by the surface area of the indentation^[28], i.e.

$$H_c = \frac{P}{\pi D \delta} \quad (2.1)$$

where D and δ denote diameter of the ball and indentation depth respectively.

2.1.2 Shore testing: Dynamic measurement of hardness

For Brinell test, one disadvantage is that the measured hardness increases as the indentation force increases, which is ascribed to work hardening and increasing of contact area. To solve this problem, a device called scleroscope was invented by A. F. Shore^[29] in 1907. In this device, a diamond-pointed hammer falls under its gravity along a tube and strikes the materials of interest. The rebound height of hammer is recorded, from which the material hardness could be calculated. By repeating Shore scleroscope testing on the same spot, the hardness will increase with the number of tests, due to work hardening^[30].

2.1.3 Other indentation techniques

In 1919, Hugh M. Rockwell patented another technique for hardness measurement termed Rockwell testing^{[31][32]}. In this test, the diamond indenter is first applied with a minor force which gives zero or reference position. Afterwards, a major force is applied, and then released while still maintaining the minor load. The indentation depth variance between the minor value and major load value is then converted to hardness. Since 1920s, other different indentation tests were developed by means of using different macroscopic indenters. Vickers hardness tests^[33] use a square pyramid so that geometrical similarity could be maintained. Knoop testing was invented to meet the need to determine both the recovered and uncovered dimensions of the indentation impression^[34]. The Knoop pyramid has unequal length edges, with one diagonal being approximately seven times the other diagonal in length^[34]. For four-side indenter, the four edges in the residual impression cannot easily meet in one point,

and to counter this problem, a three-sided pyramid indenter termed Berkovich^[35] was invented. Since it is more readily fashioned to a sharper point than the four-sided pyramid geometry, the Berkovich indenter will certainly enjoy enormous popularity in the subsequent development of commercial indentation testers^[36]. Fig 2.1 shows an approximate equivalent transformation of different hardness standards with respect to Berkovich indentation testing.

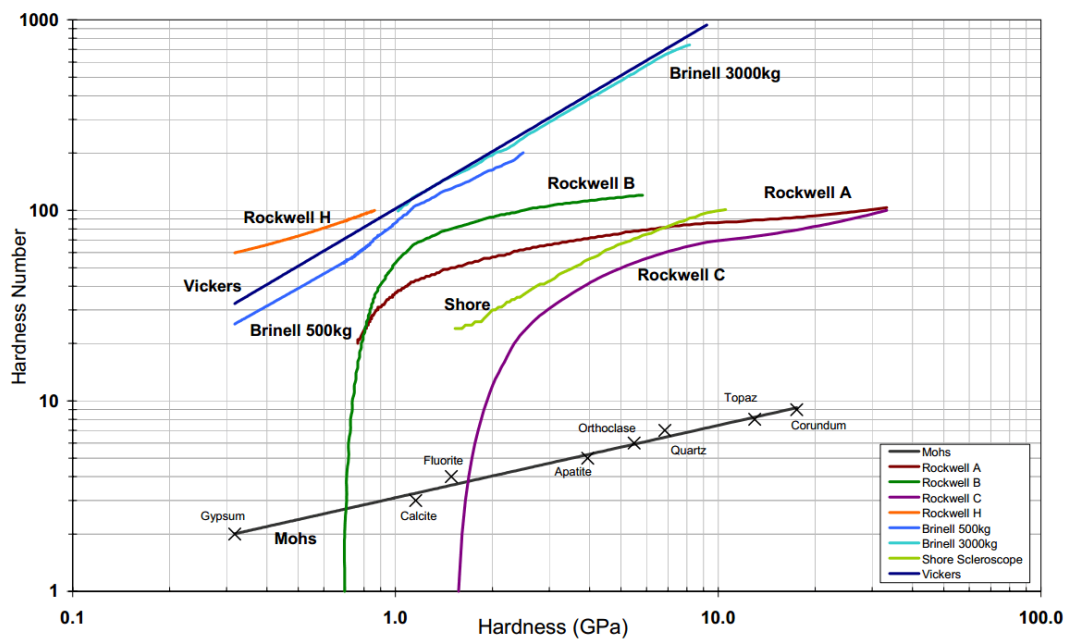


Fig 2.1 Approximate equivalent hardness translation chart for different standard hardness test with respect to Berkovich hardness^{[37][38][39]}.

2.2 Characterization of mechanical properties by nanoindentation

Nowadays, nanoindentation is one of the few experimental techniques that can directly access the mechanical properties of material at micro or even nano level. It was introduced as a means for extraction of elastic modulus and hardness by Oliver and Pharr^[40], by studying nanomechanical

response as a function of penetration depth^[41]. The materials involved in nanoindentation cover a wide range, including metal, glass, ceramics, and even biological materials. Owing to constant refinement, nanoindentation can also quantify many other mechanical properties. This section will review some of the relevant literature.

2.2.1 Young's modulus and hardness

The two mechanical parameters which are frequently determined by nanoindentation technique are Young's modulus and hardness. In 1992, Oliver and Pharr^[40] presented a method to calculate Young's modulus and hardness of materials by studying force-indentation depth curve. Their analysis considers the unloading part is purely elastic thus the Hertzian contact model could be applied to extract elastic modulus. Unlike macroscopic indentation tests, they developed an alternative method to determine contact area by measuring the penetration depth of indenter into the sample surface, rather than optical imaging method. This method undoubtedly facilitates the calculation of hardness of small scale materials. The detailed interpretation for this method will be presented in Sec. 4.2.1.

For Oliver and Pharr method, some literature focuses on secondary concepts of potential significance, including indenter geometry, sink-in and pile-up phenomenon.

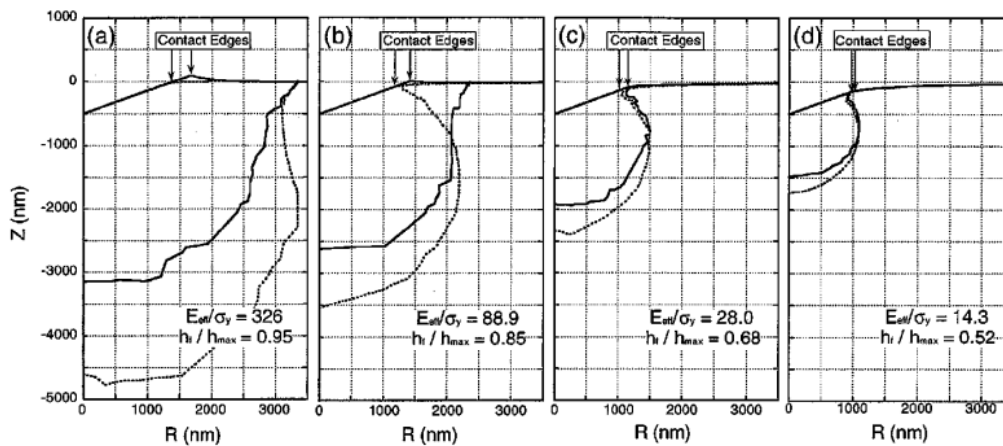
There are several different indenter geometries in common use. For macro-micro scale indentation, the frequently used indenters include Brinell sphere, Rockwell spheres, Vickers and Knoop pyramids. As mentioned before, the four-sided pyramid indenter has its disadvantage, in that the inevitable line of conjunction occurs across its tip, especially in small scale indentation. Berkovich and cube corner indenters, however, are appropriate for

nanoscale indentation, due to the fact that they can be shaped with very small tip radii by means of their three sided surfaces. Parameters of common indenters are summarized in Table 2.1.

Table 2.1 Parameters for common indenters^{[42][43]}

Indenter shape	Projected area	Semi-angle θ	Equivalent cone angle	Intercept factor ε	Geometry correction factor β
Sphere	$\approx \pi R h_p$	N/A	N/A	0.75	1
Vickers	$4h_p^2 \tan^2 \theta$	68°	70.3°	0.75	1.012
Knoop	$2h_p^2 \tan \theta_1 \tan \theta_2$	$\theta_1 = 86.25^\circ$ $\theta_2 = 65^\circ$	77.64°	0.75	1.012
Berkovich	$3^{3/2} h_p^2 \tan^2 \theta$	65.27°	70.3°	0.75	1.034
Cube Corner	$3^{3/2} h_p^2 \tan^2 \theta$	35.26°	42.28°	0.75	1.034
Cone	$\pi h_p^2 \tan^2 \theta$	θ	θ	0.727	1

For simulation convenience, pyramid indenters are treated as conical indenters with a cone angle, such that it gives the same depth-area functions as the pyramid. This allows the application of convenient axial symmetric elastic equations. This equivalent treatment is widely accepted, although there are contact solutions for pyramid indenters^{[44][45]}.

Fig 2.2 Plastic zone developed during indentation by conical indenter with different values of E_{eff}/σ_y .

The solid lines and dash lines denote elastic-perfect plastic and work hardening materials respectively^[46].

The Oliver and Pharr method is based on an elastic solution, and works well for hard ceramics when sink-in predominates, i.e. the substrate material around the indenter is well beneath the original undeformed surface. However, for soft materials undergoing high loads, the true contact area could be underestimated by up to 50% by using Oliver and Pharr method^[47]. On the other hand, pile-up (i.e. the substrate material around the indenter is above the origin surface after indentation) can also occur in material such as Al, which exhibit a low ratio of yield stress to elastic modulus and little or no strain hardening^[48]. This will result in overestimations of hardness and elastic modulus. Bolshakov and Pharr^[46] performed finite element simulation covering a wide range of elastoplastic materials in order to investigate the effect of basic mechanical parameters on this behavior. For materials with a high ratio of effective elastic modulus to yield stress E_{eff}/σ_y , pile-up is likely to occur, and increase the effective contact area as shown by Fig 2.2 (a) and (b). For materials with a low ratio of modulus to yield stress E_{eff}/σ_y , sink-in is prone to emerge, and decrease the effective contact area as shown by Fig 2.2 (c) and (d). Obviously these two behaviors cause significant error in measure contact area, and thus elastic modulus and hardness measurement.

Besides the famous Oliver and Pharr method, there are several other analyses that exist for interpreting force-displacement data from nanoindentation. M.Sakai^[49] suggested that the hysteresis loop energy U_p dissipated during the indentation loading-unloading cycle is related to the true hardness H , given as

$$U_p = \left(\frac{1}{3}\sqrt{\frac{1}{\pi \tan^2 \alpha}}\right) \frac{P^{3/2}}{\sqrt{H}} \quad (2.2)$$

where α and P denote the half-angle of the indenter and indentation load respectively. Thus hardness H can be extracted by measurement of U_p and P according to Eq. (2.2). Field and Swain^[50] presented a simple model which could describe the entire force versus the penetration behavior of indentation with a sphere, during loading and unloading in terms of four test material parameters, i.e. Young's modulus, Poisson's ratio, flow stress at the onset of full plastic flow and strain hardening index. Following Field and Swain, Fischer-Cripps^[51] presented the relationship between indentation force P and depth h during loading stage by using the Berkovich indenter, given as

$$P = E^* \left[\frac{1}{\sqrt{\pi \tan \alpha}} \sqrt{\frac{E^*}{H}} + \left(\frac{2\pi-4}{\pi}\right) \sqrt{\frac{\pi}{4}} \sqrt{\frac{H}{E^*}} \right]^{-2} h^2 \quad (2.3)$$

where E^* , H and α denote effective Young's modulus, hardness and half-angle respectively. E^* and H could be extracted by fitting the loading $F-d$ curve with Eq. (2.3).

The above studies focus on monolithic materials, whereas significant challenges emerge regarding measurement of the mechanical properties of thin films due to potential substrate effects. Although there are some analytical solutions for indentation on layered materials^{[52][53][54]}, they are either mathematically complicated or case limited. To encounter this issue, one can calculate elastic modulus and hardness from the initial part of the unloading curve and then extrapolate to zero indentation depth. Mecik et al^[55] summarized some empirical and semi-empirical formulae for extracting elastic modulus of thin films. Page et al^[56] used the continuous stiffness technique to study the mechanical properties of coated systems. When extracting film properties by nanoindentation, one needs to know how the substrate affects the measurements of films modulus and hardness. Thus, Saha et al^[57]

examined the effects of substrate on the determined mechanical properties of thin films by nanoindentation. They showed the effect of substrate on film hardness was negligible when soft films were coated on hard substrate. However, the substrate effect was observed when hard film was coated on soft substrate, which is due to substrate yields at indentation depths of less than the film thickness. To account for the substrate effect, there are several methods developed to describe the hardness of film-substrate systems. These models are based on the assumption that the composite hardness is determined by the weighted average of film and substrate hardness in proportion to the relative deformed areas or volumes. Substrate effects are often ignored by following a common rule of thumb that the indentation depth should be less than one tenth of the film thickness^{[58][59][60]}.

2.2.2 Fracture toughness

Neither elastic modulus nor hardness is unique parameters which could be determined by nanoindentation. It can also be used to characterize fracture toughness of materials and interfaces by analogy to that in conventional microscopic tests^[51]. This section reviews some of the literature which evaluates fracture toughness from the measurement of the sizes of surfaces.

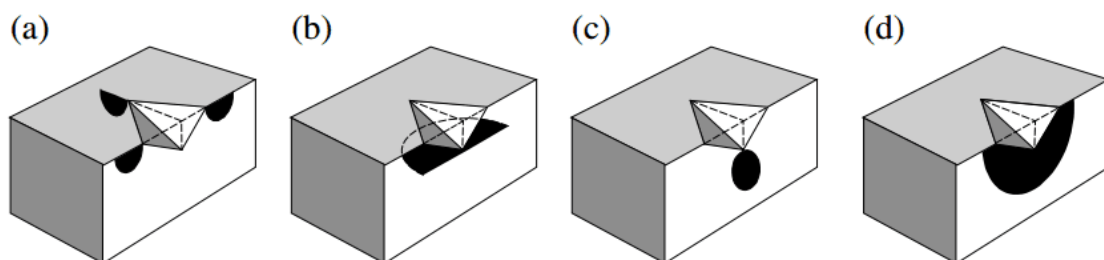


Fig 2.3 Crack systems for Vickers indenter: (a) radial cracks, (b) lateral cracks, (c) median cracks and

(d) half-penny cracks^[61].

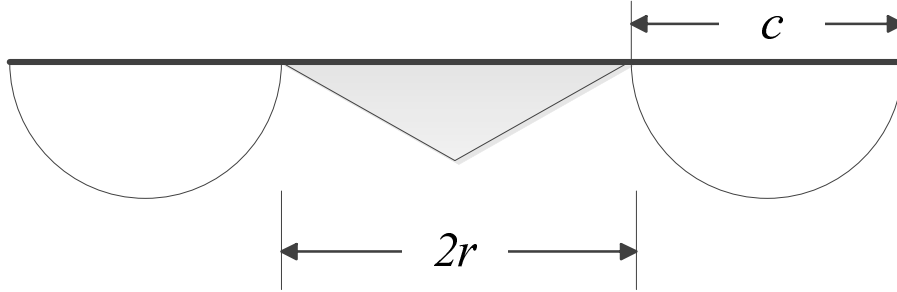


Fig 2.4 Schematic of radial crack from side view after removal of indenter.

Fig 2.3 illustrates four typical types of crack, among which radial cracks are very common in some tough ceramic materials whose lateral view is shown in Fig 2.4. Palmqvist^[62] observed that the radial crack length c is proportional to the force P . Marshall and Lawn^[63] noted this proportionality never held for median/radial crack system. They suggested that $P \propto c^{3/2}$, and they gave their expression for fracture toughness as

$$K_c = k \left(\frac{E}{H} \right)^n \frac{P}{c^{3/2}} \quad (2.4)$$

where $n = 0.5$, and k is an empirical constant equal to 0.017 ± 0.001 for median crack and 0.032 ± 0.002 for radial crack, respectively. Subsequently Anstis et al^[64] determined $n = 1.5$ and $k = 0.0098$ for Vickers-induced radial cracks. Laugier^[65] observed that crack behaviors in WC-Co composites were different from that in ceramics, and suggested that

$$K_c = x_V \left(\frac{l-c}{c} \right)^{1/2} \left(\frac{E}{H} \right)^{2/3} \frac{P}{c^{3/2}} \quad (2.5)$$

for WC-Co composites subjected to Vickers tip, where l is the distance from the center of residual impression to the end of the radial crack, and $x_V = 0.015$, is a material constant.

Dukino and Swain^[66] compared the load dependence of the radial cracks size of Vickers with

that of Berkovich and gave the Laugier expression for the Berkovich indenter as

$$K_c = 1.073x_V \left(\frac{l-c}{c}\right)^{1/2} \left(\frac{E}{H}\right)^{2/3} \frac{P}{c^{3/2}} \quad (2.6)$$

When the different models above are used to determine fracture toughness of material, one should be clear which one should be applied in terms of the indenter type, materials of interest and crack type in the exact nanoindentation. In Chapter 4, nanoindentation will be deduced on a calibration brittle material, and an appropriate model is chosen based on the specific circumstance.

2.2.3 Creep parameters

Real materials have more or less viscoelasticity property, which manifests itself as creep or relaxation phenomenon. In the nanoindentation of viscoelastic materials, time dependent creep always manifests itself as a variation of indentation depth under a constant applied load. The physical interpretation would be when viscoelastic materials are subjected to nanoindentation, the resulted stress field will yield chemical potential and diffusion fluxes which lead to the establishment of creep rate equation^[67].

In viscoelasticity, the constitutive relationship is always enlightened by the combination of spring and dashpot element. The spring element means that stress is proportional to strain, i.e. $\sigma = E\varepsilon$, whilst the dashpot element means stress is proportional to the rate of strain, i.e. $\sigma = \eta d\varepsilon/dt$, where η denotes viscosity. Different combinations of spring and dashpot elements represent different constitutive relationships, and Fig 2.5 shows three common models.

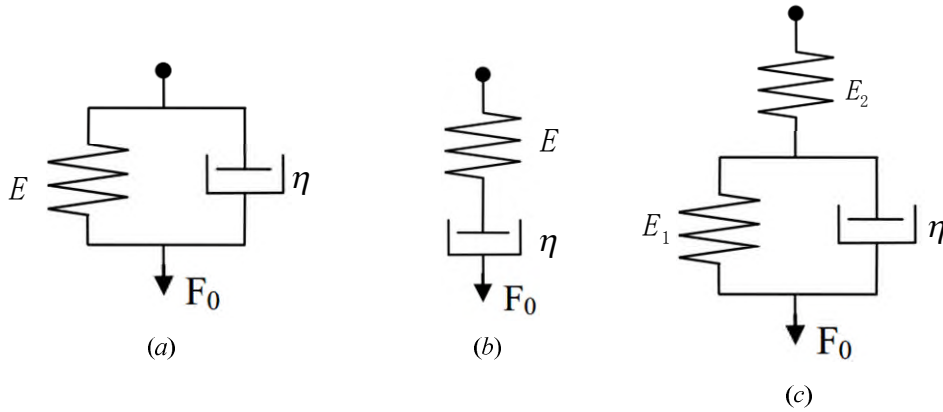


Fig 2.5 Different kinds of mechanical models: (a) Kelvin model (b) Maxwell model (c) three element model.

Nanoindentation is always abstracted as Boussinesq problem^[68], i.e. an infinite half-space is indented by an arbitrary shape of rigid axisymmetric frictionless punch. There are several analytical models for Boussinesq problem of viscoelastic materials. One of the pioneering studies of Boussinesq contact problem for viscoelastic materials is ascribed to Lee and Radok^[69]. They assumed the contact radius $a(t)$ is a monotonically increasing function of time, and replaced the elastic modulus in the elastic equations of Hertz contact with viscoelastic operators by correspondence principle. In 1966, Ting^[70] considered a more universal situation, i.e. the indenter is axisymmetric by otherwise arbitrary and the contact radius function $a(t)$ could be arbitrary, and gave its viscoelastic solutions. However, there are cumbersome integrals in Ting's solutions. Greenwood^[71] developed a relative simple analytical method by superposing an assembly of viscoelastic "Boussinesq" punch indentations provided that $a(t)$ is non-increasing. His method proved more convenient for the variation of the displacement of indenter during unloading.

When fitting creep curves to mechanical model, one should be clear what model is being

used and what parameters are to be measured. In chapter 4, an indentation will be performed on calibrating viscoelastic materials, and the aim is to set an example for determining viscoelastic parameters by nanoindentation.

2.2.4 Strain-Hardening exponent

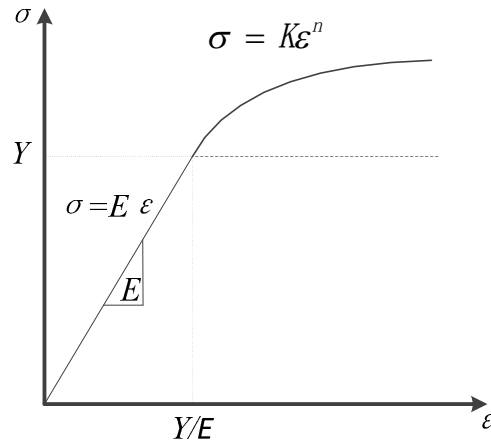


Fig 2.6 Stress-strain curve for elastic-plastic materials under uniaxial loading. Y denotes the initial yield stress beyond material begins to exhibit hardening with strain-hardening exponent n .

When the stress exceeds the yield stress Y , plasticity begins to occur in materials. However, the subsequent yield stress for some materials which has already undergone plastic deformation will increase if this material is unloaded and then reloaded, and this phenomenon is termed strain-hardening (or strain hardening). Strain-hardening is attributed to pile-up and interaction between dislocations in the material. During the hardening stage, power law is a common relation between stress and strain, i.e.

$$\sigma = Y\left(\frac{E}{Y}\right)^n \varepsilon^n \quad (0 \leq n < 1) \quad (2.7)$$

where n is strain-hardening exponent. For $n = 0$, the material is elastic-perfect plastic, and the corresponding stress-strain curve is denoted by the dash line in Fig 2.6. To determine the

strain-hardening exponent n , uniaxial loading method is always used. However, in many practical applications, uniaxial loading is not available or suitable (e.g. small scale materials). The nanoindentation test, as a non-destructive method, can then serve as an effective approach to measure the strain-hardening exponent. There are a number of methods to calculate the strain-hardening exponent. For indentation on power law isotropic hardening materials, Field and Swain^[50] suggested that the ratio of final contact radius a to critical radius a_c is related to the ratio of final load F to critical force F_c , given as

$$\frac{a}{a_c} = \left(\frac{F}{F_c}\right)^{\frac{1}{2+n}} \quad (2.8)$$

where critical force and radius correspond to first occurrence of yield. Shinohara et al^[72] performed ultral-microhardness (Hum) and Vickers hardness indentation on copper, aluminum and nickel. They observed that ultra-micro hardness Hum is function of load P , i.e. $Hum(P)$, and this function $Hum(P)$ systematically exhibits linear dependence on the strain-hardening exponent n . However, their model requires a number of measurements of hardness and load over a large range and also demands tensile tests. To counter these limitations, a generalized relation is given as

$$\frac{H(P)}{H_0(P)} = -0.83n + 0.95 \quad (2.9)$$

where $H_0(P)$ is the value of hardness corresponding to elastic-perfect plastic materials. Ahn and Kwon^[73] performed ball indentation on macroscopic scale and showed that work-hardening exponent played a main factor affecting the pile up/sink in phenomenon of various steels. For metals with low yield strain, this effect could be determined by a dimensionless constant c as

$$c^2 = \frac{a^2}{a^{*2}} = \frac{5(2-x)}{2(4+x)} \quad (2.10)$$

where a and a^* denote real contact radius and contact radius without pile up or sink in phenomenon respectively. The real contact radius is given by

$$a^2 = \frac{5(2-x)}{2(4+x)}(2Rh_c^* - h_c^{*2}) \quad (2.11)$$

where R and h_c^* denote the sphere radius and plastic depth without correction for pile up or sink in, respectively.

2.3 Adhesive contact in nanoindentation: surface and scale effect

As mentioned in Sec.1.2, surface effect plays a significant role in the mechanical behavior of material subjected to nanoindentation with a reduction of scale and surface roughness. This section presents a literature review that has been proposed for the characterization of adhesive contact. These studies consider the contact between two spheres or a sphere and an infinite half-space. They also provide methods for characterization of adhesion force data obtained from experiments, e.g. AFM indentation performed on biological cells.

2.3.1 Elastic adhesive contact between two bodies

There are several classic contact models that account for contact problems. The first analytical solution for non-adhesive contact problem (i.e. Boussinesq problem) is attributed to Hertz^[19], who solved the contact problem between two elastic spheres subjected to external compressed force. In 1932, Bradley^[20] investigated the adhesive effect on the contact between two rigid spheres and gave a formula for the pull-off force F_{off} i.e.

$$F_{off} = -2\pi\Delta\gamma R \quad (2.12)$$

where R is the reduced radius of curvature ($R = (1/R_1 + 1/R_2)^{-1}$, where R_1 and R_2 are the radii of curvature of the two spheres, respectively) and $\Delta\gamma$ is the work of adhesion ($\Delta\gamma = \gamma_1 + \gamma_2 - \gamma_{12}$,

where γ_1 and γ_2 are the surface energies of the two spheres, respectively, and γ_{12} is the interfacial energy). One of the first studies on adhesive contact between two elastic spheres is ascribed to Johnson et al^[21] (JKR model). In the JKR model, contact edge between two spheres is treated as an interfacial crack, and by requirement of equilibrium of crack propagation, applied force and mutual displacement of spheres are related by contact radius. The adhesion force is confined within the contact area, in conjunction with the Hertzian contact pressure, yielding a neck phenomenon at the contact periphery on the full off instant, and the pull-off force is

$$F_{off} = -\frac{3}{2}\pi\Delta\gamma R \quad (2.13)$$

In 1975, Derjaguin et al^[22] proposed another model for adhesive contact between two elastic spheres, known as DMT model. This model considers that adhesion force exists in an annulus area outside the contact region without deforming the surface profile. Estimation of pull-off force by DMT model is given as

$$F_{off} = -2\pi\Delta\gamma R \quad (2.14)$$

The discrepancy between these two models was mediated by Tabor parameter^[74] μ given as

$$\mu = \left(\frac{R\Delta\gamma^2}{E^{*2}z_0^3}\right)^{1/3} \quad (2.15)$$

where $E^* = [(1-\nu_1^2)/E_1 + (1-\nu_2^2)/E_2]^{-1}$ is the effective Young's modulus, (E_1 , ν_1 and E_2 , ν_2 denote the elastic modulus and Poisson's ratio of the two contacting spheres, respectively), and z_0 is the atomic equilibrium distance. In general, the DMT model holds for small and stiffer spheres ($\mu < 0.1$) whilst the JKR model is preferable for large and compliant spheres ($\mu > 5$)^[75]. Maguis^[23] used Dugdale theory of fracture mechanics, and presented an analytical solution corresponding to the transition between DMT and JKR model, which is known as

M-D model. Johnson and Greenwood^[76] presented an adhesive map specifying the valid regions of above five contact models.

The M-D solution is relatively cumbersome, and may not be feasible enough for comparison with experimental data such as atomic force microscope (AFM) measurements, and there are some studies extended from M-D model. Some simpler equations which approximate M-D solutions are presented by subsequent studies^{[77][78]}. In 1998, Greenwood and Johnson^[79] developed an alternative to the M-D model, termed double-Hertz model. Based on M-D model, Shi and Polycarpou^[80] developed a model which considers adhesive transition from noncontact to contact of elastic spheres, and their model is known as EMD model (enhanced M-D model). Schwarz^[81] presented an approximate description of intermediate regime by combining the successful assumptions of JKR and DMT models in an adapted form.

Following the study by Tabor^[74], there is a body of literature reviews^{[82][83][84]} dealing with the discrepancy between JKR and DMT models. As advised by Tabor, more novel experiments and critical theories rather than polemics were needed. Therefore, in 1980 Muller et al^[85] specified Lennard-Jones law of force as the interaction between contacting surfaces, and developed a self-consistent numerical analysis to describe behaviors of two contacting elastic spheres. The transition from DMT model to JKR model was realized by increasing the Tabor parameter. Furthermore, Muller et al^[86] pointed out that the exact form of molecular interaction law will not affect the two extremes of the transition, i.e. JKR and DMT models. In 1992, Attard and Parker^[87] presented self-consistent solutions with more numerical calculations, and showed the pull-off force is dependent on the history of the sample, and

increases with increasing maximum applied loads. The numerical solution was repeated more accurately and in greater details by Greenwood^[75], who showed that the force-displacement curve becomes S-shaped with $\mu > 1$, leading to jump in and out of contact. In order to enhance the convergence rate, Feng^[88] used an arc-length continuation algorithm which could accurately determine jump in and off behavior of contacting bodies when Tabor parameter is large.

In addition, FEM presents an effective method to solve self-consistent numerical issues. In 2004, Cho and Park^[12] modeled the adhesion force as a body force derived from Lennard-Jones 12-6 potential, and included it as subroutine in FEM. Their results showed that the dependence of pull-off force on the sphere radius is consistent with that by M-D model. Radhakrishnan and Mesarovic^[89] performed comprehensive and accurate finite-element modelling on adhesive contact. They proposed a modified Tabor parameter, in terms of which they provided meaningful discussion of the number of governing parameters for adhesive contact. There are also some studies with consideration of non-linear elasticity or inhomogeneous elasticity. Lin and Chen^[90] presented finite element modelling on adhesive contact between two spheres whose constitutive relations are hyperelastic, and developed a JKR test of soft elastic materials taking large deformation into consideration. Jin et al^[91] performed finite element modelling on adhesive contact of power-law graded elastic (i.e. elastic modulus of materials varies spatially) solids, and realized DMT-JKR transition.

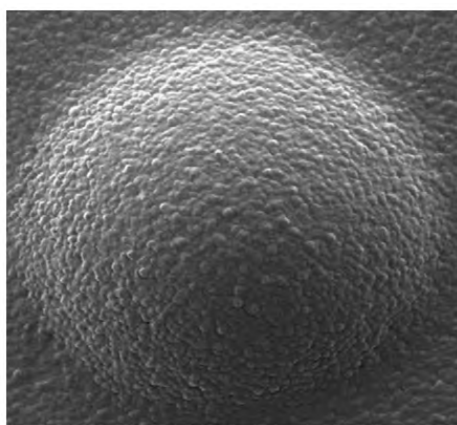
2.3.2 Elastoplastic adhesive contact between two bodies

The above literature concerns elastic deformation, however plastic deformation could occur

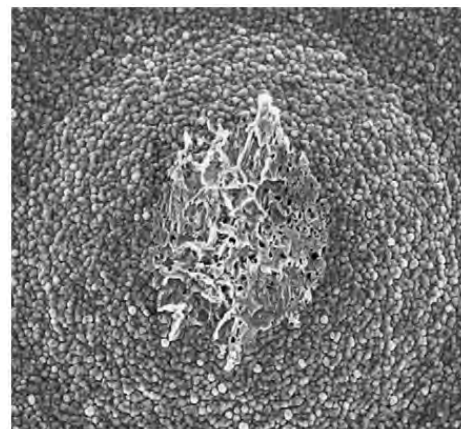
in real adhesive contact. Pashley et al^[92] indented a pointed stylus of tungsten against a nickel surface in ultrahigh vacuum, with load ranging from 0.5 to 1000 μN . With clean surfaces (strong adhesion), their experimental results suggested that surface forces alone can initiate plastic deformation. Chowdhury and Pollock^[93] performed Titanium-Titanium contact in ultrahigh vacuum ($0.1\mu Pa$), and their results suggested that plastic deformation can also occur at the micro-asperities of rough surfaces without external load.

Besides experimental investigations, there are several analytical studies concerning adhesive contact of elastic-plastic materials with some simplifications. With JKR concept, Maugis and Pollock^[18] reviewed the role of surface forces on deformation and adherence of metal micro contacts, and concluded that the stresses caused by surface force alone may be high enough to initiate plastic deformation around Hertz point. Chang et al^[94] considered Lennard-Jones law of forces acting on surface outside the contact area, and presented an elastic-plastic asperity model analyzing adhesive contact of rough surfaces based on volume conservation. Mesarovic and Johnson^[95] examined the decohesion of two adhering elastic-plastic spheres undergoing mutual indentation beyond elastic limit. They assumed the two contacting bodies only follow elastic deformation during unloading, adapted both JKR and M-D models to treat the adhesive contact, and finally provided a decohesion map which describes the effect of different physical mechanisms on decohesion. Gu and Lee^[96] investigated the adhesive contact of a rigid sphere and an elastic-perfectly plastic half-space. By taking the variation of curvature within the contacted surface into consideration, they showed that the plastic pull-force within the contact area is higher than that calculated based on a constant curvature.

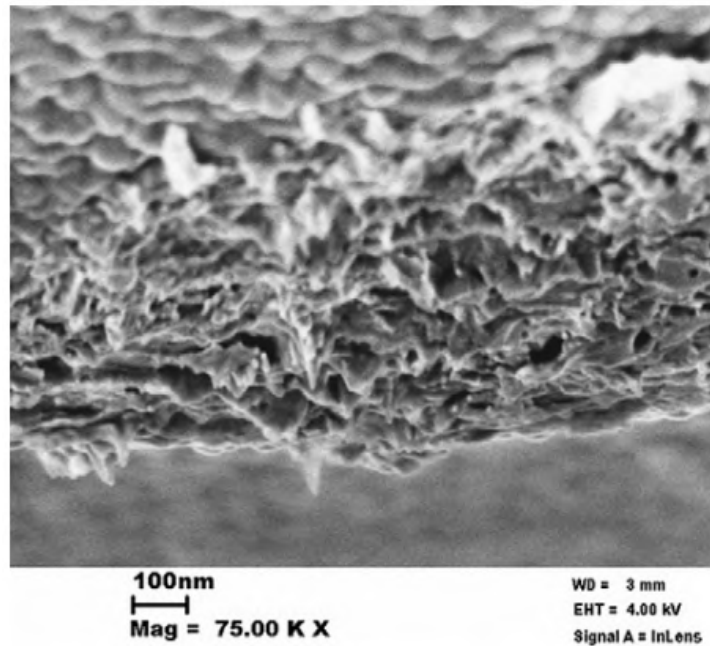
Thanks to FEM, numerical models and related approaches provide an effective way to study elastoplastic behavior of contacting bodies subjected to adhesive contact. Kogut and Etsion^[97] relieved some assumptions by Chang et al^[94], and used the finite element method to calculate the separation outside the contact area. Du et al^[98] performed finite element modelling on loading and unloading of adhesive contact between elastic-plastic spheres (made of ruthenium and aurum), which exhibit linear strain-hardening. They identified ductile separation (with plasticity) for ruthenium and brittle separation (pure elasticity) for aurum (see Fig 2.7) respectively. Kadin et al^{[99][100]} also used FEM to investigate loading and unloading of adhesive contact between rigid flat and elastic-plastic sphere, which, in any case, obeys linear kinematic hardening, and provided meaningful discussion of elastoplastic behaviors in terms of plastic shakedown. In their study, nonlinear spring elements were employed to model the adhesion force, which obeys Lennard-Jones potential. However, as Tabor parameter increases (e.g. $\mu > 2$), nonlinear spring elements will cause a convergence problem in FEM, and thus this work resorts to other solutions to describe interfacial forces and ensure convergence at the same time.



(a)



(b)



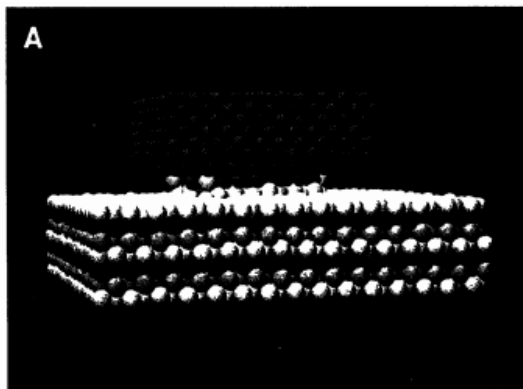
(c)

Fig 2.7 Scanning electron microscope (SEM) images of an aurum contact bump cycled at force of 200 μN . (a) The original bump before cycling; (b) the bump after several cycles and (c) its zoom in titled at 85°. The difference of surface topographies corresponding to (a) and (b) is due to adhesion forces^[98].

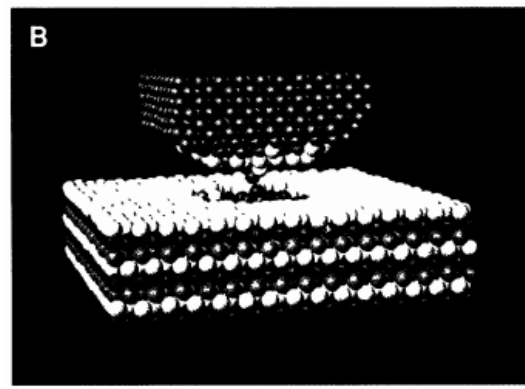
2.3.3 Solutions of Micro/Nano contact by molecular dynamics

The literature in Sec. 2.3.1 and 2.3.2 investigates adhesive contact in terms of combination of classic continuum mechanics and interfacial force, and besides molecular dynamics simulation (MDS) proves another effective method. In 1990, Landman et al^[101] used molecular dynamics simulation to investigate the atomistic mechanisms of adhesion, contact formation, nanoindentation, separation and fracture which occurred between a nickel tip and a gold surface, as shown by Fig 2.8. They recorded indentation force and energy in terms of the distance between tip and substrate, and pointed out jump in/jump out, neck, and hysteresis of force compared with displacement during separation. Leng et al^[102] conducted molecular

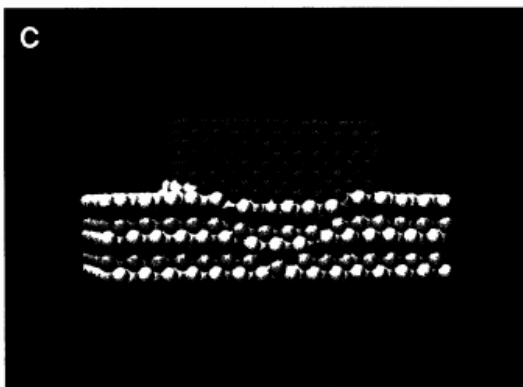
dynamics to simulate the two-dimensional adhesive contact between a flat-ended wedge and an elastic half-space. They showed that the pull off forces for contacting surfaces to peel apart conform well to those predicted by classic continuum mechanics. Zhu et al^[103] performed molecular dynamics to model adhesive contact between rigid cylinders with different radii and elastic substrate. Their simulation results showed that adhesive hysteresis phenomenon becomes significant as tip size increases at jump in and off instants, and adhesion forces have a significant effect on contact process corresponding to tip of small size. It is worth our attention that these results are also consistent with those by classic continuum mechanics.



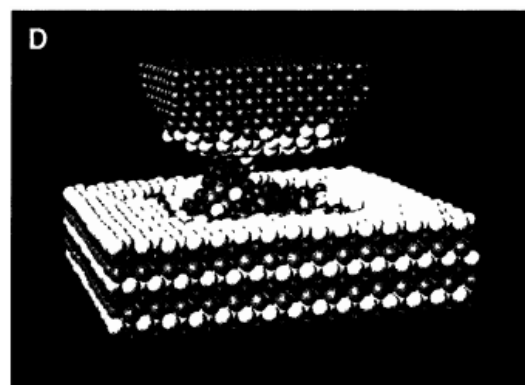
(a)



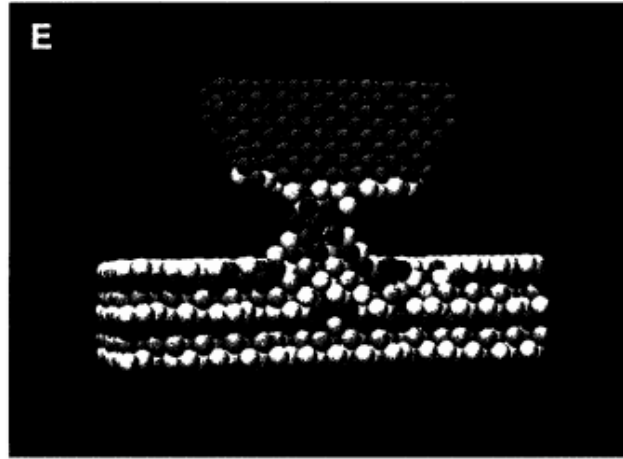
(b)



(c)



(d)



(e)

Fig 2.8 Atomic configurations of indentation between nickel indenter and aurum substrate^[101].

2.4 Application of AFM on biological materials

To date, there has been a variety of testing techniques and associated models in the field of experimental nanomechanics on biological cells. As is described in some reviews in the literature^{[104][105][106]}, these techniques include cell poking, the micropipette aspiration technique, optical and magnetic tweezers, biomembrane force probe (BFP) and atomic force microscope. Although these techniques may vary in terms of operating principles, force and displacement resolutions and magnitude of deformation^[105], their fundamental method is to apply biological cell with pre-set force and monitor the concurrent deformation.

Among these techniques, AFM was invented by Binning et al^[107] in 1986 with the function to explore surface topography. Soon, AFM evolved into a powerful tool for direct measurement of micro-structural parameters and unraveling intermolecular forces at nanoscale. Since it has the capability of operating at very high resolution in a liquid environment^[108], it is widely used to characterize surface topography, mechanical and interfacial properties of biological cells.

2.4.1 Application of AFM indentation on probing cell elasticity

By performing AFM in force spectroscopy (AFM-FS) mode with appropriate cantilever tips, AFM can indent specific points on the cell surface. The elastic modulus of cell can be extracted by fitting the force-displacement curve with an appropriate model. The first measurement of microelastic properties of animal tissue (hydrated cow tibia) by AFM indentation is ascribed to Tao et al^[109]. Dramatic variations in elastic properties across distances as small as 50 nm could be observed at high resolution. Radmacher et al^[110] performed AFM indentation (conical indenter) on cardiomyocytes, and applied Hertz contact model to determine the elastic modulus, which provides measurements of elastic properties of living cells in general.

Elson^[6] suggested that mechanical properties play a significant role in cellular processes and can serve as indicators for cellular process. Ohashi et al^[111] investigated the elastic modulus of bovine endothelial cells exposed to shear stress using an atomic force microscopy (AFM) and the finite element method (FEM). Their results showed that although the elastic moduli for control and sheared cells determined by means of FEM were higher in comparison to Hertz model fitting by a large margin, the tendency of elastic modulus between the two kinds of cells remained the same. Kuznetsova et al^[112] reviewed AFM applications for study of elastic modulus of intact cells associated with different cell events, and presented an analysis of local mechanical characteristics of different cells. Li et al^[113] carried out AFM indentation to characterize elasticity of benign and cancerous human breast epithelial cells, and showed Young's modulus of malignant breast cells was significantly lower than their non-malignant counterparts. Cross et al^[114] investigated the nanomechanical property of lung,

breast and pancreas cancer directly taken from patients by AFM. The results showed that the elastic modulus of metastatic cancer cells was more than 70% softer, with a standard deviation over five times narrower, than the benign counterparts. Thus, they indicated that mechanical analysis could distinguish cancer cells from their benign counterparts despite that they exhibited similar shapes.

2.4.2 Investigation of cell adhesion by AFM indentation

Generally speaking, AFM can allow high resolution force measurements over a large range (5pN-100nN) for displacement up to 100 μ m. Hence, it has proved an effective tool for studying many biological applications such drug/protein interactions, protein/protein interactions, cell/cell or cell/protein interactions and many biological phenomena governed by intermolecular forces^[22]. An investigation of the interfacial adhesion in molecular level is an essential part of revealing these phenomena. By using AFM indentation, Dammer et al^[115] measured binding forces intrinsic to adhesion molecules to assess their contribution to the maintenance of the anatomical integrity of multicellular organisms. Lee and Marchant^[116] measured the debonding interaction forces between RGD peptide-modified AFM probe tip and a human platelet surface from pN to nN levels of force. The results showed a considerable extension in the flexible sample surface during detachment process. By increasing pulling range in AFM, Puech et al^[117] presented a new technical method to quantitatively study cell-cell adhesion events. Friedrichs^[118] presented atomic force microscopy (AFM)-based single-cell force spectroscopy (SCFS) for quantitative study of cell adhesion, and they showed that AFM-based SCFS exhibited a more versatile force range of detection compared

to other SCFS assays. Analogous to AFM-based elasticity characterization which could serve as an index for cell physiological status, some studies also adopt cell adhesion as indicator for cell identification. Siamantouras et al^[17] used a new method to quantify mechanical and interfacial properties of MIN6 cells treated by calcimimetic R568 using AFM based SCFS. By investigating the maximum unbinding force and work of detachment, their results showed calcimimetic R568 increased cell-to-cell adhesion parameters and elastic modulus of single cells.

2.5 Summary

This chapter reviews the development of macroscopic indentation history, nanoindentation techniques, methodology on adhesive contact and application of AFM techniques on biological cells.

In Sec. 2.1, several macroscopic indentation tests were introduced and reviewed in terms of indenter shapes and characteristics.

In Sec. 2.2, nanoindentation technique was reviewed in terms of its application on measurement of mechanical properties: elastic modulus, hardness, fracture toughness, creep parameters, and strain-hardening exponent.

To provide preliminary for surface adhesion in nanoindentation, Sec. 2.3 reviewed some classic adhesive contact models, finite element method based simulation and molecular dynamic based simulation concerning adhesive contact. Studies combining surface adhesion with material plasticity, inhomogeneity and nonlinearity were also reviewed. This literature is of guiding significance for this work in terms of numerical simulations, analytical solutions

and experimental procedures of adhesive contact.

In Sec. 2.4, several techniques on measurement of cell mechanical properties were glimpsed. Multiple function of AFM was mentioned. Some typical literature investigates the mechanical properties of biological cells were reviewed. Finally, a review of studies of cell adhesion by AFM indentation was presented, which is of guiding significance for chapter 6 and chapter 7 of the present thesis.

The limitation of present research of is listed as following:

- For hard materials, this work assumes that the substrate materials obey isotropic or kinematic hardening. The hardening behavior of metal is much more complicated, e.g. it might be the combination of isotropic and kinematic hardening.
- For soft materials, i.e. biological cells in this work, the cell is treated as homogeneous while they are inhomogeneous in reality (it is comprised of cytoplasm, cytomembrane and cell nucleus). Therefore, the modeling of cell in this work corresponds to a gobal equivalent treatment.

3 Theoretical Background

This work mainly concentrates on surface forces, however it is essential to present its origin, i.e. intermolecular forces, without which it may seem very groundless. In this chapter, the first section presents some fundamental concepts about intermolecular forces, including its mechanism and mathematic expressions. Then, based on Lennard-Jones potential, the force between two surfaces is formulated. The second section introduces several classical contact models based on continuum contact mechanics, e.g. Hertz model^[19], JKR model^[21] and DMT model^[22].

3.1 Intermolecular and Surface Forces

3.1.1 Forces between two molecular (atoms)

It is a common sense that there are four types of forces in nature: in decreasing order of intensity, *strong interaction*, *electromagnetic force*, *weak interaction* and *gravitation*. The forces between atoms (or molecules) belong to the second category, which can be divided into strong bonds (i.e. its rupture needs a large absorption of energy, approximately 10^2 kcal/mole) and weak bonds (1-10 kcal/mole).

The strong bonds have the following types

- *Ionic bond*. This is a type of chemical bond due to electrostatic attraction between oppositely charged ions.
- *Covalent bond*. This bond is also a chemical bond involving the sharing of electron pairs between atoms.

- Metallic bond. This is a result of electromagnetism and describes the electrostatic attractive force that occurs between conduction electrons and positively charged metal ions.

The weak bonds include:

- *Keesom force*: force between two permanent dipoles.
- *Debye force*: force between a permanent dipole and a corresponding induced dipole
- *London dispersion force*: force between two instantaneously induced dipoles.
- *Hydrogen bond*: attraction between the lone pair of an electronegative atom and a hydrogen atom that is bonded to nitrogen, oxygen, or fluorine.

Generally speaking, Keesom, Debye and London dispersion forces are grouped together and termed *van der Waals* forces. They include attractions and repulsions between atoms, molecules, and surfaces, as well as other intermolecular forces. They are different from covalent and ionic bonding, in that they are caused by correlations in the fluctuating polarizations of nearby particles. Although *van der Waals* forces are weaker compared to covalent ionic bonds, they play a significant role in fields as diverse as supramolecular chemistry, structural biology, polymer science, nanotechnology, surface science, and condensed matter physics. For example, *van der Waals* forces determine the stability and the coagulation of colloids, in the physisorption of a molecule onto a surface.

The *van der Waals* force between atoms and/or molecules is the sum of the three different forces, which are all proportional to $1/r^6$, where r is the distance between atoms or molecules.

The corresponding potentials are *Keesom* potential $U_K(r)$, *Debye* potential $U_D(r)$ and *London* potential $U_L(r)$ whose expressions, given as

$$U_K = -\frac{1}{(4\pi\epsilon_0)^2} \frac{2\mu_1^2\mu_2^2}{3kT} \frac{1}{r^6} \quad (3.1)$$

$$U_D = -\frac{1}{(4\pi\epsilon_0)^2} \frac{\alpha_{02}\mu_1^2 + \alpha_{01}\mu_2^2}{r^6} \quad (3.2)$$

$$U_L = \frac{1}{(4\pi\epsilon_0)^2} \frac{3\alpha_{01}\alpha_{02}h\nu_1\nu_2}{2(\nu_1+\nu_2)r^6} \quad (3.3)$$

where ϵ_0 — vacuum permittivity

μ_i ($i = 1,2$) — the i th dipolar moment

k — Boltzmann constant

T — absolute temperature

r — distance between two molecules (atoms)

α_{0i} ($i = 1,2$) — electronic polarizability

$h\nu_i$ ($i = 1,2$) — first ionization energy of the molecules, where h denotes Planck constant

The total *van der Waals* potential energy U_{vdW} is the sum of the above three terms, i.e.

$$U_{vdW} = U_K + U_D + U_L = -\frac{C}{r^6} \quad (3.4a)$$

and the *van der Waals* force F_{vdW} is

$$F_{vdW} = \frac{dU_{vdW}}{dr} = \frac{6C}{r^7} \quad (3.4b)$$

where C is the constant in the atom-atom pair potential.

Actually, the energy of interaction does not tend towards infinity as indicated by Eq. (3.4) as r approaches zero. The reason is a repulsive force emerges when the electronic clouds begin to overlap, as if the molecules were impenetrable. One of the usual empirical equations for the energy of interaction is *Lennard-Jones* Potential^[119], given as

$$U = \frac{D}{r^{12}} - \frac{C}{r^6} = 4U_0 \left[\left(\frac{a}{r}\right)^{12} - \left(\frac{a}{r}\right)^6 \right] \quad (3.5)$$

where r is the distance between the two molecules (atoms), a is the distance at which the

potential is minimum, and U_0 denotes the minimum potential energy, i.e. $U_0 = C/2r_0^6$ where $r_0 = 2^{1/6} = 1.12a$. r_0 defines the radius of the *van der Waals* bond (approximately 0.1-0.2 nm). Fig 3.1 and 3.2 show the variation of normalized *Lennard-Jones* potential energy and interaction force versus normalized intermolecular distance, respectively. As can be seen from Fig 3.1 and 3.2, the total intermolecular potential and force are obtained by summing up both the repulsive and attractive components, and the range of repulsive potential (force) is shorter than its attractive counterpart.

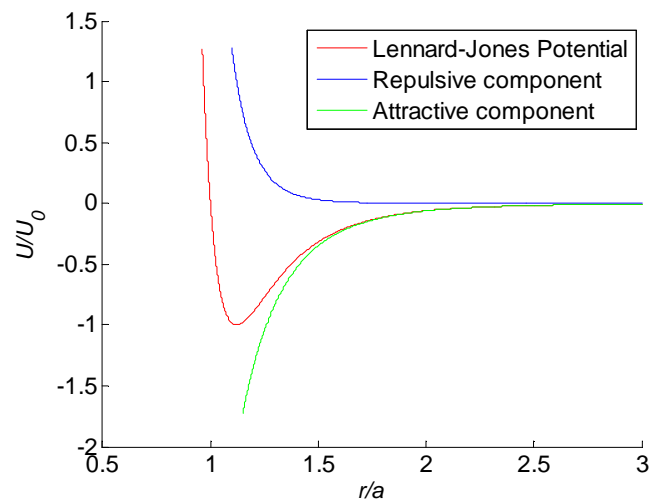


Fig 3.1 *Lennard-Jones* potential versus distance between two molecules (atoms) in reduced coordinates.

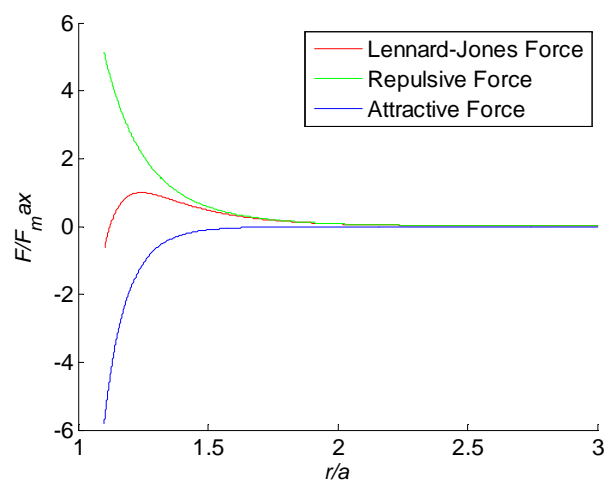


Fig 3.2 *Lennard-Jones* force versus distance between two molecules (atoms) in reduced coordinates.

3.1.2 Force between two surfaces

In general, the adhesion force F_{ad} is a combination¹ of the electrostatic force F_{el} , the *van der Waals* force F_{vdW} , the meniscus or capillary force F_{cap} and forces due to chemical bonds or acid–base interactions F_{chem} , i.e.

$$F_{ad} = F_{el} + F_{vdW} + F_{cap} + F_{chem} \quad (3.6)$$

However, the predominant component of adhesion force varies at different circumstance. In gaseous environments, capillary force always exists due to capillary condensation and adsorption of thin water films at surface. This attractive interaction is dependent on the relative humidity and the hydrophilicity of tip and sample. Therefore in dry conditions, the capillary force will disappear and *van der Waals* force and electrostatic force become the dominant. In aqueous solutions, most surfaces become charged due to dissociation of surface groups and electrostatic forces are important. However, the magnitude of electrostatic force is also dependent on electrolyte concentration and in distilled water it will disappear (so as capillary force), leaving *van der Waals* force as the main component of adhesion force. If chemical end-groups exist on the surfaces, chemical bonds may form during contact of surfaces, and chemical interactions dominate the adhesion force. After all, *van der Waals* force always contributes in most adhesive cases, and thus deserves our attention.

3.1.2.1 *Van der Waals* force between two semi-infinite planes

Before calculating the interaction force between two surfaces, consider the force between a single molecular (atom) and a plane as schematically illustrated in Fig 3.3. A sole molecule M (atom) is situated by a distance d from an infinite half-space which has n molecules per unit volume (i.e. molecular density). A is an ordinary molecule (atom) within the plane, and its

distance from M is r . α is the plane which contains A and parallel to the surface plane, and the distance between M and plane α is z . Point O is the projection of M on plane α . θ denotes the angle $\angle AMO$.

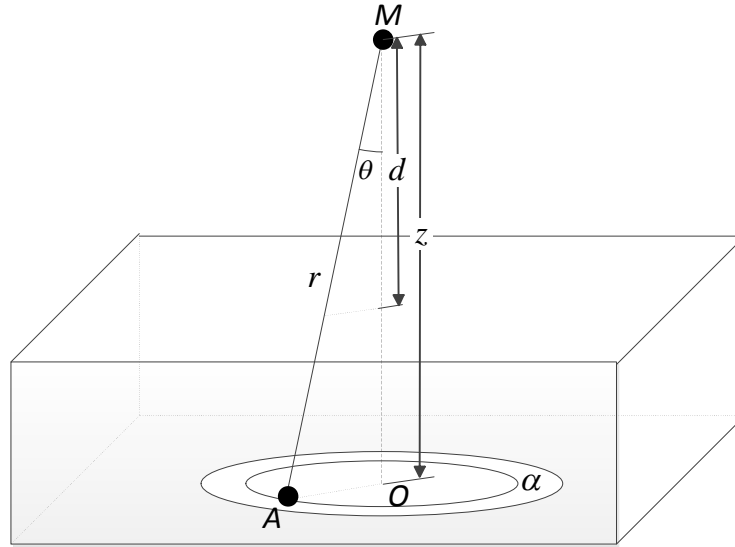


Fig 3.3 Schematic of the *van der Waals* force between a single molecule (atom) and a semi-infinite space

The projection of the attractive between M and A on OM (vertical direction) is, from Eq. (3.4b),

$$F_{OM} = \frac{6C \cos \theta}{r^7} \quad (3.7)$$

The volume of the infinitesimal annulus is

$$dV = 2\pi z^2 \frac{\sin \theta}{\cos^3 \theta} d\theta dz \quad (3.8)$$

Since *van der Waals* force can be added up, the sum of the vertical component of the attractive force within this infinitesimal annulus is

$$dF_{OM} = \frac{6C \cos \theta}{z^7} \cos^7 \theta n dV = \frac{12\pi n C}{z^5} \cos^5 \theta \sin \theta d\theta dz \quad (3.9)$$

Integrating the attractive force between a molecule and a semi-space yields

$$F_{molecule-plane} = \int dF_{\overline{OM}} = 12\pi nC \int_{z=d}^{\infty} \frac{dz}{z^5} \int_{\theta=0}^{\pi/2} \cos^5 \theta \sin \theta d\theta \quad (3.10)$$

i.e.

$$F_{molecule-plane} = \frac{\pi nC}{2d^4} \quad (3.11a)$$

and the corresponding potential energy is

$$U_{point-plane} = -\frac{\pi nC}{6d^3} \quad (3.11b)$$

The interaction force between two semi-spaces separated by as distance d is

$$F_{plane-plane} = \int_d^{\infty} \frac{\pi nC}{2z^4} dz = \frac{\pi C n^2}{6d^3} \quad (3.12a)$$

whose corresponding potential energy is

$$U_{plane-plane} = -\frac{\pi C n^2}{12d^2} \quad (3.12b)$$

Here, one introduces *Hamaker constant*, i.e. $A_H = \pi^2 n^2 C$ (for two different bodies $A_{12} = \pi^2 n_1 n_2 C_{12}$), and its typical value is $10^{-19} J$ in vacuum. Then Eq. (3.12) could be written as

$$F_{plane-plane} = \frac{A_H}{6\pi d^3} \quad (3.13a)$$

$$U_{plane-plane} = -\frac{A_H}{12\pi d^2} \quad (3.13b)$$

3.1.2.2 *Lennard-Jones forces* between two semi-infinite planes

By analogy to 3.1.2.1, it can be easy to deduce the *Lennard-Jones* force $\sigma(z)$ between two semi-infinite planes with a separation of z , given as

$$\sigma(z) = \frac{A_H}{6\pi z^3} - \frac{B}{z^9} \quad (3.14)$$

Eq. (3.14) contains one unknown, i.e. B . One introduces an equilibrium distance z_0 , i.e. $\sigma(z_0) = 0$. Then it yields

$$\sigma(z) = \frac{A_H}{6\pi z_0^3} \left[\left(\frac{z_0}{z} \right)^3 - \left(\frac{z_0}{z} \right)^9 \right] \quad (3.15)$$

and the unknown B could be derived from $\sigma(z_0) = 0$. The corresponding potential energy is

$$U(z) = - \frac{A_H}{12\pi z_0^2} \left[\left(\frac{z_0}{z} \right)^2 - \frac{1}{4} \left(\frac{z_0}{z} \right)^8 \right] \quad (3.16)$$

The work required to separate two surfaces of unit area from the equilibrium to infinity is given as

$$W_{ad} = \int_{z_0}^{\infty} \sigma(z) dz = \frac{A_H}{16\pi z_0^2} \quad (3.17)$$

and W_{ad} is normally termed *work of adhesion* (units of J/m²).

On the other hand, the creation of surface is accompanied with the disruption of intermolecular bonds, which is quantified by surface energy γ . Therefore, the *work of adhesion* W_{ad} equals the difference of surface energy $\Delta\gamma$ during separation, i.e.

$$W_{ad} = \Delta\gamma = \int_{z_0}^{\infty} \sigma(z) dz \quad (3.18)$$

where

$$\Delta\gamma = \gamma_1 + \gamma_2 - \gamma_{12} \quad (3.19)$$

where γ_i ($i = 1, 2$) denotes the surface energy of the two solids and γ_{12} is their interfacial energy.

In this work, surface energy $\Delta\gamma$ will be treated as the work of adhesion, unless specified particularly. Equating Eq. (3.17) to $\Delta\gamma$ results in

$$A_H = 16\pi z_0^2 \Delta\gamma \quad (3.20)$$

Substituting Eq. (3.20) into (3.15), one has

$$\sigma(z) = \frac{8\Delta\gamma}{3z_0} \left[\left(\frac{z_0}{z} \right)^3 - \left(\frac{z_0}{z} \right)^9 \right] \quad (3.21)$$

Eq. (3.21) gives the dependence of surface-surface interaction forces in terms of of adhesion $\Delta\gamma$, equilibrium distance z_0 , and the separation z . Differentiating Eq. (3.21) with respect to z and letting $d\sigma(z)/dz = 0$ indicate that the maximum interaction force σ_{max} equals $1.0264\Delta\gamma/z_0$, at $z = 1.2 z_0$. Fig 3.4 illustrates the dependence of the normalized interaction force σ/σ_{max} on normalized separation z/z_0 , together with its attractive and repulsive components. As can be

seen, the range of attractive force is larger than its repulsive counterpart. When $z > z_0$, attractive force exceeds repulsive force and when $z < z_0$, repulsive force surpasses attractive force. The attractive and repulsive forces are equal and opposite at $z = z_0$ and the resultant force is zero. Therefore, in theory two flat solid surfaces will stand still with an equilibrium interfacial separation of z_0 .

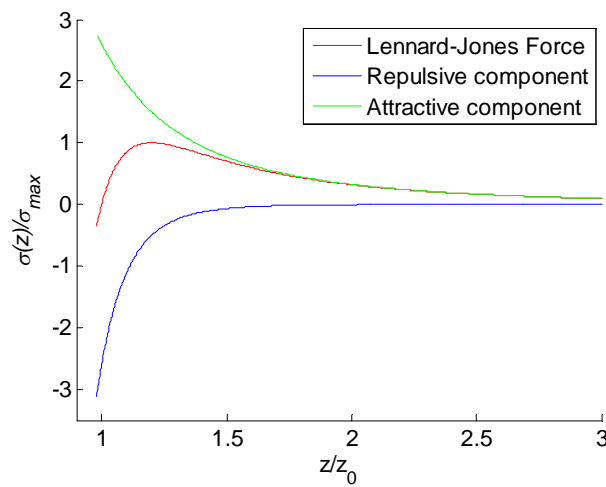


Fig 3.4 *Lennard-Jones* force corresponding to two parallel surfaces as a function of separation.

Eq. (3.21) accounts for the interaction forces between two parallel planes. However, in most cases the two pairwise surfaces are curved or inclined to each other. In fact, Derjaguin^[120] proposed this issue in terms of energy, and insisted that the interaction energy between two surfaces of small objects, whether or not parallel to each other, is the same as the energy per unit area between two parallel surfaces as long as the separation is much smaller than the size of objects involved (known as *Derjaguin approximation*). In this work, especially in the finite element method, Eq. (3.21) will be adopted to specify the interaction force between a sphere and an infinite half-space based on *Derjaguin approximation*.

3.2 Classical Contact Models

Last section provides a brief introduction on the intermolecular force between two molecules (atoms) and interaction force between parallel planes. As can be seen from the expression of *Lennard-Jones* force, it becomes increasingly significant as the two planes approach each other from infinite distance, which can potentially result in deformation of the involved planes if they are deformable. This section will provide an introduction of several contact models in the theory of classic contact mechanics. As pointed out in Sec.1.2, these contact models can generally be treated as the combination of classic continuum mechanics and surface effect, and some of them still prevail in relevant areas.

3.2.1 Hertz model: a non-adhesive contact model

Classic contact mechanics is mostly associated with Heinrich Hertz. In 1882, Hertz^[19] solved the problem of normal contact between two elastic spheres, as shown by Fig 3.5 (a), i.e. he formulated the relationship between the normal force and the normal mutual approach of the two spheres.

There are several assumptions for Hertz model, namely:

- The material of the two contacting spheres is homogenous, isotropic and linearly elastic. No plastic deformation occurs during contact process.
- The radius of contact area is much smaller than either radius of the two contacting spheres or, to be strict, radius of the curvature of the curved contact area.
- The contacting surfaces are smooth, frictionless and no adhesive stress exists.
- The elastic deformations are small and hence geometric nonlinearities are not taken into consideration.

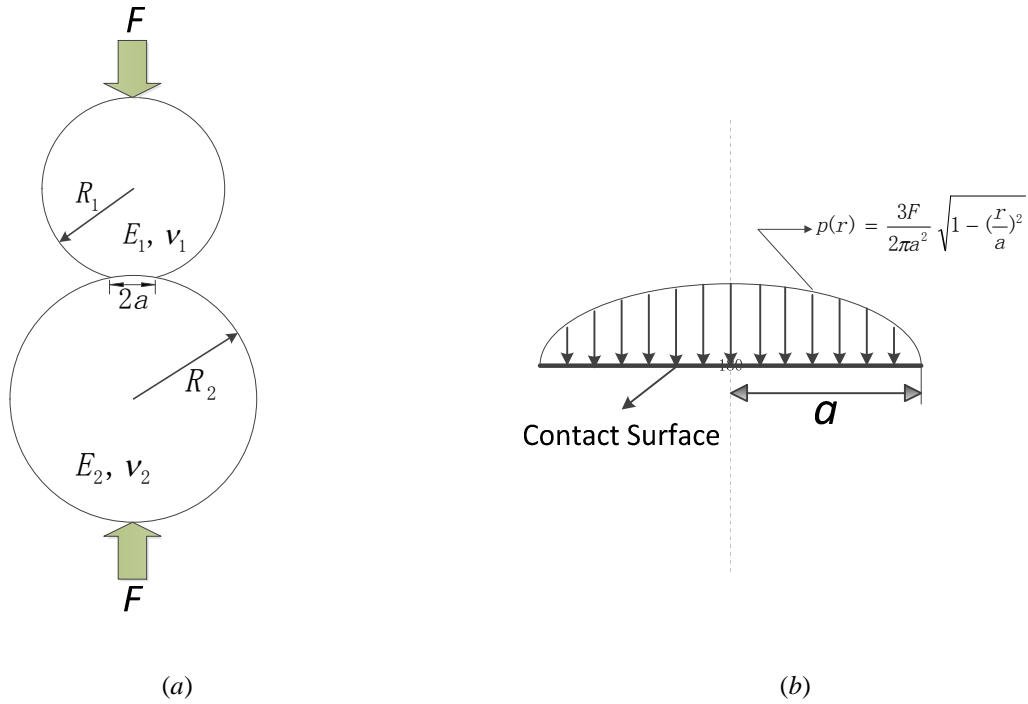


Fig 3.5 Schematic of (a) contact of two elastic spheres subjected to normal force F and (b) the distribution of compressive pressure in contact area.

Based on these assumptions, the dependence of force F on contact radius a is given as:

$$F = \frac{4E^*a^3}{3R} \quad (3.22)$$

where R is the reduced radius of curvature ($R = (1/R_1 + 1/R_2)^{-1}$, where R_1 and R_2 are the radii of curvature of the two spheres, respectively), $E^* = [(1-\nu_1^2)/E_1 + (1-\nu_2^2)/E_2]^{-1}$ is the effective Young's modulus, (E_1, ν_1 and E_2, ν_2 denote the elastic modulus and Poisson's ratio of the two contacting spheres, respectively). In an extreme case, if $R_i \rightarrow \infty$ ($i = 1, 2$), the i th sphere will tend to be an infinite half-space, and then the reduced radius of curvature R equals the that of the finite sphere. Therefore, the contact between an infinite half-space is treated as a special circumstances for contact between spheres. The relationship between mutual approach δ and contact radius a is given as:

$$\delta = \frac{a^2}{R} \quad (3.23)$$

where $\delta = \delta_1 + \delta_2$, and δ_i ($i = 1, 2$) denotes the displacement of i th sphere center during the elastic deformation. If one sphere remains still during contact, mutual approach can also be regarded as penetration of one sphere into the other. Therefore, in this work, we do not deliberately distinguish mutual approach from penetration unless specified particularly.

The distribution of compressive pressure $p(r)$ in contact region is given as:

$$p(r) = \frac{3}{2} \frac{F}{\pi a^2} \sqrt{1 - \left(\frac{r}{a}\right)^2} \quad (3.24)$$

which exhibits an elliptical profile as shown in Fig 3.5(b). As can be seen from Eq. (3.24), the ratio of maximum compressive stress to its average counterpart is 1.5. Besides, there are two derivative forms of Hertzian contact model for cylindrical and conical indenter, which are listed in Table 3.1.

Table 3.1 Solution for non-adhesive contact of cylindrical and conical indenter

Shape	F - a	δ - a	Contact pressure
Cylinder	$F = 2aE^*\delta$	N/A	$p(r) = -\frac{F}{2\pi a^2} \left[1 - \left(\frac{r}{a}\right)^2\right]^{-1/2}$
Cone	$F = \frac{\pi}{2} E^* a^2 \cot\alpha$	$\delta = \frac{\pi}{2} a \cot\alpha$	$p(r) = -\frac{F}{\pi a^2} \cosh^{-1}\left(\frac{a}{r}\right)$

In a macroscopic scale, the interaction forces between two contacting surfaces are insignificant compared with other dominant forces e.g. gravity, and thus the Hertz model, without consideration of adhesion forces, has proved a decent description for contact behavior in this case. However, as the characteristic length of the two contacting bodies reduces, the ratio of surface area to volume increases, and thus adhesion forces resulting from intermolecular forces cannot be ignored any longer. In 1930, *London theory of van der Waals*

$forces^{[121]}$ was presented, and since then many efforts were made to investigate the effect of intermolecular adhesion on the contact behavior of two bodies. In the following context, several adhesive contact models will be introduced based on relevant assumptions.

3.2.2 Bradley Model: Adhesive contact between two rigid bodies

When two clean, smooth and dry surfaces are brought into close proximity, they will stick to each other by the attractive *van der Waals forces*. In 1932, Bradley^[20] presented a means to calculate the adhesion forces between two rigid spheres with perfectly smooth surface. As illustrated in Fig 3.6, when two rigid spheres approach each other, the attractive force F can be assessed by integration, since intermolecular forces can be added up.

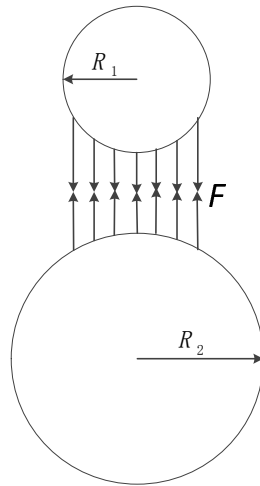


Fig 3. 6 Schematic of non-contact adhesion between two rigid spheres

$$F = 2\pi \int_0^{\infty} r\sigma(h)dr \quad (3.25)$$

where $\sigma(h)$ is the local interaction force and h is the local separation. By approximating the spherical shape to a parabolic shape, the dependence of local separation h on local radius r is given as

$$h(r) = h_0 + \frac{r^2}{2R} \quad (3.26)$$

where R is the reduced radius of curvature and h_0 is the surface separation at $r=0$.

Differentiating h with respect to r yields

$$Rdh = r dr \quad (3.27)$$

Substituting Eq. (3.27) into right side of Eq. (3.25) yields

$$F = 2\pi R \int_{h_0}^{\infty} \sigma(h) dh \quad (3.28)$$

The integral on the right hand of Eq. (3.28) represents the area enclosed by the $\sigma(h)$ - h curve from $h=h_0$ to infinity, and thus the force needed to maintain equilibrium of the two rigid spheres is solely dependent on h_0 , once $\sigma(h)$ is specified. By letting $h_0 = z_0$, the integral on the right hand of Eq. (3.28) is actually the expression of work of adhesion $\Delta\gamma$ (see Eq. (3.18)), i.e. the maximum value of this integral. Therefore, the maximum value of adhesion force can be expressed as

$$F_{max} = 2\pi R \Delta\gamma \quad (3.29a)$$

irrespective of the exact dependence of interaction forces $\sigma(h)$ on separation h . The maximum adhesion force is the force needed to tear two stick rigid spheres from $h_0 = z_0$ to infinity, and it is termed *pull-off* force, i.e.

$$F_{off} = 2\pi R \Delta\gamma \quad (3.29b)$$

As can be seen from the derivation process, Bradley model does not take deformation into consideration, which restricts its application. Owing to this disadvantage, the subsequent adhesive contact models consider deformable bodies.

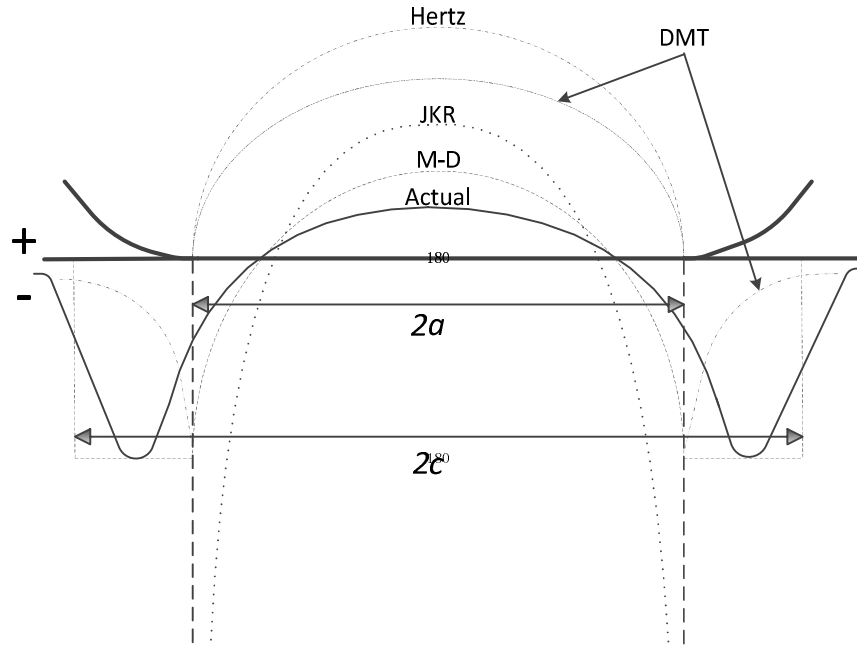


Fig 3.7 Distribution of contact stress (2-D) predicted by different contact models. The positive pressure denotes compressive force whilst the negative pressure denotes attractive force.

3.2.3 JKR model: reference to fracture mechanics

In 1971, Johnson et al^[21] studied the adhesive contact between two elastic spheres. By reference to fracture mechanics, the contact periphery is regarded as a crack. According to the Griffith's criterion, the equilibrium of crack propagation is achieved when the release rate of strain energy G equals the work of adhesion, i.e. $G = \Delta\gamma$, they presented an analytical solution as

$$\delta = \frac{a^2}{R} - \sqrt{\frac{2\pi a \Delta\gamma}{E^*}} \quad (3.30)$$

$$a = \left\{ \frac{3FR}{4E^*} \left[1 + \frac{3\pi\Delta\gamma R}{F} + \sqrt{\frac{6\pi\Delta\gamma R}{F} + \left(\frac{3\pi\Delta\gamma R}{F} \right)^2} \right] \right\}^{1/3} \quad (3.31)$$

where δ , a and F denote mutual approach (penetration), contact radius and external force. It can be seen from above equations that if no adhesion is assumed i.e. $\Delta\gamma = 0$, the equations

(3.30) and (3.31) are reduced to Herzian contact model. Substituting Eq. (3.31) into Eq. (3.30) can yield the dependence of force F on mutual approach δ , which is illustrated by Fig 3.8(a) in reduced coordinates. At the point M , adhesive force reaches its maxima, which is termed full off force for JKR model. Further calculation indicates

$$F_{off} = \frac{3}{2} \pi \Delta \gamma R \quad (3.32)$$

and the corresponding minimum contact radius is given as

$$a_{min} = \left(\frac{9\pi\Delta\gamma R^2}{8E^*} \right)^{1/3} \quad (3.34)$$

The contact pressure in contact region is expressed as

$$p(r) = \frac{2E^*a}{\pi R} \left[1 - \left(\frac{r}{a} \right)^2 \right]^{1/2} - \left(\frac{2\Delta\gamma E^*}{\pi a} \right)^{1/2} \left[1 - \left(\frac{r}{a} \right)^2 \right]^{-1/2} \quad (r < a) \quad (3.35)$$

and its distribution is shown by Fig 3.7 (dotted line). The negative pressure denotes attractive force as expected, and it acts only within the contact region. Because of adhesion forces, the contact area (radius) predicted by JKR model is larger than its Hertzian counterpart given the same external load. From the second term at the right side of Eq. (3.35), it can be seen that the pressure will exhibit a square root singularity as $r \rightarrow a$, which is consistent with the stress singularity occurring at the crack tip in linear elastic fracture mechanics.

Essentially, in JKR model, a strong adhesive force is supposed to act at the equilibrium distance z_0 , which could be treated as a delta function^[81] as illustrated by Fig 3.8(b). For any distance larger than z_0 , interaction forces disappears. In JKR model the attractive force is a short-range force with almost infinite magnitude at equilibrium distance z_0 , and this explains why there are no interaction forces outside the contact zone and stress singularity at the contact periphery.

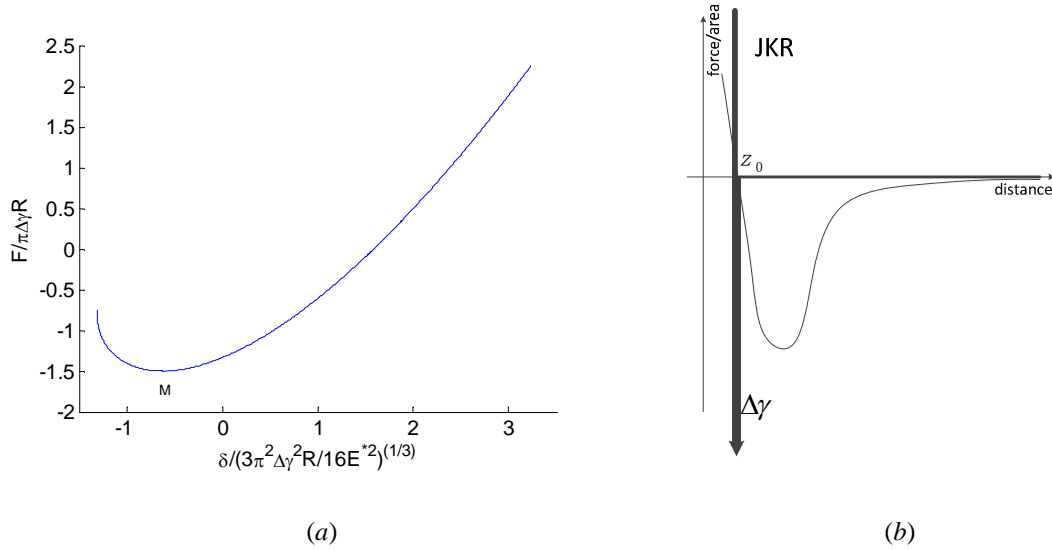


Fig 3.8 (a) Relation between force F and mutual approach δ , in reduced coordinates. (b) The interaction forces in JKR (bold line) in comparison with realistic interaction (thin line), and positive and negative value represent repulsive and attractive interaction forces, respectively.

3.2.4 DMT model: the profile outside the contact area remains its Hertzian counterpart

In 1975, Derjaguin et al^[22] presented another adhesive contact model (known as DMT model) using a “thermodynamic” approach. Unlike JKR model, DMT model assumes that adhesion forces exist at an annular zone outside the contact region without deforming the contacting bodies. Although this model does not result in any analytical solution, it estimates that the pull-off force is $2\pi\Delta\gamma R$, i.e. the same as that of Bradley model. In an approximation to the initial DMT model, Maugis^[23] proposed the following effective Hertzian force $F_H^{\text{DMT-M}}$

$$F_H^{\text{DMT-M}} = F + 2\pi\Delta\gamma R \quad (3.36)$$

where F denotes the externally applied force. He stated that the dependence of effective Hertzian force $F_H^{\text{DMT-M}}$ on contact radius a still obeys that of Hertz model, i.e.

$$F_H^{\text{DMT-M}} = \frac{4E^* a^3}{3R} \quad (3.37)$$

Substituting Eq. (3.37) into Eq. (3.36) yields

$$F = \frac{4E^*a^3}{3R} - 2\pi\Delta\gamma R \quad (3.38)$$

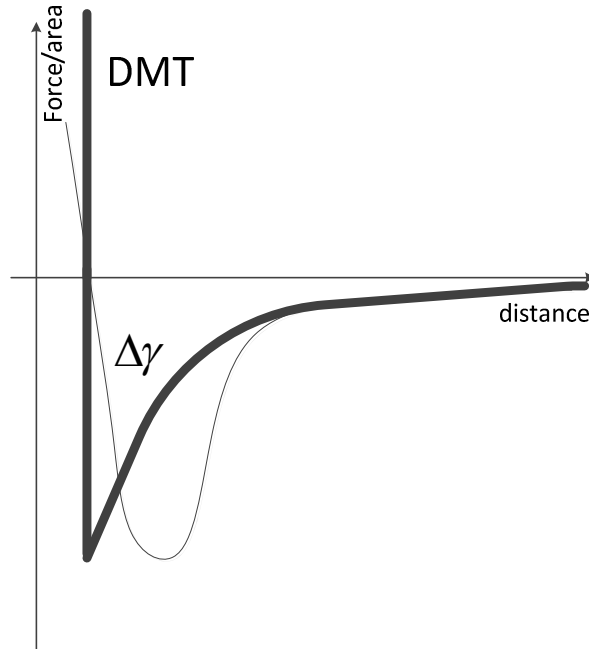


Fig 3.9 Schematic of the interaction forces in DMT model (bold line) compared with realistic interaction (thin line).

Since DMT model ignores the effect of adhesion forces outside the contact area on the profile, the stress distribution should obey Hertzian compressive stress inside the contact area, as shown by Fig 3.7. In essence, the adhesion forces in DMT model could be treated as long-range forces of basically *van der Waals* type^[81] (see Fig 3.9), which explains why there are attractive forces outside the contact zone, as assumed by this model.

As can be seen from Eq. (3.32) and (3.38), there is an apparent discrepancy at the prediction for the pull-off force between JKR and DMT model, and this discrepancy even led

to conflict. In 1976, Tabor^[74] compared these two models, and indicated that the main disadvantage of JKR model was the neglect of adhesion forces outside the contact region, whilst that of DMT model was neglect of deformation due to adhesion forces outside the contact area. He also pointed out that besides JKR model, there was also stress discontinuity in DMT model, i.e. the stress tends to zero at $r = a^-$, whereas it becomes negative (attractive) at $r = a^+$ as can be seen in Fig 3.7. Tabor estimated the discontinuity of displacement at the contact periphery was in the order of $(\Delta\gamma^2 R/E^*2)^{1/3}$, stating that if this discontinuity of displacement is close to equilibrium distance z_0 , JKR model should be modified to account for attractive force outside the contact region. Finally, this conflict was mediated by the introduction of Tabor number^[74], i.e.

$$\mu = \left[\frac{R\Delta\gamma^2}{E^*2z_0^3} \right]^{1/3} \quad (3.39a)$$

or more concretely

$$\mu = \left[\frac{(1-\nu^2)^2 R\Delta\gamma^2}{E^2 z_0^3} \right]^{1/3} \quad (3.39b)$$

which could be viewed as the ratio of the elastic surface displacement at the instant of separation to the effective range of surface force characterized by the atomic equilibrium distance z_0 ^[75]. In general, the DMT model applies for $\mu < 0.1$ (hard materials, small radius of curvature and low work of adhesion), whilst the JKR model applies for $\mu > 5$ (soft materials, large radius of curvature and high work of adhesion).

3.2.5 Maugis–Dugdale (M-D) model: a transition from DMT to JKR model

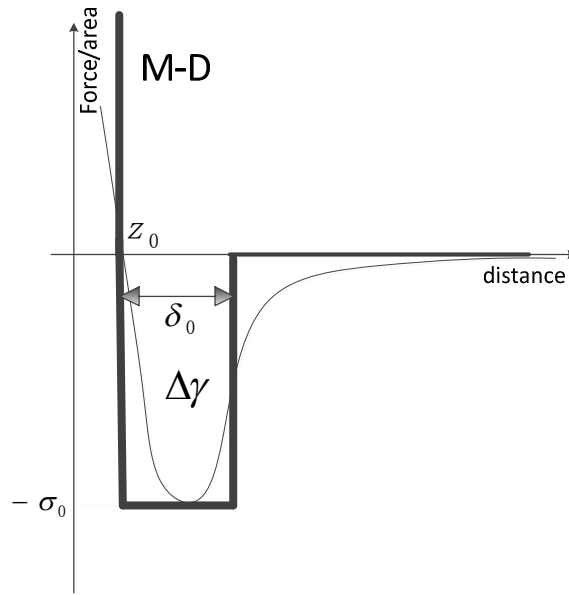


Fig 3.10 Schematic of the interaction force used in M-D (bold solid line) in comparison with realistic interaction (thin line). The area enclosed by the bold solid line with respect to abscissa is the same as that of the thin line, implying the interaction force used in M-D model gives the same work of adhesion as that of the real one.

In 1992, Maugis^[23] introduced an analytical solution to account for intermediate range between JKR and DMT model based on *Dugdale* model^[122], known as Maugis-Dugdale (M-D) model. This model considers the interaction forces between two surfaces follow *Dugdale* model, as shown by Fig 3.10, i.e.

$$\sigma(h) = \begin{cases} -\sigma_0 & z_0 < h \leq \delta_0 \\ 0 & h > \delta_0 \end{cases} \quad (3.40)$$

where h denotes the distance between two surfaces. The magnitude of σ_0 is selected so that it coincides with the maximum *Lennard-Jones* interaction force, i.e. $\sigma_0 = 1.0264\Delta\gamma/z_0$; since the work of adhesion in *Dugdale* model should equals $\Delta\gamma$ (work of adhesion of *Lennard-Jones* law), i.e. $\Delta\gamma = \sigma_0\delta_0$, it can be shown that $\delta_0 = 0.9743z_0$. In contrast to JKR model, in M-D model the adhesion force of intensity $-\sigma_0$ extends a distance of δ_0 above the surface (see Fig

3.7), which can account for long-range interaction forces. By analogy to JKR model, this model treats the region in proximity to contact periphery as a crack, and according Griffith criterion (see Sec. 3.2.3), M-D model presents an analytical solution for external force F and mutual approach (penetration) δ in terms of contact radius a , i.e.

$$F = \frac{4a^3 E^*}{3R} - 2a\sigma_0 [a\sqrt{c^2 - a^2} + c^2 \operatorname{arcsec}(\frac{c}{a})] \quad (3.41a)$$

$$\delta = \frac{a^2}{R} - \frac{2\sigma_0}{E^*} \sqrt{c^2 - a^2} \quad (3.41b)$$

respectively, where c denotes the critical radius at which *Dugdale force* vanishes, as shown by

Fig 3.7. The contact radius a and critical radius c are related by

$$\frac{a^2 \sigma_0}{\pi R \Delta \gamma} [(m^2 - 2) \operatorname{arcsec} m + \sqrt{m^2 - 1}] + \frac{4\sigma_0^2 a}{\pi E^* \Delta \gamma} [\sqrt{m^2 - 1} \operatorname{arcsec} m - m + 1] = 1 \quad (3.42)$$

where $m = c/a$. By introducing the following dimensionless parameters

$$\bar{a} = a \left(\frac{4E^*}{3\pi \Delta \gamma R^2} \right)^{1/3} \quad (3.43a)$$

$$\bar{c} = c \left(\frac{4E^*}{3\pi \Delta \gamma R^2} \right)^{1/3} \quad (3.43b)$$

$$\lambda = \sigma_0 \left(\frac{9R}{2\pi \Delta \gamma E^*} \right)^{1/3} \quad (3.43c)$$

$$\bar{F} = \frac{F}{\pi \Delta \gamma R} \quad (2.46d) \quad (3.43d)$$

$$\bar{\delta} = \delta \left(\frac{16E^{*2}}{9\pi^2 \Delta \gamma^2 R^2} \right)^{1/3} \quad (3.43e)$$

where λ is termed transition parameter, and it is related to Tabor parameter by $\lambda = 1.16\mu$. Eq.

(3.41a) and (3.42) can be rewritten as

$$\bar{F} = \bar{a}^3 - \lambda \bar{a}^2 [\sqrt{m^2 - 1} + m^2 \operatorname{arcsec} m] \quad (3.44a)$$

$$\bar{\delta} = \bar{a}^2 - \frac{4\lambda \bar{a}}{3} \sqrt{m^2 - 1} \quad (3.44b)$$

and

$$\frac{\lambda \bar{a}^2}{2} [(m^2 - 2) \operatorname{arcsec} m + \sqrt{m^2 - 1}] + \frac{4\lambda^2 \bar{a}}{3} [\sqrt{m^2 - 1} \operatorname{arcsec} m - m + 1] = 1 \quad (3.45)$$

respectively.

M-D model also gives the distribution of the contact pressure as

$$p(r) = \begin{cases} -\frac{\sigma_0}{\pi} \arccos\left(\frac{2a^2 - c^2 - r^2}{c^2 - r^2}\right) + \frac{2aE^*}{\pi R} \sqrt{1 - \left(\frac{r}{a}\right)^2}, & r \leq a \\ -\sigma_0 & a \leq r \leq c \end{cases} \quad (3.46)$$

As can be seen from Eq. (3.46), contact stress exhibits continuity at $r = a$ and attractive forces are never confined to the contact region, i.e. it remains $-\sigma_0$, which is consistent to Fig 3.7.

Although DMT model results in analytical solutions, there is inconvenience for its application which is due to its implicit form. To counter this disadvantage, many subsequent studies developed simpler solutions, which provide good approximation to M-D model^{[77][78][81]}.

3.2.6 Comparison of five contact models and subsequent studies

Fig 3.11 shows the dependence of reduced force $F/\pi\Delta\gamma R$ on reduced penetration $\delta/(3\pi^2\Delta\gamma^2R/16E^*)^{1/3}$ for the four contact models (except Bradley model). As can be seen, there is no adhesion force in Hertz model. As transition parameter λ increases, the force-penetration curve, and the pull-off force predicted by M-D model exhibit decent transition from DMT to JKR model.

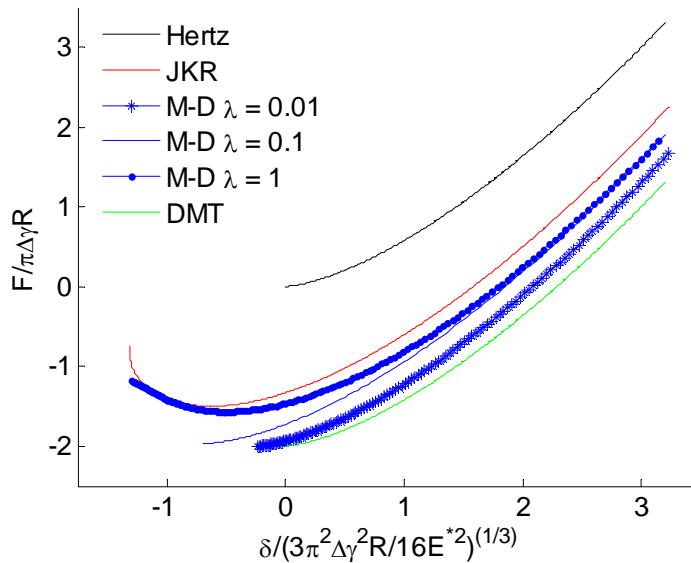


Fig 3.11 Dependence of reduced force on reduced penetration corresponding to Hertz, JKR, M-D and

DMT models.

In 1997, Johnson and Greenwood^[76] presented an adhesive map specifying the application range of the above contact models, as shown by Fig 3.12. As can be seen, when the external force is larger than adhesion force by a large margin, i.e. $F_{ext}/\pi\Delta\gamma R \gg 1$, the latter can be neglected, which corresponds to Hertz model. DMT model is appropriate for small adhesion force ($0.01 < \lambda < 0.1$), while JKR model is suitable for large adhesion force ($\lambda > 10$). For the intermediate range ($0.1 < \lambda < 10$), M-D model is advisable. The comparisons of hypothesis and limitation corresponding to these five models are listed in Table 3.2.

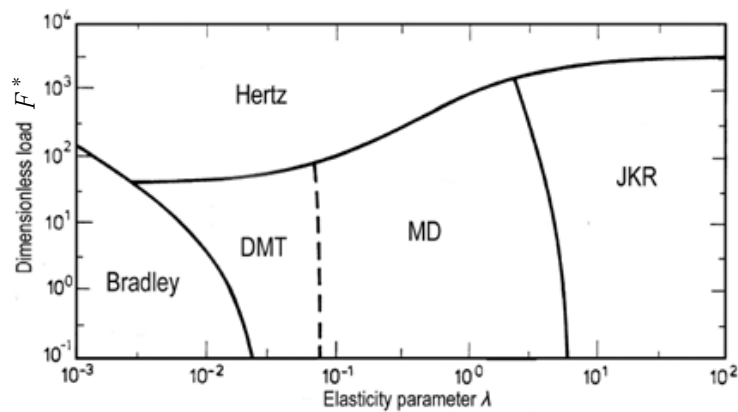


Fig 3.12 Adhesive map^[76]. The vertical coordinates denotes external load reduced by $\pi\Delta\gamma R$, i.e. $F^* = F_{ext}/\pi\Delta\gamma R$. The map applies to contact between pure elastic bodies.

Table 3.2 Comparison of the different assumptions and limitations for the five contact models

model	Assumption	Limitation
Hertz	non-adhesive, linear elastic, small deformation	invalid at low ration of load to contact surface
Bradley	Contacting bodies are rigid	invalid for deformable bodies
JKR	interaction forces confined in contact region	underestimation of load
DMT	interaction forces has no effect on profile	underestimation of contact area
M-D	interaction forces follow Dugdale model	The solution is implicit and cumbersome

Although these five contact models are regarded as classic, they have been undergoing refinement and development. In 1995, Maugis^[123] extended the JKR model by using the exact expression for the profile of elastic sphere, so that it can account for adhesive contact with large contact area. The results were in good agreement with published experiments. Yao et al^[124] pointed out that previous contact models neglected the requirement that adhesion strength must not exceed the theoretical strength, and hence there should be overestimation and misguidance in the adhesive map. They took strength limit into consideration and made corresponding modification for the adhesive map. Sun et al^[125] investigated the interaction forces between two silica nanospheres after contact, including the *van der Waals* (vdW) attraction, Born repulsion, and mechanical contact forces by molecular dynamics (MD) simulations. They conducted a comparison between JKR and DMT models in terms of force-displacement curve and contact radius, and showed that these two models can only be used to provide the first approximation, with some deviation from the MD simulated results.

4 Quantification of Mechanical Properties by Nanoindentation: a carrier for surface force study

4.1 Introduction

Although this work concentrates on surface adhesion, it is nevertheless appropriate to start it by deducing nanoindentation, which could be viewed as a “carrier” of surface adhesion, and without which study on surface adhesion may not always find its significance of the application.

This chapter presents a routine procedure to show how to quantify mechanical properties, i.e. elastic modulus, hardness, fracture toughness and viscosity of calibration materials by nanoindentation. In Sec. 4.2, basic analyses for quantification of above mentioned mechanical properties are discussed; Sec. 4.3 will introduce the instruments employed in this chapter and several materials suitable for calibration standards; results and discussion will be presented in Sec.4.4, and Sec.4.5 gives summary.

4.2 Experiment-based Methods

As mentioned previously, the force-displacement curve obtained by nanoindentation contains a wealth of information. The quantification of mechanical properties from the information involves theoretical models based on various assumptions. This section will introduce credible means to assess elasticity, hardness, fracture toughness and viscosity of materials.

4.2.1 Oliver and Pharr Method

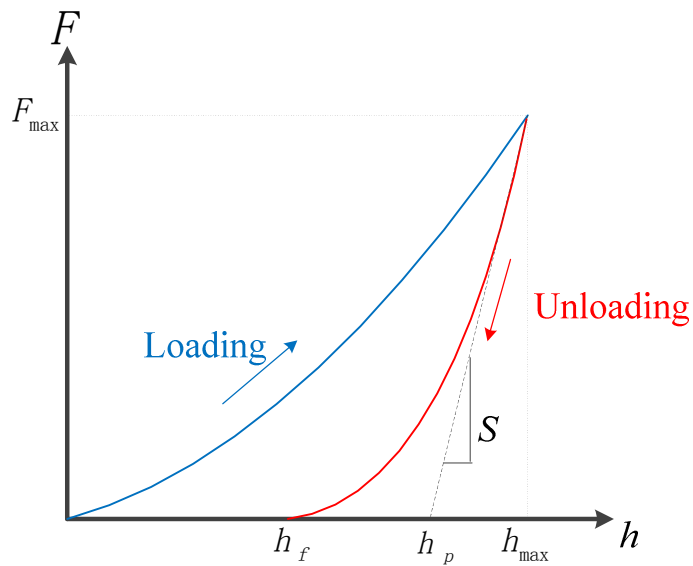


Fig 4.1 A typical force-indentation depth (displacement) curve obtained from nanoindentation.

Nanoindentation instruments are typically load-controlled machines, with concurrent measurement of indentation depth of a hard probe tip. Fig 4.1 illustrates a typical force-indentation depth curve (F - d curve) obtained from nanoindentation on metal. Unlike uniaxial, multiaxial or pure shear testing where stress-strain curve could be obtained straightforwardly, the determination of mechanical parameters of material by nanoindentation is indirect. During the loading stage, several kinds of material responses to strain may occur, e.g. elasticity, plasticity and even phase transformation (e.g. monocrystalline silicon subjected to indentation). However, for most materials, response to the unloading part is mainly composed of elastic deformation (to be strict, materials with kinematic hardening can also exhibit plasticity during unloading). Although there are many analyses for extraction of elastic modulus and hardness from force-displacement curve (see Sec. 2.2.1), Oliver and Pharr^[40] method is used in this chapter.

4.2.1.1 Cylindrical indenter

Fig 4.2(a) illustrates the substrate material indented by a cylindrical punch. The distinguishing feature of cylindrical punch indentation is that the contact radius remains constant throughout the whole loading-unloading process. Therefore, the F - d curve exhibits a straight line at the beginning of loading and the whole unloading stage as shown by Fig 4.2 (b). During retraction, indentation force F and indentation depth h are related by

$$F = 2aE^*h \quad (4.1)$$

where a and E^* denote radius of the cylinder (contact radius) and effective Young's modulus respectively. Differentiating Eq. (4.1) with respect to h yields

$$\frac{dF}{dh} = 2aE^* = 2\sqrt{\frac{A}{\pi}}E^* \quad (4.2)$$

where A and dF/dh denote the contact area and slope of the unloading line. Pharr et al^[126] suggested that Eq. (4.2) holds for any axisymmetric indenter. On the other hand, as can be seen from Fig 4.2 (b), one has

$$\frac{dF}{dh} = \frac{F_{max}}{h_e} \quad (4.3)$$

where F_{max} and h_e denote the maximum indentation force and elastic displacement during unloading respectively, which could be directly measured from the F - d curve. Thus equating Eq. (4.3) to (4.2) enables one to calculate effective elastic modulus E^* and further E .

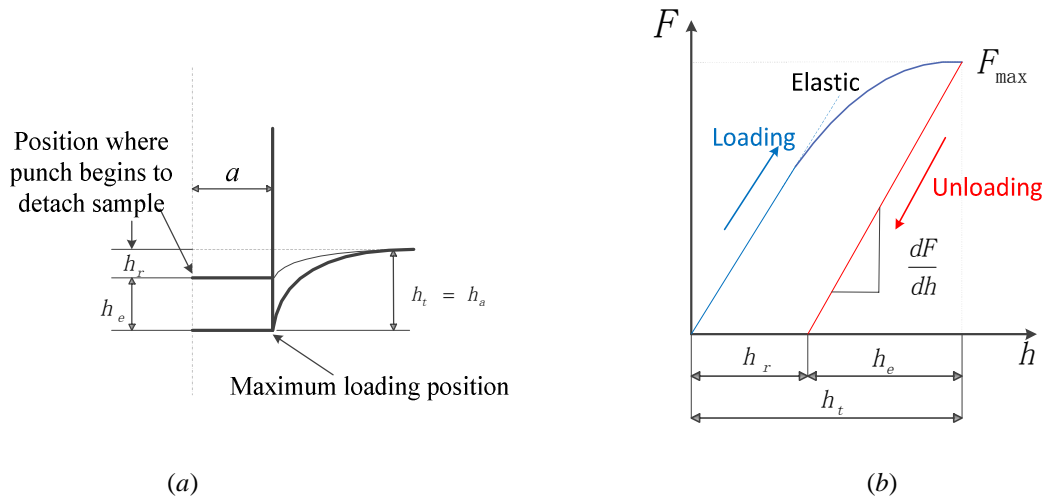


Fig 4.2 Schematic of substrate material indented by cylinder punch. (b) The corresponding $F-d$ curve.

h_t and h_r denote the maximum indentation depth and depth of residual impression respectively. h_a is the depth of the contact periphery.

In mechanics theory, the constant stiffness exhibited in unloading part of $F-d$ curve corresponding to cylindrical indentation is attributed to its linear boundary conditions, i.e. the contact area remains invariant. However, for other kinds of indenters, e.g. conic, Berkovich or sphere, this invariance never holds and the situation is more complicated.

4.2.1.2 Berkovich indenter

Some studies classify cylinder punch as blunt indenter, since plasticity occurs late in the $F-d$ curve during loading, as shown by Fig 4.2 (b), which implies considerable load is needed to initiate yield. In this regard, cylinder punch does not enjoy as much popularity as sharp indenter, e.g. Berkovich and conic where plasticity could occur at very early stage as shown by Fig 4.3 (c).

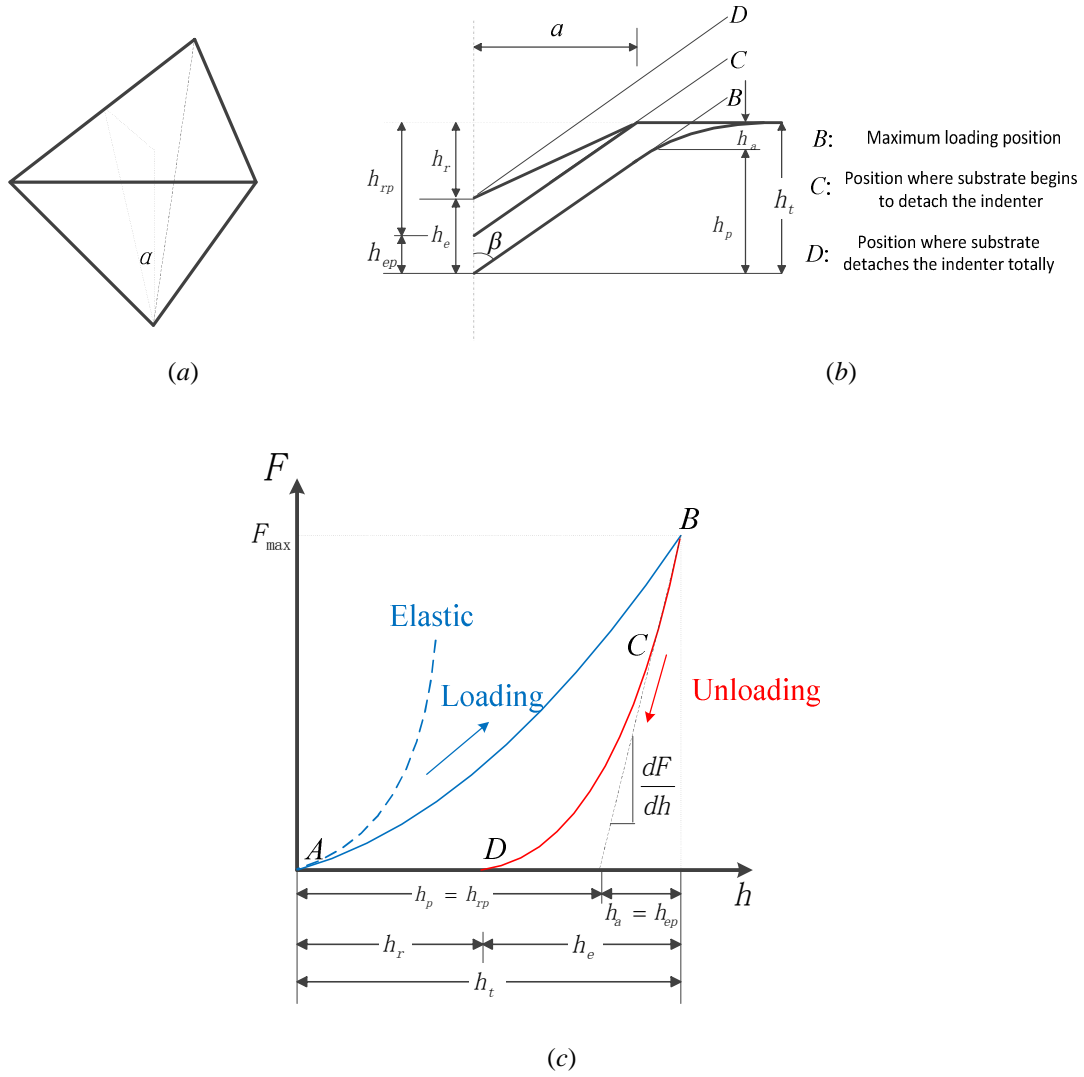


Fig 4.3 (a) Schematic of Berkovich. α denotes the half-angle to face. (b) Schematic of substrate material indented by conic indenter. (c) The corresponding $F-d$ curve.

Fig 4.3 (a) illustrates the schematic of a Berkovich indenter, with a face angle $\alpha = 65.27^\circ$ which gives the same projected area-to-depth ratio as Vickers. Fig 4.3 (b) shows the whole retraction process. At the maximum indentation position B, for a Berkovich indenter the dependence of the projected contact area A on the depth beneath the contact periphery h_p is given as

$$A = 3\sqrt{3}h_p^2 \tan^2 65.27 = 24.5h_p^2 \quad (4.4)$$

For the purpose of simplification, Berkovich is always approximated as a conic with a semi-angle $\beta = 70.3^\circ$ which gives the same projected area-to-depth ratio as the Berkovich indenter. The stage from point B to D (see Fig 4.3(b)) consists of only elastic deformation. According to Hertzian contact model, for a conic indenter, the relationship between maximum indentation force F_{max} and unloading elastic deformation h_e is

$$F_{max} = \frac{2E^* \tan\beta}{\pi} h_e^2 \quad (4.5)$$

The local vertical displacement h of the substrate surface is a function of local radial distance r from the symmetry axis, given as

$$h = \left(\frac{\pi}{2} - \frac{r}{a}\right) a \cot\beta \quad (4.6)$$

where a denotes contact radius at maximum loading. According to Eq. (4.6), on the contact periphery, i.e. $r = a$, one has

$$h_a = \left(\frac{\pi}{2} - 1\right) a \cot\beta \quad (4.7)$$

where h_a denotes the depth of the periphery beneath the original surface. On the symmetry axis one has

$$h_e = \frac{\pi}{2} a \cot\beta \quad (4.8)$$

Combining Eq. (4.7) and (4.8) results in

$$h_a = \left(1 - \frac{2}{\pi}\right) h_e \quad (4.9)$$

From Fig 4.3 (c), one can directly obtain total indentation depth h_t , elastic deformation h_e and depth of residual impression center h_r . It is apparently shown that

$$h_t = h_e + h_r = h_a + h_p \quad (4.10)$$

Substituting Eq. (4.9) into Eq. (4.10) one gets

$$h_p = h_t - \left(1 - \frac{2}{\pi}\right) h_e \quad (4.11)$$

Substituting Eq. (4.11) back into Eq. (4.4) yields

$$A = 24.5[h_t - (1 - \frac{2}{\pi})h_e]^2 \quad (4.12)$$

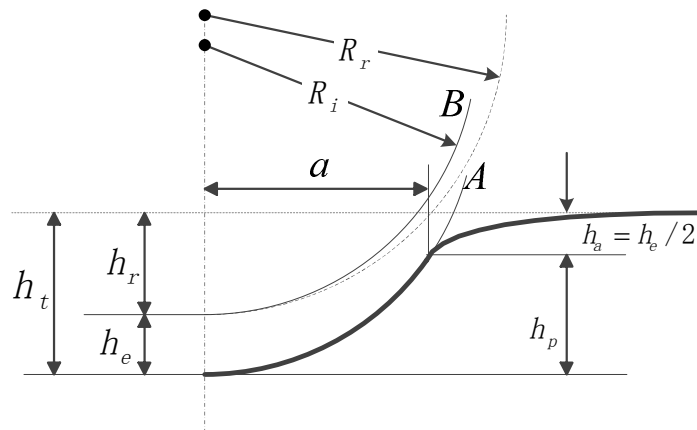
Doerner and Nix^[127] noticed for Berkovich indenter, the $F-d$ curve corresponding to the beginning of unloading is a line segment for a lot of materials, as shown by the section between point B and C in Fig 4.3 (c). Consider Fig 4.3 (b), at the beginning of retraction (the section between B and C), the contact region remains fairly steady, which is analogous to cylindrical indentation as shown by Fig 4.2 (b). Doerner and Nix^[127] considered that Eq. (4.2) still holds during this stage, regardless of the exact shape of indenter. Substituting Eq. (4.12) into Eq. (4.2) results in

$$E^* = \frac{1}{2} \sqrt{\frac{\pi}{24.5}} \frac{dF}{dh} \frac{1}{[h_t - (1 - \frac{2}{\pi})h_e]} \quad (4.13)$$

where dF/dh denotes the slope of curve at beginning of retraction, which could also be measured directly from experimental data. One can also obtain value of hardness according to its definition, given as

$$H \equiv \frac{F_{max}}{A} = \frac{F_{max}}{24.5[h_t - (1 - \frac{2}{\pi})h_e]^2} \quad (4.14)$$

4.2.1.3 Spherical indenter



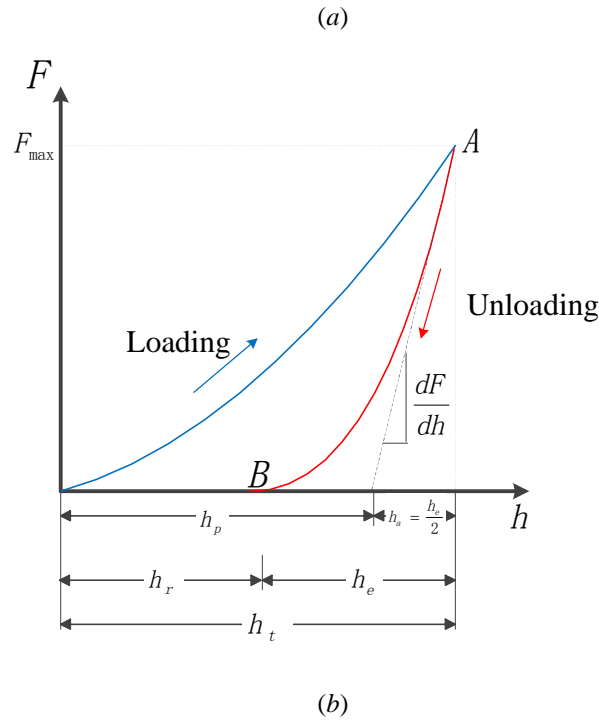


Fig 4.4 (a) Schematic of substrate material indented by spherical indenter. (b) The corresponding F - d curve. R_i denotes the radius of the sphere, and R_r denotes the radius of curvature at the center of the residual impression.

Besides the above two indenters, spherical indenter is also commonly used. Fig 4.4 (a) illustrates substrate material indented by a spherical indenter. During the unloading stage (From point A to B), only elastic deformation occurs, and thus one can apply Hertz contact model for this stage. According to Hertz model, the elastic deformation at the symmetry axis is twice the displacement of the contact periphery, i.e.

$$h_a = \frac{1}{2}h_e \quad (4.15)$$

The contact radius is given by

$$a = \sqrt{Rh_e} \quad (4.16)$$

where R denotes the effective radius, given by

$$R = \frac{R_r R_i}{R_r - R_i} \quad (4.17)$$

where R_i and R_r denote the radius of indenter and radius of curvature at the center of the residual impression, respectively. In this case, the projected contact area at maximum loading A is

$$A = \pi a^2 = \pi R h_e \quad (4.18)$$

At the beginning of unloading, the contact between indenter and substrate surface remains steady, and thus the slope of $F-d$ curve is constant as shown by Fig 4.4(b). Therefore the cylindrical punch equations (i.e. Eq. (4.2)) can be applied. Substituting Eq. (4.18) into Eq. (4.2) yields

$$E^* = \frac{1}{2} \frac{dF}{dh} \frac{1}{\sqrt{R h_e}} \quad (4.19)$$

Likewise, one has the expression for hardness according to its definition:

$$H \equiv \frac{F_{max}}{A} = \frac{F_{max}}{\pi R h_e} \quad (4.20)$$

where F_{max} , h_e and dF/dh could be measured in Fig 4.4(b).

4.2.2 Fracture toughness

As introduced in Sec. 2.2.2, when indentation test is performed on brittle materials, cracks are often observed around the impression. In material science, crack is characterized by *fracture toughness*, which quantifies the ability of a material containing a crack to resist fracture. There are a number of studies accounting for extraction of fracture toughness of material by nanoindentation, and this chapter presents one widely used means developed by Lawn et al^{[63][64][128]}.

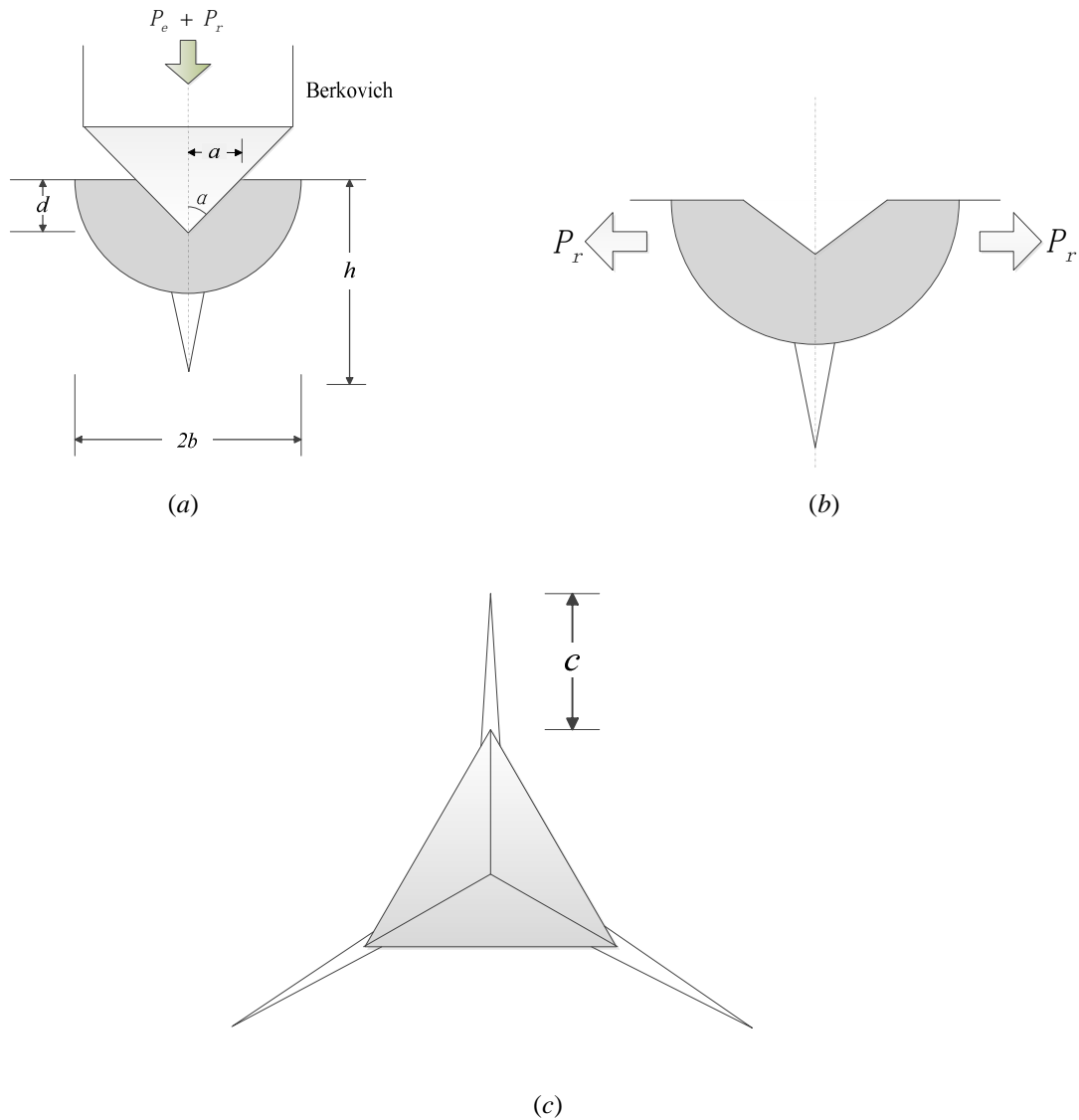


Fig 4.5 Schematic of median crack: (a) elastic-plastic configuration at full load (b) residual configuration of complete unloading (c) radial crack

Fig 4.5 shows the crack configuration produced by Berkovich indentation on brittle material (e.g. silicon wafer). P_e and P_r denote the elastic and plastic field component of applied load, respectively. α is the face angle of the Berkovich indenter. a , b , d , and h denote characteristic contact dimension, characteristic dimension of impression in radial direction, indentation depth and dimension of median crack. c represents the length of surface crack from corner to the end as shown by Fig 4.5 (c). By experiment, Marshall and

Lawn^[63] showed that, for the fully developed median/radial cracks, as shown by Fig 4.5 (a), the proportionality $K_e \propto P/h^{3/2}$ always holds, i.e.

$$K_e = \frac{\chi_e P}{h^{3/2}} \quad (4.21)$$

where χ_e is a constant, dependent on indenter angles, contact friction and free surface effects, and K_e denotes the elastic component of stress intensity factor^[129]. An analogous expression could also be given for the residual stress intensity factor K_r , given as

$$K_r = \frac{\chi_r P}{h^{3/2}} \quad (4.22)$$

where χ_r is another dimensionless indenter-substrate constant.

When the growth evolution of median cracks is under equilibrium conditions, the stress intensity factor K caused by externally applied load equals fracture toughness K_c , i.e.

$$K = K_e + K_r = K_c \quad (4.23)$$

During the loading stage, substituting Eq. (4.21) and (4.22.) into Eq. (4.23) yields

$$K_c = \frac{\chi_e P}{h^{3/2}} + \frac{\chi_r P}{h^{3/2}} \quad (4.24a)$$

By analogy, during unloading stage, one has

$$K_c = \frac{\chi_e P_m}{h^{3/2}} + \frac{\chi_r P_m}{h^{3/2}} \quad (4.24b)$$

where P_m denotes the maximum indentation force. During its growth, if the crack maintains a semicircular front throughout its evolution, the equilibrium median radius at maximum load $P = P_m$ is

$$h_M = \left[\frac{(\chi_e + \chi_r) P_m}{K_c} \right]^{2/3} \quad (4.25a)$$

And the equilibrium radius at completely unloading $P = 0$ is

$$h_R = \left(\frac{\chi_r P_m}{K_c} \right)^{2/3} \quad (4.25b)$$

The elastic-plastic configuration in Fig 4.5 (a) could be subdivided into elastic

component at full load plus residual component at complete unload. For elastic situation, the elastic component of K_c reaches its maxima when $P = P_m$ and will disappear at complete unloading. The plastic component of K_c reaches its maxima when $P = P_m$ but will maintain this maximum value during unloading. The crack growth is irreversible, so that Eq. (4.25b) cannot represent an attainable equilibrium configuration unless $h_R > h_M$. The only way to realize this inequality is let $\chi_e^R < 0$, i.e. suppress crack growth during the loading (superposing a reversible surface compressive stress^[63]). Therefore, the median crack reaches its maxima during loading and radial crack continues its growth until complete unloading. Since our work focuses on the radial crack after complete unloading, the elastic component could be neglected and thus Eq. (4.23) could be rewritten as

$$K_c = K_r = \frac{\chi_r P_m}{h^{3/2}} \quad (4.26)$$

where the constant χ_r is to be estimated in order to calculate K_c .

Consider the indented surface in the unloaded state as shown by Fig 4.5 (b). One has the following assumptions to evaluate χ_r

- (1) The characteristic area (shaded area) in Fig 4.5 (a) is removed from prospective contact site, and replaced by an unstressed elastic half space.
- (2) The impression will induce plastic deformation for the removed segment, whose contact radius, and indentation depth are a and d respectively, so that the irreversible strain associated with the impression is accommodated by an expansion in characteristic zone dimension at constant volume of material. Let δV and V denote the volume of the impression and volume of the zone respectively. Consider the material volume remains invariant, one has

$$\frac{\delta V}{V} = \frac{a^2 d}{2b^3} = \frac{\cot\alpha}{2} \left(\frac{a}{b}\right)^3 \quad (4.27)$$

(3) In order to restore the removed segment to its original characteristic radius b , a hydrostatic compression across the outer boundary

$$p_b = \kappa \frac{\delta V}{V} = \frac{\cot\alpha}{6} \frac{E}{(1-\nu)} \left(\frac{a}{b}\right)^3 \quad (4.28)$$

is applied, where κ denotes bulk modulus, i.e. $\kappa = E/3(1 - \nu)$. It should be borne in mind that it is different from that obtained at the impression at load P , i.e. the indentation hardness,

$$H = \frac{P}{\alpha_0 a^2} \quad (4.29)$$

where α_0 is a indenter geometry constant.

(4) One reinserts the compressed segment into its initial position, restores coherence at the interface, and let the system relax. In doing so, the plastic zone can induce effective outward residual force P_r on the crack as shown by Fig 4.5 (b). Assuming that p_b remains invariant during crack growth, the value of P_r could be obtained by integrating the horizontal stress components of p_b over the zone cross section within the crack zone, i.e.

$$P_r = \zeta p_b b^2 \quad (4.30)$$

where ζ is an integration constant.

When the crack is well developed, i.e. $h \gg b$, P_r could be simplified as a concentrated force. Assuming the crack geometry is penny-like, the stress intensity corresponding to residual field force may be written as

$$K_r = \frac{f(\varphi) P_r}{c^{3/2}} \quad (4.31)$$

where $f(\varphi)$ is an angular function introduced to allow for the effects of the free surface. For the case involved in this work, Eq. (4.22) turns into

$$K_r = \frac{\chi_r P}{c^{3/2}} \quad (4.32)$$

Substituting Eq. (4.28) into (4.30), and combining it with Eq. (4.31) and (4.32) yield

$$\chi_r = \frac{\zeta f(\varphi)}{6\alpha_0(1-\nu)} \frac{a E}{b H} \cot\alpha \quad (4.33)$$

For an infinite isotropic elastic-plastic matrix, according to Lawn's theory, one has

$$\frac{b}{a} \approx \left(\frac{E}{H}\right)^m (\cot\alpha)^{1/3} \quad (4.34)$$

where $m \approx 1/2$. Substituting Eq. (4.34) into (4.33) results in

$$\chi_r = \lambda_r(\varphi) \left(\frac{E}{H}\right)^{1/2} (\cot\alpha)^{2/3} \quad (4.35)$$

where λ_r is a dimensionless term independent of the indenter/substrate system. Substituting Eq. (4.35) back into (4.26) yields

$$K_c = \frac{\varepsilon \left(\frac{E}{H}\right)^{1/2} P}{c^{3/2}} \quad (4.36)$$

where $\varepsilon = \lambda_r(\varphi)(\cot\alpha)^{2/3}$. ε is a dimensionless term which is only dependent on radial crack configuration caused by impression, and its typical value is 0.016.

4.2.3 Viscosity parameter

Creep phenomenon is often observed in indentation testing for some viscoelastic materials such as polymer. Originally speaking, creep is the tendency of a solid material to move slowly or deform permanently under the influence of constant mechanical stresses. In indentation testing, creep manifests itself as the phenomenon that indentation depth is still increasing when the indentation force remains constant (known as hold period) as shown by the red curve in Fig 4.6. Ascribed to the viscoelasticity, a blowing out or "nose" at the beginning of retraction will be observed if without hold period, as shown by the black curve in Fig 4.6. In

“nose” situation, the slope is negative which will paralyze the application of Oliver and Pharr method. Therefore, the indentation force is always maintained at its maxima for a period to relieve or exclude the “nose” effect as shown by the red curve in Fig 4.6.

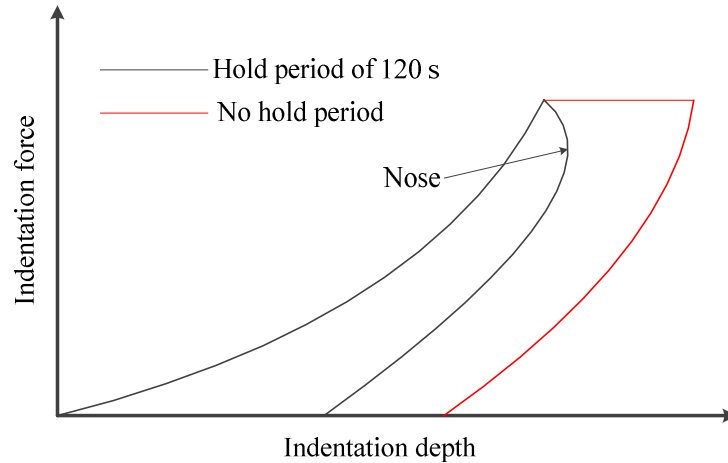


Fig 4.6 Illustration of Force-displacement curves for PMMA (Poly Methyl Methacrylate, viscoelastic material).

The viscoelastic property of material could be characterized by different combinations of discrete elastic and viscous elements, i.e. spring and dashpot. It is known that the spring element (see Fig 4.7 (a)) obeys Hookean theory, i.e.

$$\sigma = E\varepsilon \quad (4.37a)$$

$$\tau = G\gamma \quad (4.37b)$$

where σ , τ , ε and γ denote normal stress, shear stress, normal strain and shear strain respectively; E , G represent Young's modulus and shear modulus respectively. One of most distinguishing feature for elastic constitutive relation is its time-independence, e.g. instantaneous elastic deformation and recovery, as shown by Fig 4.7 (b).

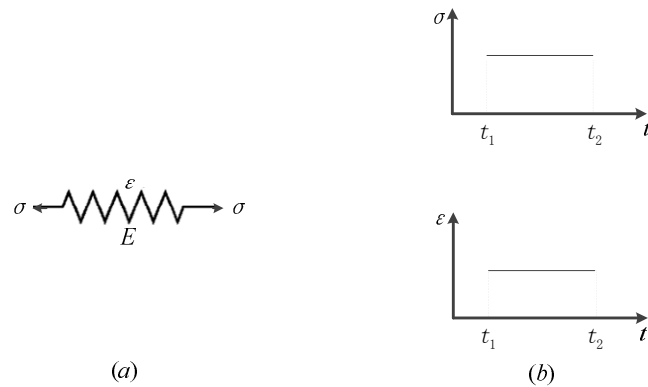


Fig 4.7 Schematic of elastic component of viscoelastic materials

The dashpot element obeys newton law of viscosity as shown by Fig 4.8 (a), i.e.

$$\sigma = \eta \frac{d\varepsilon}{dt} \quad (4.38a)$$

$$\tau = \eta_1 \frac{d\gamma}{dt} \quad (4.38b)$$

where η and η_1 denote viscosity, and $d\varepsilon/dt$ is strain rate. Dashpot exhibits rheological behavior.

For example, if the stress is a step function, i.e. $\sigma = \sigma_0 H(t)$, the corresponding strain is $\varepsilon = \sigma_0 t / \eta$ according to Eq. (4.38b), i.e. steady state flow, as illustrated by Fig 4.8(b). $H(t)$ denotes unit step function, i.e.

$$H(t) = \begin{cases} 1, & t \geq 0 \\ 0, & t < 0 \end{cases} \quad (4.39)$$

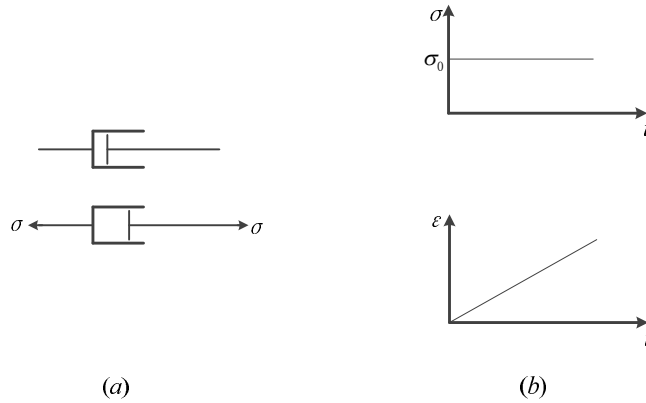


Fig 4.8 Schematic of viscous component of viscoelastic materials

Generally speaking, there are three common models, termed:

- *Kelvin–Voigt model*. This is comprised of a dashpot and a spring connected in parallel, as illustrated by Fig 4.9 (a). Its constitutive relation is given as

$$\sigma = E\varepsilon + \eta \frac{d\varepsilon}{dt} \quad (4.40)$$

- *Maxwell model*. This can be represented by a spring and a dashpot connected in series, as illustrated by Fig 4.9 (b). This model can be represented by the following equation:

$$\frac{d\varepsilon}{dt} = \frac{\sigma}{\eta} + \frac{1}{E} \frac{d\sigma}{dt} \quad (4.41)$$

- *Three element model*. This consists of a dashpot and a spring connected in parallel, and then connected to another spring in series, as illustrated by Fig 4.9 (c). The corresponding constitutive relation is given as

$$\sigma + \frac{\eta}{E_1 + E_2} \frac{d\sigma}{dt} = \frac{E_1 E_2}{E_1 + E_2} \varepsilon + \frac{\eta E_2}{E_1 + E_2} \frac{d\varepsilon}{dt} \quad (4.42)$$

where σ and ε denote overall stress and strain as shown by Fig 4.9 (a), (b) and (c).

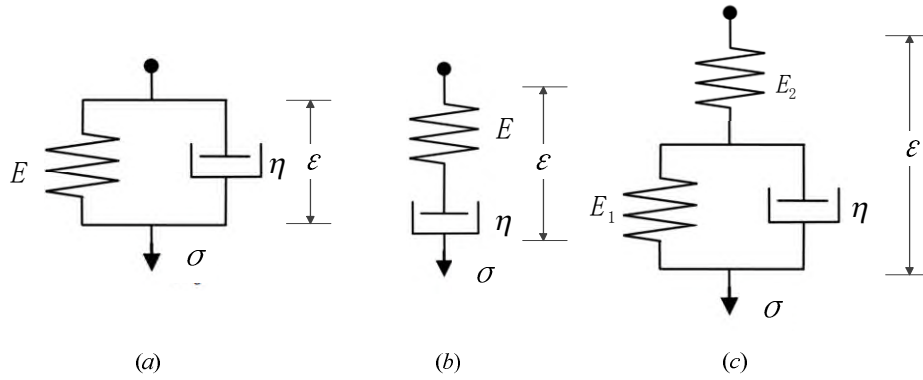


Fig 4.9 Three common mechanical models: (a) Kelvin–Voigt model (b) Maxwell model (c) Three element model.

In creep indentation tests, the load is controlled, and thus the concurrent displacement of the indenter is monitored. In general, the load is applied such that it reaches its maxima F_{max} in a very short time compared with its subsequent hold time. In this regard, the indentation force $F(t)$ could be approximated as a Heaviside step function, i.e.

$$F(t) = F_{max}H(t) \quad (4.43)$$

If the indenter is a conic, for the elastic case, one has

$$h^2 = \frac{\pi(1-\nu^2)}{2E}F \quad (4.44)$$

where h and F denote indentation depth and force respectively. For its viscoelastic counterpart, both Radok^[69] and Ting^[70] offered a general solution to linear viscoelastic Boussinesq problem provided the contact radius is non-decreasing as mutual approach increases. According to their theory, substituting the elastic modulus in the Hertz contact model with the modulus-displacement convolution in the time domain leads to the relationship between the indentation depth and the applied force as:

$$h^2(t) = \frac{\pi}{2} \cot\alpha (1 - \nu^2) J(t) * F(t) \quad (4.45)$$

where $J(t)$ denotes the creep compliance, which is the dependence of strain on time provided

unit constant stress. Table 4.1 lists the expression of creep compliance for the above three models. The asterisk denotes convolution, i.e.

$$J(t) * F(t) = \int_{\xi=0}^t J(t-\xi) \frac{d}{d\xi} F(\xi) d\xi \quad (4.46)$$

Performing Laplace transform on both sides of Eq. (4.45) yields

$$\mathcal{L}[h^2(t)] = \frac{\pi}{2} \cot\alpha (1 - \nu^2) \mathcal{L}[J(t)] \mathcal{L}\left[\frac{dF(t)}{dt}\right] \quad (4.47)$$

Substituting Eq. (4.43) into right side of Eq. (4.47) results in

$$\mathcal{L}[h^2(t)] = \frac{\pi}{2} \cot\alpha (1 - \nu^2) \mathcal{L}[J(t)] F_{max} \quad (4.48)$$

Performing inverse Laplace transform on Eq. (4.48) yields

$$h^2(t) = \frac{\pi}{2} \cot\alpha (1 - \nu^2) J(t) F_{max} \quad (4.49)$$

Generally speaking, it is always assumed that some soft materials are incompressible, i.e. $\nu = 0.5$. Therefore, fitting Eq. (4.49) with the h^2 - t curve obtained by experiment can determine the viscoelastic parameters. It should be borne in mind that Eq. (4.49) is only valid when the force-time function $F(t)$ is approximated as a Heaviside step function. In order to realize this approximation, the loading time t_l is controlled in a small range whilst the hold time t_h is set very long, and an advisable ratio of t_l/t_h is 1/10. Besides, Eq. (4.49) is only applicable for conic indenter, and the cylindrical and spherical counterparts can be obtained by analogous derivation, as summarized in Table 4.2.

Table 4.1 Creep Compliance for the three common models

Model Name	Creep Compliance $J(t)$	
Kelvin–Voigt	$\frac{(1 - e^{-Et/\eta})}{E}$	
Maxwell	$\frac{1}{E} + \frac{1}{\eta} t$	
Three element	$1/E_2 + (1 - e^{-t/\tau})/E_1$	$\frac{1}{E_1} + \frac{1 - e^{-t/\tau}}{E_1}$ where $\tau = \eta/E_1$

Table 4.2 Dependence of indentation depth on time for different indenters corresponding to Heaviside step load

Indenter Type	$h(t)$	Notes
Cylinder	$\frac{(1 - \nu^2)}{2a} J(t) F_{max}$	a denotes the radius of the cylinder
Sphere	$[\frac{3(1 - \nu^2)}{4\sqrt{R}} J(t) F_{max}]^{2/3}$	R denotes the radius of the sphere
Conic	$[\frac{(1 - \nu^2)\pi}{2} \cot\alpha J(t) F_{max}]^{1/2}$	α denotes the half angle of the conic

4.3 Experiment Process and Instrument Introduction

4.3.1 Instrumentation

Generally speaking, many instrumented indentation systems (i.e. nanoindentation) can be illustrated by Fig 4.10 regardless of differences. The force is often applied by using either electromagnetic or electrostatic actuation, and a capacitive sensor is usually utilized to measure concurrent displacement^[130]. There are many commercial instrumented indentation systems available developed by various manufacturers such as Hysitron, Inc. (Minneapolis, MN), CSIRO (Australia), Nano Instruments (MTS System Corp.), Micro Materials Ltd. (UK) and CSM Instruments (Switzerland). The instrumented indentation systems by different manufacturers are almost identical with some minor differences. For example, the axis of indenter of instruments systems by CSM is vertical, as shown by Fig 4.10, so as CSIRO, Hysitron, Nano Instruments, but for Micro Materials, its indenter is horizontal. To take another example, Hysitron instruments systems adopt the same sensor to measure indentation force and displacement, whilst the rest four instruments measure force and displacement by different means.

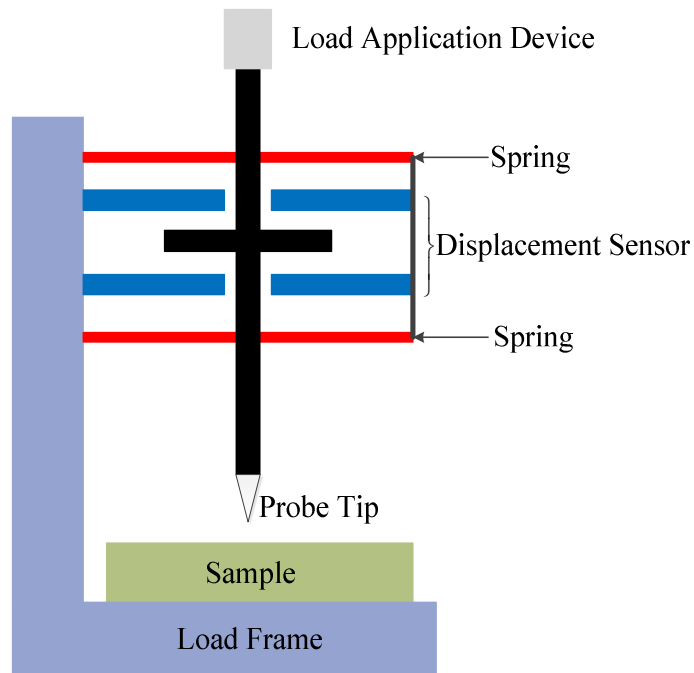


Fig 4.10 Schematic illustration of an instrumented indentation system.

4.3.2 Nanoindentation Tester NHT²

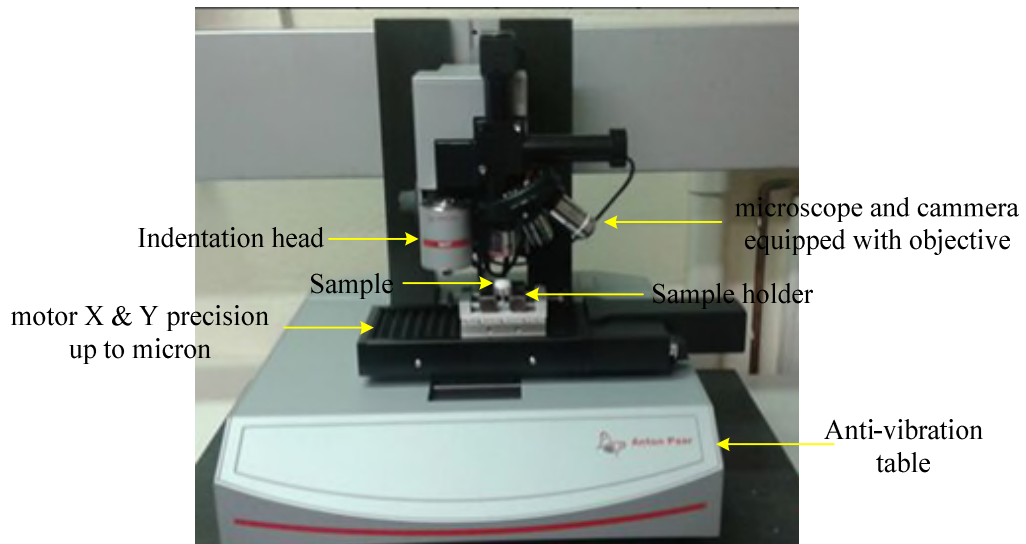


Fig 4.11 The Nano Indentation Tester NHT² manufactured by CSM instruments

The instrumented indentation systems employed in this work is Nanoindentation Tester NHT²,

and it belongs to CSM Instruments. Fig 4.11 shows its photography and main components. The NHT² is designed to provide low loads with depth measurements in the nanometer scale. The system can characterize a broad spectrum of materials, e.g. organic, inorganic, hard and soft materials. The mechanical properties which can be measured by this system include hardness, elastic modulus, creep, fracture toughness, etc. The maximum force can reach 500mN with a resolution of $0.01\mu N$, and the maximum indentation depth is $200\mu m$ with a resolution of $0.01nm$. The load frame stiffness is much larger than $10^7N/m$.

The NHT² uses an already established method detailed, as follows. An indenter tip with known geometry is driven into a specific site of the material of interest. An increasing normal load is applied, and after reaching a pre-set maximum value, it is reduced until partial or complete relaxation. This procedure can be performed repeatedly. The relative position of the indenter with respect to the sample surface (i.e. indentation depth) is precisely monitored by a differential capacitive transducer. The NHT² can operate in dynamic or quasi-static loading model where the latter model is adopted throughout this chapter.

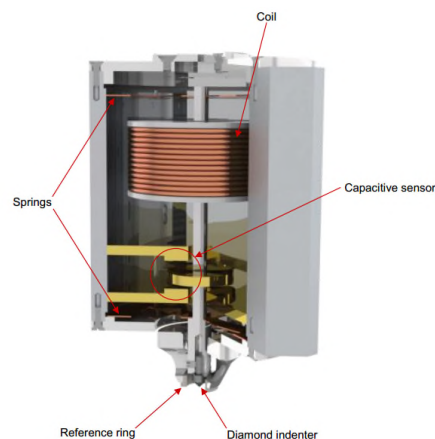


Fig 4.12 Schematic of profile map of the NHT² head

The core of NHT² is the indenter head, whose main components are illustrated in Fig 4.12. At the beginning of indentation, the head is moved downwards until the reference ring touches the substrate sample. The load is applied by a displacement actuator which consists of an electromagnetic coil. The coil is used to control the movement of the indenter shaft. The capacitive sensor, which is mounted near the indenter tip, records the vertical displacement of the indenter. It is noteworthy that in NHT² the applied load could be accurately specified by the electromagnetic coil which is different from the loading method in AFM as mentioned in Sec. 1.1.2.

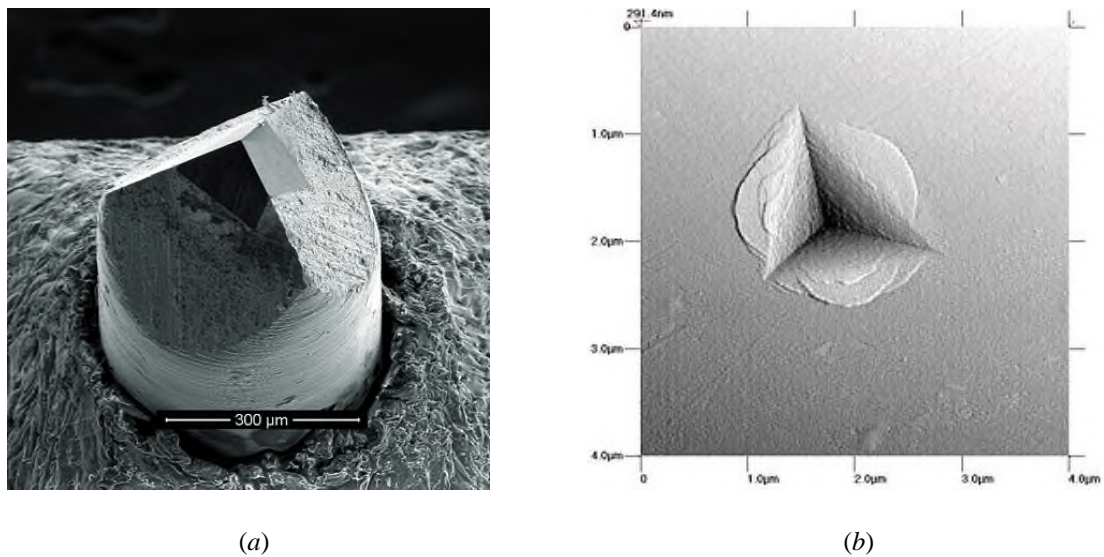


Fig 4.13 (a) Microscope of the Berkovich diamond indenter (b) Typical residual impression induced by the Berkovich indenter on ductile materials

There are many kinds of indenter available in NHT², and the Berkovich indenter is employed throughout this chapter, whose microscope is shown in Fig 4.13 (a). The Berkovich pyramid used in this work is made of diamond brazed into steel, as can be seen from Fig 4.13 (a). It has a face angle $\alpha = 65.27^\circ \pm 0.3^\circ$, with a tip radius $< 0.2\mu\text{m}$. Before penetration into sample, the NHT² operation system determines the location of the material surface. The

typical residual impression on ductile materials induced by the Berkovich indenter is shown in Fig 4.13 (b).

4.3.3 Sample Preparation



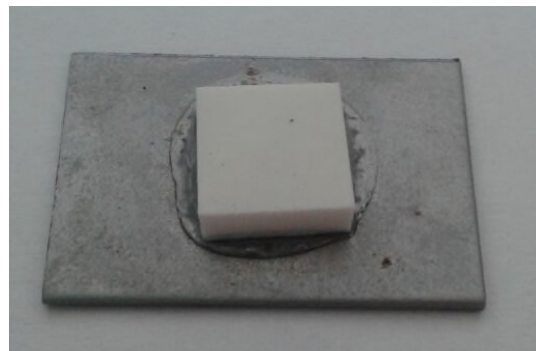
(a)



(b)



(c)



(d)

Fig 4.14 (a) Copper and (b) Fused silica (c) Silicon Wafer (d) polystyrene

Fig 4.14 shows the samples used in nanoindentation test. Copper and fused silica are provided by CSM Instruments company. The silicon wafer and polystyrene were glued to an iron sheet, which acts as substrate to support the sample. Both copper and fused silica were indented for calibration of elastic modulus and hardness. Silicon wafer and polystyrene were indented for calibration of fracture toughness and viscoelastic parameters, respectively. The typical values

of these parameters are listed in Table 4.3 and 4.4.

Table 4.3 Material properties of copper, fused silica and silicon wafer.

Typical Value	Elastic modulus (GPa)	Hardness (GPa)	Yield Stress (MPa)	Poisson's ratio	fracture toughness (MPa•m ^{1/2})
Copper ^[131]	128	3.8	440	0.34	N/A
Fused silica ^[132]	72	8.8	1150	0.17	N/A
Silicon wafer ^{[133][134]}	150	10	950	0.22-0.28	0.83-0.95

Table 4.4 Viscoelastic properties of polymeric materials^[51]

Model	2-element		3-element			4-element			
	E	η	E_1	E_2	η	E_1	E_2	η_1	η_2
Copolymer	0.09	1.69	0.16	0.103	0.135	0.17	0.14	2.9	0.7
Cross-linked	0.94	41.2	1.03	2.73	11.2	1.05	4.7	72.6	7.7

4.3.4 Experimental Procedure

4.3.4.1 Copper and fused silica

The maximum force for copper and fused silica are 50mN and 20 mN respectively. In order to relieve the viscosity effect, the indentation force is set to pause at the maximum force for 10 s.

For both materials, the loading and unloading speeds are 100mN/min.

4.3.4.2 Silicon wafer

For silicon wafer, the maximum force is 400 mN, with a pause of 2.5 s, and the loading/unloading rate is 200mN/min. After complete unloading, optical microscope was employed to measure the length of radial crack, as shown by Fig 4.5 (c).

4.3.4.3 Polystyrene

The maximum force for polystyrene was 1.7 mN applied by ramp loading within 12s,

followed by a pause of 120 s. Since the loading time is only one tenth of the pause time, the force-time relationship could be approximated as Heaviside step function.

4.4 Finite Element Analysis

With the availability of finite element analysis program, it is appropriate to perform a numerical approach to the simulation of force-displacement responses for substrate undergoing nanoindentation.

In the finite element method, the specification of material mechanical property plays a paramount role in determining the simulative results. In the absence of detailed information about the materials of interest, a linear elastic and elastic-perfectly plastic material response usually give enough results. Von Mises yield criterion (yield criterion will be elaborated in next chapter) is specified to realize the transition from elastic to plastic deformation.

Finite element simulations were performed with the multi-purpose finite code ABAQUS (version 6.13-4). The ABAQUS/STANDARD solver was used in all simulations throughout this chapter. To simulate the Berkovich indenter, a conic with semi-angle 70.3° was modeled, which gives the same projected area-to-depth ratio as the Berkovich indenter. To mediate the matter of fact, the apex of the conic indenter is modeled with spherical tip with a radius $R = 0.2\mu\text{m}$ (see Fig 4.15). The half-space was densely partitioned for a shallow depth while coarser partition was adapted as the depth increases. The finite element mesh was designed to provide a high density of nodes at the contact region, to capture the details of the displacement and stress fields, as shown by Fig 4.15. The distance between two adjacent surface nodes of the refined mesh is equal to $\sim 0.01R$. The half-space was modeled with 31100 four-node, bilinear, axisymmetric, quadrilateral elements (CAX4) consisting of 31361

nodes. The nodes at the bottom and left boundaries of the mesh were constrained against displacement in the vertical and horizontal directions, respectively.

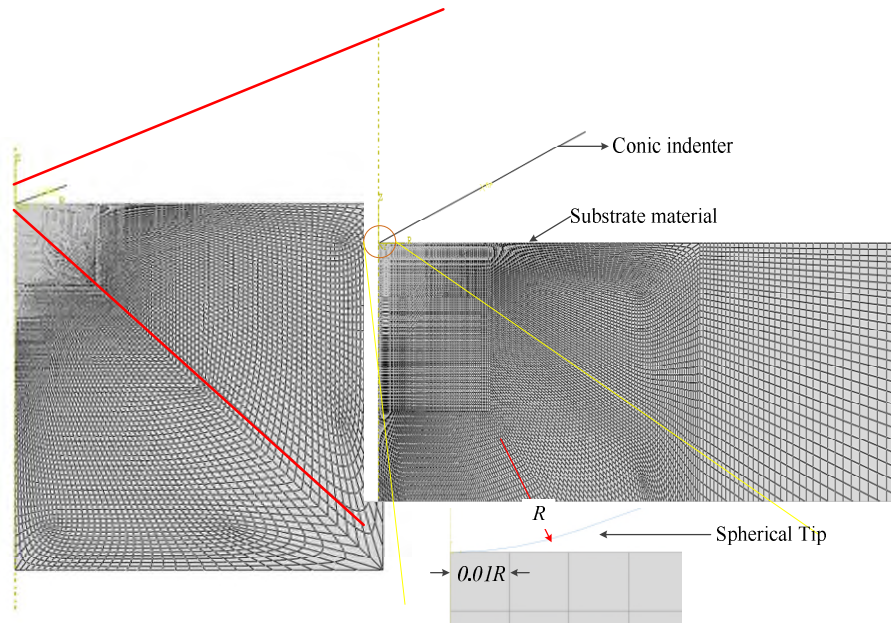


Fig 4.15 Finite element model of a rigid conic in close proximity with a deformable half-space. The indenter-substrate is axial symmetrical, and thus only one section is plotted for illustration.

4.5 Results and Discussion

4.5.1 Copper and Fused Silica

4.5.1.1 Indentation Impression

Fig 4.16 (a) shows a microscope image of the indent on copper by the Berkovich indenter. The wrinkles and convex edge circled by the ellipse indicates occurrence of pile-up. In pile-up phenomenon, the material plastically uplifts around the contact impression which is schematically illustrated in Fig 4.16 (b). When pile-up occurs, the contact area is larger than predicted by elastic contact theory, and hence both hardness and elastic modulus are overestimated. The effect of pile-up on the estimated hardness and elastic modulus will be

discussed in Sec.4.5.1.2. For each sample, indentations were repeated in a matrix comprised of 100 indentation spots. Within the matrix, each indent was aligned with constant interval of $25\mu\text{m}$ as shown by Fig 4.16 (c).

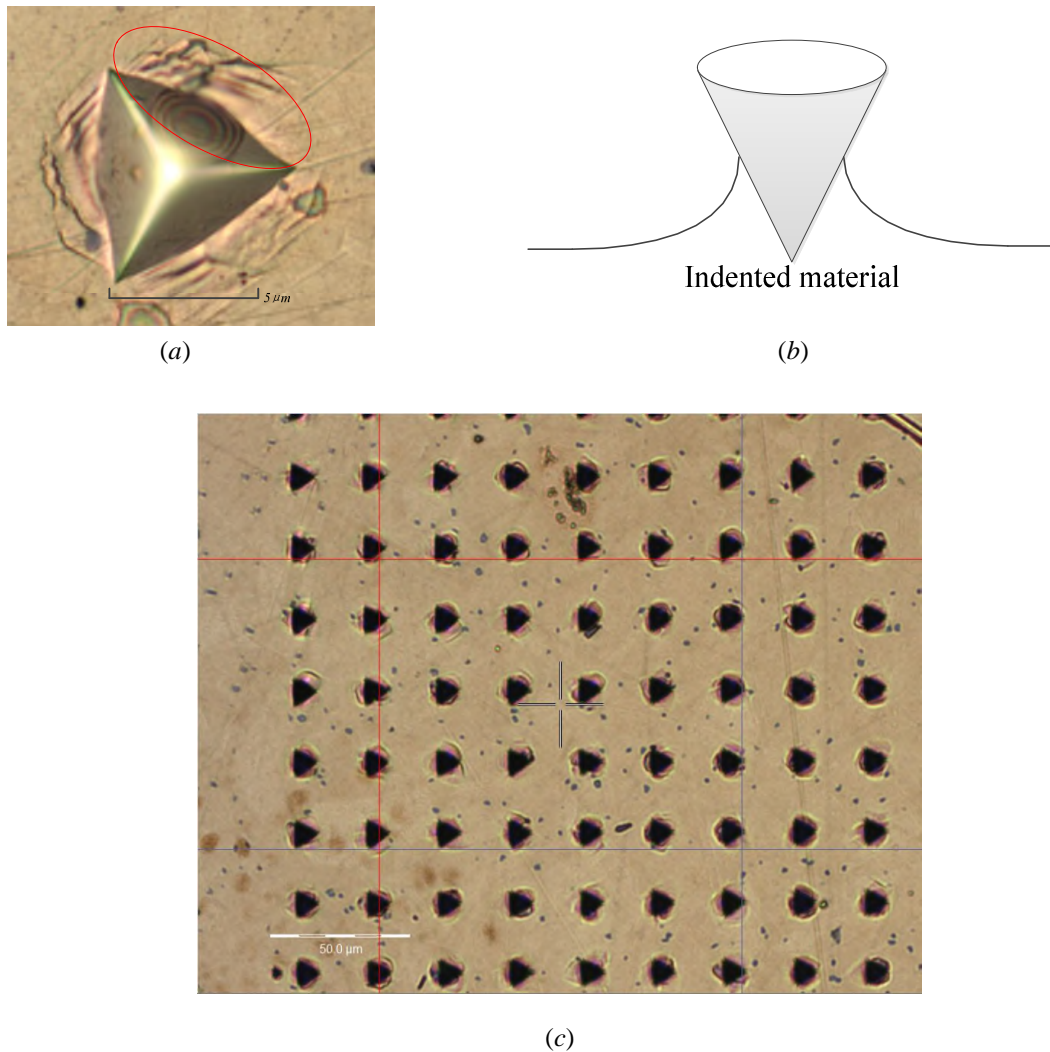


Fig 4.16 (a) A single indentation impression on copper substrate; (b) Cross sectional view of pile-up during indentation; (c) A matrix of indentation impressions where the distance between two adjacent spots is $25\mu\text{m}$.

4.5.1.2 Force-displacement curve

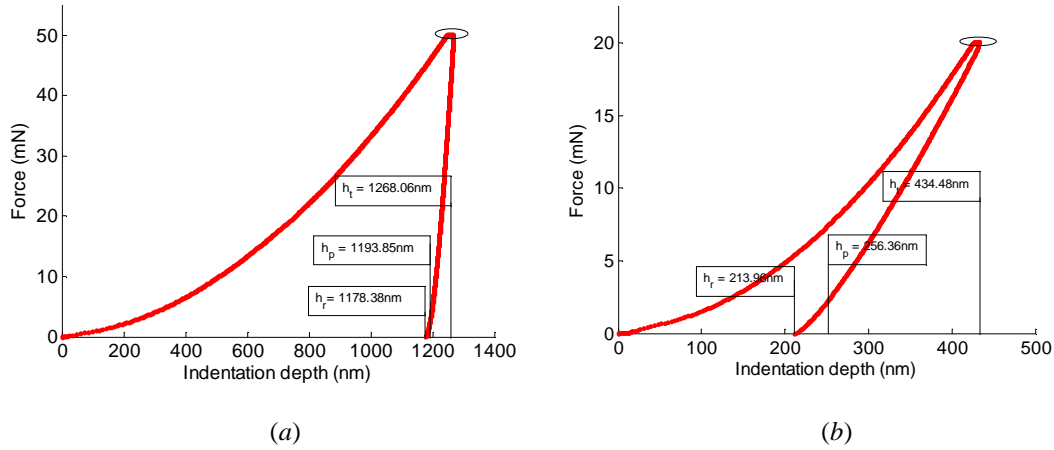
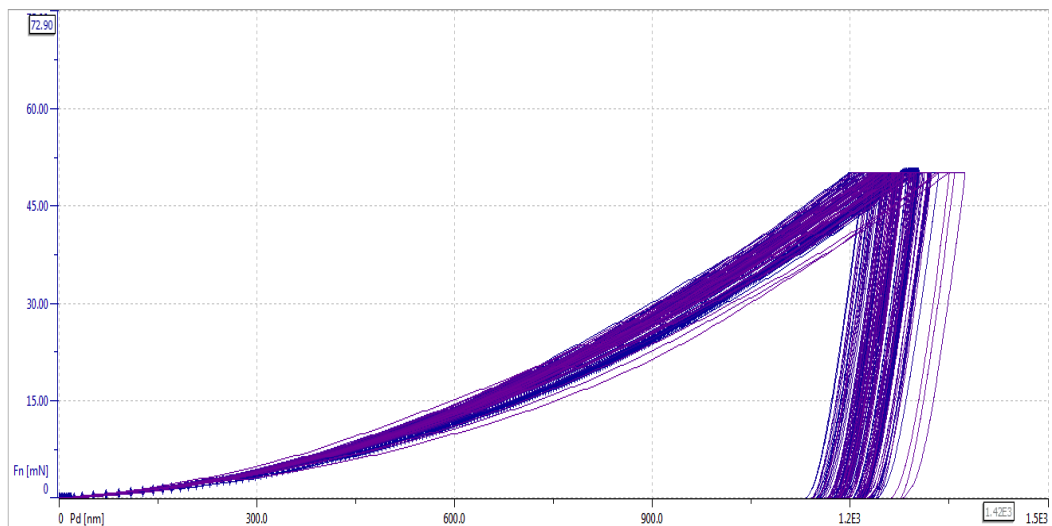


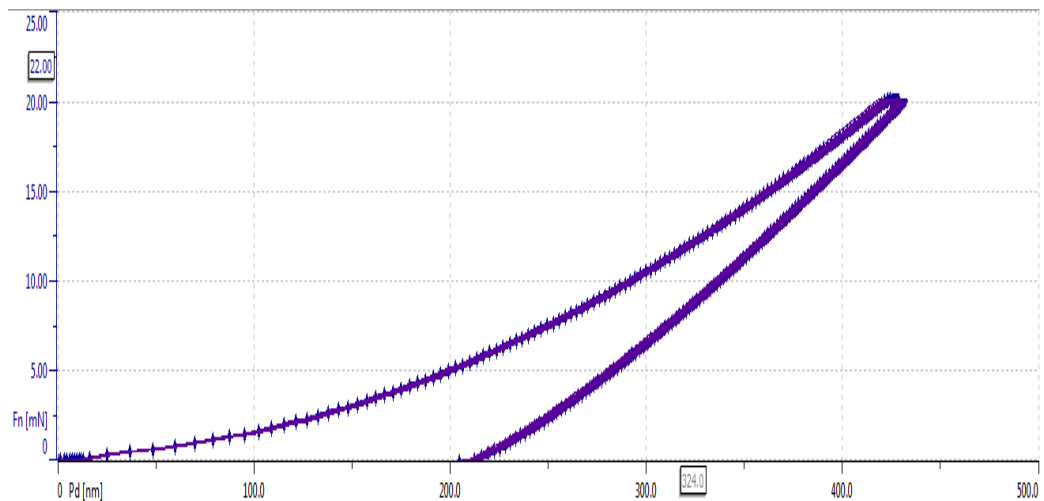
Fig 4.17 Force-displacement curve for Berkovich indenter on (a) copper and (b) fused silica. Both the loading and unloading rate is 100mN/min with a pause of 10s at the maximum force. The displacement origin is set where the indentation depth is zero such that they are identical. The corresponding maximum indentation depth h_t , depth of residual impression h_r and depth beneath the contact periphery h_p are marked in the plot.

Fig 4.17 (a) and (b) show a typical force-displacement ($F-d$) curve for copper and fused silica respectively. As expected, the gap area between loading and unloading curve indicates plastic deformation. The slope of the unloading part remains constant during most part of retraction, revealing that the Berkovich indenter maintains good contact with the substrate during this period. For both materials, the maximum indentation depth is smaller than $1.5 \mu\text{m}$ which is much smaller than 1/10 of sample height (see Fig.4.14 (a) and (b)), and thus the substrate effect could be excluded. As can be seen from the circle part of $F-d$ curve in Fig 4.17, the indenter keeps penetrating the material when the force pauses at its maximum value, revealing that copper and fused silica also exhibit creep. As can be seen from Fig 4.17 (a), the slope of the retraction is high, while its counterpart in Fig 4.17 (b) is low, indicating that copper exhibits higher stiffness than that of fused silica.

Fig 4.18 (a) and (b) show the repeatability of $F-d$ curves obtained by the NHT². As can be seen from Fig 4.18 (a), there is some substantial difference in the $F-d$ curves from 100 curves, which may be due to thermal drift or (and) material inhomogeneity. The curves of retraction are nearly parallel with appreciable offsets. Since parallel retraction curves will produce the same unloading stiffness dF/dh , and h_p , they will in turn yield similar effective Young's modulus E^* and hardness H according to Eq. (4.13) and (4.14). On the other hand, the difference between individual $F-d$ curves obtained from fused silica is not significant as can be seen from Fig 4.18 (b).



(a)



(b)

Fig 4.18 Force-displacement curves corresponding to 100 repeated indentations for (a) copper and (b) fused silica.

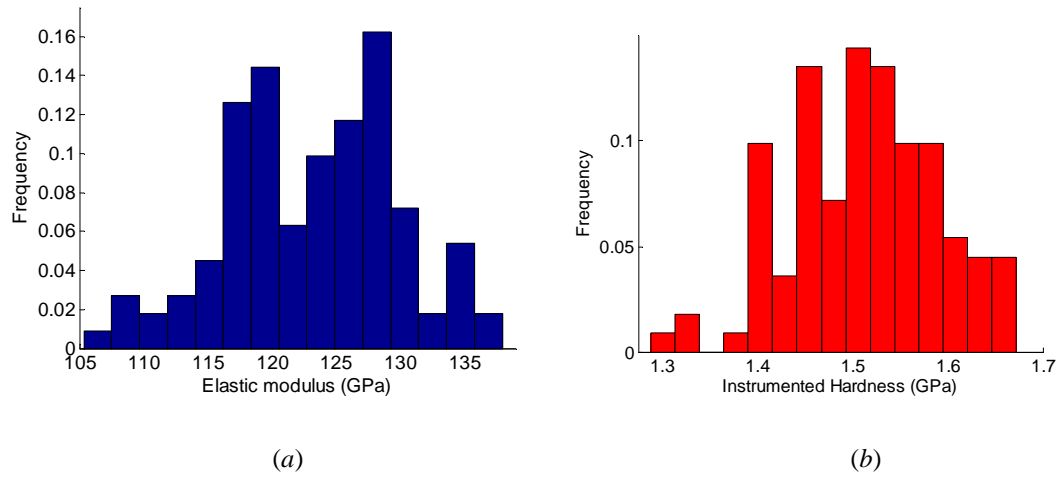


Fig 4.19 Distribution of density of (a) Young's modulus and (b) hardness for copper

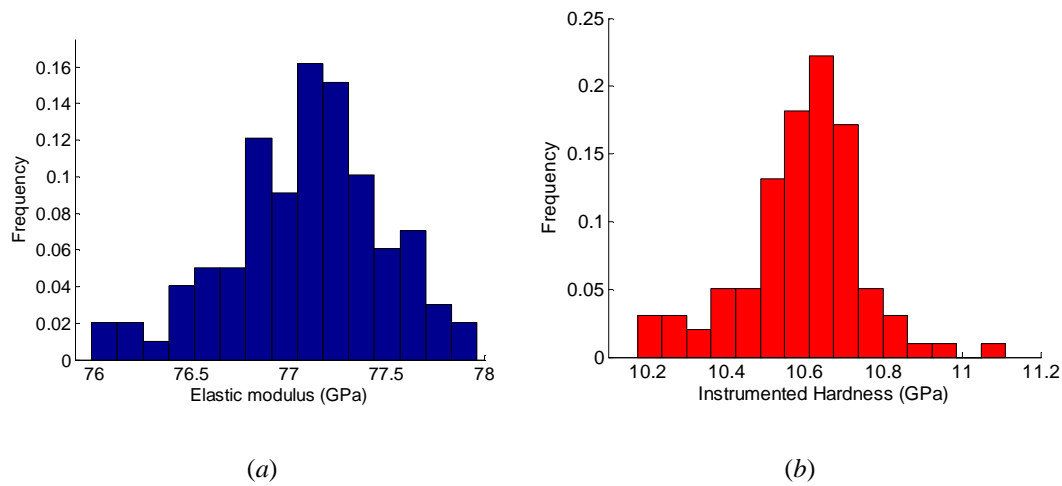


Fig 4.20 Distribution of density of (a) Young's modulus and (b) hardness for fused silica

Table 4.5 List of the statistics results for the two determined parameters

	Young's modulus (GPa)			Hardness (GPa)		
	mean	Std dev	median	mean	Std dev	median
copper	123.17	6.71	123.39	1.51	0.078	1.51

fused silica	77.09	0.4	77.12	10.5	0.98	10.61
--------------	-------	-----	-------	------	------	-------

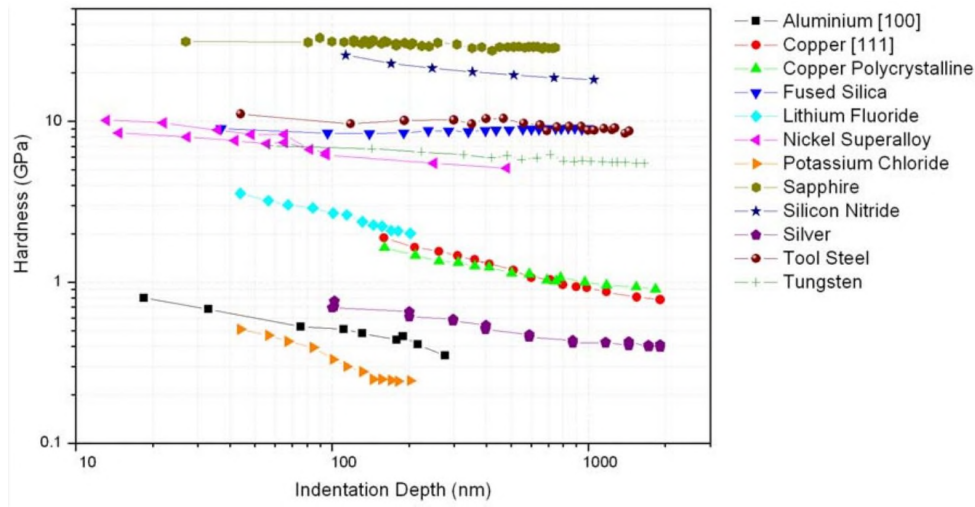


Fig 4.21 Dependence of hardness on indentation depth corresponding to several materials^{[135][136][137]}.

After using the Oliver and Pharr method on the 100 $F-d$ curves, statistics was performed on the calculated Young's modulus and hardness, and the results are shown in Fig 4.19, 4.20 and Table 4.5. From Table 4.5, it can be seen that the estimated Young's moduli of the two materials are close to their typical value as listed in Table 4.3. The estimated hardness for the two materials, however, differs from their typical values by a considerable margin, and the interpretation is as follows. As can be seen from Eq. (4.13) and (4.14), the modulus is proportional to $1/A^{1/2}$ while hardness depends on $1/A$, i.e. hardness is more severely affected by contact area A than modulus. Therefore, any phenomenon that can affect contact area, e.g. pile-up and sink-in could induce more derivation to estimated hardness than that to elastic modulus. As reviewed in Sce.2.2.1, Bolshakov and Pharr^[46] performed extensive finite element analysis on the effect of material properties on the shape of deformation zone during simulative indentation. Materials with high ratio of elastic modulus to hardness, i.e. E/H tend

to exhibit pile-up phenomenon, which will overestimate hardness as analyzed in Sec.4.5.1.1. In addition to pile-up and sink-in, hardness is also affected by indentation depth, termed Indentation Size Effect. This effect is characterized by an increase in hardness by decreasing the ratio indentation depth/size, which is accounted for by a large body of literature^{[135][136][137]}. Fig 4.21 illustrates hardness as a function of indentation depth for several materials. As can be seen, the hardness of fused silicon is not sensitive to indentation depth, and thus it is mainly influenced by pile-up (or sink in) phenomenon. For copper, hardness decreases monotonically as indentation depth increases. Although pile-up phenomenon can overestimate hardness, indentation size effect becomes dominant in deep indentation depth (1000nm). Notably, the copper hardness corresponding to indentation depth of 1000 nm in Fig 4.21 approximates our estimated value (see Table 4.5), whose corresponding indentation depth is also close to 1000 nm, as shown in Fig 4.17 (a). Thus the calculated values of hardness of copper and fused are justified.

4.5.1.3 Comparison of Simulative and Experimental Results

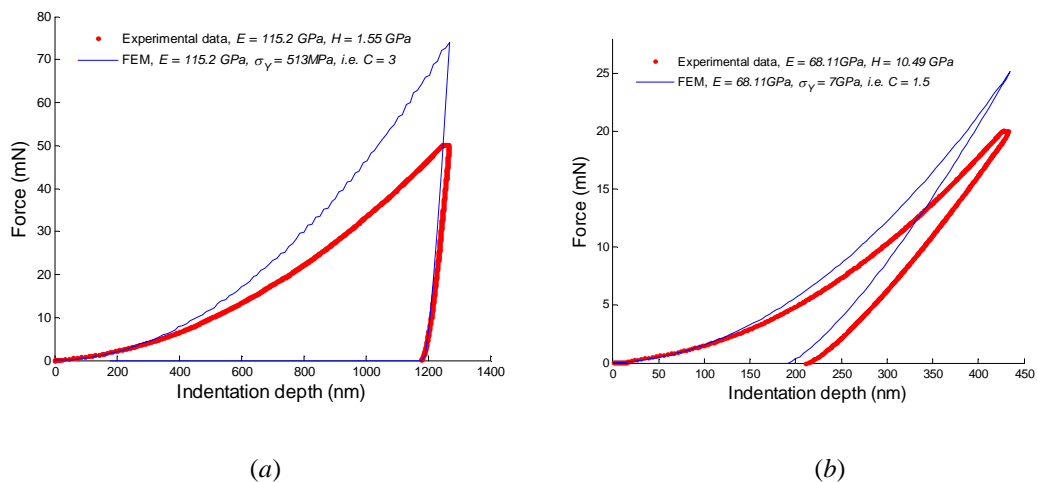


Fig 4.22 Comparison between FEM results and experimental data corresponding to (a) copper and (b)

fused silica

In FEM, displacement was controlled in order to ensure convergence of iteration, and hence the maximum indentation depth obtained from experiment was used as input. For the property setup, the Young's moduli determined from experimental data were input as elasticity parameter. In order to specify the elastic-perfect plastic properties, the initial yield stress σ_Y needs to be well estimated. Experiments^[51] show that the hardness H is proportional to the material yield or flow stress Y in compression as:

$$H \approx CY \quad (4.50)$$

Y is the stress where first plastic yielding occurs. For material with high ratio E/Y (such as copper), one has $C \approx 3$, while for material with low ratio E/Y (such as fused silica), one has $C \approx 1.5$. In this section, the parameter Y in FEM was input according to Eq. (4.50).

Fig 4.22 (a) and (b) show the force-displacement curve produced by finite element method and nanoindentation corresponding to copper and fused silica respectively. It can be seen that the FEM results differ from its experimental counterpart significantly, and interpretations are as follows. First, the FEM uses elastic-perfect plastic manner with no strain hardening. However, the real material may exhibit more complicated strain hardening manners, e.g. isotropic hardening, kinematic hardening or their combination (the concept of isotropic and kinematic hardening will be elaborated in Chapter 5). In elastic-perfect plastic manner, material transits from elastic to plastic response abruptly (see Fig 2.6), while in practice, especially for metals, a gradual transition is more to be expected. Second, even if the material obeys elastic-perfect plastic manner, Eq. (4.50) is merely an empirical relationship between hardness and yield stress, and its validity depends on indenter shape, size, open angle, the

ratio E/Y and pile-up (or sink in) phenomenon. As a matter of fact, as can be seen from Table 4.3, the ratio $H/Y \approx 8.6$ for copper and 7.6 for fused silica respectively which are far from their empirical values as provided by Eq. (4.50).

4.5.2 Silicon Wafer

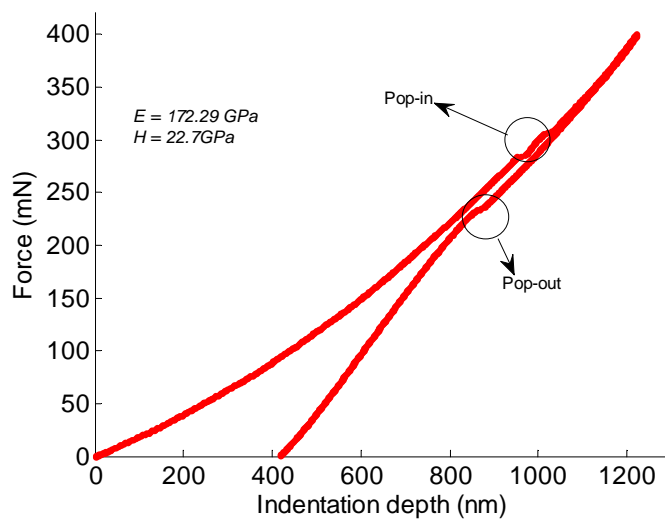


Fig 4.23 Typical Force-displacement curve for silicon wafer.

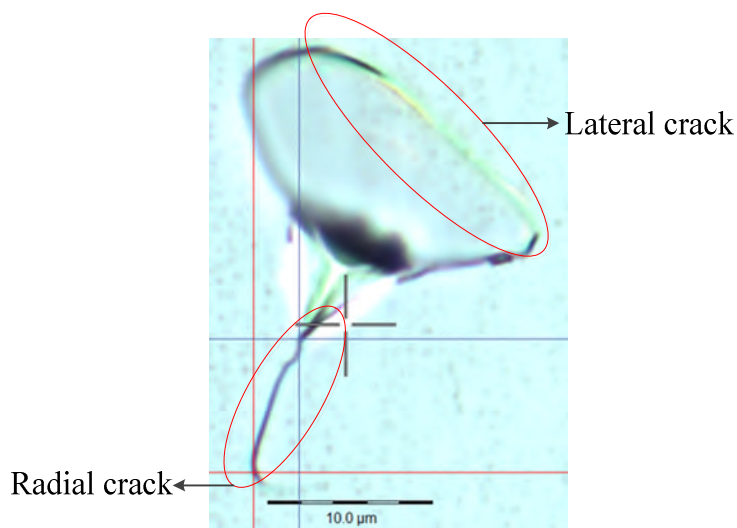


Fig 4.24 Optical microscope of an indentation impression at 400 mN force in silicon wafer.

Fig 4.23 shows a typical force-displacement curve for silicon wafer subjected to Berkovich

nanindentation. There are several discontinuities during loading and unloading, termed pop-in (during loading) and pop-out (during unloading) respectively. A possible reason is sudden crack occurs during loading and unloading, as indicated by the circle in Fig 4.24. Significant evidence produced by some study^[138] suggested that a pressure-induced phase transformation occurs in pure silicon subjected to indentation which manifests itself as the above mentioned pop-in and pop-out events.

Fig 4.24 shows the optical morphology of the residual impression after complete unloading. The crack circled by the left bottom ellipse denotes radial crack, and the top right ellipse circles lateral crack. This lateral crack originates from beneath the surface and results in chipping of the silicon surface^[51].

The Oliver and Pharr method was routinely employed to calculate Young's modulus and hardness, and the length of radial crack was measured by optical microscope built-in NHT² nanoindenter (see Fig 4.11). With Young's modulus $E = 172.29$ GPa, a hardness $H = 22.7$ GPa and a radial crack length $c = 8.45 \mu\text{m}$, one can obtain fracture toughness of almost $0.718 \text{ MPa}\cdot\text{m}^{1/2}$ according to Eq. (4.36), which is close to its typical value as shown by Table 4.3.

4.5.3 Polystyrene

Consider the three element model (see Fig 4.9 (c)) whose creep compliance is

$$J(t) = \frac{1}{E_2} + \frac{1}{E_1} \left(1 - e^{-\frac{E_1}{\eta}t}\right) \quad (4.51)$$

mathematically speaking, as $E_2 \rightarrow \infty$, Eq. (4.51) will reduce to the creep compliance of Kelvin model, and as $E_1 \rightarrow 0$, Eq. (4.46) will reduce to the creep compliance of Maxwell model.

Therefore, three element model is a universal form, and both Maxwell and Kelvin model can be viewed its special circumstances. Hence, the three element model is used to fit the creep

curve. In order to fit the creep curve of the polystyrene sample, judicious adjustment of E_1 , E_2 and η are used. Values of these parameters that provide a good fit are selected as the measured viscoelastic parameters of the sample as shown by Fig 4.25, and their order of magnitude can almost coincide with the typical value as shown in Table 4.4.

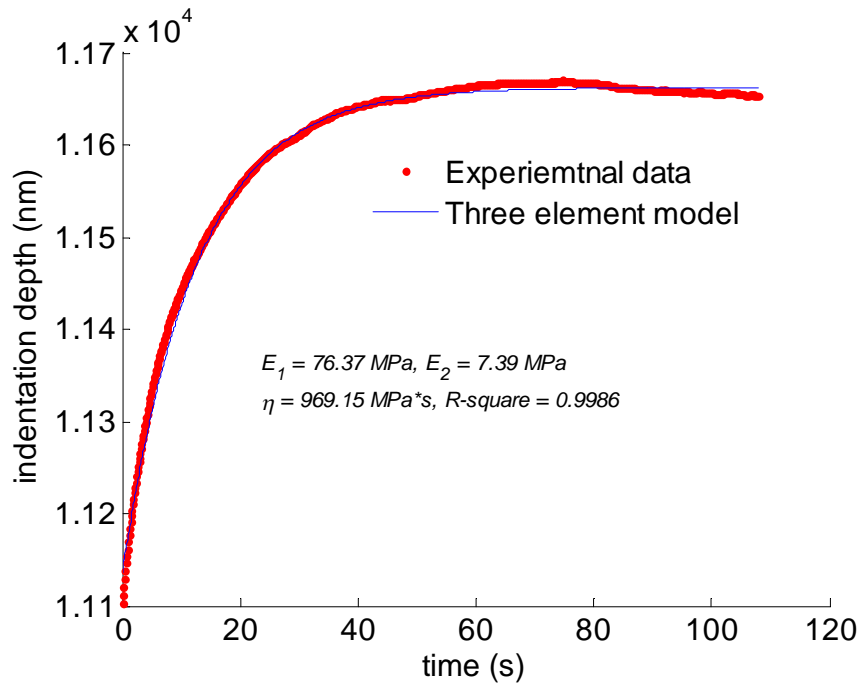


Fig 4.25 Displacement-time curve and its best fitting by using three element model.

4.6 Chapter Summary

In this chapter, the applications of nanoindentation techniques were performed on several calibration materials. Based on the experimental results, quantification of mechanical properties was conducted in terms of relevant basic analyses. Meanwhile, finite element method was employed to verify some assumptions. The following conclusions can be made in this chapter:

- (1) The determined Young's moduli of copper and fused silica approximate their typical counterparts, but the case for hardness is different. For fused silica, the deviation of hardness is probably ascribed to pile-up phenomenon, whilst for copper, the offset may

also be attributed to indentation size effect and pile-up, where the former dominates the latter.

- (2) Creep phenomenon was observed in copper and fused silica by nanoindentation, and thus it can be seen that nominally elastic materials may more or less consist of viscous properties.
- (3) By finite element simulation, it is indicated that the empirical relation between hardness and yield stress may not be a good description to account for plastic properties and work hardening.
- (4) Silicon wafer is a typical brittle material. Both pop-in and pop-out events were observed during nanoindentation on silicon wafer. Radial and lateral cracks occur in the residual impression in microscope, and the latter causes chipping of the silicon surface. The fracture toughness of silicon wafer estimated by Lawn's method approaches its typical value.
- (5) The three element model proves a good characterization for viscoelastic constitutive relationship of polystyrene. By fitting with the experimental data, both elastic moduli and viscosity coincide with the typical values in order of magnitude.

5 Effects of adhesion on shakedown behavior of microcontacting bodies

5.1 Introduction

Theoretical analysis, numerical simulation and experiments are referred to as three basic means of scientific research. In this chapter, studies are conducted mainly by the second method. Nanoindentation belongs to microcontact, and it is appropriate to consider surface effects on microcontact where adhesion forces dominate bulk forces due to high ratio of surface area to volume. In this chapter, nanoindentation is viewed as microcontact in general. Chapter 3 introduces several classic contact models taking surface adhesion into consideration. Nevertheless, adhesion-induced deformation is assumed to be purely elastic in these models, while in practice, a high adhesion force can induce plastic deformation, even without externally applied load. On the other hand, the interfacial forces used in these models are approximation to their real counterpart, and there are substantial differences. Owing to these two aspects, it is still impossible to obtain analytical solution for most real adhesive contact problems where interfacial forces and the surface profile are mutually dependent, and the constitutive relation exhibits elastic-plastic property. In this regard, computational simulation proves to be an efficient means to solve such self-consistent adhesive contact problems.

The investigation of adhesion effects on microcontact is of guiding significance for the studying the durability of miniaturized systems subjected to cyclic loading. Obviously contact fatigue and wear due to surface adhesion forces exert adverse effect on the lifetime of

miniaturized systems subjected to cyclic loading, e.g. microelectromechanical (MEMS) system^{[139][140]}, nanoelectromechanical (NEMS) system, and head/disk interface (HDI)^[141]. By means of finite element simulation, a number of analyses interpret the above issues by the model of nanoindentation, i.e. microcontact subjected to cyclic loading, and they suggest that adhesion forces play a significant role in affecting the mechanical behavior of contacting bodies.

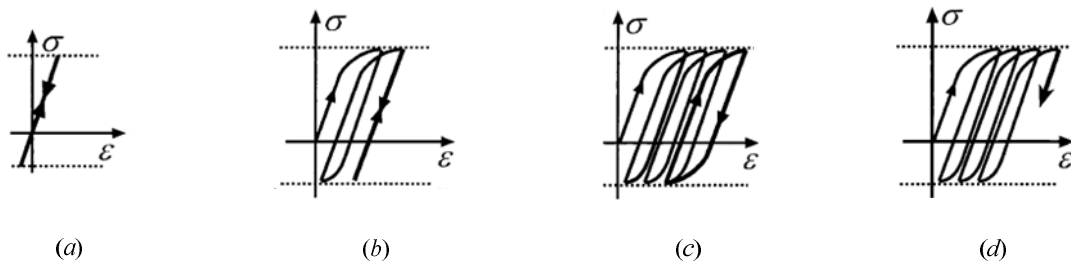


Fig 5.1 Schematic of stress-strain curve for (a) pure elastic (b) elastic shakedown (c) plastic shakedown and (d) ratchetting^[142].

Generally speaking, the mechanical response of engineering structures to cyclic loading is dependent on its mechanical properties (e.g. elastic modulus, initial yield stress and work hardening rules) and features of the cyclic load (e.g. its maximum and minimum values). When the effective stress is below elastic limit, only elastic deformation occurs as shown by Fig 5.1 (a). If the stress is slightly higher than the elastic limit, plastic deformation will emerge in the first cycle, which causes residual stress such that only elastic deformation occurs in subsequent cycles. Since the initial elastic-plastic response of the structure shakes down to wholly elastic behavior, this phenomenon is known as *elastic shakedown*, as illustrated in Fig 5.1 (b). Once the stress exceeds elastic shakedown limit, the structure may exhibit reverse or

alternating plasticity over each cycle known as *plastic shakedown* as shown by Fig 5.1 (c). Structures undergoing plastic shakedown will fail after a finite number of load cycles due to low-cycle fatigue. Alternatively the structure may provide net increments of plastic strain within each cycle as illustrated by Fig 5.1 (d), and the strain will accumulate until gross plastic deformation and eventually incremental plastic collapse occurs. This response is called as *ratchetting*.

For microcontact, not only elastic shakedown limit, but also the surface forces are crucial to understanding failure of microcontact subjected to cyclic loading. Kadin^[99] used finite element method and Lennard-Jones potential to model repetitive adhesive contact between a rigid surface and an elastoplastic sphere. By specifying the sphere with a kinematic strain hardening manner, they investigated the effect of surface adhesion on the shakedown behaviors of the indenter-substrate system. Song and Komvopoulos^[143] used the same means to simulate repetitive adhesive contact between a rigid sphere and an elastic-perfect plastic half-space, and their results showed that plastic shakedown can also occur even for a small maximum normal displacement due to the low yield strength of the material. Nevertheless, there are rare studies on the shakedown behavior of isotropic hardening materials subjected to repetitive adhesive contact.

The main goal of this chapter is to investigate the effect of adhesion forces on shakedown behavior of spherical microcontact subjected to cyclic loading. To accomplish this objective, an elastoplastic half-space is modeled to be indented by a rigid sphere subjected to cyclic loading-unloading. To provide a thorough investigation, the work hardening rule of indented material takes two basic forms, i.e. isotropic hardening and kinematic hardening, to account

for potential plastic shakedown. The interaction force between the rigid spherical indenter and the substrate obeys a more accurate law, i.e. Lennard-Jones potential. Finite element method is employed to solve the self-consistent adhesive contact problem due to mutual dependence of interaction forces and the surface profile.

5.2 Propaedeutics

In physics and materials science, plasticity describes the deformation of a material undergoing non-reversible changes of shape in response to applied forces^[144]. The physical mechanisms for plasticity can vary widely. For brittle materials such as rock and concrete, plasticity is mainly due to slip at microcracks, and for metal, plasticity is a consequence of dislocations at crystalline scale.

5.2.1 Yield criteria

It is common sense that if the load on a material exceeds a critical value, the deformation is irreversible. Consider a simple case, i.e. a metal rod whose section area is A_c is loaded by a tensile force F as shown by Fig 5.2. The tensile stress on the section of the rod σ equals F/A_c . If σ is within elasticity range, the corresponding deformation is reversible, e.g. point A in Fig 5.2. Once this stress exceeds a critical value Y (i.e. point B in Fig 5.2), plastic (irreversible) deformation occurs. This point is known as yield point, and the critical stress Y is termed yield stress. The standard to determine the occurrence of yield is called yield criterion. For uniaxial loading (tensile or compressive), yield criterion is given as

$$\sigma = \frac{F}{A_c} = Y \quad (5.1)$$

where yield stress Y can be tensile or compressive.

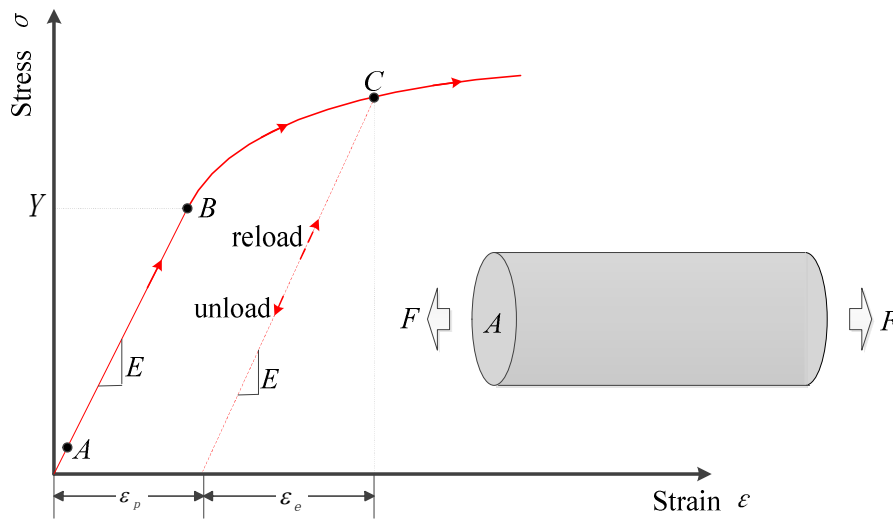


Fig 5.2 Stress–strain curve showing typical yield behavior for nonferrous alloys in uniaxial loading

In practice, materials are subjected to multiaxial loading, and yield criterion is given by a universal form as

$$f_0(\sigma_i) = 0 \quad (5.2)$$

where σ_i ($i = 1, 2, 3$) denotes three principal stresses which constitute a principal stress space. The points whose three principal stresses satisfy Eq. (5.2) in stress space will generate a curved surface, termed yield surface. Thus the concept of yield criterion is often expressed as yield surface. There are two commonly used yield criteria, namely Tresca criterion and the von Mises criterion.

5.2.1.1 Tresca criterion

Tresca criterion assumes yield occurs when the maximum shear stress τ_{max} exceeds a critical value k , i.e.

$$\tau_{max} \geq k \quad (5.3)$$

The maximum shear stress can be given in terms of the maximum principle stress σ_1 and

minimum principle stress σ_3 as

$$\tau_{max} = \frac{\sigma_1 - \sigma_3}{2} \quad (5.4)$$

Substituting Eq. (5.4) into Inequality (5.3) yields

$$\frac{\sigma_1 - \sigma_3}{2} \geq k \quad (5.5)$$

Tresca criterion proves a relatively good assumption for metals. It is observed that this criterion does not take the middle principle stress σ_2 into consideration, and this issue is countered in von Mises criterion.

5.2.1.2 Von Mises criterion

Von Mises criterion is based on Tresca criterion, but considers that hydrostatic stresses do not contribute to the yield. It suggests that yield occurs when the second deviatoric stress invariant J_2 reaches a critical value, given as

$$J_2 = \frac{1}{6} [(\sigma_1 - \sigma_2)^2 + (\sigma_2 - \sigma_3)^2 + (\sigma_3 - \sigma_1)^2] = \frac{Y^2}{3} \quad (5.6)$$

where Y denotes yield stress in uniaxial loading. It is part of a plasticity theory that applies best to ductile materials, such as metals.

5.2.2 Work hardening

For uniaxial loading, as shown by Fig 5.2, after stress exceeds yield stress, if the material is unloaded and then reloaded, one can find the subsequent yield stress (see point C in Fig 5.2) is higher than the previous one, and this phenomenon is known as work hardening (or strain hardening, cold working). The physical mechanisms for work hardening are dislocation movements and dislocation generation within the crystal structure of the material^[145].

Although it is observed in uniaxial loading, work hardening can be extended to more general

case, where the yield surface may change size, shape and even position, and can be described as

$$f(\sigma_{ij}, K_i) = 0 \quad (5.7)$$

where K_i denotes one or some hardening parameters which vary during plastic deformation and determine the evolution of yield surface, and σ_{ij} ($i, j = 1, 2, 3$) represents stress component. The description of the dependence of yield surface change on plastic deformation is called *hardening rule*. There are three main common hardening rules, i.e. *isotropic hardening*, *kinematic hardening* and mixed hardening. In the following, a brief introduction to isotropic and kinematic hardening rules is presented, and mixed hardening is a combination of isotropic and kinematic hardening.

5.2.2.1 Isotropic hardening

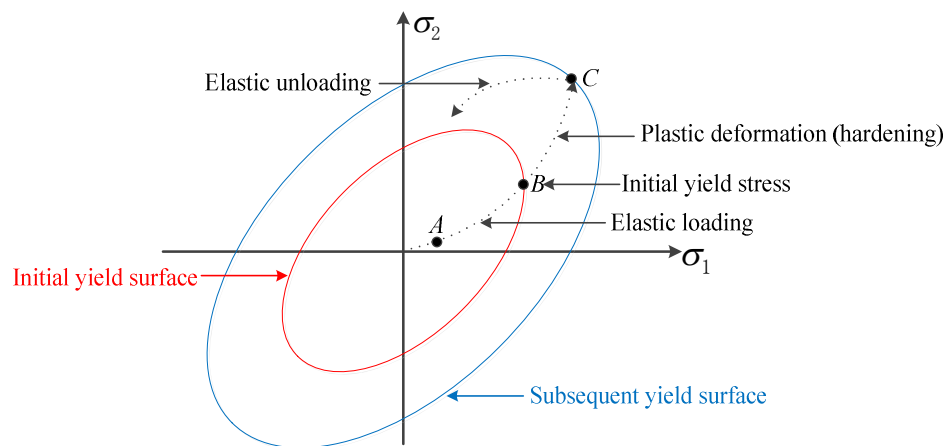


Fig 5.3 Schematic for the expanding of yield surface in isotropic hardening

Isotropic hardening postulates that the yield surface expands uniformly about its origin of stress space while the location of its center remains invariant as illustrated by Fig 5.3. In

particular, the yield surface can be formulated as

$$f(\sigma_{ij}, K_i) = f_0(\sigma_{ij}) - K_i = 0 \quad (5.8)$$

where $f_0(\bullet)$ denotes the initial yield surface. For the von Mises yield surface, at initial yield, one has

$$f_0(\sigma_{ij}) = \sqrt{\frac{(\sigma_1 - \sigma_2)^2 + (\sigma_2 - \sigma_3)^2 + (\sigma_3 - \sigma_1)^2}{2}} - Y = 0 \quad (5.9)$$

or more universally

$$f_0(\sigma_{ij}) = \sqrt{\frac{3}{2} s_{ij} s_{ij}} - Y = 0 \quad (5.10)$$

where Y is the first yield stress for uniaxial tension, s_{ij} denotes deviatoric stress, i.e.

$$s_{ij} = \sigma_{ij} - \frac{\sigma_1 + \sigma_2 + \sigma_3}{3} \delta_{ij} \quad (5.11)$$

where repeated subscripts denote Einstein summation convention. Here δ_{ij} represents Kronecker delta function, i.e.

$$\delta_{ij} = \begin{cases} 0 & \text{if } i \neq j \\ 1 & \text{if } i = j \end{cases} \quad (5.12)$$

Substituting Eq. (5.9) into (5.8) yields

$$f(\sigma_{ij}) = \sqrt{\frac{(\sigma_1 - \sigma_2)^2 + (\sigma_2 - \sigma_3)^2 + (\sigma_3 - \sigma_1)^2}{2}} - (Y + K_i) = 0 \quad (5.13)$$

How hardening parameter K_i changes with plastic deformation should be determined by other assumptions.

5.2.2.2 Kinematic hardening

The *kinematic hardening* dictates that the yield surface translates from its initial position during plastic deformation while its profile remains unchanged as shown by Fig 5.4. Kinematic hardening implies that if the material undergoes stretch in one direction, its tensile yield strength in this direction is increased, while the local initial compressive yield strength after stretch is actually reduced. This phenomenon is termed Bauschinger effect as shown by

Fig. 5.5. The equation for the yield surface takes the general form as

$$f(\sigma_{ij}, K_i) = f_0(\sigma_{ij} - \alpha_{ij}) \quad (5.14)$$

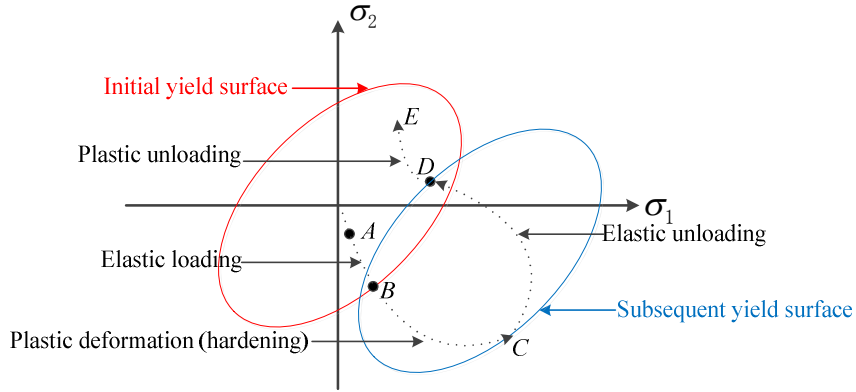


Fig 5.4 Schematic for the translation of yield surface in kinematic hardening. Although point E is within the initial yield surface, it is no longer contained by subsequent yield surface, and thus plasticity occurs during the path from D to E.

where the hardening parameter α_{ij} ($i, j = 1, 2, 3$) is known as *shift-stress*. For the von Mises yield surface again, one can easily get the equation for the strengthened yield surface as

$$f(\sigma_{ij}, K_i) = \sqrt{\frac{3}{2}(s_{ij} - \alpha_{ij}^d)(s_{ij} - \alpha_{ij}^d)} - Y = 0 \quad (5.15)$$

where α_{ij}^d denotes the deviatoric part of α_{ij} , i.e. $\alpha_{ij}^d = \alpha_{ij} - \delta_{ij} \cdot (\alpha_{11} + \alpha_{22} + \alpha_{33})/3$.

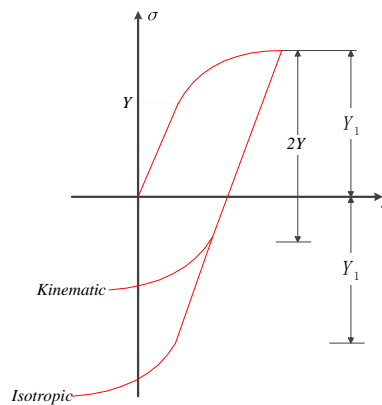


Fig 5.5 Comparison between isotropic and kinematic hardening in terms of stress-strain curve

5.2.2.3 Mixed hardening rules

More complicated hardening rules can be used. For example, the mixed hardening rule can be viewed as the combination of both isotropic and kinematic hardening, whose general form is

$$f(\sigma_{ij}, K_i) = f_0(\sigma_{ij} - \alpha_{ij}) - K_i \quad (5.16)$$

where α_{ij} and K_i are determined by other presumptions.

5.2.3 Flow curve

The idea of modelling plastic deformation and hardening in a multiaxial situation is analogous to the data from a simple test. For example, in uniaxial loading, after the stress exceeds the yield stress Y for the first time, one can have the data shown in Fig 5.6 (a), and further extract the dependence of stress σ on plastic strain ε^p , i.e. $\sigma = h(\varepsilon^p)$. Before extending this dependence to multiaxial situation, it is essential to define a scalar **effective stress** σ_{eff} and a scalar **effective plastic strain** ε_{eff}^p , and then the following assumption is introduced: for a complicated multiaxial loading case, the dependence of **effective stress** on **effective plastic strain** is the same as its uniaxial loading counterpart, as shown by Fig 5.6 (b).

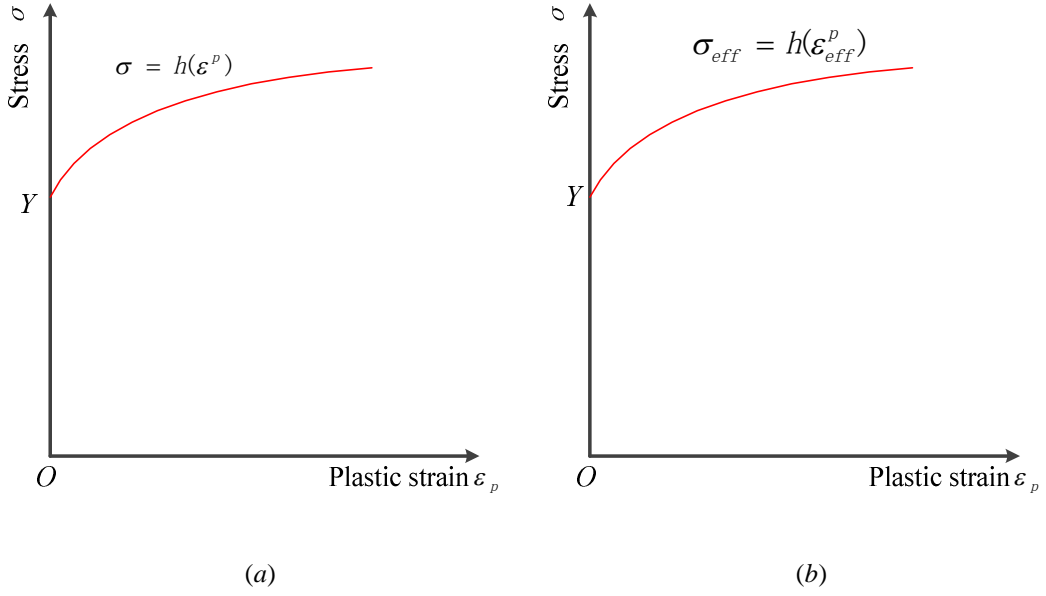


Fig 5.6 The flow curve for (a) uniaxial stress-plastic strain and (b) effective stress-effective plastic strain

For a von Mises material (i.e. materials obeying von Mises yield criterion), it is appropriate to define the effective stress as

$$\sigma_{eff}(\sigma_{ij}) = \sqrt{3J_2} = \sqrt{\frac{(\sigma_1 - \sigma_2)^2 + (\sigma_2 - \sigma_3)^2 + (\sigma_3 - \sigma_1)^2}{2}} \quad (5.17)$$

which has the essential property that at yield in uniaxial loading, effective stress equals yield stress. The effective plastic strain (Von Mises plastic strain) is defined as

$$\varepsilon_{eff}^p = \int d\varepsilon_{eff}^p = \int \sqrt{\frac{2}{3} d\varepsilon_{ij}^p d\varepsilon_{ij}^p} = \frac{\sqrt{2}}{3} \sqrt{(d\varepsilon_1^p - d\varepsilon_2^p)^2 + (d\varepsilon_2^p - d\varepsilon_3^p)^2 + (d\varepsilon_3^p - d\varepsilon_1^p)^2} \quad (5.18)$$

where ε_i^p ($i = 1, 2, 3$) denotes three principle plastic strains (see Fig 5.2) and ε_{ij}^p ($i, j = 1, 2, 3$) denote plastic strain components in strain space. In this chapter, two basic hardening manners are considered, i.e. power law isotropic hardening and bilinear kinematic hardening whose relationship between effective stress and effective plastic strain are given in Table 5.1, and illustrated in Fig 5.7.

Table 5.1 Details of the two hardening models used in this chapter

Hardening Rule	Formulae	Notes
power law isotropic hardening	$\frac{\sigma_{eff}}{Y} = \left(\frac{E}{Y} \varepsilon_{eff}^p + \frac{\sigma_{eff}}{Y}\right)^n$ (5.19)	$0 \leq n < 1$, $\sigma_{eff} > Y$ E denotes Young's modulus
bilinear kinematic hardening	$\sigma_{eff} = \frac{EE_T}{E-E_T} \varepsilon_{eff}^p + Y$ (5.20)	E_T denotes tangential modulus $\sigma_{eff} > Y$ $E_T < E$

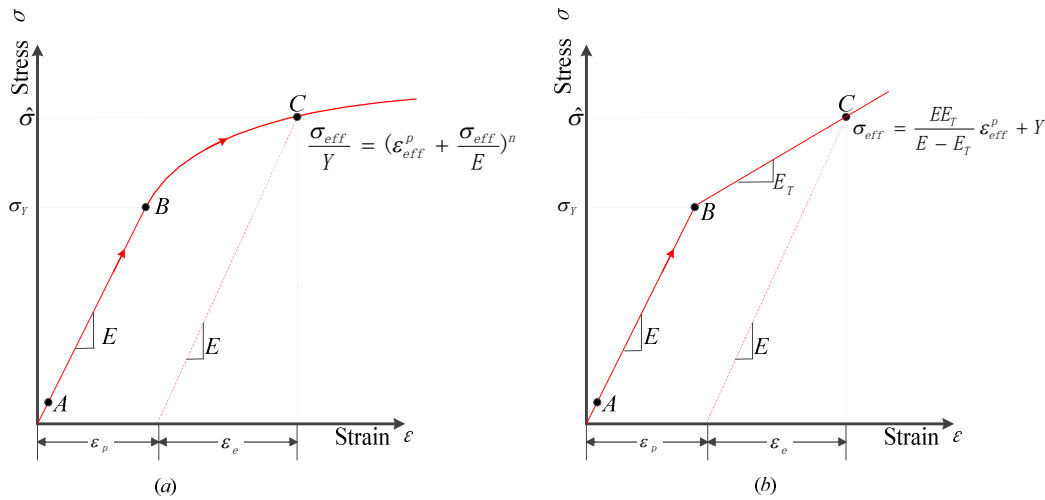


Fig 5.7 Schematic of dependence of effective stress on effective plastic strain for (a) power law isotropic hardening and (b) bilinear kinematic hardening.

5.3 Finite element model

It is an appropriate means to abstract microcontact as contact between two spheres or one sphere with infinite semi-space. In this chapter, for simplicity, the latter model is used as shown by Fig 5.8. Prior to contact, the half-space retains its original shape if no interfacial forces exist as shown by Fig 5.8 (a), whereas the presence of interfacial forces will deform the half-space as shown by Fig 5.8 (b). Assuming that the interaction forces between the rigid spherical indenter and the infinite half-space obey Lennard-Jones potential given by Eq. (3.21), one has

$$\sigma(r) = \frac{8\Delta\gamma}{3z_0} \left\{ \left[\frac{z_0}{H(r)} \right]^3 - \left[\frac{z_0}{H(r)} \right]^9 \right\} \quad (5.21)$$

where $\sigma(z)$ and $H(r)$ denote local interaction forces and local separation between indenter surface and substrate surface respectively, as shown by Fig 5.8 (b).

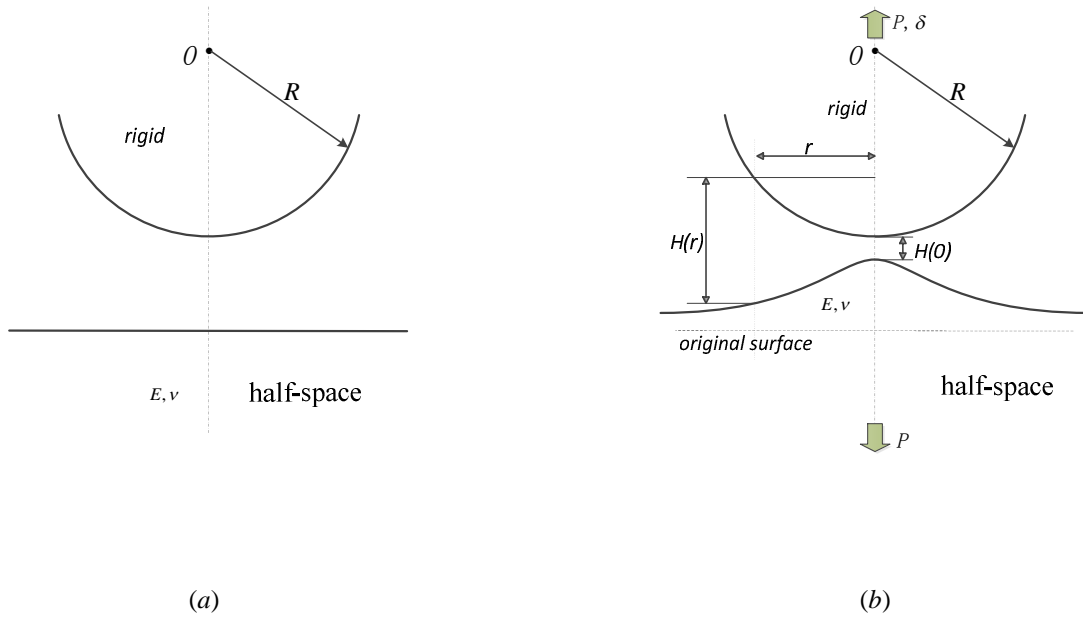


Fig 5.8 Schematic of (a) non-adhesive contact and (b) adhesive contact between a rigid spherical indenter and a deformable half-space

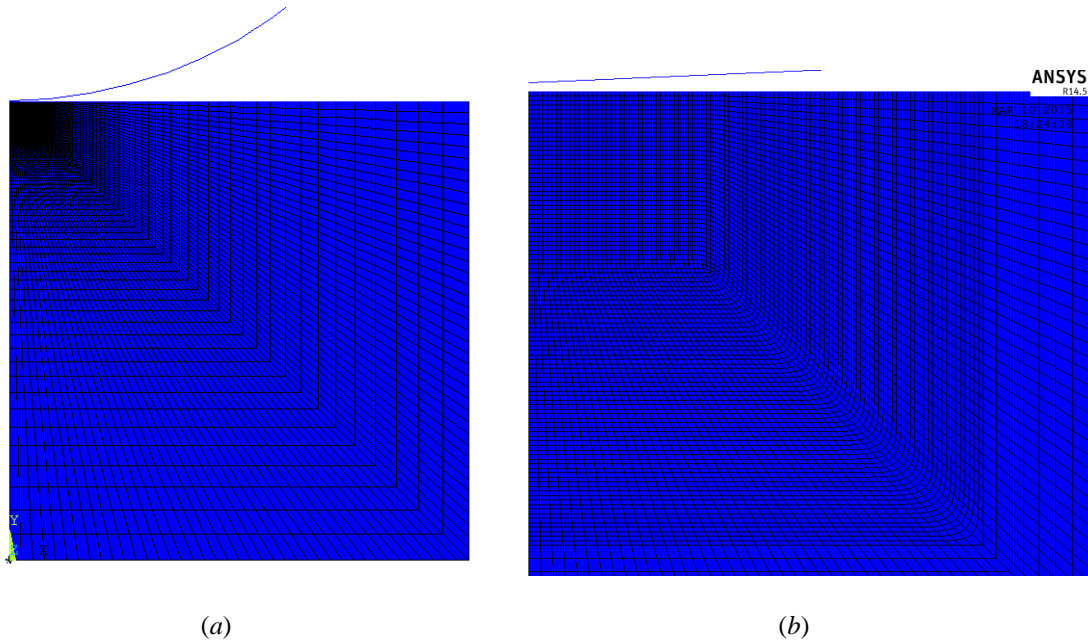


Fig 5.9 Schematic of FE model of adhesive contact between a rigid sphere and a deformable half-space for (a) overview and (b) its amplification at contact region.

Based on the model in Fig 5.8, the commercial ANSYS 14.5 package was used to solve the axisymmetrical (2D) elastoplastic adhesive contact problem with only one half of the axisymmetric hemisphere section (see Fig 5.9). The nonlinear geometry option was selected to accommodate potential large deformation. The mesh and boundary conditions were conducted in the same way as that in Sec.4.4, as can be seen from Fig 5.9 (a) and (b). The Lennard-Jones force given by Eq. (5.21) was included by using the user subroutine USERINTER in ANSYS. To ensure convergence, the finite element simulation in this chapter adopted displacement-control method. Before specifying plastic property, only elastic parameters, i.e. E and ν were input for running, and the resulted elastic responses were compared with existing results obtained by self-consistent method^[75] for justification. In the property manager, The von Mises yield criterion was used as yield criterion. Work hardening was realized by two means, i.e. power law isotropic hardening and bilinear kinematic

hardening listed in Table 5.1.

5.4 Results and discussions

5.4.1 Pure elastic adhesive contact

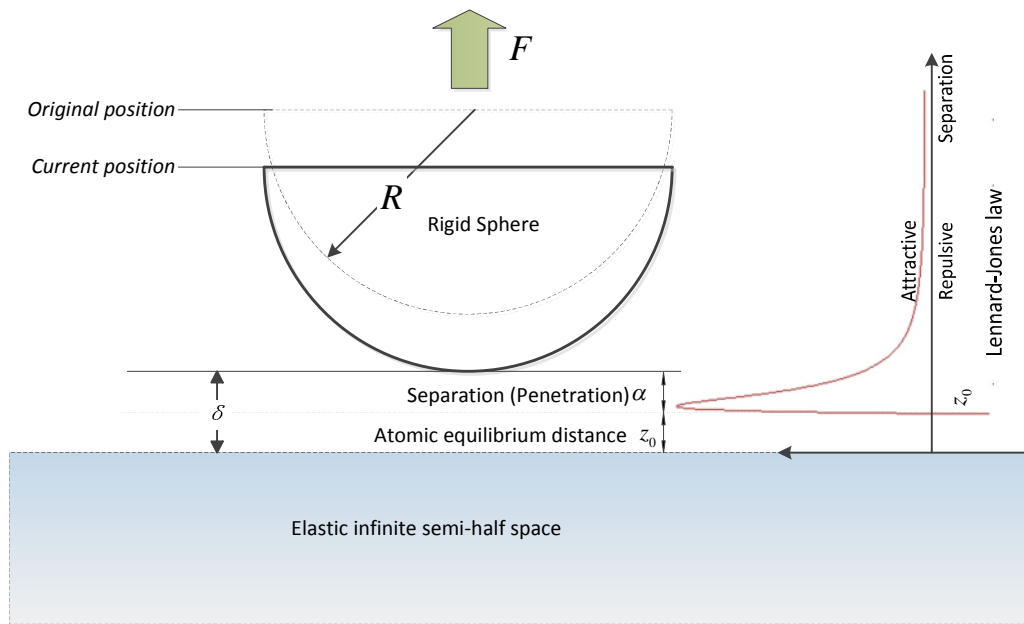


Fig 5.10 Schematic of a pure elastic half-space indented by a rigid spherical indenter. The interaction force obeys Lennard-Jones potential, where the dotted line represents zero force space.

Fig 5.10 illustrates adhesive contact between a rigid sphere and an elastic half-space. α denotes the vertical distance between the apex of the sphere and the zero force line. Positive α and negative α represent separation and penetration respectively. F denotes resultant interaction force between the indenter and the half-space. Positive F and negative F represent attraction and repulsion. According to Eq. (3.39b), if one adjusts Young's modulus E and fixes the rest four parameters whose values are as listed in Table 5.2, Tabor parameter μ can vary correspondingly.

Table 5.2 Parameters studied in the adhesive contact

Work of adhesion $\Delta\gamma$ (J/m^2)	Atomic equilibrium distance z_0 (nm)	Radius of the rigid sphere R (nm)	Poisson's ratio ν
0.46	0.34	1000	0.1

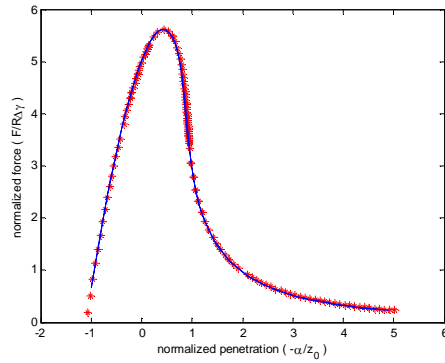
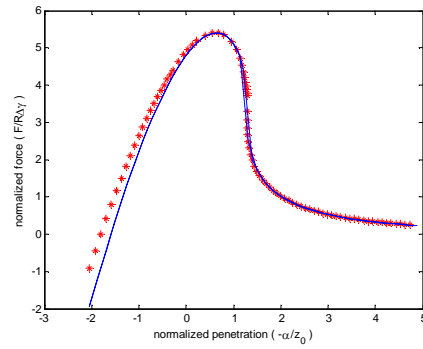
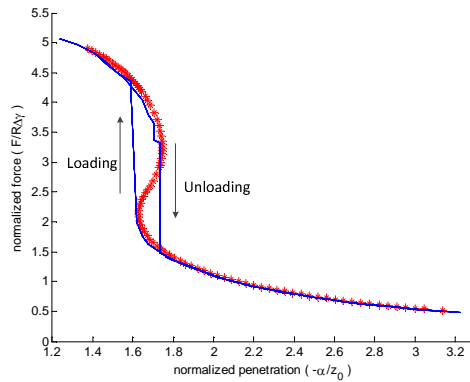
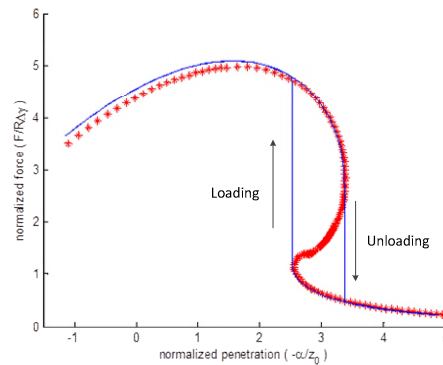
(a) $\mu = 0.5$ (b) $\mu = 0.75$ (c) $\mu = 1.0$ (d) $\mu = 2.0$

Fig 5.11 Dependence of normalized force $F/\pi R \Delta\gamma$ on normalized penetration $-\alpha/z_0$ for (a) $\mu=0.5$, (b) $\mu = 0.75$, (c) $\mu = 1.0$ and (d) $\mu = 2.0$. The blue line and red asterisk represent results by using our FE simulation and self-consistent method^[75], respectively.

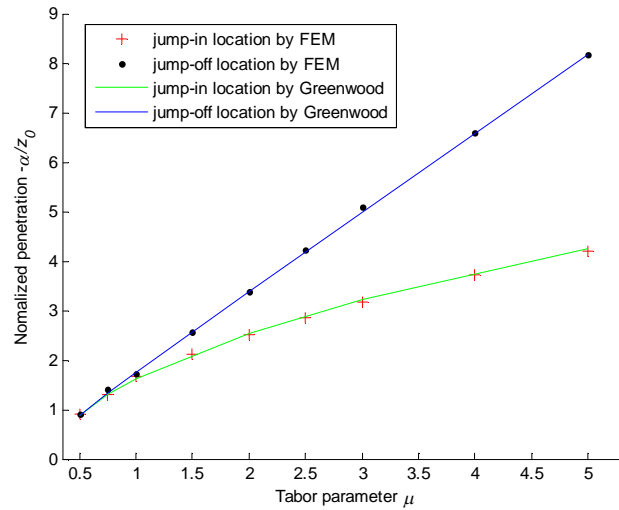


Fig 5.12 Dependence of jump-in and jump-out position (in terms of normalized penetration $-a/z_0$) on Tabor parameter μ .

The comparison between FEM results and its self-consistent counterpart is mainly in terms of the force-penetration curve and the dependence of instability jump positions on Tabor parameter. Fig 5.11 shows the relationship between normalized force $F/\pi R\Delta\gamma$ and normalized penetration $-a/z_0$ of four different μ values by using FEM and self-consistent method. As can be seen from Fig 5.11 (a) and (b), as $\mu < 1$, the results by FEM coincide with its self-consistent counterpart well. As $\mu \geq 1$, i.e. Fig 5.11 (c) and (d), the normalized force-penetration curve by FEM almost overlap its self-consistent counterpart except the jump-in and jump-out instants. Greenwood pointed out that, the jump-in and jump-out phenomena manifest themselves by the “S” shaped curve in self-consistent method, whereas in the finite element method, this instability jump is characterized by vertical lines (i.e. “brittle” jump), and thus the divergence here is ascribed to these two different computational methods. In addition, the dependence of instability location ($-a/z_0$) on Tabor parameter μ obtained by FEM is consistent with its self-consistent counterpart, as shown by Fig 5.12. Therefore, on the whole, the finite element

method developed in this chapter is verified.

5.4.2 Power law isotropic hardening

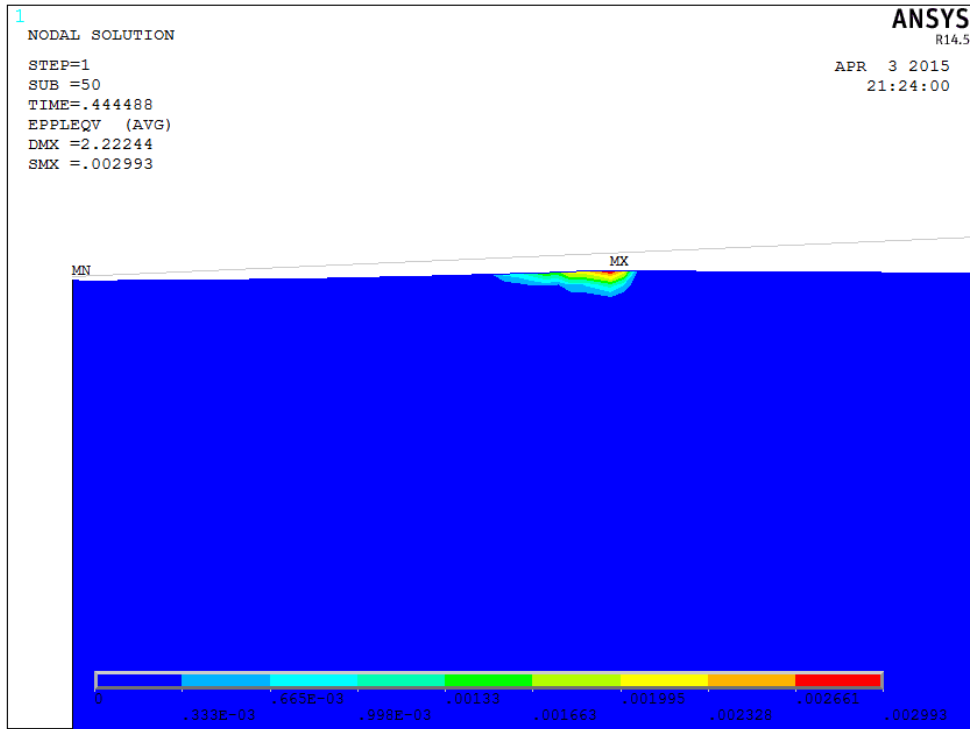
As is indicated by Fig 5.11, and also by many other studies^{[75][87][88]}, for pure elastic adhesive contact, the dimensionless load-displacement curves are solely dependent on Tabor parameter μ . In this chapter, i.e. elastoplastic adhesive contact, similar to the finding by some previous studies, the dimensionless load-displacement curves are also dependent on another dimensionless called plasticity parameter S ^{[98][99]}, given as

$$S = \frac{\Delta\gamma}{Yz_0} \quad (5.22)$$

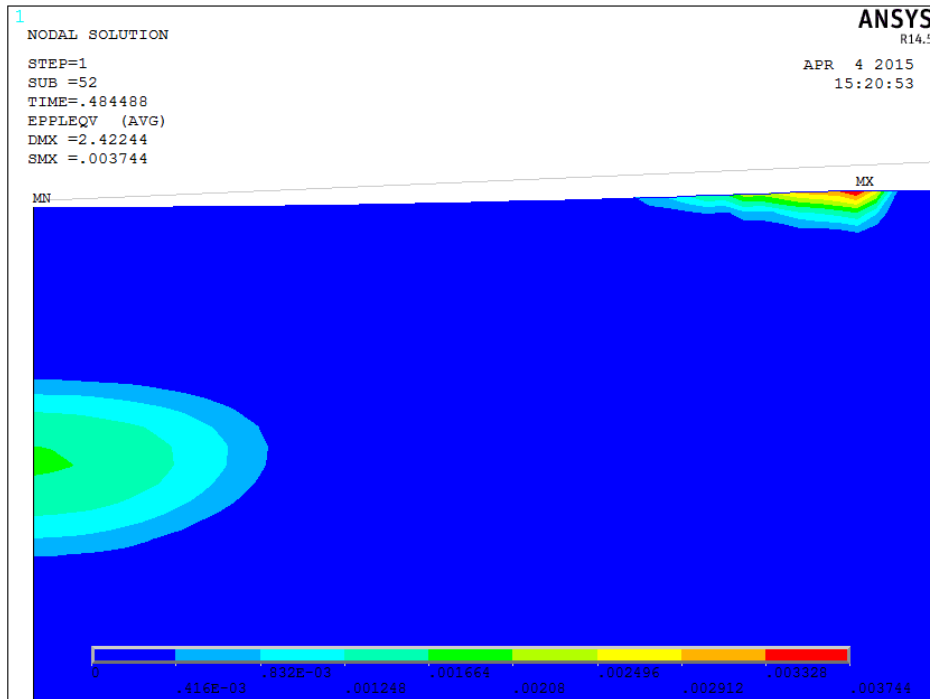
where Y denotes the initial yield stress of the elastoplastic material. High value of S indicates considerable plastic deformation with contact region. According to Eq. (5.22), if initial yield stress Y is adjusted while the values of rest two parameters are chosen by reference to Table 5.2, S can also vary correspondingly.

5.4.2.1 Von Mises Plastic Fields

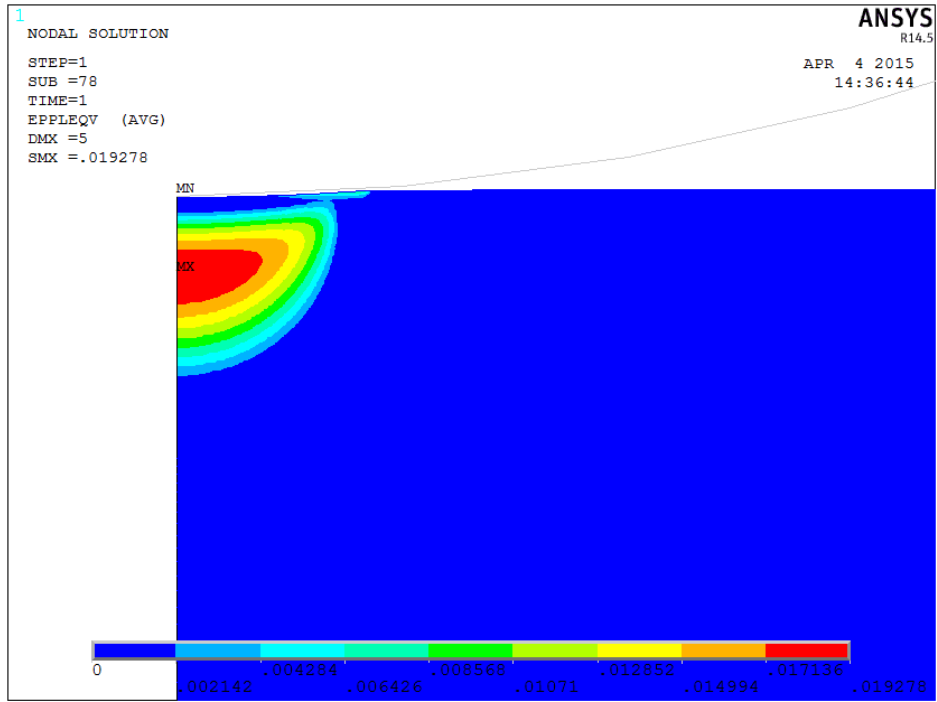
Although Sec.5.4.1 provides one verification method for FEM in Sec. 5.3, it still conforms to elastic constitutive relationship. In this section, analyses of the plastic strain fields are presented to verify the adoption of plastic properties, i.e. hardening manner.



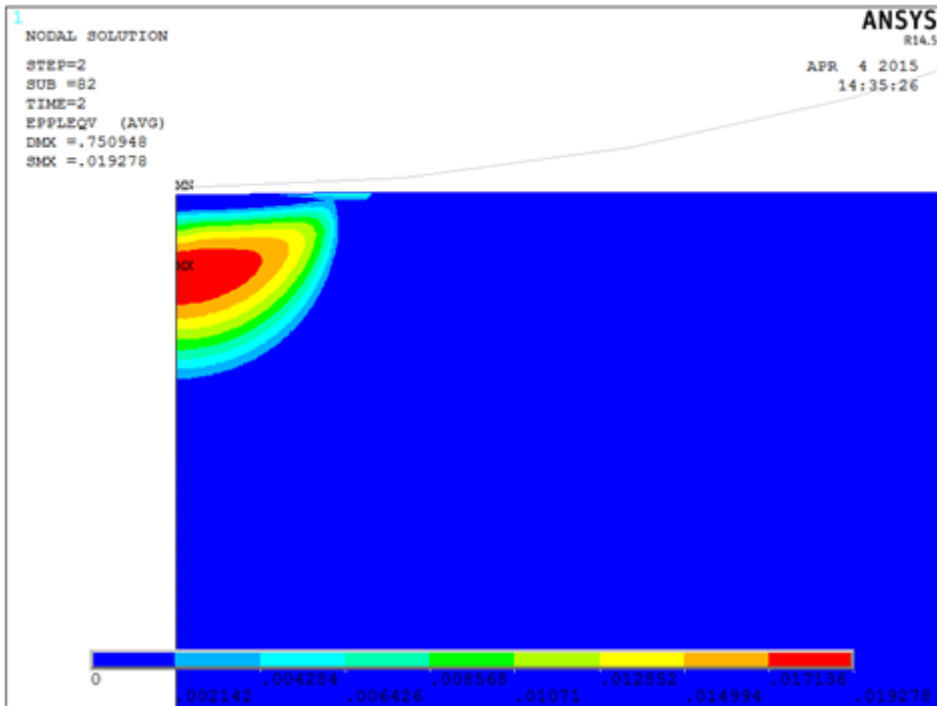
(a) $\mu = 1, n = 0.5, Y = 1\text{GPa}, \delta/z_0 = -0.65$



(b) $\mu = 1, n = 0.5, Y = 1\text{GPa}, \delta/z_0 = -1.24$



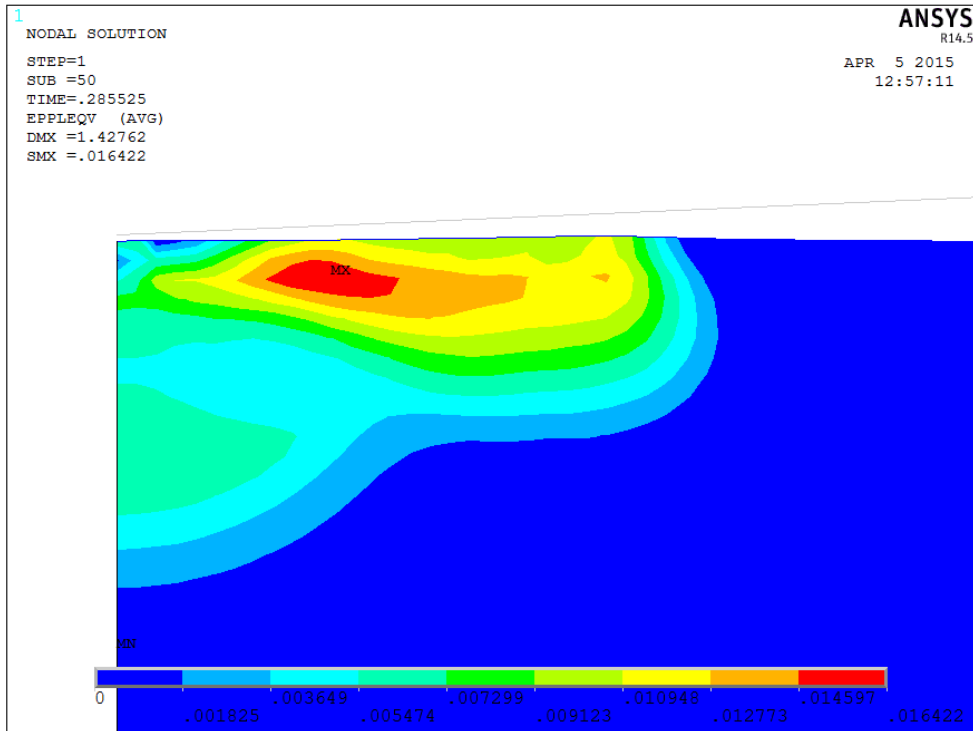
(c) $\mu = 1, n = 0.5, Y = 1\text{GPa}, \delta/z_0 = -8.82$



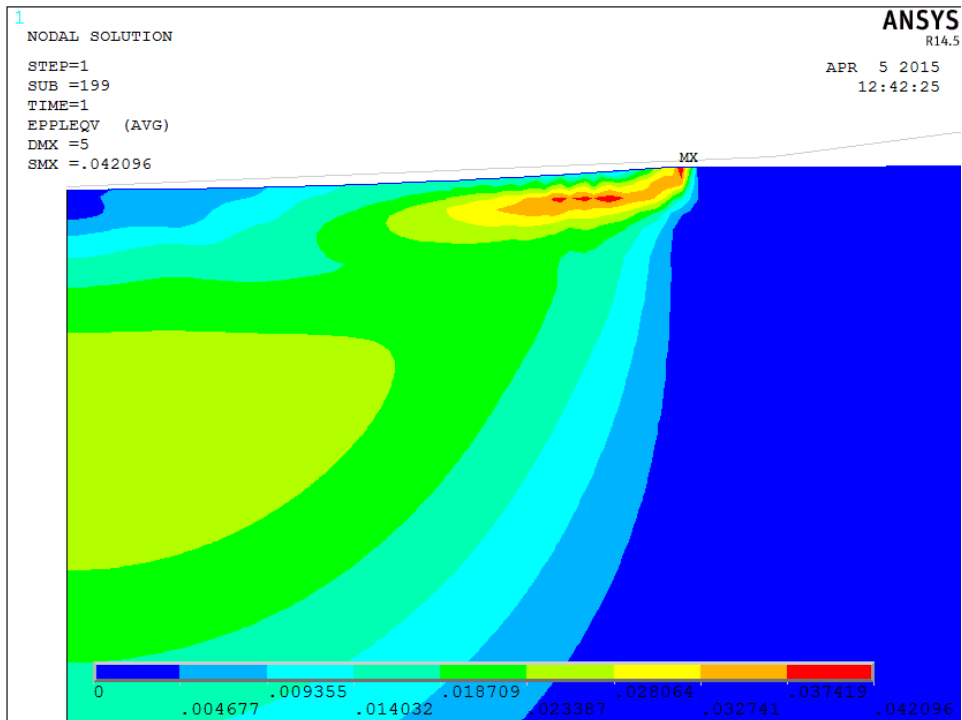
(d) $\mu = 1, n = 0.5, Y = 1\text{GPa}, \delta/z_0 = 3.67$

Fig 5.13 Von Mises plastic strain fields during indentation for different penetrations where $\mu = 1, S =$

1.35.



(a) $\mu = 1, n = 0.5, Y = 0.5\text{GPa}, \delta/z_0 = 1.68$



(b) $\mu = 1$ (Tabor parameter), $n = 0.5, Y = 0.5\text{GPa}, \delta/z_0 = -8.82$

Fig 5.14 Von Mises plastic strain fields during indentation for different penetrations where $\mu = 1, S =$

2.7 for (a) first plastic deformation (b) maximum indentation position

Fig 5.13 presents the von Mises plastic strain fields of the half-space (elastic-perfect plastic material, $n = 0$), corresponding to four different values of indentation depth. Herewith, δ denotes the vertical distance between the lower apex of the spherical indenter and the original surface as shown in Fig 5.10, i.e. $\delta = \alpha + z_0$. Positive δ and negative δ represent separation and penetration respectively. For non-adhesive contact (i.e. $S = 0$) between a rigid spherical indenter and an elastoplastic half-space, Chang et al⁹⁴ gave the critical penetration δ_c to initiate first plastic deformation as

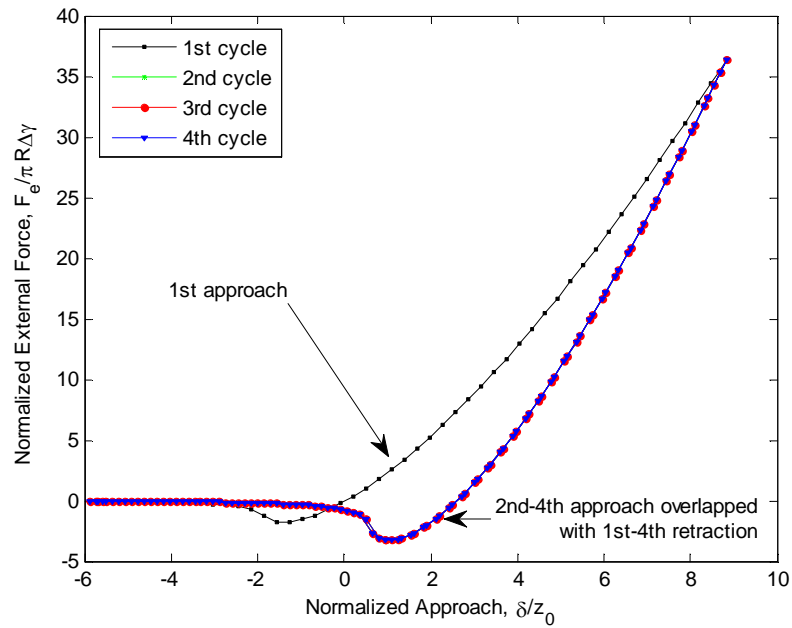
$$\delta_c = -\left(\frac{\pi KH}{2E^*}\right)^2 R \quad (5.23)$$

where $K = 0.454 + 0.41\nu$, $H = 2.8Y$ denotes the hardness of substrate material. Substituting the parameter values in Table 5.2 into Eq. (5.23) yields the critical penetration $\delta_c \approx -2.59z_0$. For adhesive contact, this critical penetration δ_c is $-0.65z_0$, corresponding to a plastic strain up to 0.3% as shown by Fig 5.13 (a) (i.e. $S = 1.35$). For a larger value of $S = 2.7$, the first plastic strain up to 1.4% can be observed, even if the indenter is not in contact with the substrate as indicated by Fig 5.14 (a), i.e. positive δ . Therefore, the critical δ to initiate first yield stress increases as S increases.

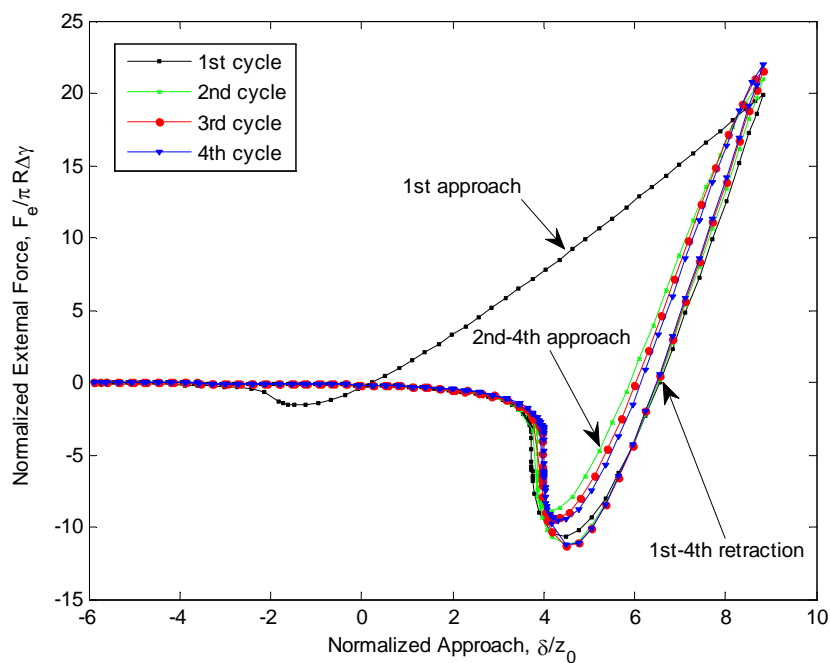
As the approach increases, the region beneath the surface along the axis of symmetry begins to yield as shown in Fig 5.13 (b). At maximum approach (i.e. maximum penetration), the plastic strain (about 2%) at this region has exceeded that at the contact periphery (about 0.8%), as shown in Fig 5.13 (c). It can be seen that the plastic strain fields are maintained as if frozen during retraction by comparison Fig 5.13 (c) and (d). In fact, this is due to isotropic hardening, i.e. during loading stage, only elasticity can occur, and thus plastic strain remains

unaffected. Therefore, it can be concluded that the isotropic hardening manner is implanted into FEM, and the following results should be trustworthy.

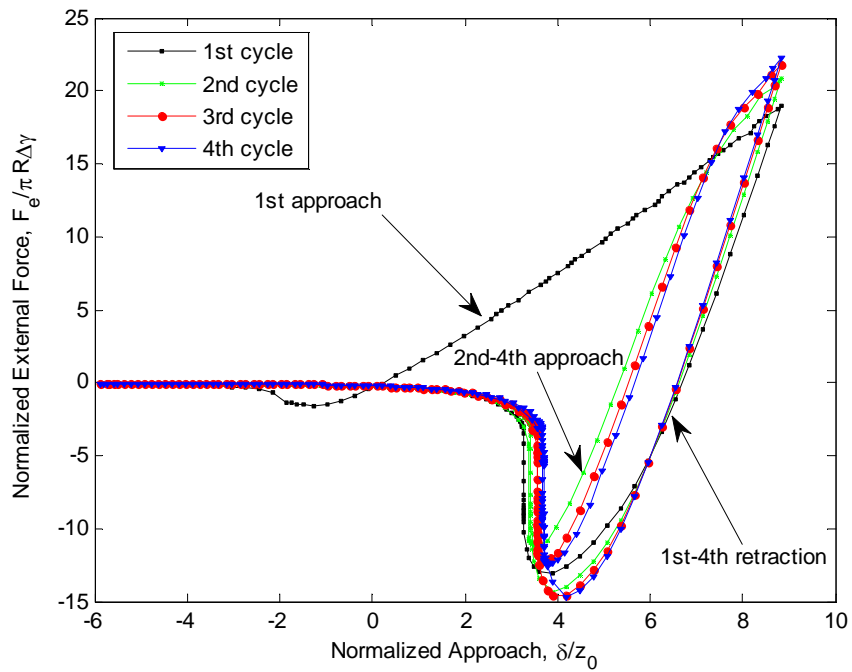
5.4.2.2 Multiple loading-unloading cycles



(a)



(b)



(c)

Fig 5.15 Normalized force versus normalized displacement for four consecutive loading-unloading cycles with $\mu = 0.45$, $Y = 0.5 \text{ GPa}$, $\delta_{max}/z_0 = -8.82$, $S=2.7$ for (a) $n = 0.75$, (b) $n = 0.15$ and (c) $n = 0.1$.

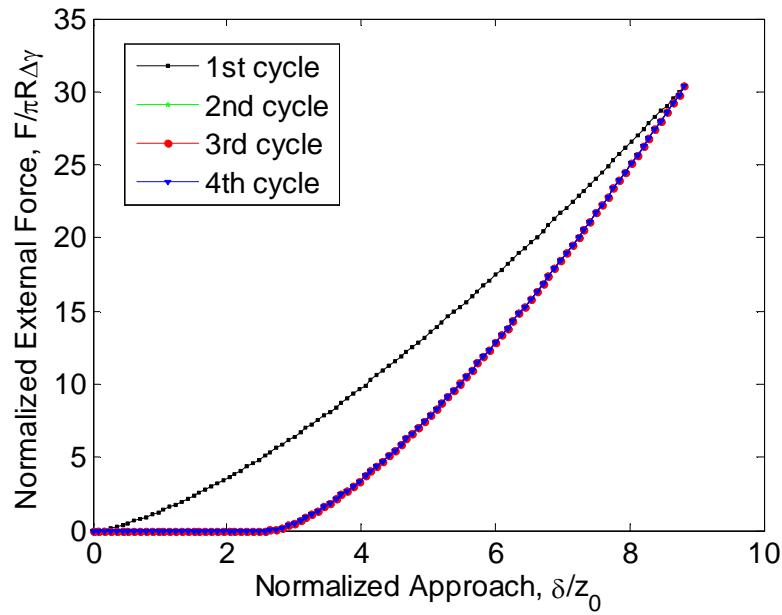


Fig 5.16 Normalized force versus normalized displacement for four consecutive loading-unloading cycles corresponding to non-adhesive contact. $Y = 0.5\text{GPa}$, $\delta_{max}/z_0 = -8.82$, $n = 0.15$.

Fig 5.1 provides one means to judge the types of shakedown behavior when a structure is subjected to cyclic loading, i.e. from the stress-strain relationship curve, which anyhow is obviously infeasible in practice. In this section, the force-penetration curve is analyzed to investigate the shakedown types.

Fig 5.15 shows the dependence of the normalized force on a normalized approach consisting of 4 consecutive approach and retraction corresponding to three hardening exponents, i.e. $n = 0.75, 0.15, 0.1$. For $n = 0.75$, it can be seen that plastic deformation almost occurs in the first loading-unloading cycle since the subsequent curves almost coincide as shown by Fig 5.15(a), which indicates elastic shakedown at a stable state. This is analogous to the case in non-adhesive repetitive contact, where theoretically speaking, plastic deformation only occurs during the first cycle, and the subsequent cycles absolutely overlap with each other. For $n = 0.15$ (see Fig 5.15 (b)), one can see there is enclosed area by each subsequent

cycle implying it does not shake down to elastic behavior. Since the value of enclosed area remains steady, and the maximum indentation force tends to converge with increasing number of loading-unloading cycles, one can judge that it is not ratchetting. In fact, the indenter-substrate system shakes down to a steady state of non-accumulative cyclic plastic deformation which resembles plastic shakedown. Fig 5.16 illustrates the non-adhesive counterpart of Fig 5.15 (b), and as can be seen that plastic deformation only occurs in the first cycle, with subsequent cycles shaking down to pure elastic behaviors. Thus, by comparing Fig 5.15 (b) and Fig 5.16, it is indicated that surface adhesion causes plastic shakedown in this situation.

As n decreases to 0.1 (see Fig 5.15 (c)), the enclosed area by each subsequent cycle is larger than that in Fig 5.15 (b), implying that material with lower hardening exponent n is more likely to undergo plastic shakedown provided other identical conditions. On the other hand, this implication is due to that plasticity is prone to occur in material with lower hardening exponent n , and hence plastic shakedown (or ratchetting) rather than elastic shakedown is more preferable. For a further interpretation, consider two extrema:

- $n \rightarrow 1$, i.e. pure elastic situation, and then only elastic shakedown is possible.
- $n \rightarrow 0$, i.e. elastic-perfect plastic material, plasticity is very likely to emerge, so as plastic shakedown or ratchetting in cyclic loading situations.

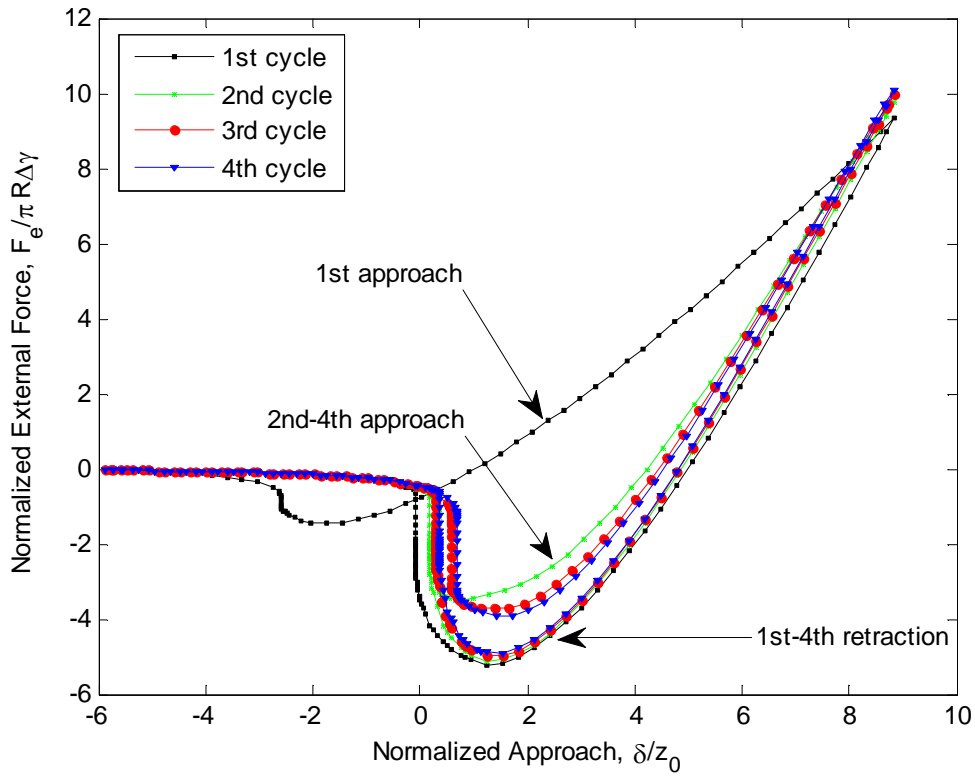


Fig 5.17 Normalized force versus displacement for four consecutive loading-unloading cycles with $\mu = 1$, $Y = 0.5\text{GPa}$, $\delta_{max}/z_0 = -8.82$, $S=2.7$, $n = 0.1$.

Fig 5.17 shows the variation of normalized force with the normalized approach for $\mu = 1$, $S = 2.7$, and $n = 0.1$. First one can judge it resembles to plastic shakedown by the same means as last paragraph. Compared with Fig 5.15 (c), the enclosed area by each subsequent loading-unloading cycle is smaller, implying accumulative plastic strain is less significant as Tabor parameter increases. This trend can be interpreted as follows: the substrate material is more compliant (lower E) as tabor parameter increases, and can accommodate less plastic work compared with that in more stiffer material (material corresponding to high tabor parameter) given the same indentation depth, resulting a relief in plastic shakedown as indicated by the smaller enclosed area in Fig 5.17 compared with Fig 5.15(c). To facilitate further explanation, consider an extrema, i.e. $\mu \rightarrow \infty$, the material is extremely compliant

($E \rightarrow 0$), and thus plasticity is unlikely to happen, i.e. only elastic shakedown is possible.

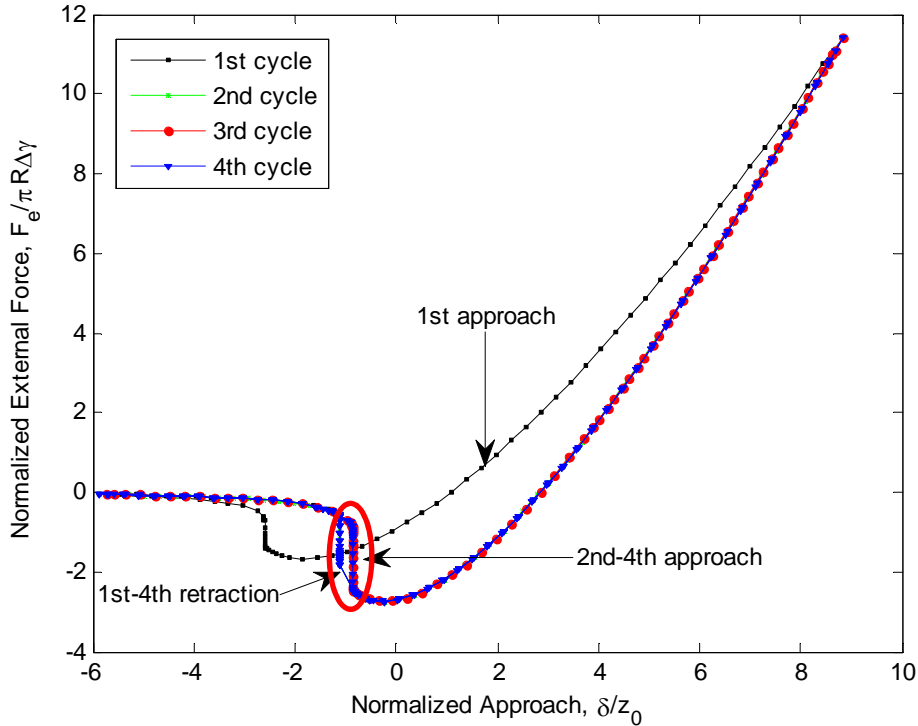


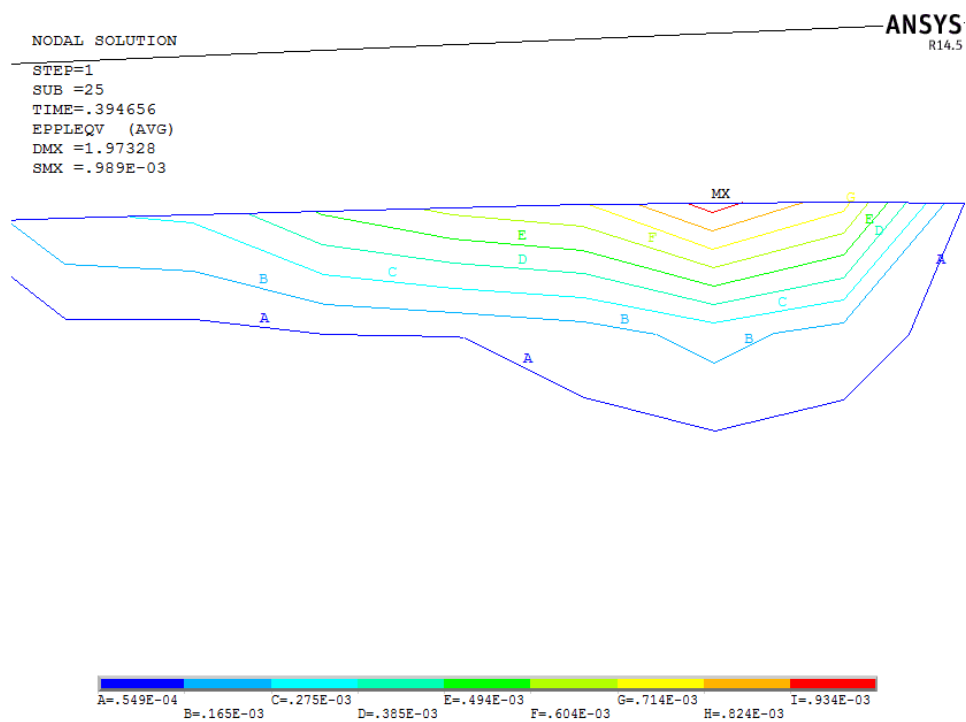
Fig 5.18 Normalized force versus displacement for four consecutive loading-unloading cycles with $\mu = 1$, $Y = 1 \text{ GPa}$, $\delta_{max}/z_0 = -8.82$, $S=1.35$, $n = 0.1$.

If the value of S is decreased by increasing yield stress Y (values of $\Delta\gamma$ and z_0 are maintained as that in Fig 5.17), one can see the plastic deformation almost occurs in the first cycle and subsequent cycles nearly overlap with each other, resembling to elastic shakedown, as shown by Fig 5.18. It should be borne in mind that the present elastic shakedown is different from classical elastic shakedown, where the loading and unloading paths should overlap with each other absolutely. In the present case, although the small area (as circled by the red ellipse) enclosed by each subsequent cycle indicates energy dissipation, it is due to jump instabilities rather than plastic dissipation. In the finite element method, artificial damping was used to compensate for local instabilities. Therefore, since plastic dissipation

does not occur in subsequent cycles, the cyclic behavior should be regarded as elastic shakedown. Since the yield stress is increased in this case, which means the yield threshold is enhanced, plasticity is unlikely to occur, and so is plastic shakedown.

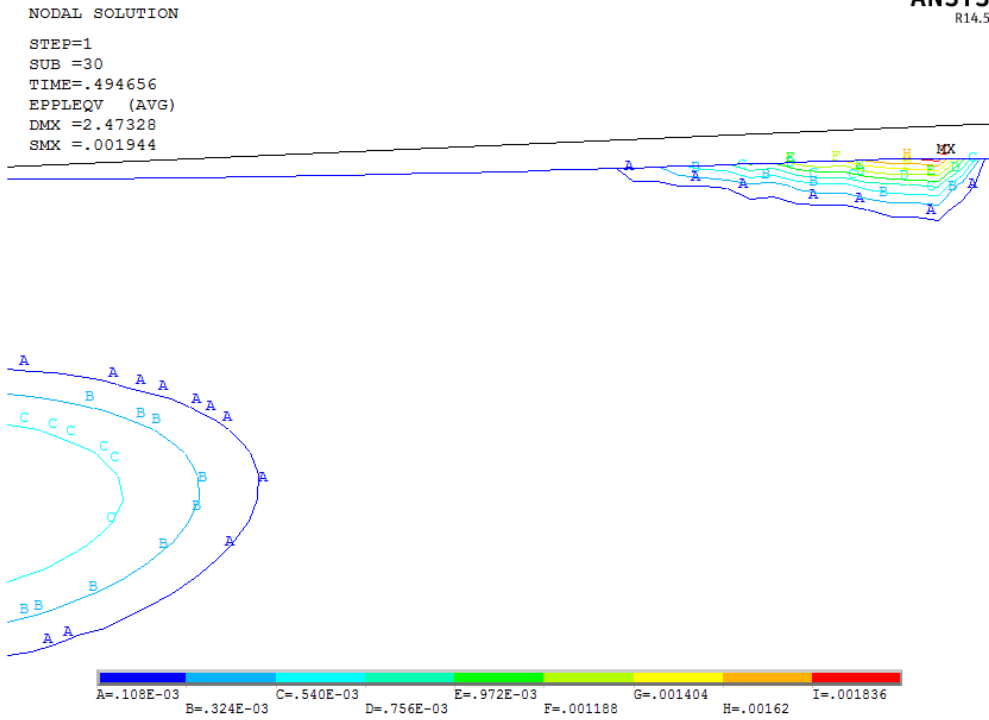
5.4.3 Bilinear Kinematic Hardening Model

5.4.3.1 Von Mises Strain Fields



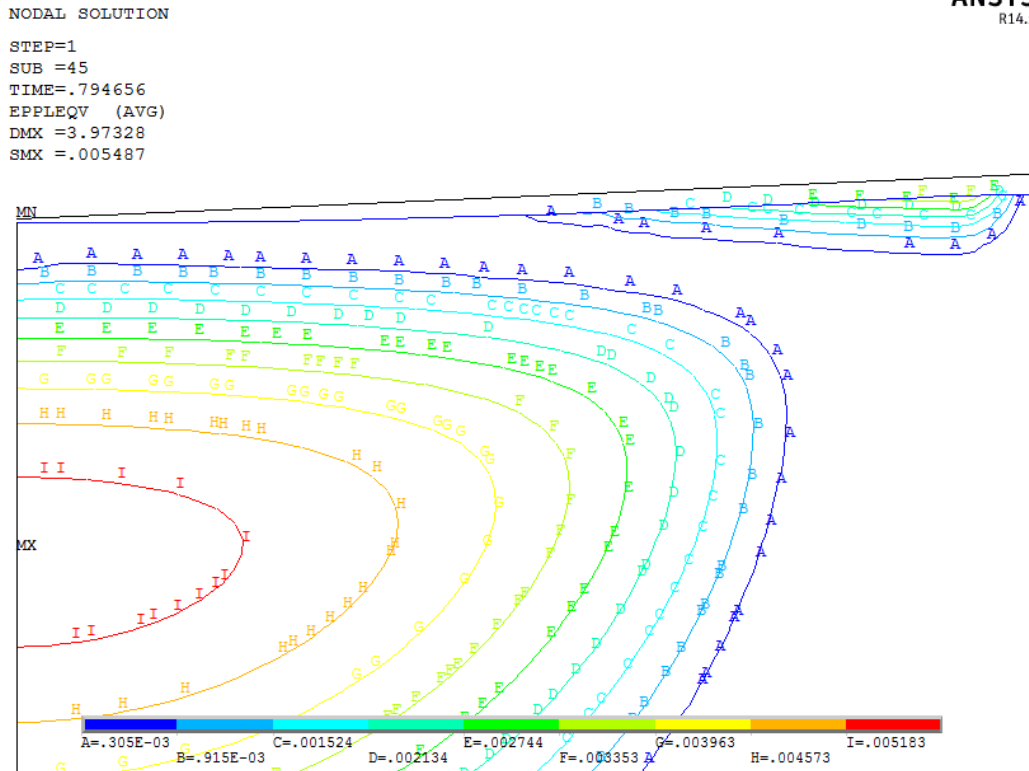
(a) $\delta/z_0 = 0.08$

ANSYS
R14.5



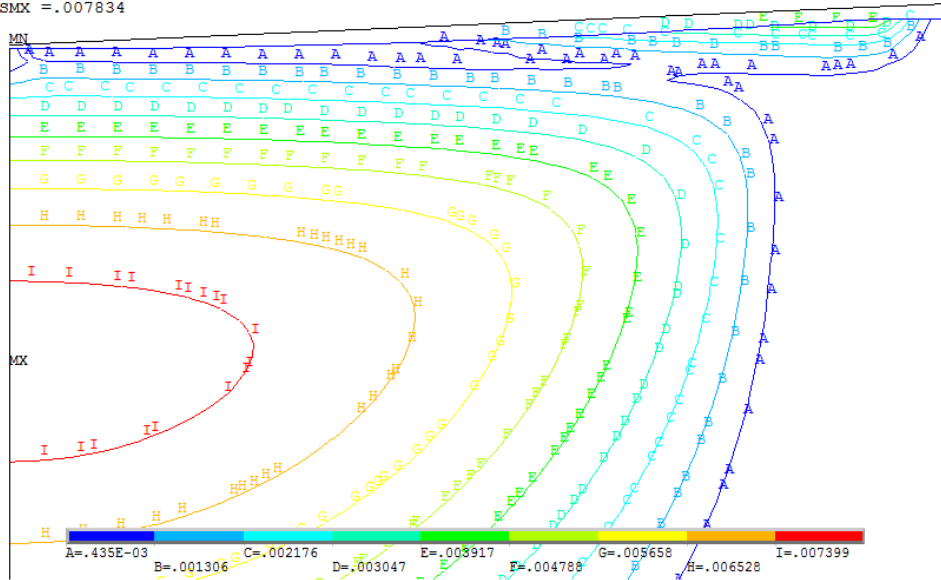
(b) $\delta/z_0 = -1.39$

ANSYS
R14.5



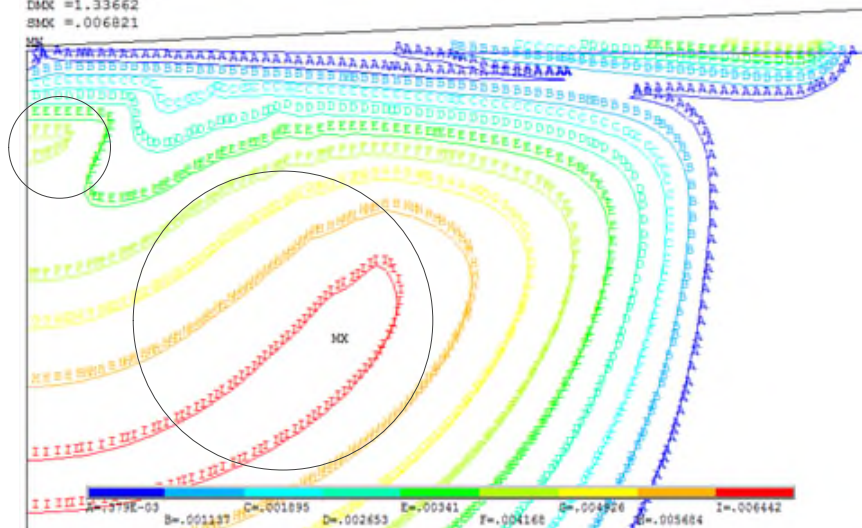
(c) $\delta/z_0 = -5.8$

NODAL SOLUTION
STEP=1
SUB =56
TIME=1
EPFLQV (AVG)
DMX =5
SMX =.007834



(d) $\delta/z_0 = -8.82$

NODAL SOLUTION
STEP=2
SUB =40
TIME=1.73268
EPFLQV (AVG)
DMX =1.33662
SMX =.006821



(e) $\delta/z_0 = 1.95$

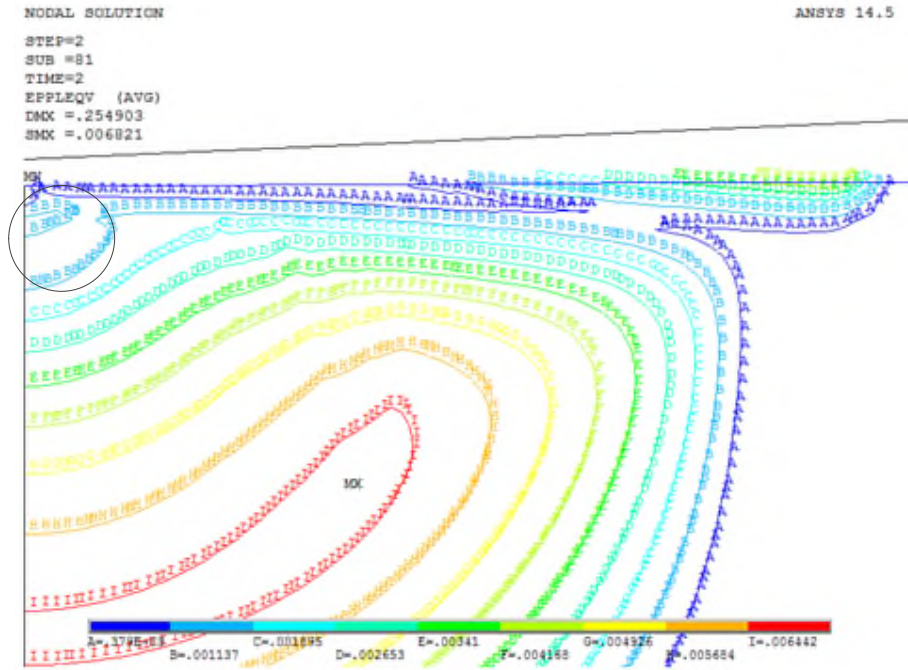


Fig 5.19 Von Mises plastic strain fields for different penetration where $\mu = 0.5$, $Y = 0.5\text{GPa}$, $S=2.7$, $E_T/E = 0.5$

In this section, plastic strain fields are routinely analyzed for the same reason as that in Sec. 5.4.2.1. Fig 5.19 presents the von Mises plastic strain field inside the half-space corresponding to six approach values with the same combination of $\mu = 0.5$, $Y = 0.5\text{GPa}$, $S=2.7$, $E_T/E = 0.5$. As can be seen from Fig 5.19 (a), an initial plastic strain up to 0.1% is observed at the contact periphery corresponding to $\delta = 0.08z_0$. As approach increases, plasticity also appears on the axis of symmetry beneath the surface as shown in Fig 5.19(b), and the value of plastic strain corresponding to this area begins to exceed that at contact periphery with further approach as shown by Fig 5.19(c). At the maximum approach $\delta = -8.82z_0$, the maximum plastic strain up to 0.78% is observed at the axis of symmetry, while at the contact periphery, the plastic strain is up to 0.4% as shown in Fig 5.19(d). During

unloading stage, one can observe that the plastic strain fields keep altering by comparing Fig 5.19 (d), (e) and (f) (e.g. the circled area), which differs from the phenomenon in Sec.5.4.2.1 where plastic strain fields are maintained. Essentially, this is the distinguishing feature of kinematic hardening whose subsequent yield surface is translated and plastic deformation can still occur during unloading as illustrated by Fig 5.4.

5.4.3.2 Multiple loading-unloading cycles

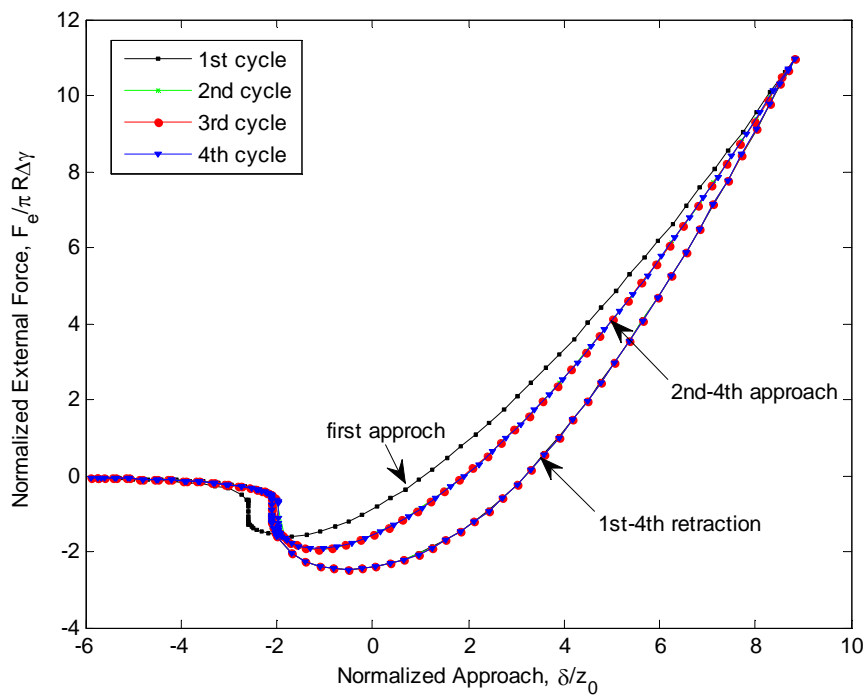


Fig 5.20 Normalized force versus displacement for four consecutive loading-unloading cycles with $\mu =$

1, $Y = 0.5\text{GPa}$, $S=2.7$, $E_T/E = 0.5$

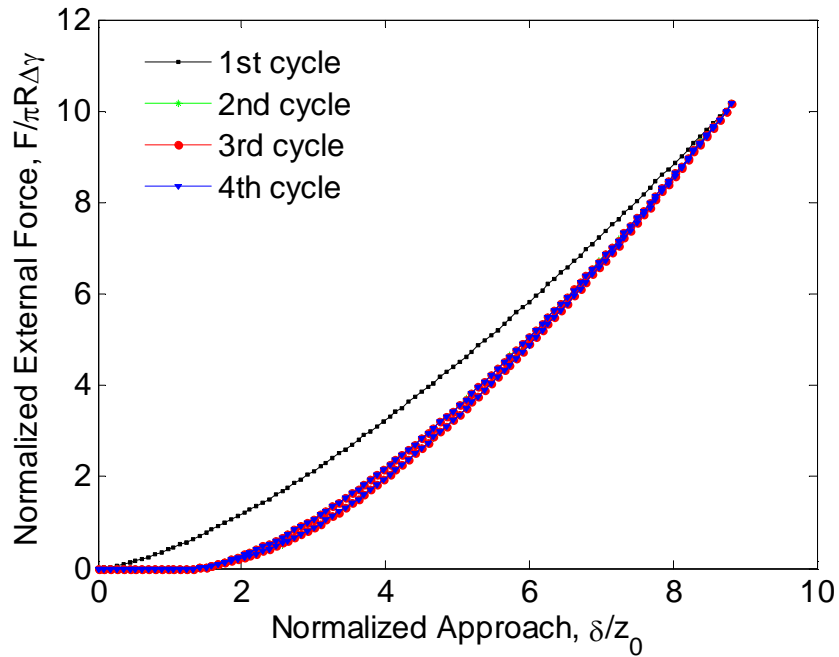


Fig 5.21 Normalized force versus displacement for four consecutive loading-unloading cycles corresponding to non-adhesive contact.

In this section, analysis of dimensionless force-penetration curve is routinely presented for the same purpose as that in Sec. 5.4.2.2. Unlike Sec.5.4.2.2, the ratio E_T/E replaces the hardening exponent n , and together with μ and S acts as governing parameters.

Fig 5.20 shows the variation of normalized force with the normalized approach for $\mu = 1$, $S=2.7$, $E_T/E = 0.5$. Except the loading half of first cycle, each loading half of subsequent three cycles can overlap with each other, and each unloading half of the four cycles can also coincide. The areas enclosed by the three subsequent cycles are almost identical, implying a steady-state plastic shakedown. Compared with Fig 5.17, it is indicated that the whole system can converge to a steady-state plastic shakedown with less cycles in kinematic hardening situation. Fig 5.21 is the non-adhesive counterpart of Fig 5.20, it can be seen that for kinematic materials, plastic deformation only occurs in the first cycle and the subsequent

cycles shake down to elastic behaviors if no surface adhesion exists.

If S is halved by doubling yield stress Y while other two governing parameters (i.e. $\Delta\gamma$ and z_0) in Fig 5.20 are maintained, it can be seen that plastic shakedown is inconspicuous as indicated by Fig 5.22. In fact, as can be seen, the subsequent cycles almost overlap with each other, implying a trend to elastic shakedown, and this is due to that material with high yield stress is unlikely to undergo plastic deformation, and thus plastic shakedown as is previously interpreted.

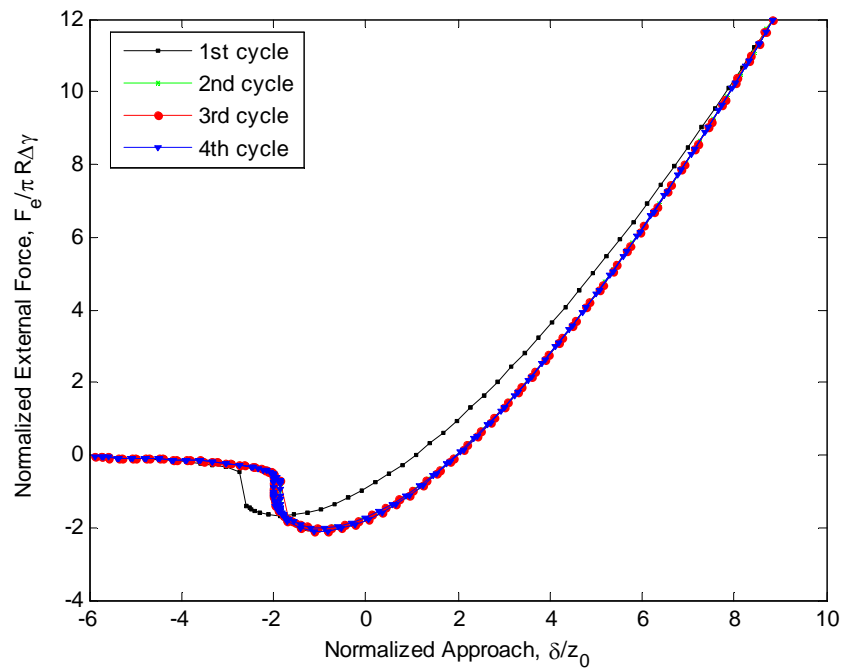


Fig 5.22 Normalized force versus displacement for four consecutive loading-unloading cycles with $\mu =$

1, $Y = 1\text{GPa}$, $S = 1.35$, $E_T/E = 0.5$.

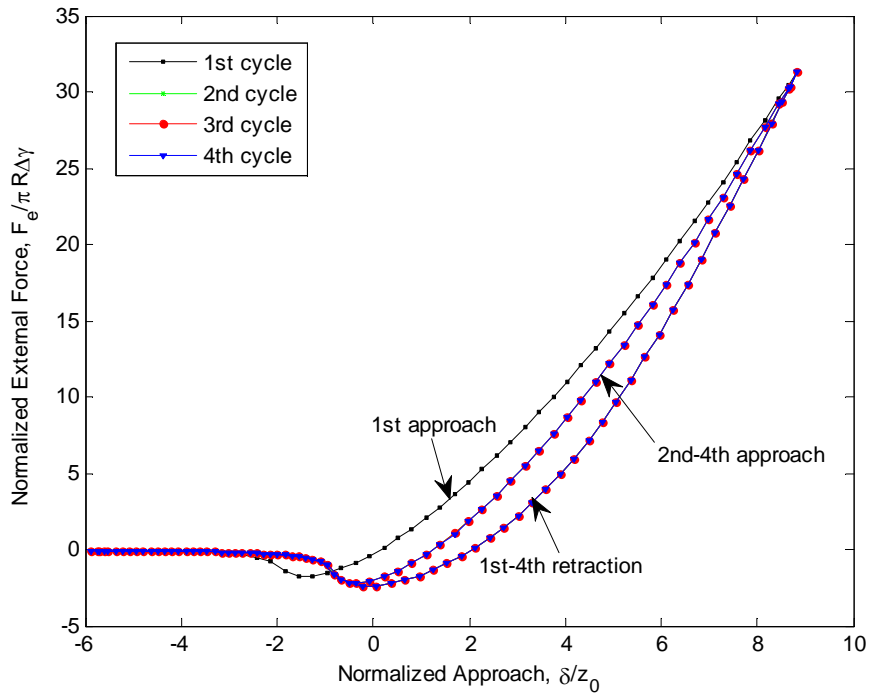


Fig 5.23 Normalized force versus displacement for four consecutive loading-unloading cycles with $\mu = 0.5$, $Y = 1\text{GPa}$, $S=1.35$, $E_T/E = 0.5$.

If Tabor parameter μ decreases to 0.5 while the rest parameters in Fig 5.22 are maintained, one can find plastic shakedown reoccur as shown by Fig 5.23. The interpretation for this difference is that stiffer materials (low value of Tabor parameter μ) are likely to undergo plastic deformation given other identical conditions as former interpretation.

Consider tangential modulus E_T decreases to one tenth of E with other two parameters unchanged as that in Fig 5.23, one can observe that plastic shakedown also occurs in this situation (see Fig 5.24) with difference that the enclosed area by subsequent cycles is significantly larger than that in Fig 5.23. The potential reason for this difference is that materials with low value of E_T/E are more likely to undergo plasticity provided other same conditions. For a further interpretation, consider two extrema:

- $E_T/E \rightarrow 1$, i.e. elastic material, then elastic shakedown is more likely to occur
- $E_T/E \rightarrow 0$, i.e. elastic-perfect plastic material, then plasticity is more likely to happen, and so as plastic shakedown.

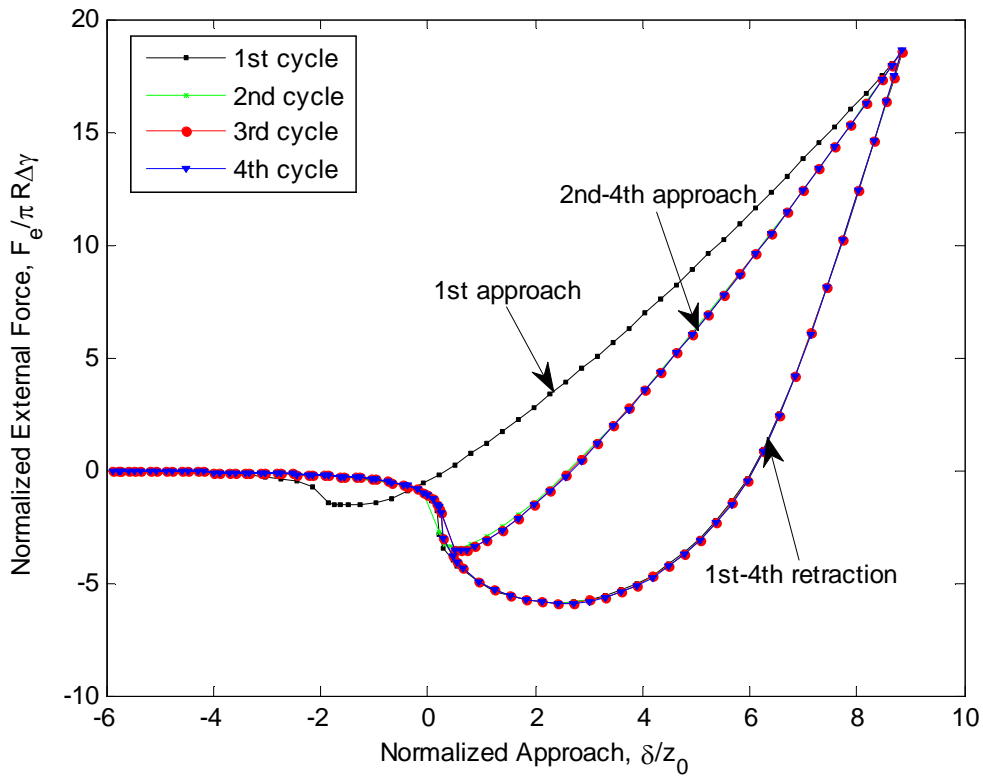


Fig 5.24 Normalized force versus displacement for four consecutive loading-unloading cycles with $\mu = 0.5$, $Y = 1\text{GPa}$, $S=1.35$, $E_T/E = 0.1$.

5.5 Summary

In this chapter, repetitive adhesive contact between a rigid spherical indenter and an elastoplastic half-space was studied by means of finite element simulation. The following conclusions can be made in this chapter

- By only inputting elastic parameters in FEM, the results coincide well with that by using self-consistent method in terms of force-penetration curve and relationship between the

position of instability jump and Tabor parameter. In FEM, jump instabilities manifest themselves as brittle jumps.

- Apart from Tabor parameter for its elastic counterpart, in adhesive contact, there is another parameter S governing the mechanic behavior of the indenter-substrate system. In adhesive contact, lower indentation depth is needed to initiate first yield of substrate material compared with its non-adhesive counterpart. As S increases, the first yield can even occur before contact.
- The plastic strain field is an important index for the implementation of hardening manner in finite element simulation. Plastic strain field is maintained in isotropic hardening materials during retraction of indenter, which differs from its kinematic hardening counterpart.
- In non-adhesive repetitive contact, only elastic shakedown can happen, whereas in its adhesive counterpart, there is probability for the occurrence of plastic shakedown, as long as the relevant governing parameters are appropriately selected. It is surface adhesion that incurs potential plastic shakedowns.
- Plastic shakedown can also occur in isotropic hardening materials undergoing repetitive adhesive contact. For isotropic hardening material, Tabor parameter, plasticity parameter and hardening exponent govern the dimensionless force-penetration curve. Low Tabor parameter, high plasticity parameter and low hardening exponent result in plastic shakedown, whilst high Tabor parameter, low plasticity parameter and high hardening exponent lead to elastic shakedown.
- For kinematic hardening material, Tabor parameter, plasticity parameter and ratio of E_T/E .

Low Tabor parameter, high plasticity parameter and low ratio of E_T/E yield to plastic shakedown, opposed to high Tabor parameter, low plasticity parameter and high ratio of E_T/E that cause elastic shakedown.

6 Determination of *Work of Adhesion* of Pancreatic MIN6 cells under AFM indentation (Spherical probe)

6.1 Introduction

As quantified initially by Tabor parameter, if the contacting bodies are extremely soft, adhesion forces become significant. Johnson-Kendall-Roberts model of adhesion has proved successful in quantifying the *work of adhesion* between two soft elastic bodies. Shull^{[25][26]} provided a remarkable view of this theory and the experimental methods, where he indicated that adhesion forces are important when the contacting bodies are sufficiently small or extremely compliant, including living cells and soft tissues i.e. adhesion forces should play an important role in cell indentation.

Conventionally speaking, cell indentation is frequently realized by means of atomic force microscope (AFM) instrumentation. As mentioned in Chapter 1, the atomic force microscope (AFM) is a powerful instrument for studying topographical and mechanical properties such as elastic modulus and viscoelasticity for biological materials^[146]. The high resolution and reasonably fast speed of AFM measurements have made it possible to investigate the topography and mechanical properties of living biological cells or tissues^{[147][148]}, which is of significant biomedical importance. The topography and mechanical properties are reliable indicators of cellular physiological status, because they are determined by cytoskeleton together with the cytoplasm membrane and numerous proteins^[8]. Any change in cellular physiology may cause alternations in its topographical or mechanical behaviors. As a result, the correlations between cytoskeleton and its topographical and mechanical properties could

lead to possible medical diagnosis of pathological cells by comparing these properties determined from AFM indentation with its normal counterpart. A pioneering example using AFM in medical diagnostics was reported by Zachee^[8] where changes in shape of red blood cells were observed in patients after splenectomy. Another typical example is given by Lekka^[7] who showed that chitosan has more significant effect on stiffness of normal than cancer cells.

However, in many of the AFM indentations, conditions were chosen such that the *van der Waals* forces are expected to dominate¹. The adhesion, characterized as adhesion force, is mainly derived from *van der Waals* forces. As a result, adhesion forces are inevitably associated with performance in atomic force microscopy (AFM) indentation. On the other hand, since the adhesion between cells or micro-particles is interfacial property affected by combination of cyto-membrane and cytoskeleton, detection of variation in cell adhesion behavior may serve as alternative method for single-cell-based diagnostics.

Since the adhesion between the cell membrane and the micro-particle is crucial, a model that could quantitatively study cell adhesion would be necessary for results interpretation. Although Hertz contact theory has been routinely used for determination of cell elasticity based on AFM indentation experiments, it might not work appropriately for adhesive contact as indicated by analyses in Chapter 1. Generally, for cell-to-cell indentation, adhesion has been characterized the maximum unbinding force (F_{max}) and work of detachment (W_D) obtained from force-versus-displacement curve (retraction part) acquired from AFM indentation^{[17][149][150]}, as illustrated in Fig 6.1. As pointed in Chapter 1, these two parameters may not be intrinsic enough to feature cell adhesion since both of them are dependent of the

size and profile of the indenter as well as the indentation depth. Alternatively, a previous study^[151] adapted work of adhesion to characterize cell adhesion since it is independent of indentation depth and AFM tip geometry and thus might depict cell adhesion essentially.

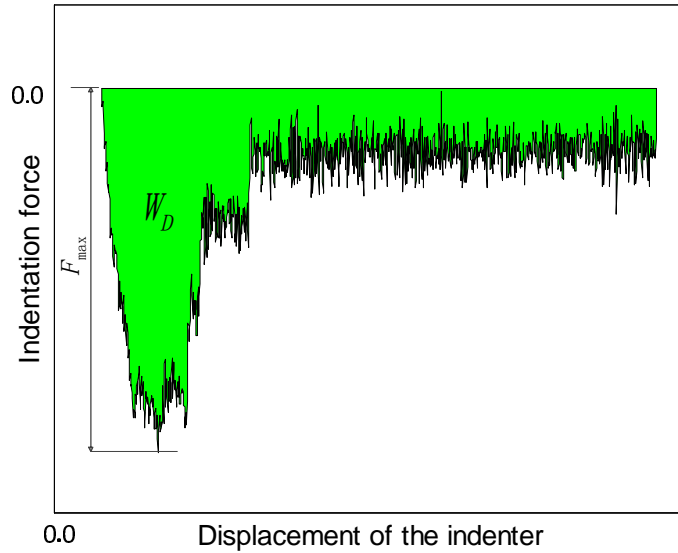


Fig 6.1 Schematic of the retraction part of force-displacement curve from cell AFM indentation. The green area enclosed by the curve and horizontal axis denotes work of detachment (W_D) whilst the minimum (negative) value of indentation force denotes maximum unbinding force (F_{max}).

In this chapter, in light of adhesive contact between AFM tip and cell, the cell is first considered as a spherical shape, and Johnson-Kendall-Roberts (JKR) model is applied to fit the force-displacement curves obtained from AFM indentation experiments^[17]. Then the cell is treated as a layer with finite thickness to provide more realistic modeling. In this regard, a more “generalized” JKR model^{[25][26]} is used to fit the force-displacement curves. It is found that both the models provide good agreement with experimental results of force-displacement curves. The “generalized” model has the potential to be implemented in various studies that are investigating malignant cells for the accurate detection of work adhesion in AFM

indentation.

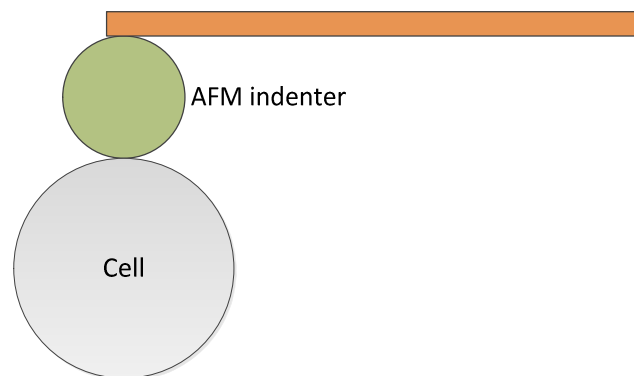
6.2 Methodology

6.2.1 Data preparation

The data used for testing the theoretical model (see Fig 6.1) were extracted from the recently reported AFM indentation experiments of pancreatic cells^{[17][152]}. The cell preparation and experimentation have been described in detail elsewhere^[17]. Herewith, we have used MIN6 cells cultured for 48h with low glucose which are named as Sample A and cells cultured in 48h +R568 are named as Sample B^{[17][152]} (In following context, Cell B is also termed as treated cell).

6.2.2 Theoretical model

In general, the cells spread on substrate in various shapes, some like spheres and some like pancakes^{[17][152]}. Therefore, this chapter considers cells to have either spherical or flattened shapes, as shown in Fig 6.2 (a) and (b), respectively.



(a)

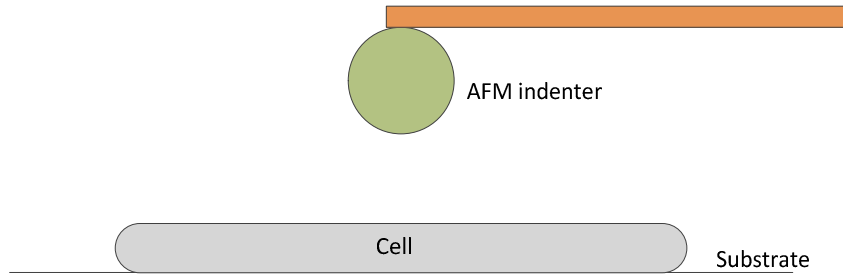


Fig 6.2 Schematic diagrams of the AFM bead tip in contact with cells of (a) spherical shape and (b) flattened shape

In this chapter, the cell is firstly treated as a homogeneous, incompressible and linear elastic sphere with a typical diameter of $25\mu\text{m}$, where the pre-stress tension in cyto-membrane can be neglected^[151] (assumption of pure elasticity of the cell will be justified in the next section). Here, the assumption of homogeneity is given, and thus a global equivalent elastic model of the cell can be studied^[153]. Moreover, only pure elastic deformation occurs in loading and unloading stages with no plastic deformation being considered.

As indicated by Sec.3.2.4, both DMT^[22] and JKR^[21] models are applicable to adhesive contact between two micro-particles. Sec.3.2.4 has claimed the application range of these two models in terms of Tabor parameter μ given as.

$$\mu = \left[\frac{R_{p-c}\Delta\gamma^2}{E_{p-c}^* z_0^3} \right]^{1/3} \quad (6.1)$$

where $\Delta\gamma$ denotes the work of adhesion of the probe-cell system, $E_{p-c}^* = [(1-\nu_p^2)/E_p + (1-\nu_c^2)/E_c]^{-1}$ is the effective Young's modulus, (E_p , ν_p and E_c , ν_c denote elastic modulus and

Poisson's ratio of the two contacting spheres, probe and cell, respectively), R_{p-c} is the reduced radius of curvature ($R_{p-c} = (1/R_p + 1/R_c)^{-1}$), where R_p and R_c denote the radius of the probe and cell respectively, and z_0 is the atomic equilibrium distance at which the repulsive force equals to attractive force. For the adhesive contact between a cell and a polystyrene bead (polystyrene bead is used in the AFM indentation because it is easier to glue to the AFM cantilever), the radius of MIN6 cell R_c is typical of $12.5\mu m$, and the elastic modulus E_c of cell is in the order of several hundred Pascal. Previous studies have found the value of E_c is about $500Pa$ by using Hertz contact theory to fit the $F-d$ curve of an AFM indented MIN6 cell^[17]. The work of adhesion $\Delta\gamma$ ranges from 20 to $100\mu J/m^2$, and here $\Delta\gamma$ is assumed to be $50\mu J/m^2$ ^{[2][151]}. A typical value for z_0 is $0.5nm$ and cell is treated as incompressible, i.e. Poisson's ratio $\nu_c = 0.5$. The elastic modulus of the bead can be treated infinite since it is very rigid compared with the delicate cell, i.e. $E_{p-c}^* = E_c/(1-\nu_c^2)$. Substituting these parameter values into Eq. (6.1), the Tabor parameter is calculated approximately $\mu = 556$ and thus the JKR model is more preferable in this case ($\mu > 5$).

Fig 6.2(a) illustrates schematically the spherical cell subjected to a micro-bead indenter. According to JKR model, the applied indentation force F and the indentation depth δ are related by:

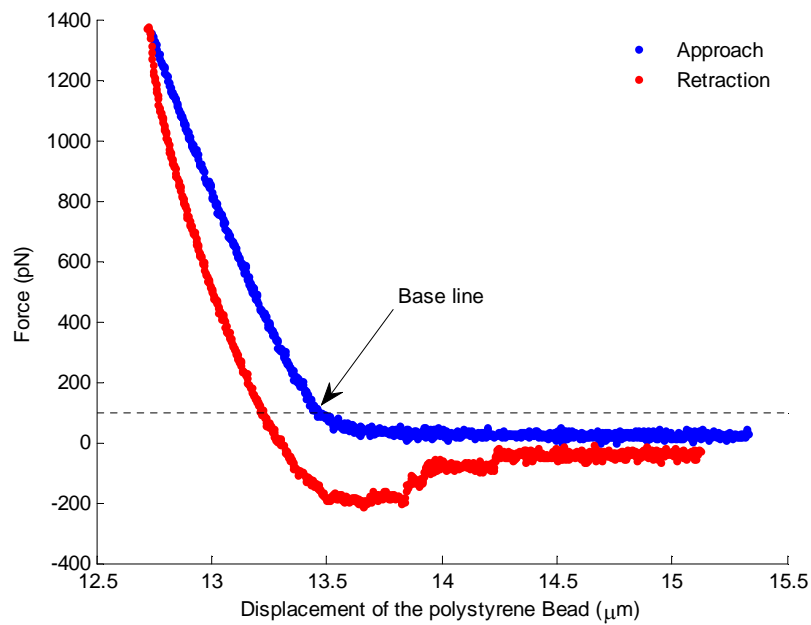
$$\delta = \frac{a^2}{R_{p-c}} - \sqrt{\frac{2\pi a \Delta\gamma}{E_{p-c}^*}} \quad (6.2)$$

$$a = \left\{ \frac{3FR_{p-c}}{4E_{p-c}^*} \left[1 + \frac{3\pi\Delta\gamma R_{p-c}}{F} + \sqrt{\frac{6\pi\Delta\gamma R_{p-c}}{F} + \left(\frac{3\pi\Delta\gamma R_{p-c}}{F} \right)^2} \right] \right\}^{1/3} \quad (6.3)$$

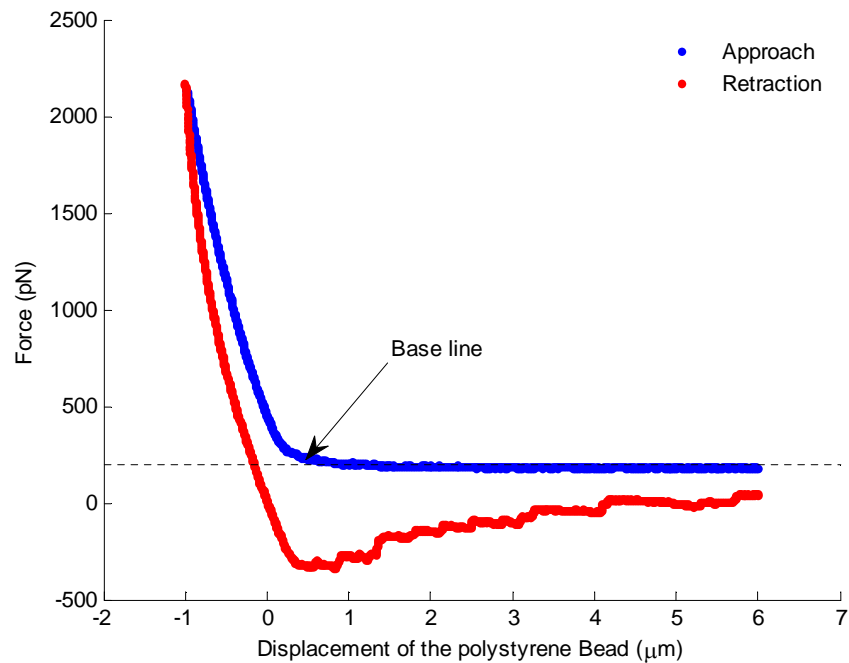
where a denotes contact radius.

6.3 Results and Discussions

Fig 6.3 shows the result of force against displacement corresponding to MIN6 cells. The micro-bead was initially made contact to the cell with the applied force of 100pN as the baseline. The maximum indentation depth of cell is approximately $0.7\mu\text{m}$. Thus, the substrate effect is negligible since the indentation is smaller than 10% of the sample thickness^{[154][155][156]}.



(a)



(b)

Fig 6.3 Example of force-versus-displacement curves obtained by AFM indentation on (a) sample A and (b) sample B cells.

6.3.1 Verification of Cellular Viscous Properties

The enclosed area between the loading and unloading curves where force is positive (compressive force) reveals that the cell exhibits viscoelastic property, as shown in Fig 6.3.

The gap suggests the energy supplied by the tip is not fully recovered by the cell (while in an absolute elastic material it will be fully recovered), which confirms that living cells are viscoelastic^[157]. The viscoelastic behavior is ascribed to intrinsic viscoelasticity of the cytoplasm^[158]. Viscous relaxation time is one typical time scale for characterizing this viscoelastic behavior which causes difference in force indentation measurements if different indentation velocities are applied^{[113][159]}. The influence of viscosity effect on cell indentation

can be reduced or even neglected if an indentation is performed in a time that is much longer than the force relaxation time of the cell^[160]. Therefore, before fitting JKR model to the experimental data, the viscous relaxation time of the cell-AFM indentation system has to be estimated and then the evaluated viscous relaxation time can be compared with the characteristic time of indentation (loading time). In general, elastic properties are derived from the unloading curve as the unloading process is of purely elastic nature. As one assumes, there is no plastic deformation occurs in the cell indentation. Thus the energy loss is considered due to viscoelastic properties. Viscoelastic Hertz contact model can be fitted to the loading part of the F - d curve to determine the viscous relaxation time. According to Hertz model, if the cell is regarded as pure elastic, the dependence of indentation force (F) on indentation depth (δ) is expressed as:

$$F = \frac{4\sqrt{R}}{3(1-\nu^2)} E \delta^{3/2} \quad (6.4)$$

where E , ν denote the Young's modulus and Poisson's ratio of the cell respectively. For its viscoelastic counterpart, according to Sec.4.2.3, substituting the elastic modulus in the Hertz contact model with the modulus-displacement convolution in the time domain leads to the relationship between the indentation depth $\delta(t)$ and the applied force $F(t)$ as:

$$F(t) = \frac{4\sqrt{R}}{3(1-\nu^2)} E(t) * [\delta(t)]^{3/2} \quad (6.5)$$

where $E(t)$ is the relaxed modulus, and

$$E(t) * [\delta(t)]^{3/2} = \int_{\xi=0}^t E(t-\xi) \frac{d}{d\xi} [\delta(\xi)]^{3/2} d\xi \quad (6.6)$$

In our indentation experiment, because the bead approached and detached the cell in a constant speed v , the indentation depth can be described as:

$$\delta(t) = vt \quad (6.7)$$

In order to determine the viscoelastic response for this indentation system, Eq. (6.5) is transformed into the Laplace domain and solved for stress/strain ratios:

$$\overline{F(s)} = \frac{4\sqrt{R}}{3(1-\nu^2)} \overline{E(s)} \cdot \overline{\delta(s)^{3/2}} \quad (6.8)$$

where $\overline{F(s)} = \int_0^\infty F(t)e^{-st} dt$, $\overline{E(s)} = \int_0^\infty E(t)e^{-st} dt$, and $\overline{\delta(s)^{3/2}} = \int_0^\infty [\delta(t)]^{3/2} e^{-st} dt$

Substitution of Eq. (6.7) into Eq. (6.8) yields:

$$\overline{F(s)} = \frac{4\sqrt{R}\nu^{3/2}}{3(1-\nu^2)} \overline{E(s)} \cdot \frac{\Gamma(5/2)}{s^{5/2}} \quad (6.9)$$

Where $\Gamma(\bullet)$ is gamma function. In this chapter a Kelvin model was applied to describe the viscoelasticity of MIN6 cells shown in Fig 6.4. Here E denotes the Young's modulus and η is the viscosity coefficient.

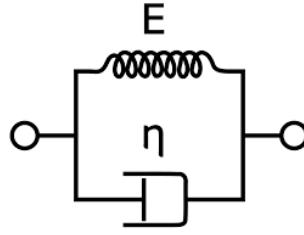


Fig 6.4 Schematic diagram of Kelvin model where a dashpot is in parallel with a spring undergoing the same deformation.

Thus, the constitutive relationship for the cell is:

$$\sigma = E\varepsilon + \eta \frac{d}{dt} \varepsilon \quad (6.10)$$

where σ and ε denote stress and strain for any point within the cell. Transforming Eq. (6.10)

into its Laplace domain results in:

$$\frac{\overline{\sigma(s)}}{\overline{\varepsilon(s)}} = (E + \eta s) \quad (6.11)$$

where $\overline{\sigma(s)} = \int_0^\infty \sigma(t)e^{-st} dt$, $\overline{\varepsilon(s)} = \int_0^\infty \varepsilon(t)e^{-st} dt$. According to the correspondence principle⁶⁹, the general elastic and viscoelastic solutions can be combined in the Laplace

domain to obtain an equation describing the modulus of Young's modulus, i.e.

$$\overline{E(s)} = \frac{\overline{\sigma(s)}}{\overline{\varepsilon(s)}} = (E + \eta s) \quad (6.12)$$

Substituting of Eq. (6.12) into Eq. (6.9), and transforming the Laplace form back into its time domain, yields:

$$F(t) = \frac{4\sqrt{RE}v^{3/2}}{3(1-\nu)} \left(t^{3/2} + \frac{3}{2}\tau t^{1/2} \right) \quad (6.13)$$

where $\tau = \eta/E$ is the relaxation time.

It should be borne in mind that Kelvin model is just one special circumstance of three-element solid and the estimated viscous relaxation time should coincide in order with its Kelvin counterpart if the loading curve is fitted by a more universal three-element model. However, since this model can allow an explicit expression between force and time, Kelvin model is preferred herewith for simplicity of calculation.

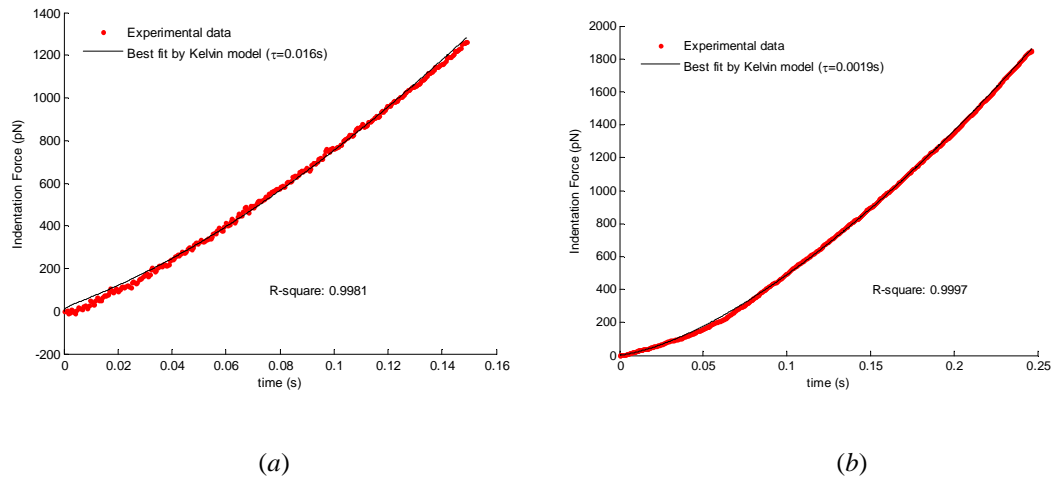


Fig 6.5 Typical force-versus-time curves during loading part and the best fitting curves by using Kelvin model for (a) sample A and (b) sample B.

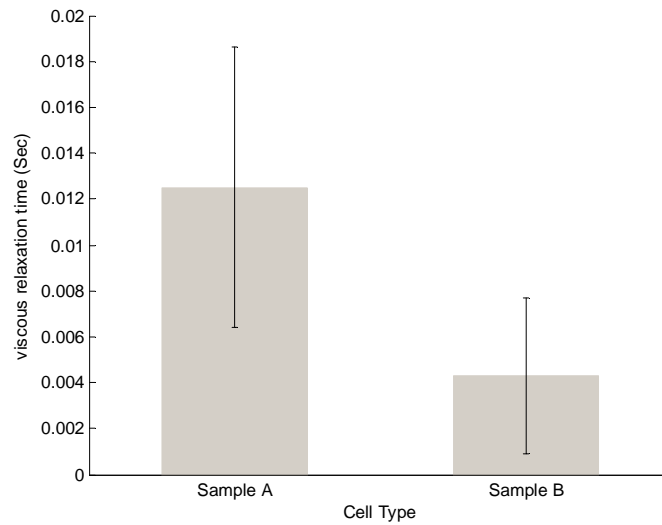


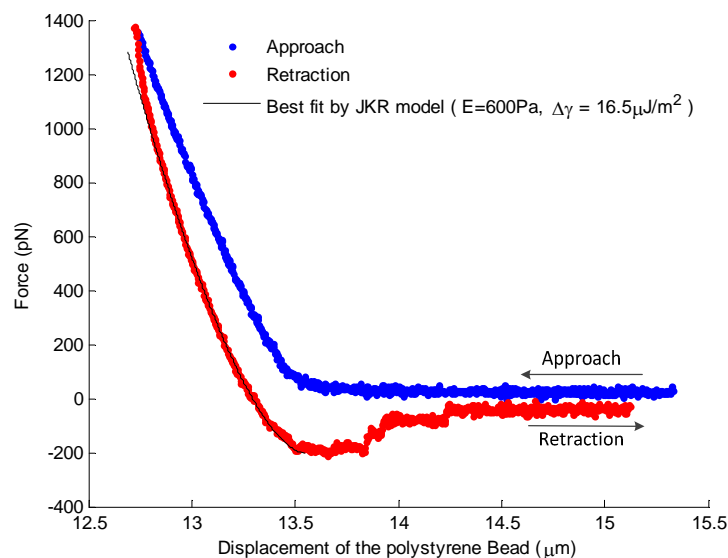
Fig 6.6 Viscous relaxation time of the two type cells. The data are presented as average values with standard deviations.

Fig 6.5 (a) and (b) show the force-time curves obtained from the loading part and their best fitting curves by Kelvin model corresponding to MIN6 cells. There are 24 of sample A and 3 of sample B F-d curves. The determined viscous relaxation time of MIN6 cells is shown in Fig 6.6. The average value of viscous relaxation time of sample A is 0.0125 sec which is less than one tenth of loading time as seen in Fig 6.5(a), and for sample B, the value is 0.0045 sec which is almost 1/60 of the loading time as shown in Fig 6.5(b). As a result, the influence of viscoelasticity can be excluded if the MIN6 cell is treated as pure elastic.

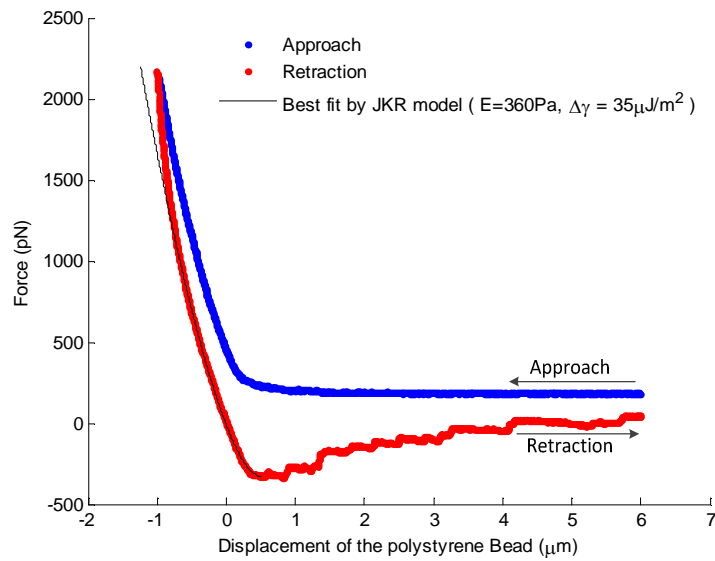
6.3.2 Fitting results by using JKR model of bead on spherical cell

Fig 6.7 presents typical results of the force-displacement curves obtained by AFM indentation and the best fitting curves by using JKR model for the retraction part of MIN6 cells. During the loading stage (as illustrated in blue lines in Fig 6.7), the sensed reaction force is dominated initially by the stiffness of the AFM cantilever and then by the stiffness of the

measured cell. For the unloading process, as shown in red lines in Fig 6.7, the indentation force decreases to a negative region which represents adhesive forces between the cell and the indenter. The adhesion force is characterized as a short-range force (the adhesive force in JKR model is considered as short-range force), and will not significantly affect the force-displacement curve during the loading stage. Before the contact breaks, the short-range adhesion force starts to show the effect, and thus the adhesion force is characterized as pull-force (the negative force region in Fig 6.7) which is needed to overcome the adhesion force during indenter retraction. Consequently, only the retraction stage, as shown in red lines in Fig 6.7, can be used to facilitate a direct fitting by JKR model even though theoretically speaking both loading and unloading parts are influenced by adhesion force^[151]. It can be seen that the JKR model fits very well with most of the unloading curve data except for the beginning part. This is because the initial unloading part was influenced by the creeping effect of the cell-indenter interaction. Therefore, the JKR model can best describe the experimental results of the unloading curve as shown above.



(a)



(b)

Fig 6.7 Typical force-displacement curves and the best fitting curves by using JKR model for (a)

Sample A and (b) Sample B cells.

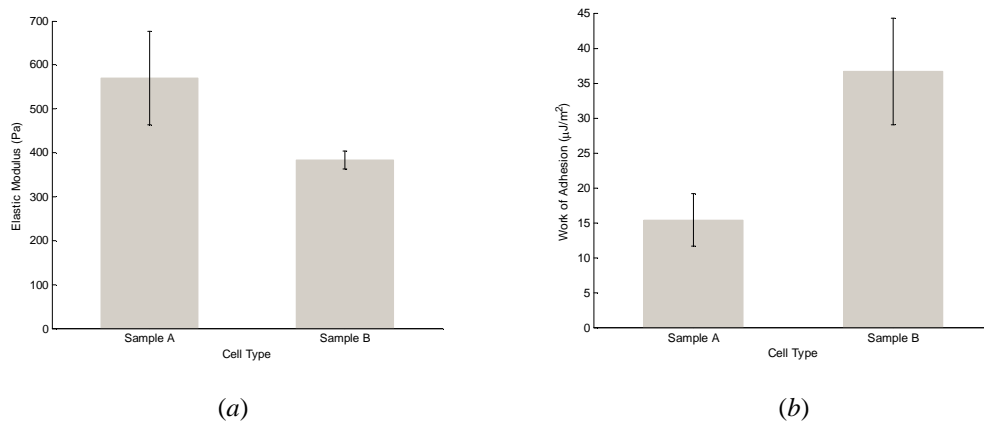


Fig 6.8 Statistics of (a) Young's modulus and (b) work of adhesion respectively.

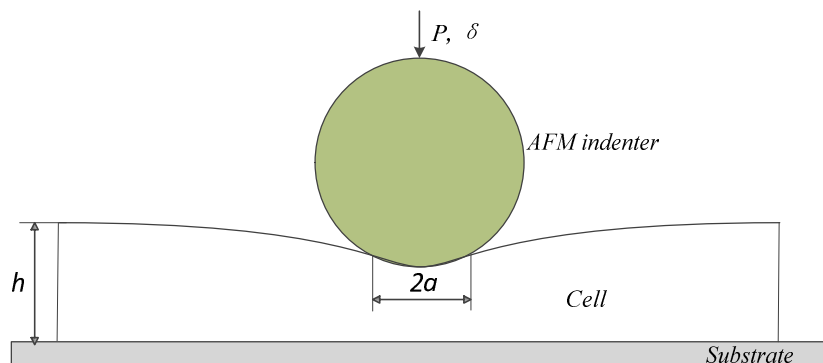
During the loading section, the indentation force increases monotonically as the indenter approaches the cell until the preset indentation depth of $12.72\mu\text{m}$ is reached with the maximum force of 1357pN . Afterwards, the force decreases monotonically to zero and then becomes negative as the indenter retracts. The force decreases and then bottoms at its

minimum value implying the bead begins to detach the cell. A further retraction of the probe suggests the indentation force begins to yield accompanying with some sudden abrupt decrease of adhesion force as shown in Fig 6.7. This jump-off phenomenon is very commonly observed in some cell AFM indentation experiments. In practice this part of the retraction curve is difficult to model and many efforts have been made previously. Sirghi et al^[151] observed this jump-off instability in their mouse fibroblast AFM indentation experiments and attributed this sudden decrease of adhesion force to discontinuous decrease of tip-cell membrane contact area. According to his assumption, tethering of cell membrane to the AFM tip surface at a certain contact line will result in jump in contact area, and this tethering is followed by a sudden detachment and tethering to another contact line. Moreover, such consecutive tethers and detaches of the cell and AFM tip are also reported and analyzed by Sun et al^[161] Fitting JKR model to this abrupt force variation will cause errors in determination of the work of adhesion and thus this abrupt discontinuous part after maximum adhesion force has been discarded during fitting.

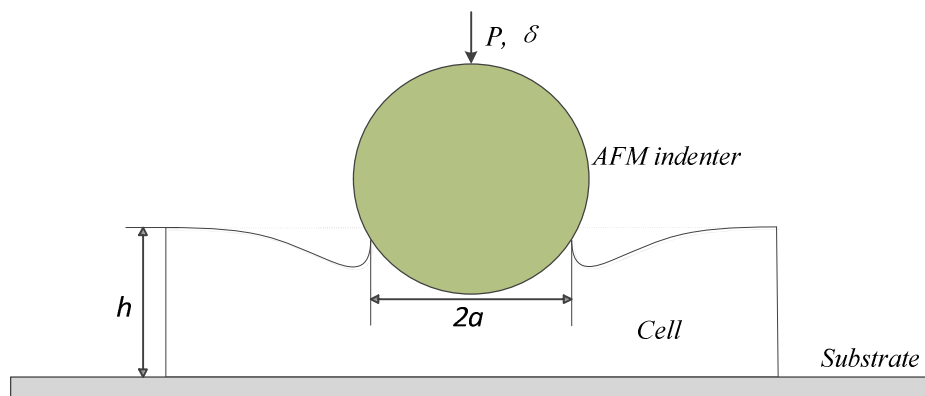
Fig 6.8 shows the fitting results of extracted Young's modulus and work of adhesion from 24 of sample A and 3 of sample B force-displacement curves by using JKR model of bead on spherical cell. Fig 6.8(a) shows the average elastic modulus for sample A cells is $380Pa$, and sample B is $570Pa$, whilst the average work of adhesion is $36.7\mu J/m^2$ for sample A and $15.4\mu J/m^2$ for sample B, as shown in Fig 6.8 (b). It is worth noting that the determined work of adhesion coincides with the previously reported values^[151] in the same order of magnitude.

6.3.3 Fitting results by JKR model of bead on flattened cell

In the previous section, cell was assumed as a sphere subjected to AFM indentation. The contact radius is small enough compared with the thickness of the cell, and thus the cell can be treated as semi-infinite space. However, this assumption does not always hold because cell may exhibit mobility under indentation. The height of the cell may be reduced to a finite-size compared with contact radius and in this regard the extracted parameters will be influenced by the effect of finite size. In this section, cell is considered to be flattened with finite thickness, and this represents a more realistic model. Here, we first propose a thickness value of $25\mu\text{m}$, the same as the diameter of the spherical cell. Compared with the bead on a spherical cell, the effect of finite-size on the determined parameters needs to be verified. For simplicity, the cell can be regarded as a flat sheet with finite thickness subjected to AFM indenter, as illustrated in Fig 6.9 (a).



(a)



(b)

Fig 6.9 (a) Schematic diagram of the non-adhesive contact between a rigid bead and an elastic layer with finite thickness h . (b) Scheme of the adhesive contact between a rigid bead and an elastic layer.

First, the contact is treated as non-adhesive, frictionless, and for this case, Shull et al^{[25][26]} gave a semi-empirical approximation for the dependence of applied load P' , indentation depth δ' and compliance C on the contact radius a as

$$P' = P_h(a)f_p\left(\frac{a}{h}\right), f_p\left(\frac{a}{h}\right) = 1 + \beta\left(\frac{a}{h}\right)^3 \quad (6.14)$$

$$\delta' = \delta_h(a)f_\delta\left(\frac{a}{h}\right), f_\delta\left(\frac{a}{h}\right) = 0.4 + 0.6e^{\left(-\frac{1.8a}{h}\right)} \quad (6.15)$$

$$C = C_h(a)f_c\left(\frac{a}{h}\right), f_c^{-1}\left(\frac{a}{h}\right) = 1 + \left[\frac{0.75}{(a/h)+(a/h)^3} + \frac{2.8(1-2\nu)}{(a/h)}\right]^{-1} \quad (6.16)$$

where P_h and δ_h are the externally applied load and indentation depth respectively corresponding to a contact radius a in Hertzian contact model. C_h is the compliance of Hertz contact model with a contact radius a , i.e.

$$P_h(a) = \frac{4Ea^3}{3(1-\nu^2)R} \quad (6.17)$$

$$\delta_h(a) = a^2/R \quad (6.18)$$

$$C_h(a) = \frac{1}{2aE^*} \quad (6.19)$$

$\beta = 0.15$ for the frictionless case, and $\beta = 0.33$ for the full-friction case. $f_p(\bullet)$ and $f_\delta(\bullet)$ are geometric factors which mediate the effect of thickness. From Eq. (6.14) and (6.15), it is shown that P' and δ' will reduce to P_h and δ_h when $h \gg a$.

Second, by analogy to the derivation of *JKR* model, Shull^{[25][26]} developed the “generalized” *JKR* model to describe the adhesive contact between a rigid indenter and a flat sheet with finite thickness, as shown in Fig 6.9(b). In this “generalized” model, the expressions for the energy release rate \mathcal{G} is extended to the adhesion of relatively thin layers by using the

approximation of compliance given by Eq. (6.16). Simple expressions are only available for incompressible materials with $\nu = 0.5$ as

$$\mathcal{G} = \frac{(P' - P)^2}{8\pi E^* a^3} f_{Gp} \left(\frac{a}{h} \right), f_{Gp} \left(\frac{a}{h} \right) = \frac{0.56 + 1.5(a/h) + 3(a/h)^3}{[0.75 + (a/h) + (a/h)^3]^2} \quad (6.20)$$

$$\mathcal{G} = \frac{E^*(\delta' - \delta)^2}{2\pi a} f_{G\delta} \left(\frac{a}{h} \right), f_{G\delta} \left(\frac{a}{h} \right) = 1 + 2.67 \left(\frac{a}{h} \right) + 5.33 \left(\frac{a}{h} \right)^3 \quad (6.21)$$

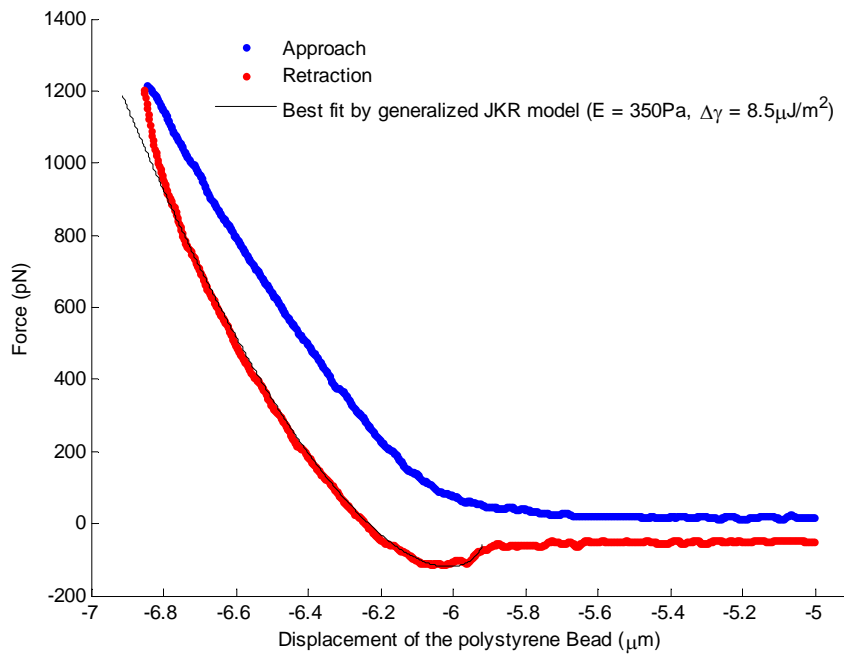
where P' and δ' are the applied load and indentation depth corresponding to contact radius a as given by Eq. (6.14) and (6.15) when adhesion is absent. $f_{Gp}(\bullet)$ and $f_{G\delta}(\bullet)$ are also geometric correction factors. By letting $\mathcal{G} = \Delta\gamma$, equilibrium is reached and thus the externally applied load P and indentation depth δ are related by the contact radius a by transforming Eq. (6.20) and (6.21) into

$$P = P' - \sqrt{8\pi E^* a^3 \Delta\gamma f_{Gp}^{-1} \left(\frac{a}{h} \right)} \quad (6.22)$$

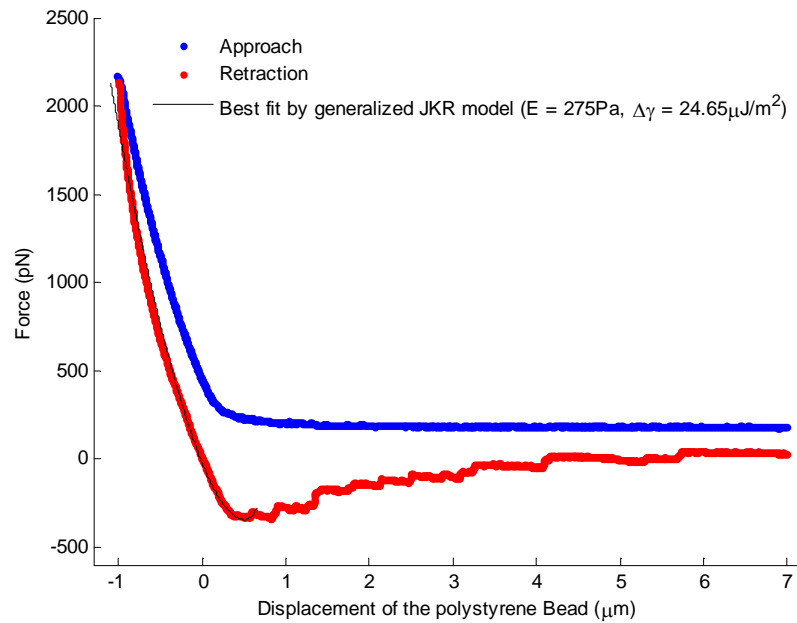
$$\delta = \delta' - \sqrt{\frac{2\pi a \Delta\gamma}{E^*} f_{G\delta}^{-1} \left(\frac{a}{h} \right)} \quad (6.23)$$

where P and δ are the indentation force and depth respectively in flattened cell indentation.

For comparison purpose, we have carried out the modelling process on flattened cells with variable thickness of $25\mu\text{m}$ (case 1), $14\mu\text{m}$ (case 2), $9\mu\text{m}$ (case 3) and $3\mu\text{m}$ (case 4). As mentioned before, the cells may have spread on substrate with different shapes and thicknesses. Thus the penetration depth within 10% of the film thickness could not be guaranteed in reality. To accommodate the situation, we have chosen the possible film thickness from the thickest (case 1) to the thinnest (case 4).

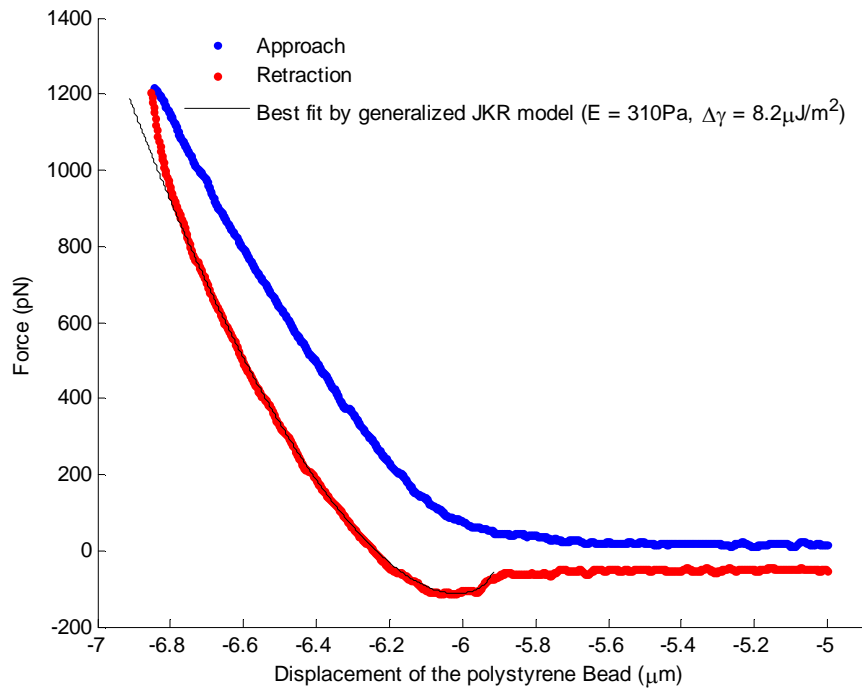


(a)

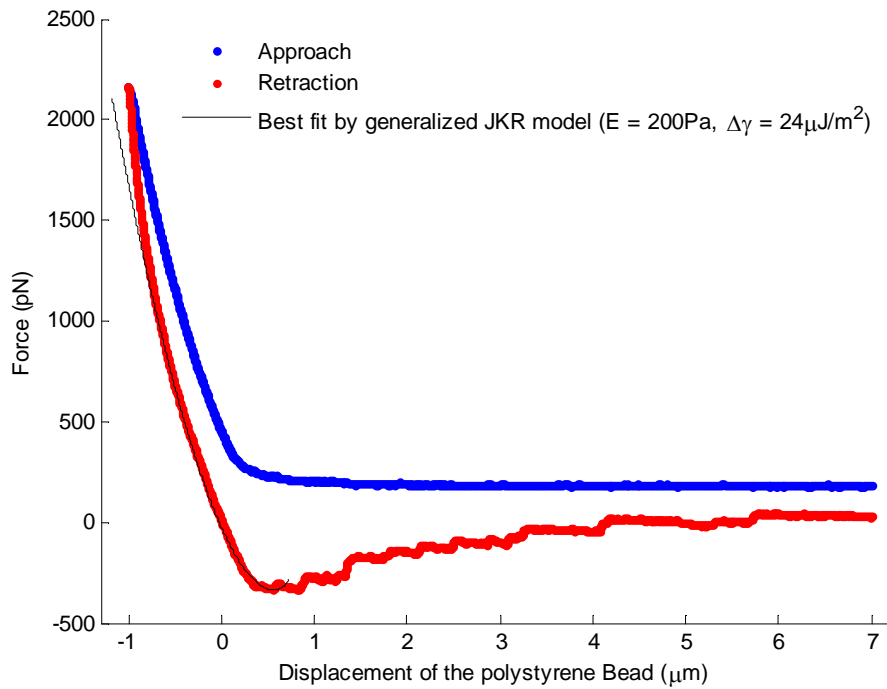


(b)

Fig 6.10 Typical force-displacement curves and the best fitting curves by using “generalized” JKR model for (a) normal and (b) treated cells corresponding to case 1.



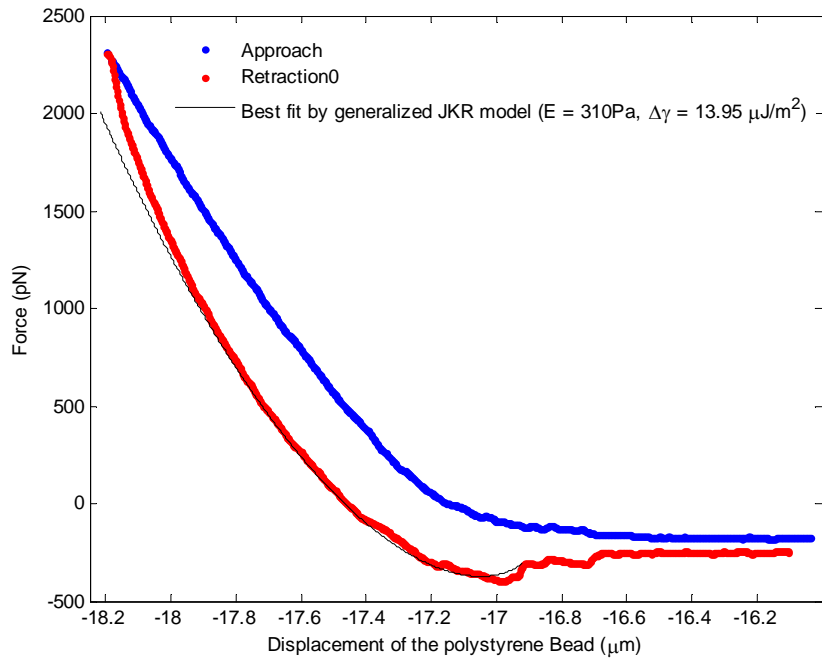
(a)



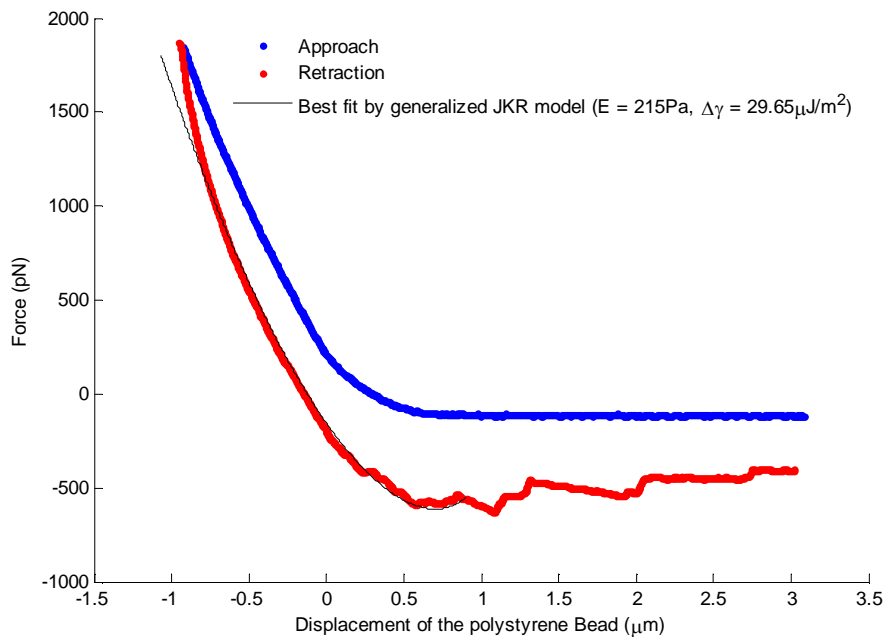
(b)

Fig 6.11 Typical force-displacement curves and the best fitting curves by using “generalized” JKR

model for (a) normal and (b) treated cells corresponding to case 2.



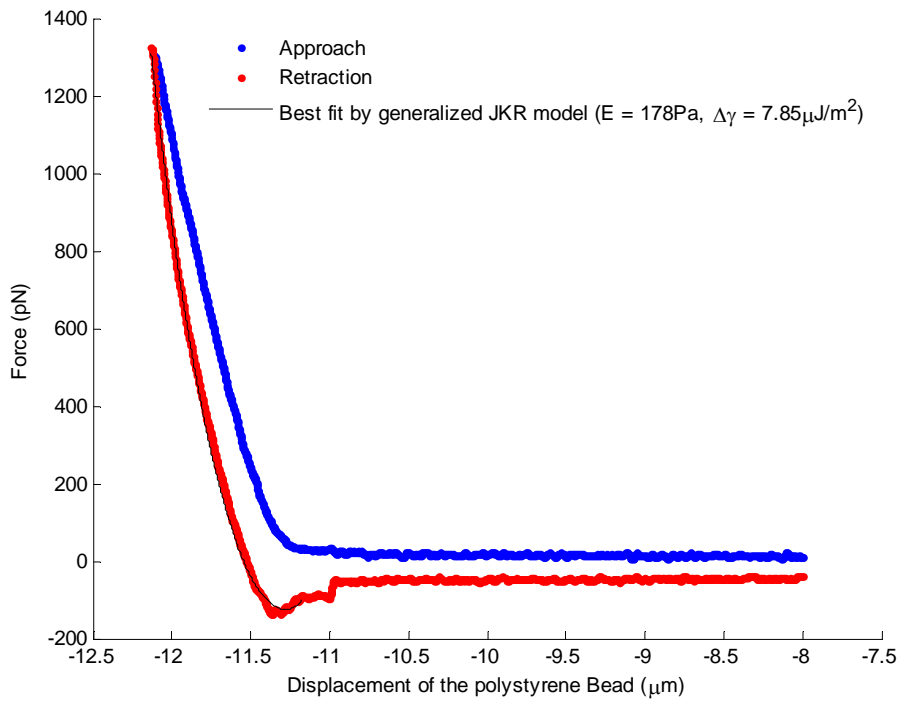
(a)



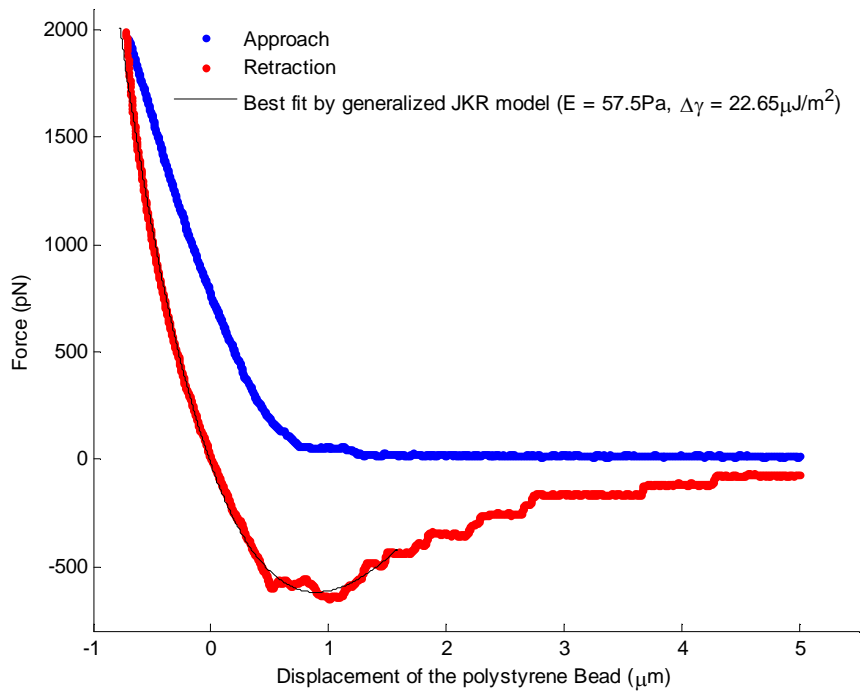
(b)

Fig 6.12 Typical force-displacement curves and the best fitting curves by using “generalized” JKR

model for (a) normal and (b) treated cells corresponding to case 3.



(a)



(b)

Fig 6.13 Typical force-displacement curves and the best fitting curves by using “generalized” JKR

model for (a) normal and (b) treated cells corresponding to case 4.

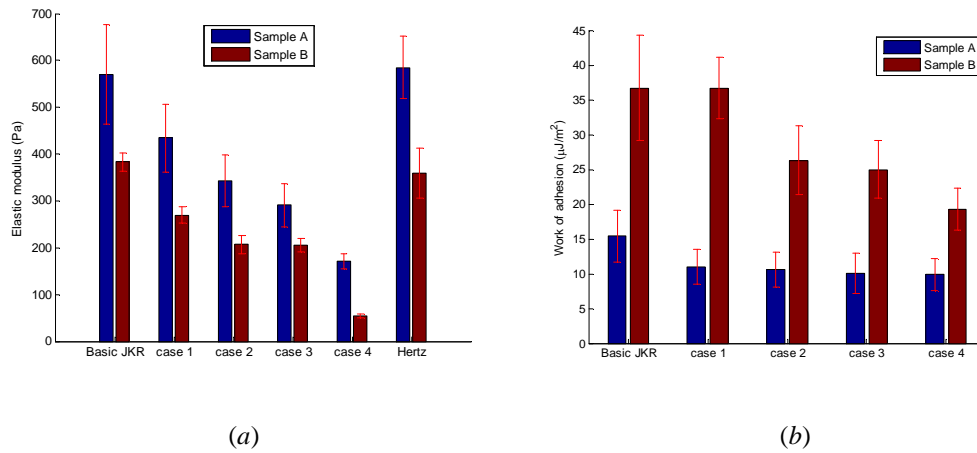


Fig 6.14 The statistics of (a) Young's modulus and (b) work of adhesion for both sample cells determined by all the models in this chapter

Table 6.1 Values of Young's modulus determined by the two JKR models and Hertz model.

Cell Type	Bead on Spherical Cell (Pa)	Bead on Flatten Cell Case 1 (Pa)	Bead on Flatten Cell Case 2 (Pa)	Bead on Flatten Cell Case 3 (Pa)	Bead on Flatten Cell Case 4 (Pa)	Hertz contact model
sample A	570±107	434±72	343±55	291±45	171±16.7	558±67
sample B	383±20	270±18	207±20	206±14	54±4	360±53

Table 6.2 Values of work of adhesion determined by the two JKR models.

Cell Type	Bead on Spherical Cell ($\mu\text{J}/\text{m}^2$)	Bead on Flatten Cell Case 1 ($\mu\text{J}/\text{m}^2$)	Bead on Flatten Cell Case 2 ($\mu\text{J}/\text{m}^2$)	Bead on Flatten Cell Case 3 ($\mu\text{J}/\text{m}^2$)	Bead on Flatten Cell Case 4 ($\mu\text{J}/\text{m}^2$)
sample A	15.39±3.73	11±2.5	10.6±2.5	10.1±2.9	9.92±2.32
sample B	36.67±7.64	36.7±4.4	26.3±4.9	25±4.2	19.3±3.08

Fig 6.10-6.13 present the aforementioned force-displacement curves obtained by AFM indentation and the best fitting curves by the "generalized" JKR model with four different

thicknesses. It is suggested that the “generalized” JKR model can also fit the experimental results of the unloading curve.

Fig 6.14 (a) and (b) show the statistics of determined Young’s modulus and work of adhesion from the aforementioned 24 sample A and 3 sample B force-displacement curves, and the calculated values are listed in Table 6.1 and 6.2.

For comparison purpose, one has also applied Hertz contact model to fit the loading part of the force-displacement curve, and found out that the calculated Young’s modulus of the MIN6 cells is very close to that determined by basic JKR fitting. However, the fitting result by Hertz model is not as good as those by JKR and “generalized” JKR models as indicated by Fig 6.15.

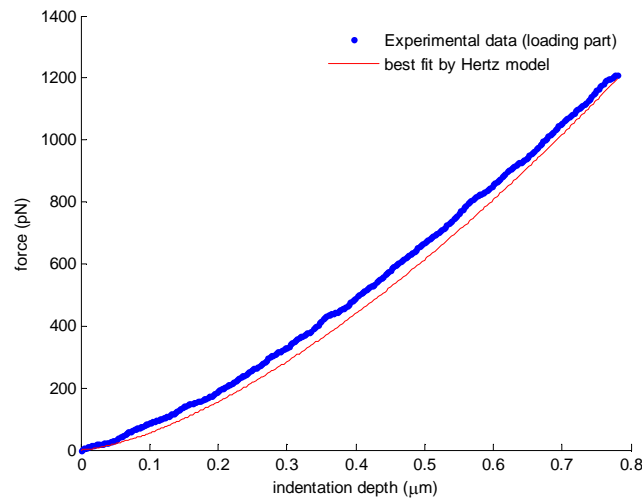


Fig 6.15 Typical force-indentation depth curve (loading part) and the best fitting curves by Hertz contact model

It can be seen from Fig 6.14 (a), for sample B, the elastic modulus calculated by “generalized” JKR model is close to that of basic JKR for case 1, remains fairly steady for the cases 2 and 3, and decreases to a much smaller value for the very thin case 4. The results

show that the elastic modulus of Sample A is in general higher than that of Sample B. For the determined work of adhesion of cells, Sample B is much higher than Sample A. This indicates that sample B cells are softer and exhibit higher adhesion.

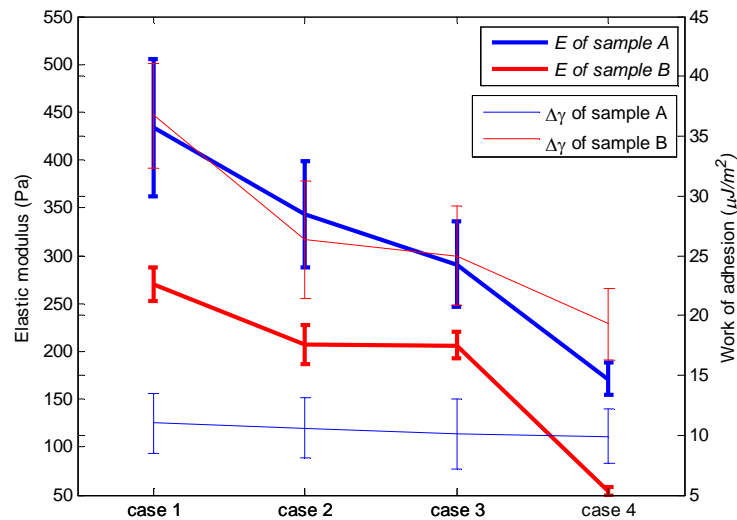


Fig 6.16 Statistics of Young's modulus (bold solid lines) and work of adhesion (thin solid lines) for Sample A (blue lines) and Sample B (red lines) with four thickness cases.

Fig 6.16 presents a direct comparison between the four cases for sample A and B in terms of Young's modulus (Pa) and work of adhesion ($\mu\text{J}/\text{m}^2$). The determined work of adhesion of Sample A maintains almost the same value of $10\mu\text{J}/\text{m}^2$ regardless of the cell thickness, while the counterpart sample B decreases dramatically as cell thickness decreases (see the red thin solid line in Fig 6.16), which is attributed to the fact that softer material (sample B) is more sensitive to the substrate effect. For both samples, the determined Young's modulus decreases as the cell thickness decreases. This trend seems inconsistent with the general perception that substrate effect may lead to an increase in the calculated Young's modulus. However, it

should be born in mind that the situation here is very different and can be explained as follows. For the four cases, we use different thicknesses to fit the same force-displacement curve. If we use Eq. (6.14) – (6.16) to fit the loading part of the $F-d$ curve, the compliance C is fixed regardless of the cell thickness. Substituting Eq. (6.19) into (6.16) yields

$$C = \frac{f_c(a/h)}{2aE^*} \quad (6.24)$$

For the same contact radius a , smaller thickness h corresponds to larger a/h , resulting to lower $f_c(a/h)$, and hence the determined E^* should decrease in order to keep the same compliance C . Although we used Eq. (22) and (23) to fit the retraction part of the $F-d$ curve, the involvement of work of adhesion will not alter the effect of cell thickness on the determined Young's modulus in general, and conclusively, thinner thickness will produce lower Young's modulus by fitting the same $F-d$ curve. It is worth noting that the case 1 and case 4 are two extreme situations and cases 2 and 3 are more realistic representation of the concerned cells.

6.3.4 Finite element simulation

In JKR model, a strong adhesive force is assumed to act at the equilibrium distance z_0 , which is treated as a Delta function enclosing an area $\Delta\gamma^{[81]}$ as shown by Fig 3.8 (b). Since the results by self-consistent method can be applied to JKR model if $\mu \geq 5$ (see Sec. 3.2.4), the force-displacement curve by FEM method developed in Sec. 5.4 could be used to fit the existing $F-d$ data from MIN6 cell indentation with respect to retraction part.

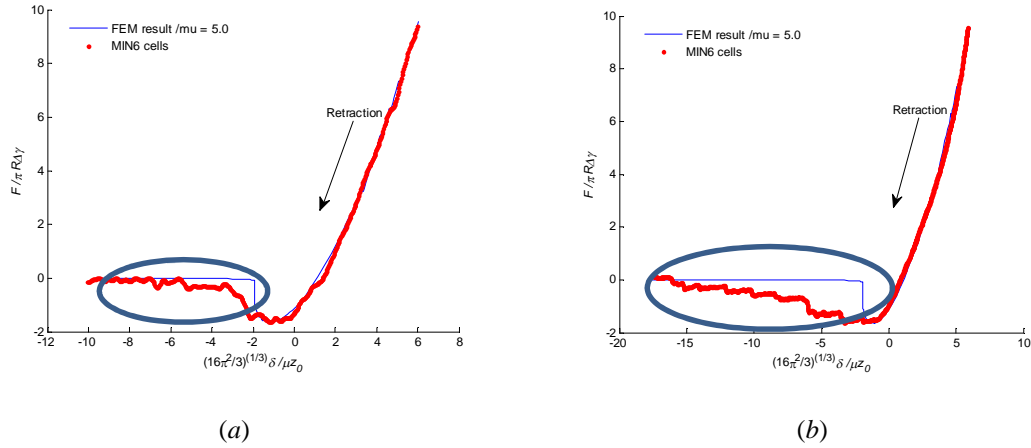


Fig 6.17 Typical force-displacement curves and the best fitting curves by using FEM ($\mu = 5$) for (a) Sample A and (b) Sample B cells (in reduced coordinates). The red bold and thin blue lines denote experimental data and *FEM* simulation results, respectively.

Fig 6.17 shows the fitting results corresponding to FEM and experimental data. For the FEM, the value of R , z_0 and $\Delta\gamma$ are listed in Table 5.2, while for the experimental data, $R = R_{p-c} = (1/R_p + 1/R_c)^{-1}$, E and $\Delta\gamma$ were selected such that good fit would be presented. As may be seen from Fig 6.17, the F - d curve by FEM can mostly overlap its experimental counterpart except the area circled by the ellipses. For the cells, the stepwise curve is due to multiple tethers as analyzed in Sec 6.3.2, which is ascribed to cell inhomogeneity after all. In the FEM, nevertheless, the elastic substrate is assumed to be homogeneous, resulting in the “brittle” separation as shown by the vertical curve in Fig 6.17. In general, the FEM can also describe the retraction process of cell with AFM probe.

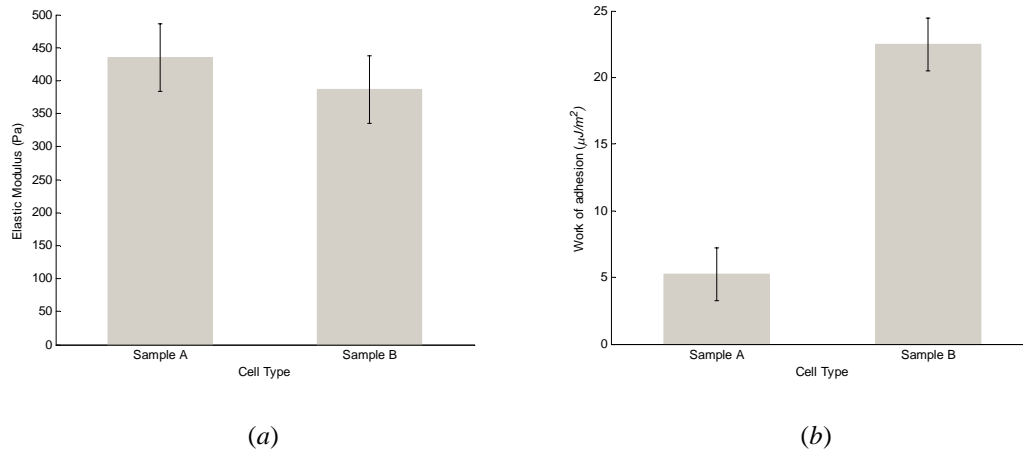


Fig 6.18 Results of extracted Young's modulus and work of adhesion respectively. The data are presented as average values with standard deviations.

Fig 6.18 shows the fitting results of extracted Young's modulus and work of adhesion from 24 (sample A) and 3 (sample B) force-displacement curves by using *FEM* model of bead on spherical cell. Fig 6.18 (a) shows the average elastic modulus for sample A cells is 435Pa , and sample B is 386Pa , whilst the average work of adhesion of sample A and B is $5.2\mu\text{J}/\text{m}^2$ is $24.5\mu\text{J}/\text{m}^2$ respectively as shown in Fig 6.18(b). Although the values of these two parameters differ from that in Fig 6.8 by a small margin, the tendency of them (E and $\Delta\gamma$) between cell A and B is the same.

6.4 Summary

In this chapter, the adhesion between the surface of polystyrene micro-bead and cyto-membrane of biological cells has been investigated. The adhesion at the contact between AFM tip and the cell, Johnson-Kendall-Roberts (JKR) model has been used to fit the force-displacement curves obtained. The effect of viscoelasticity of cell under the AFM indentation can be neglected since the extracted viscous relaxation time is very small

compared with the loading time period. The MIN6 cell has been modeled as first a sphere and then a flattened cell with different thicknesses. Firstly, the cell and the indenter are modeled as two spheres, and the JKR model has been applied to fit the experimental data of the retraction part of the force-displacement curves. Secondly, the indented cell is treated as a layer with four different finite thicknesses, and “generalized” JKR model is used to fit the same force-displacement curves. Summary is listed as follows:

- The results have shown that both the basic JKR and “generalized” JKR models can effectively describe the behavior of the unloading force-deformation curves.
- The “generalized” JKR model can be used for more realistic cell modelling with various cell thicknesses and both models can identify the property variations of the two types of cells.
- FEM proves an effective means to simulate the $F-d$ curve. Although the values of parameters extracted by FEM differs from that of JKR fitting, the tendency of them between control cell and treated cell remain the same.

7 Determination of Work of Adhesion of human hepatocellular carcinoma by AFM indentation (Vickers probe)

7.1 Introduction

In last chapter, JKR model was applied to a very soft material, i.e. MIN6 cells, to characterize its surface adhesion. Both Young's modulus, and work of adhesion can identify the difference between normal and treated cell. In terms of this method, this chapter will apply JKR model to characterize the difference between another biological cell and its treated counterpart, i.e. human hepatocellular carcinoma and its fullereneol treated counterpart.

Fullerene family has been playing an important role for potential applications in biomedicine such as cancer diagnosis and therapy^{[162][163][164]}. The fullereneol can induce apoptosis process which is associated with cytoskeleton disruption^[165]. Cancer cells affected by fullereneols could exhibit variations in mechanical properties such as elastic stiffness and these changes in cancer progression are helpful to understand the individual differences between normal and cancer cells^{[166][167]}. The atomic force microscope (AFM) indentation can offer an accurate mechanical measurement of individual living cells^{[110][168][169]}. On the other hand, the adhesion phenomenon, characterized as negative force in the experimental force-displacement curves obtained in AFM indentation, was widely reported over the last two decades^{[150][160][170][171]}. The adhesion behavior of cells with other nanoparticles is crucial for the biocompatibility of implants^[172]. In recent years, it has become clear that adhesion molecules are involved in tethering cells to specific locations^[173]. Adhesion molecules are transmembrane molecules that are linked to cytoskeletal elements (actin)^[117]. Since fullereneols

have appreciable effect on cytoskeletal structures, the adhesion property of cancer cyto-membrane may also alter due to fullereneol treatment.

This chapter will present investigation of mechanical properties by AFM nanoindentation on human hepatocellular carcinoma cells treated with fullereneol for 24, 48 and 72 hours. Atomic force microscope is routinely used to investigate the morphology and biomechanical properties of living carcinoma cells, and adhesion phenomenon (negative force) is detected in the obtained force-displacement curves. It is found that adhesion phenomenon is dependent on time duration of fullereneol treatment. The control cells and the cells exposed to fullereneol for 24 hours showed insignificant adhesion while the rest two kinds of cells exhibited conspicuous adhesion. The fitted JKR model provides good agreement with the experimental results. The changes of the determined work of adhesion ($\Delta\gamma$) due to different periods of fullereneol treatment are provided.

7.2 Methodology

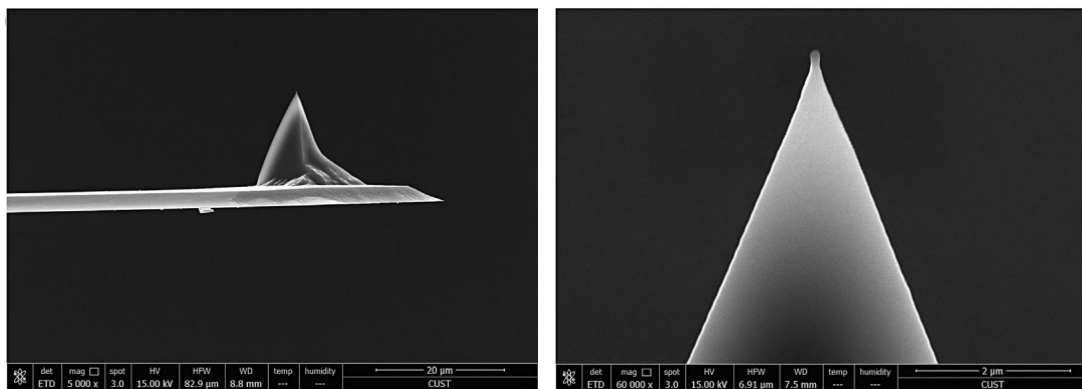
7.2.1 Cell Preparation

SMCC-7721 cells were obtained from Roswell Park Memorial Institute (RPMI)-1640 media with 10% of fetal bovine serum (FBS) and antibiotics (penicillin–streptomycin solution). The commercial water-soluble fullereneol powder with the general formula $C_{60}(OH)_{24}$ was dissolved in deionized water at a concentration of 2.7mM/ml, and it was then diluted with RPMI-1640 media with 10% of FBS to 0.53mM/ml, which was used for the fullereneol treatment solution stored at 41 °C. The Maintenance of SMCC-7721 cells and sample preparation have been described in detail elsewhere^[167]. Here, one labeled control cells as cell A, which were not exposed to fullereneol and being cultured for 24 hours in the physiological

solution, and marked cells exposed to fullerenol for 24, 48 and 72 hours as cell *B*, *C* and *D* respectively. In this chapter, cell *B* (treated for 24 hours) consists of 12 live cells, while others are 7 cells each.

7.2.2 Atomic force microscope

The module of the AFM employed in this chapter is JPK NanoWizard® 3 Bioscience, which was used for both indentation and cell imaging. It was mounted on an inverted microscope, allowing the AFM and optical microscope imaging together. The criterion for cantilever selection is that the compliance of the cantilever should be around the range of the sample compliance. For very soft and delicate cells, the softest cantilevers are available with spring constants ranging from 10 to 30 mN/m . Therefore, a silicon nitride cantilever whose spring constant is 30 mN/m , was adopted for cell-bead indentation in this chapter. The probe is a square pyramid tip (Vickers) with a half-opening angle of 25° (half-angle to face), and its radius and height are 10 nm and 2.5 – 8 μm respectively as illustrated in Fig 7.1. The approach and retraction speeds were kept constant at approximately 2.5 $\mu m/s$ for all experiments to relieve viscosity effect.



(a)

(b)

Fig 7.1 Microscope of (a) top of cantilever and (b) the silicon nitride indenter.

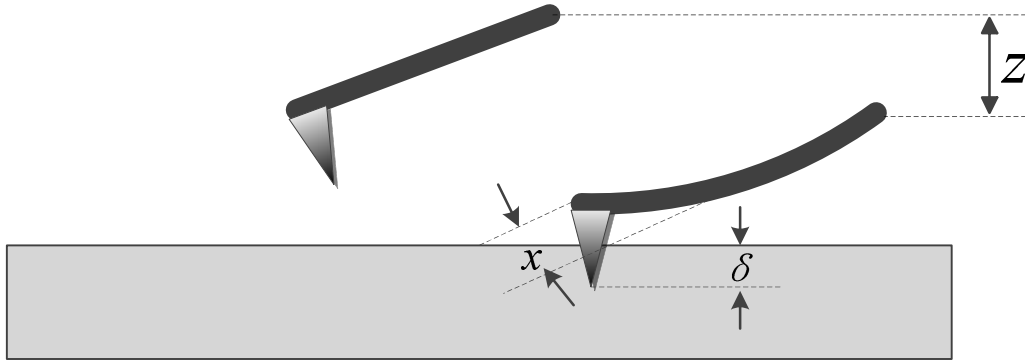


Fig 7.2 Scheme of principle of force-displacement measurement by AFM.

Fig 7.2 illustrates the principle how AFM obtains the force-displacement curve. The sample substrate is fixed by setup. The AFM cantilever is moved vertically by the piezoelectric scanner. Owing to the compliance of the cantilever, the vertical displacement z of bottom of the cantilever does not equal the indentation depth δ after the apex of indenter begins to penetrate the sample substrate. The cantilever itself will undergo a deflection x as shown by Fig 7.2. For geometrical relation, one has

$$z = x + \delta \quad (7.1)$$

If the deflection of cantilever is small, the indentation force F will be proportional to the deflection x as

$$F = kx \quad (7.2)$$

As mentioned Sec. 1.1.2, the deflection of the cantilever x could be measured in terms of the signal $(A + C) - (B + D)$, and the vertical displacement z is pre-set. The remaining two unknowns, i.e. F and δ could be determined by combination of Eq. (7.1) and (7.2).

7.3 Theoretical model

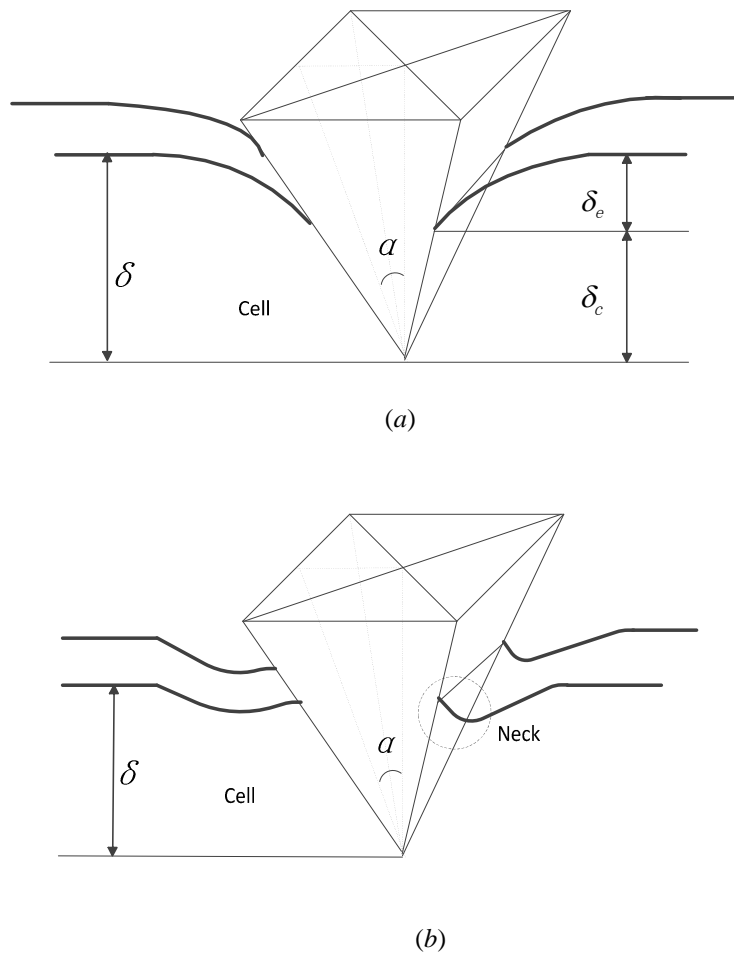


Fig 7.3 Schematic of (a) non-adhesive and (b) adhesive contact between a Vickers indenter and a compliant semi-infinite space. α denotes the half-angle to face. The neck area in the circle in (b) is ascribed to adhesion force.

Fig 7.3 illustrates the schematic of a soft living cell indented by a Vickers indenter, and in this chapter, it is routinely simplified by contact between a conic and substrate material. During the approach and retraction processes, the viscosity effect can be neglected, and only elastic deformation is considered. As can be seen from Fig 7.1, the tip size of the silicon nitride probe is less than that of size of SMCC-7721 cell (see Fig 7.8) by at least two orders of magnitude, and thus the cell could be treated as a semi-infinite space. For a non-adhesive contact between

an elastic half space and an axis symmetric indenter, Sneddon^[174] gave the vertical depth of the contact periphery δ_e and the contact depth δ_c as

$$\delta_e = \varepsilon \delta \quad (7.3a)$$

$$\delta_c = (1 - \varepsilon) \delta \quad (7.3b)$$

where δ denotes indentation depth, and ε is a coefficient dependent on the geometry of the indenter-sample contact. For a conical indenter $\varepsilon = 1 - 2/\pi$. During the retraction, the stiffness of the indenter-substrate, is given as

$$S = \frac{dP}{d\delta} = \frac{2Ea}{(1-\nu^2)} \quad (7.4)$$

where a denotes the radius of the contact periphery and ν is the Poisson's ratio which is set as 0.5, indicating the cytoplasm is incompressible^[110]. P is the load applied on the indenter. For a non-adhesive situation, elastic force F_e is the sole component of P .

$$P = F_e \quad (7.5)$$

For a conic, the contact depth δ_c and the contact radius a are related by

$$a = \delta_c \tan \alpha \quad (7.6)$$

For a pyramid indenter, Eq. (7.4) never holds because the contact area is no long a circle. However, numerical analysis^{[175][176]} indicate that Eq. (7.6) is still valid if a is substituted by an effective contact radius

$$a = a^* = \sqrt{\frac{A}{\pi}} \quad (7.7)$$

where A is the projected contact area, and the corresponding error for a square pyramid indenter is 0.012 compared with conical indenter. According to the geometry shown in Fig 7.3 (a), one has

$$A = (2\delta_c \tan \alpha)^2 \quad (7.8)$$

Substituting Eq.(7.8) into Eq.(7.7) yields

$$a^* = \frac{4\delta \tan\alpha}{\pi^{3/2}} \quad (7.9)$$

Substituting Eq.(7.9) into Eq.(7.4) and integrating the stiffness S with respect to δ results in

$$P = F_e = \frac{4Et \tan\alpha}{(1-\nu^2)\pi^{3/2}} \delta^2 \quad (7.10)$$

If the adhesion is taken into consideration, the force applied on the indenter P should be comprised of elastic (F_e) and adhesion (F_a) terms, i.e.

$$P = F_e + F_a \quad (7.11)$$

The adhesion component term can be given as

$$F_a = -\frac{d}{d\delta}(-\Delta\gamma A_c) \quad (7.12)$$

where $\Delta\gamma$ and A_c denote work of adhesion and contact area respectively. The latter is given as

$$A_c = 4\delta_c^2 \frac{\tan\alpha}{\cos\alpha} \quad (7.13)$$

Ignoring the effect of adhesion on the deformation, the contact depth δ_c is still determined by

Eq. (7.3b). Substituting Eq.(7.13) into Eq.(7.12) yields

$$F_a = -\frac{32\Delta\gamma \tan\alpha}{\pi^2 \cos\alpha} \delta \quad (7.14)$$

Substituting Eq. (7.14) into (7.11) results in

$$F = \frac{4Et \tan\alpha}{\pi^{3/2}(1-\nu^2)} \delta^2 - \frac{32\Delta\gamma \tan\alpha}{\pi^2 \cos\alpha} \delta \quad (7.15)$$

Owing to the second term in Eq. (7.15), negative value of force is given when the indentation depth is small enough, which is commonly observed in many *AFM* indentation experiments on living cells^{[160][170]}. As indicated, when $\Delta\gamma$ equals zero (no adhesion), Eq. (7.15) will reduce to its non-adhesive counterpart, i.e. Eq. (7.10).

7.4 Results and discussion

7.4.1 Post-processing of indentation data

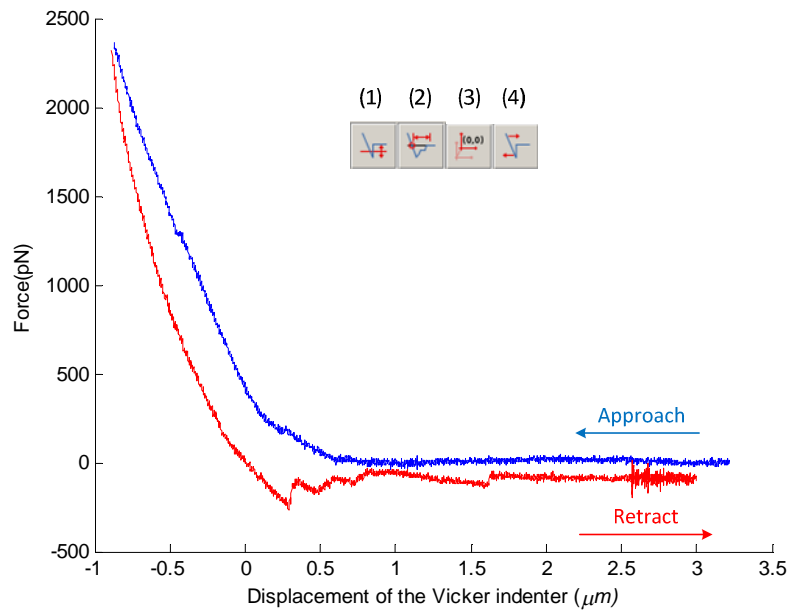


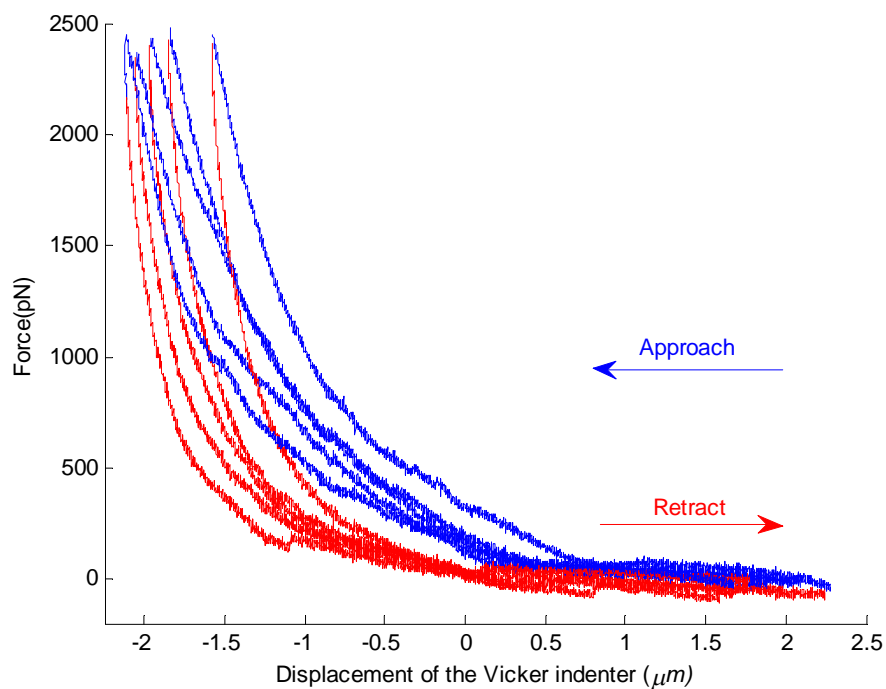
Fig 7.4 Processing of raw force-displacement curve obtained from *AFM* indentation.

Fig 7.4 shows a raw force-displacement curve obtained from *AFM* indentation. The notch peaks at the right side of the curve is attributed to environmental noise or particles on the media. The enclosed area between the loading and unloading curves may be ascribed to viscoelasticity of the cytoplasm and energy dissipation caused by cell stretching of cell membrane during indentation. Due to movement of the aqueous solution, function (1) is adopted to remove the baseline offset in vertical deflection before further processing. In general, the part of the curve on the right is flat, and there is no force between tip and surface, giving the force baseline. Afterwards, function (2) is selected to automatically determine the point where the force curve crossed the zero force line, and this point is set as origin of the x axis. It is worth noting that this point does not necessarily equal the contact point where the *AFM* indenter touch the cyto-membrane and therefore only could be treated as an indication point for fitting a mechanical model^[177]. When the “contact point” is determined, function (3) is used to translate the coordinated system so that the origin overlaps with the “contact point”.

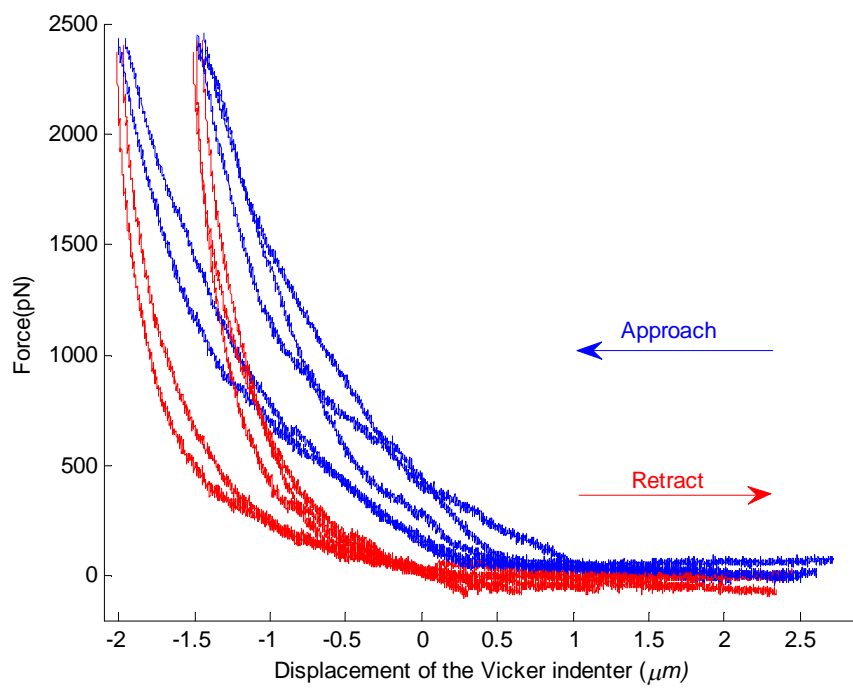
The following operation (4) automatically corrects the deflection value for the bending of the cantilever, and gives the tip sample separation. This operation is very important for the application of fitting by Hertz or JKR model.

7.4.2 Original experimental data

During indentation measurements, live cells were generally indented 3-4 times at the same spot and 5 different spots for one cell. Fig 7.5 shows the repeatability of $F-d$ curves obtained by the AFM indentations. It may be seen that there is insignificant difference between $F-d$ curves from the same indentation point within one cell as shown by Fig 7.5 (a). Likewise, the $F-d$ curves corresponding to different positions within the same cell just differ by a small margin with each other as shown by Fig 7.5 (b), which is likely ascribed to height variation of the cell.

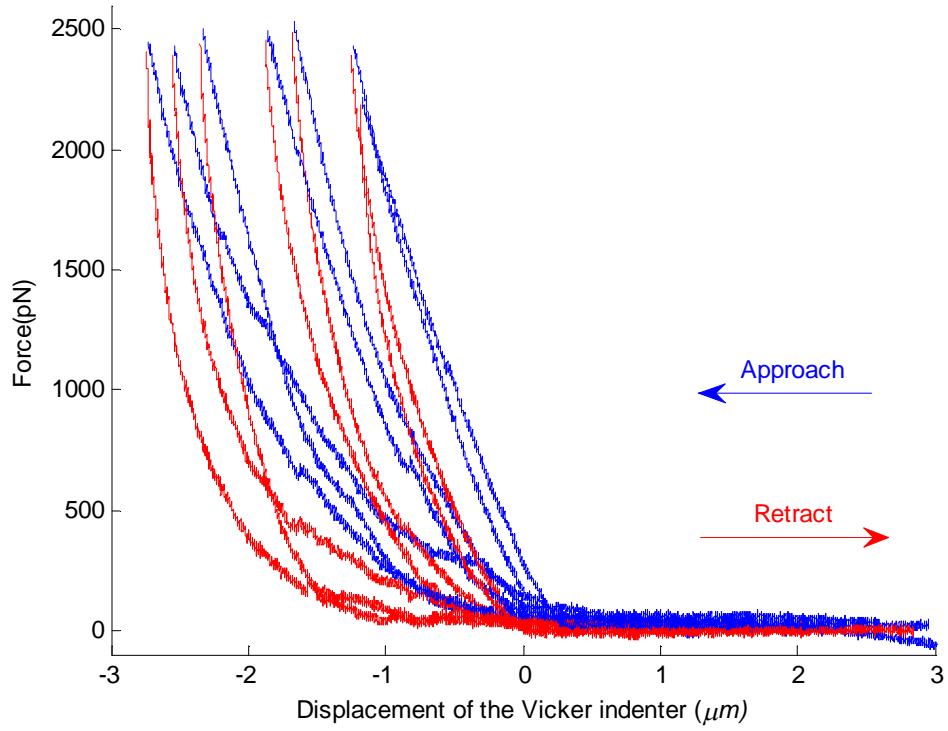


(a)

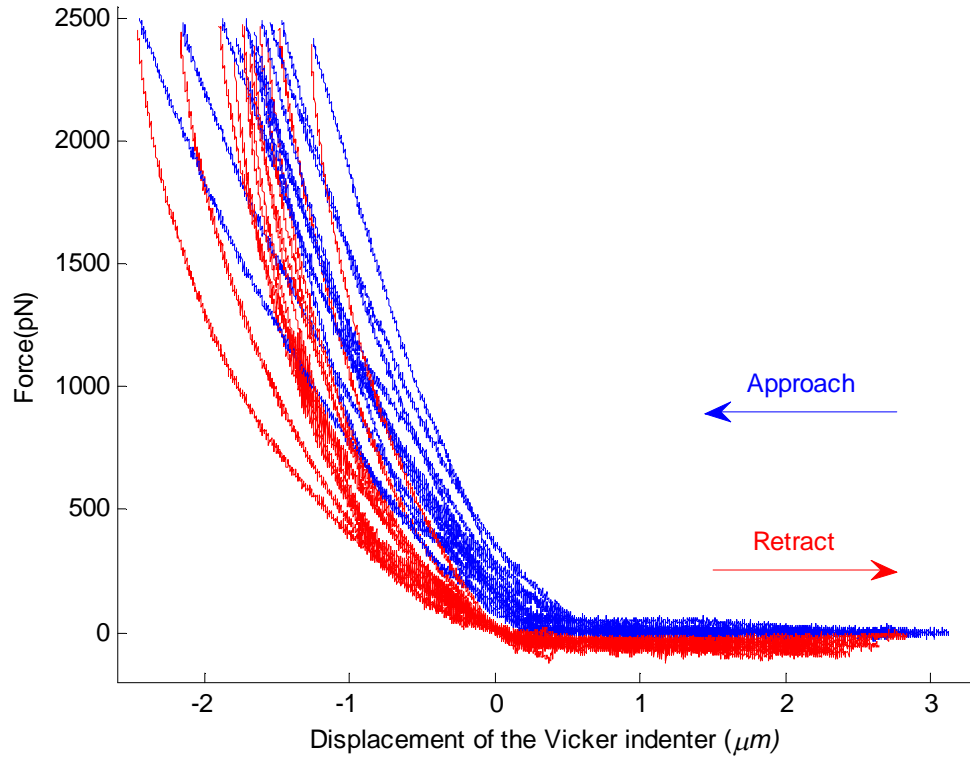


(b)

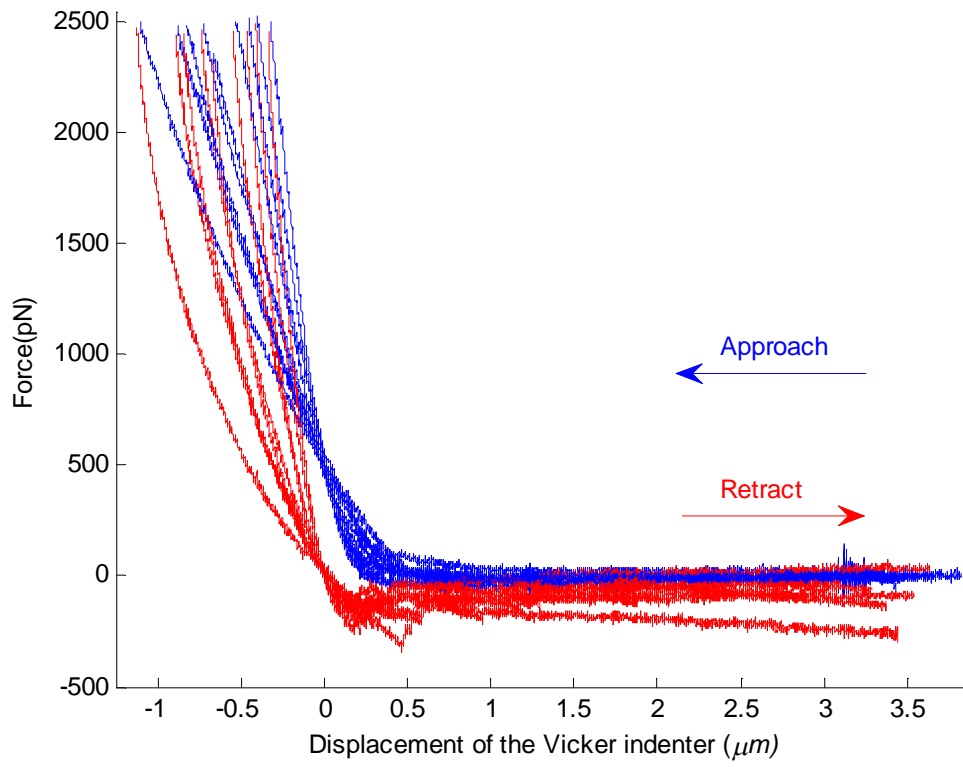
Fig 7.5 Typical $F-d$ curves corresponding to (a) repeated indentations at the same point and (b) different indentation positions within the same cell.



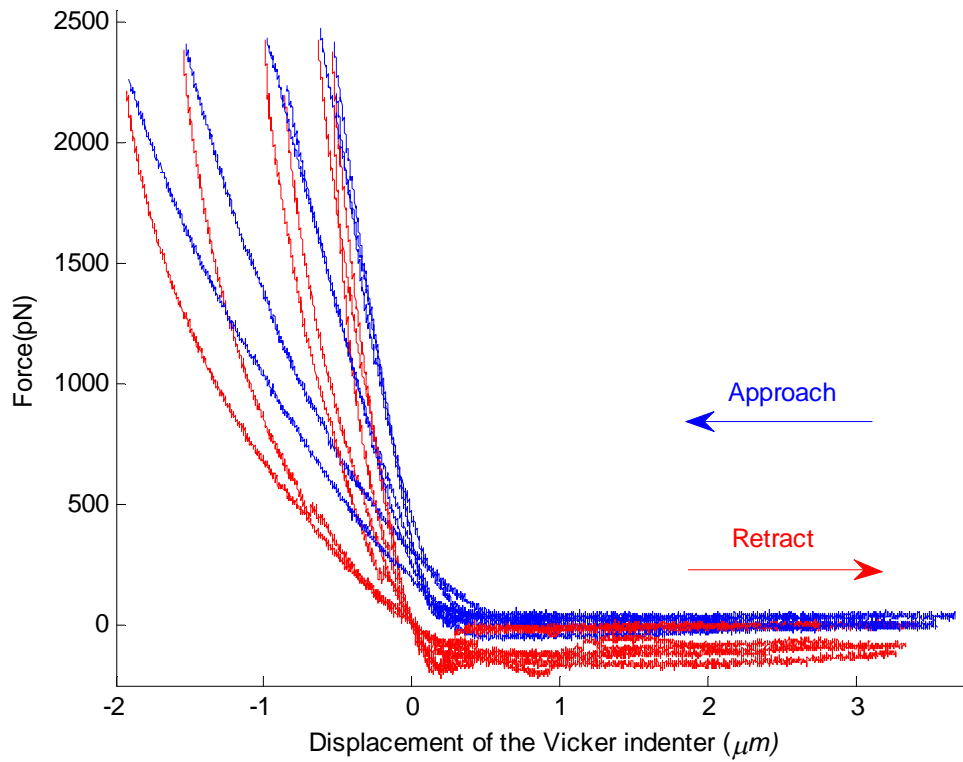
(a)



(b)



(c)



(d)

Fig 7.6 Example of force-displacement curves obtained by AFM indentation on (a) control cells, cells exposed to fullereneol for (b) 24 hours, (c) 48 hours and (d) 72 hours respectively.

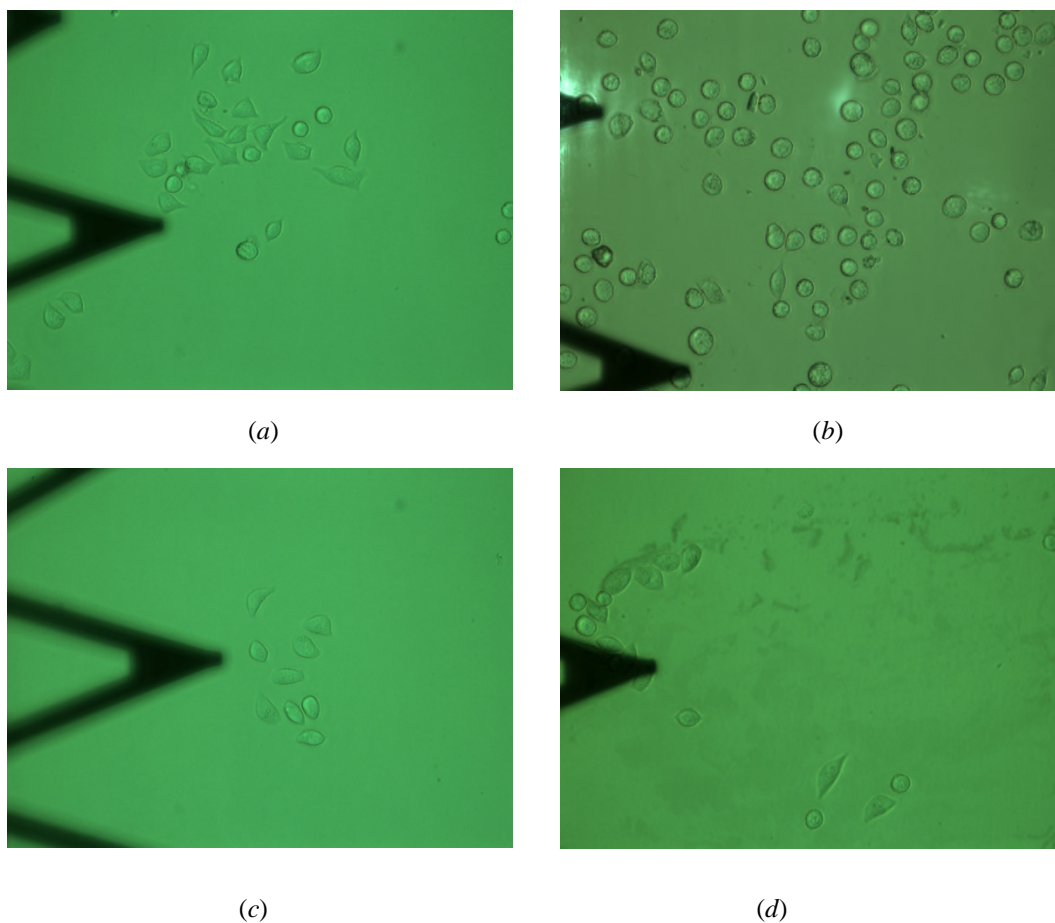


Fig 7.7 Top view of microscope of AFM of (a) control cells, cells exposed to fullereneol for (b) 24 hours, (c) 48 hours and (d) 72 hours respectively. The triangle is the *AFM* cantilever.

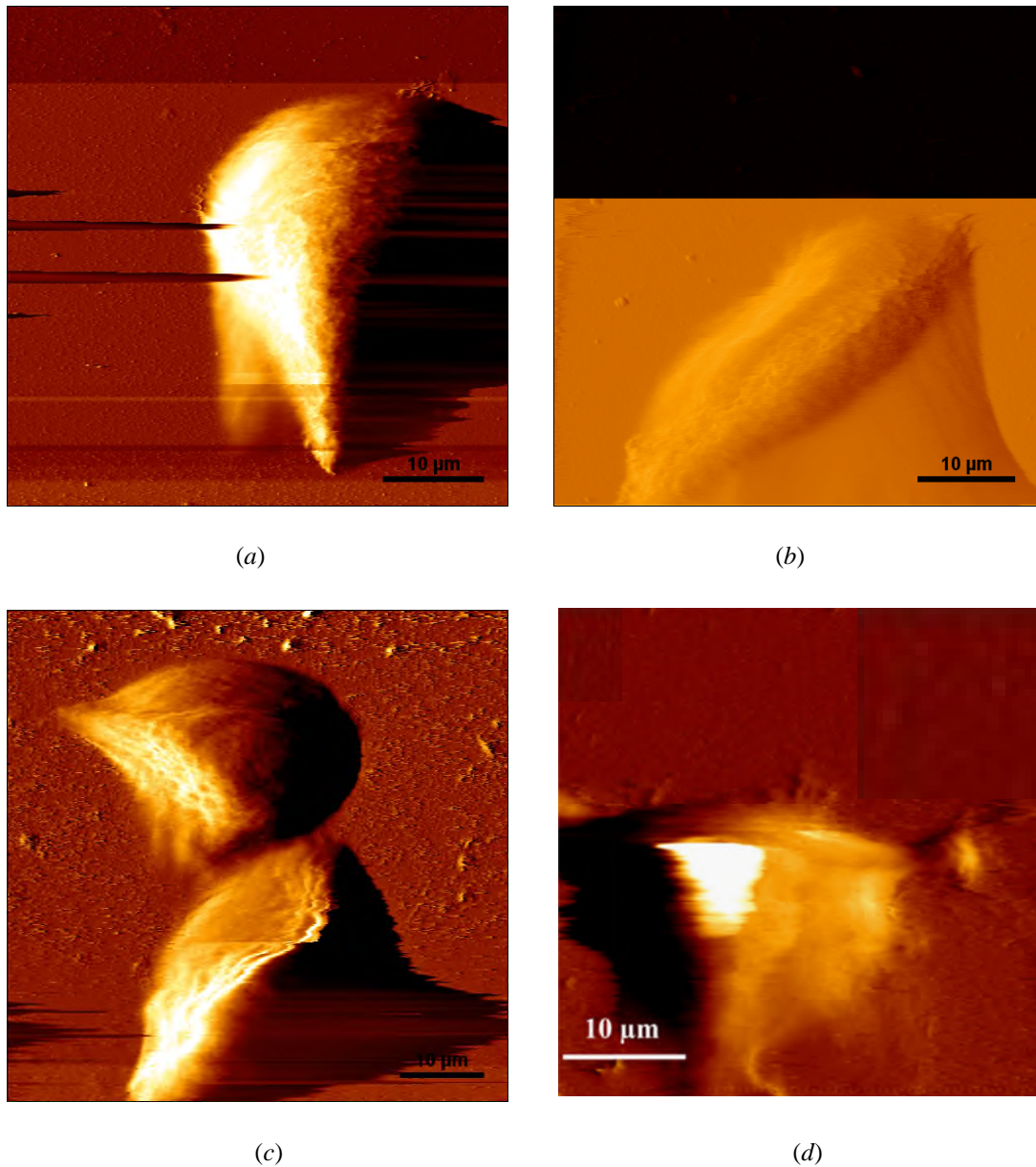
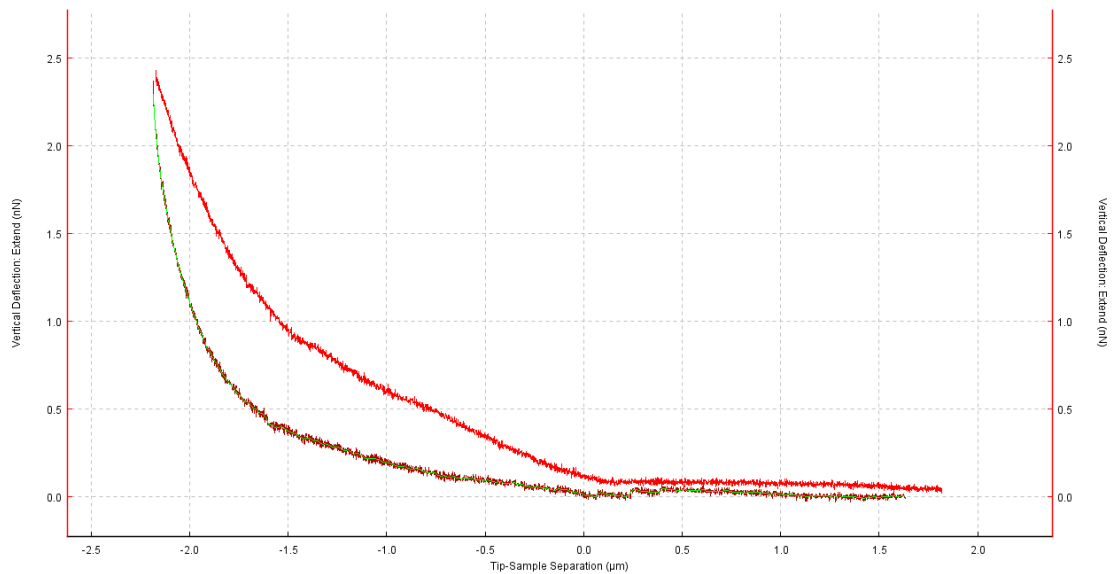


Fig 7.8 AFM deflection imaging of (a) control cells, cells exposed to fullereneol for (b) 24 hours, (c) 48 hours and (d) 72hours.

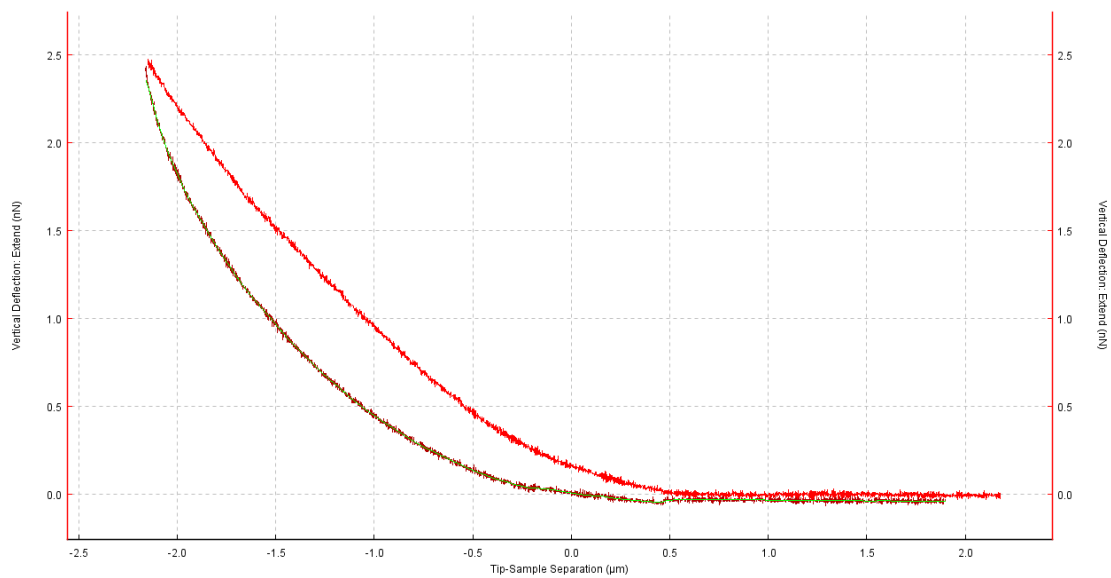
Fig 7.6 presents the result of force-displacement curves for the four types of SMCC-7721 cells after the above mentioned treatments. The maximum indentation force is approximately 2500 pN regardless of type of the cells, while the maximum indentation depth varies from cell to cell, and it is estimated that the maximum indentation depth ranges from 1 to 2 μm. For the cell C and D, adhesion force is characterized by the negative force region

during retraction of AFM indenter, as illustrated by the red line in Fig 7.6 (c) and (d). However, adhesion force is not noticeable for cell A and B during retraction as shown in Fig 7.6 (a) and (b).

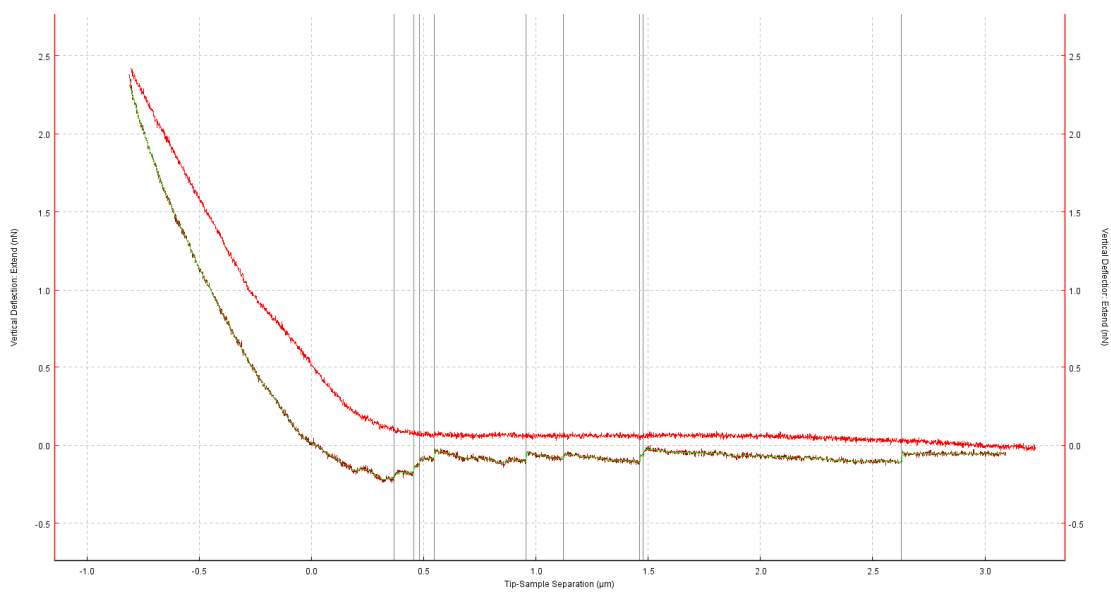
Fig 7.7 shows the optical morphological imaging the living SMCC-7721 cells. It indicates that the cells were cultured in monolayers and organized in low proximity between each other. Fig 7.8 shows the AFM vertical deflection imaging of living SMCC-7721 cells. From the scale bar, one may predict the diameter of the cell may ranges from 20 to 30 μm , and hence the indentation depth is less than 10% of the cell height so that the substrate effect could be excluded.



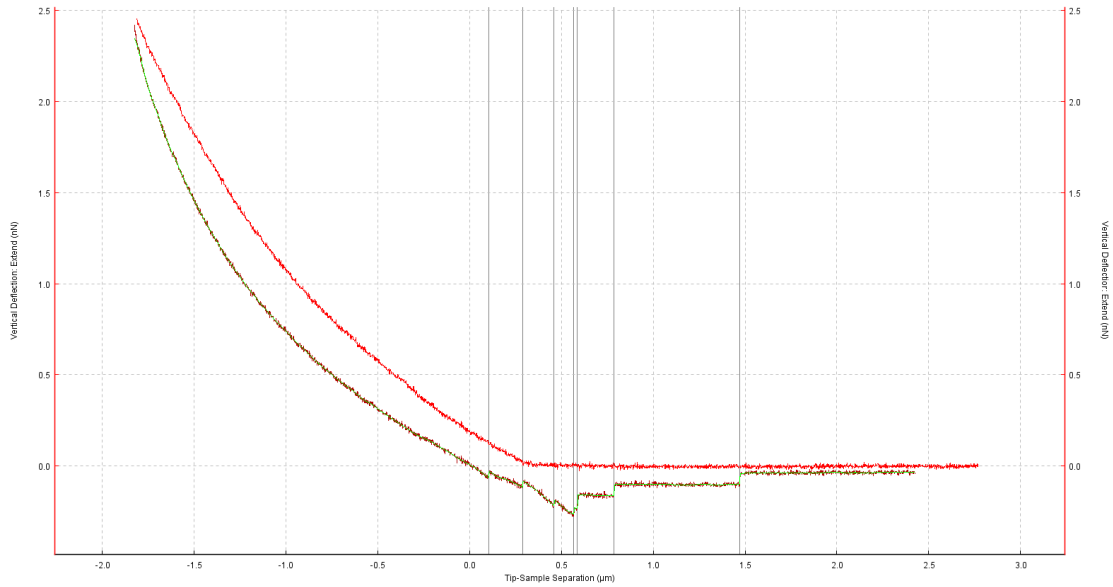
(a)



(b)




(c)



(d)

Fig 7.9 Tether rupture events during unloading stage for (a) control cells, cells exposed to fullereneol for (b) 24 hours, (c) 48 hours and (d) 72hours. The vertical solid line indicates the unbinding event.

As mentioned in Fig 1.2, the adhesion force is manifested by the stepwise jump events (also shown by Fig 7.9 (c) and (d)), which implies ductile unbinding. In addition, the type of force curves that show steps are adhesion curves from cell binding events. The usual interpretation for these steps is membrane tethers pulled out from the cell surface as discussed in last chapter. Therefore, we use the function of step fitting  to investigate the unbinding events in the retraction process of the force-displacement curve. The unbinding events are characterized by the displacement plateaus corresponding to a fairly constant force. With the same fit parameters, significant unbinding events are observed for cell C and D as shown in Fig 7.9(c) and (d), while unbinding events are inconspicuous for cell A and B as shown in Fig 7.9(a) and (b). This observation result is consistent with foregoing conclusion that adhesion mainly occurs in retraction part of force-displacement curve of cell C and D.

7.4.3 Control cells and cells exposed to fulleranol for 24 hours (Non-adhesion case)

Since adhesion phenomenon is insignificant in cell *A* and *B*, the non-adhesive Hertz contact model (Eq. (7.10)) is adopted to fit the retraction part of the force-displacement curve corresponding to cell *A* and *B*. To calculate elastic modulus, the JPK data processing software itself offers a function called Elasticity fit which is based on Hertz contact model as shown by Fig 7.10. The Hertz model can fit most part of the retraction curve except the place where the indenter detaches the cell, as circled in Fig 7.10.

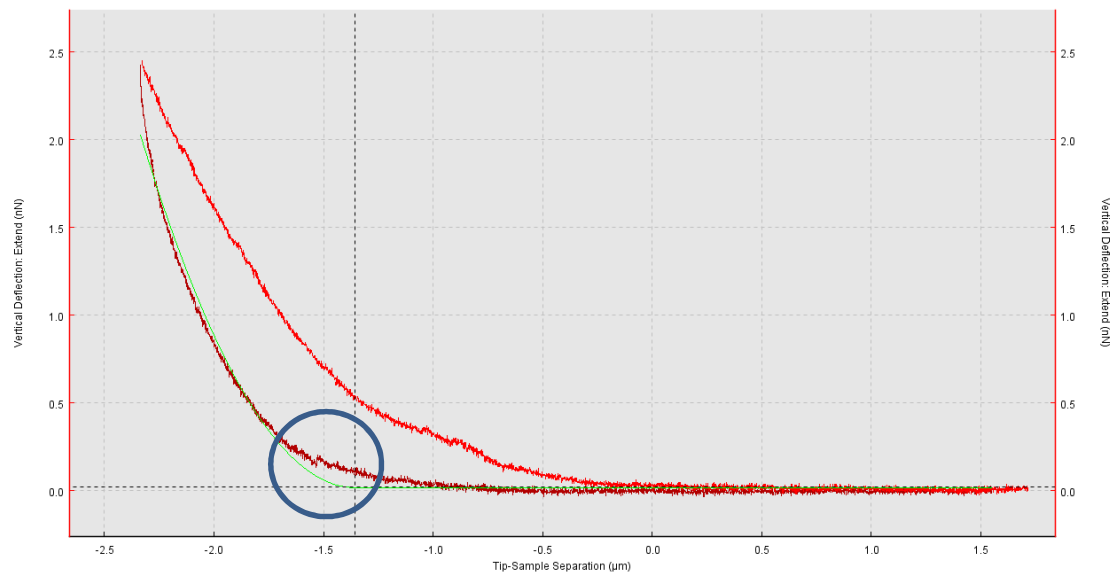


Fig 7.10 The retraction part of $F-d$ curve obtained from cell *A* and *B* is fitted by Hertz model.

Table 7.1 Young's modulus from cell *A2* (Unit: kPa)

location	1st	2nd	3rd	4th	Average	Std
1	2.697	2.403	2.171	2.096	2.34	0.27
2	2.033	2.113	2.253	2.179	2.14	0.094
3	2.146	2.82	2.565	2.389	2.48	0.284
4	2.401	2.024	2.321	2.512	2.31	0.209
5	2.568	2.356	2.86	2.028	2.45	0.351

Table 7.2 Young's modulus from cell *B1* (Unit: kPa)

location	1st	2nd	3rd	4th	Average	Std
1	1.76	1.811	1.879	1.109	1.64	0.36
2	1.332	1.562	1.663	1.531	1.5	0.14
3	1.699	1.773	1.715	1.82	1.75	0.056
4	1.831	1.923	2.234	2.324	2.08	0.24
5	1.985	2.099	2.065	1.887	2.01	0.094

Tables 7.1 and 7.2 give the extracted Young's modulus at five different positions within the same cell. Four indentations were repeated in every position. It can be seen that the determined Young's modulus values from different positions within the same cell remain steady. The calculated Young's modulus values for all cells are shown in Fig 7.11. Each individual bar represents one cell, expressed as average \pm standard deviation. It is noted that the determined Young's modulus varies from one cell to another. For cell *A*, the Young's modulus mainly ranges from 2 to 3.1 kPa, and only Young's modulus values of cell *A1* and *A6* are beyond this range by a considerable margin. For cell *B*, most Young's modulus ranges from 1 to 2 kPa or even lower, and only Young's modulus values of *B3*, *B8* and *B12* are beyond this range. Fig 7.12 shows the overall result for the control cells and the cells treated for 24 hours. The data indicate that fullereneol decreased the elastic modulus by 43% after 24 hour treatment, suggesting that cells treated with fullereneol become considerably compliant.

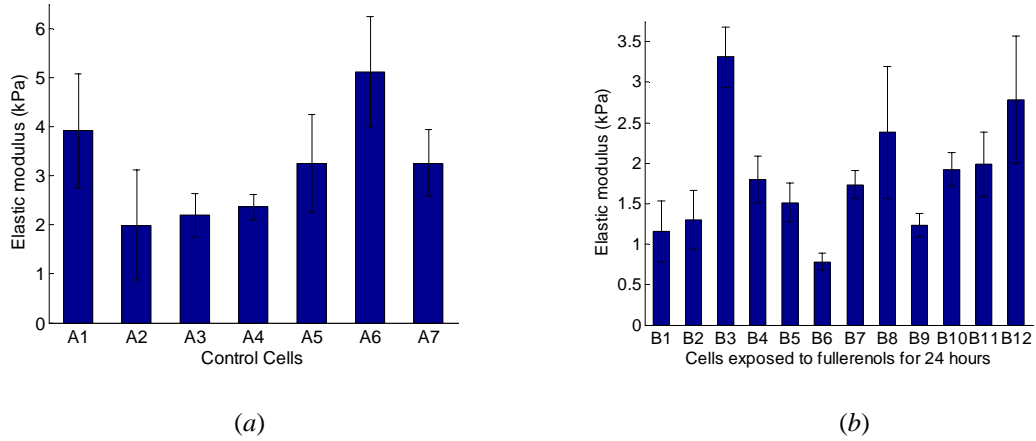


Fig 7.11 The determined Young's modulus for (a) control cell and (b) cells exposed to fullerenols for 24 hours. The data are presented as average values with standard deviations.

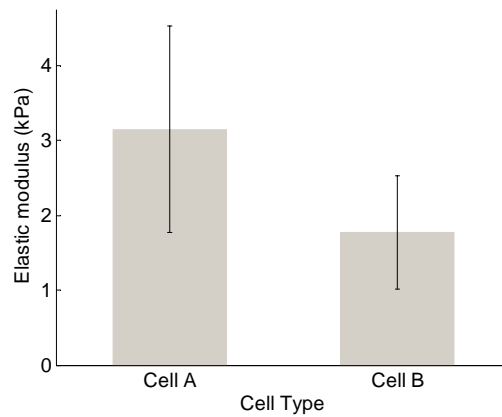
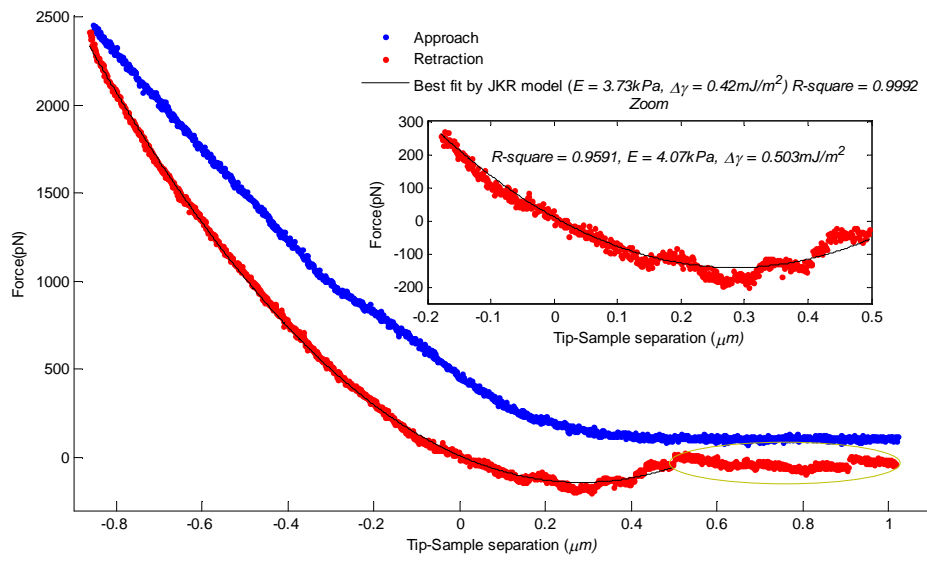
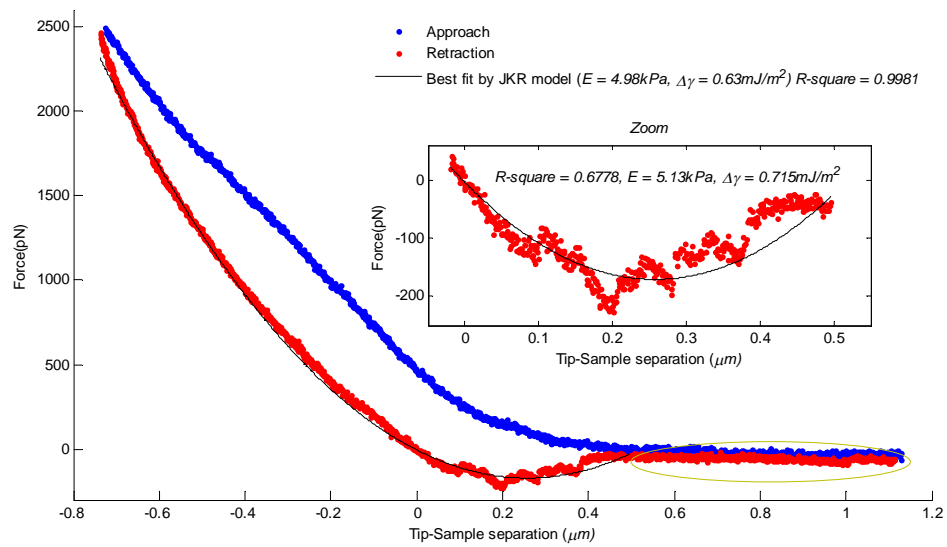


Fig 7.12 The comparison of determined Young's modulus between cell A and B.

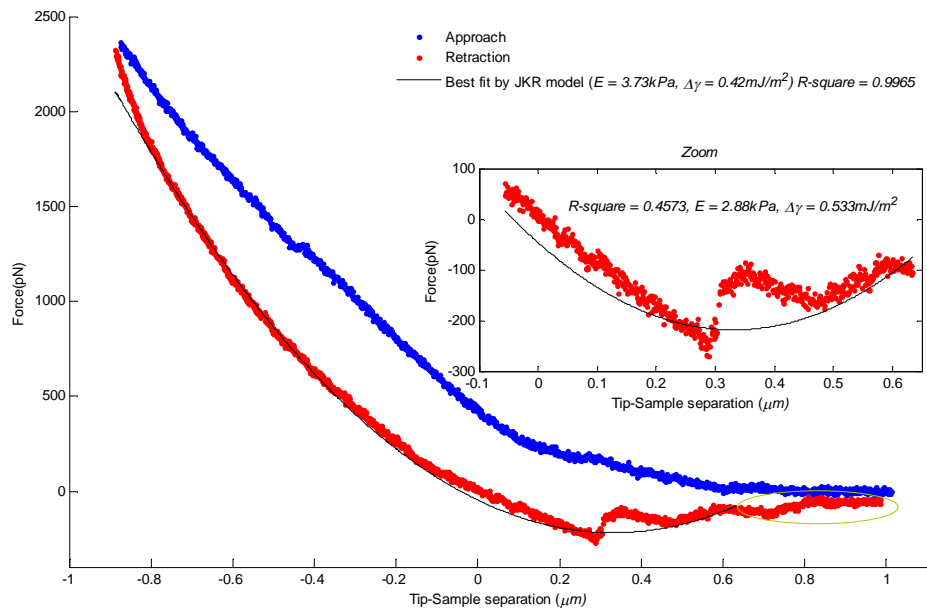
7.4.4 Cells exposed to fullereneol for 48 and 72 hours (Adhesion case)



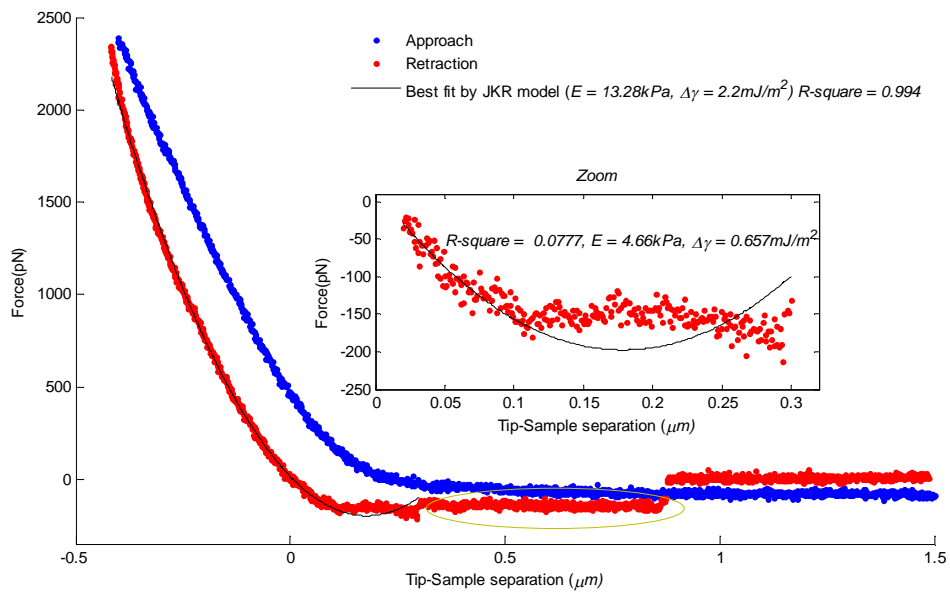
(a)



(b)



(c)



(d)

Fig 7.13 Typical force-displacement curves and the best fitting curves by using JKR model. The zoom box denotes the “local fitting”.

Fig 7.13 presents typical results of the force-displacement curves obtained by AFM

indentation on cells *C* and *D*, and the best fitting curves by using JKR model for the retraction parts. Sudden jumps of indentation force occur during retraction process, which is characterized by the “wave” as shown in the zoom box area. These sudden variations of the force can be ascribed to discontinuous decrease of the contact area between the tip and cell membrane. This is due to one tethering of cell membrane to AFM tip surface followed by a sudden detachment and tethering to another contact line^[151], as shown by Fig 7.14. Since fitting of F - d curve with discontinuous steps will cause error in the estimation of work of adhesion, the last section of F - d curve corresponding to considerable discontinuous adhesive force, as indicated by oval circle in Fig 7.13, were discarded from fitting^[151]. Moreover, if the curve itself consists of significant and abrupt force discontinuity, it will be discarded for numeral statistics too, as shown by Fig 7.15 as an example. In general, the JKR model can best describe the experimental results of the unloading curve as shown above.

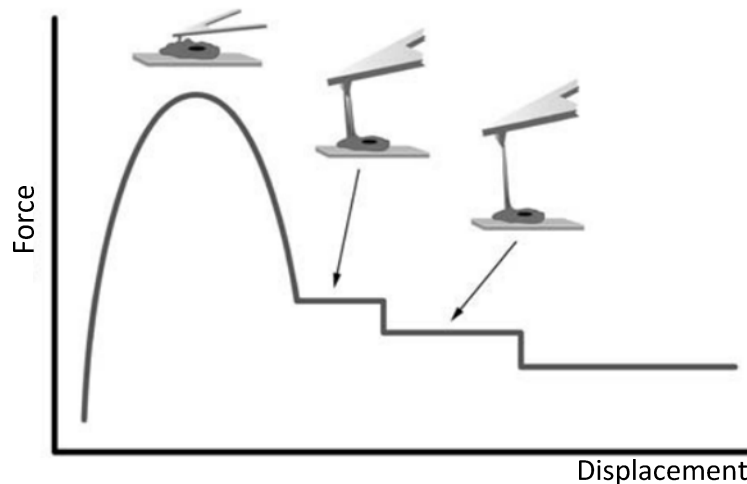


Fig 7.14 Scheme of cyclic tethering and detachment during unloading¹⁶¹.

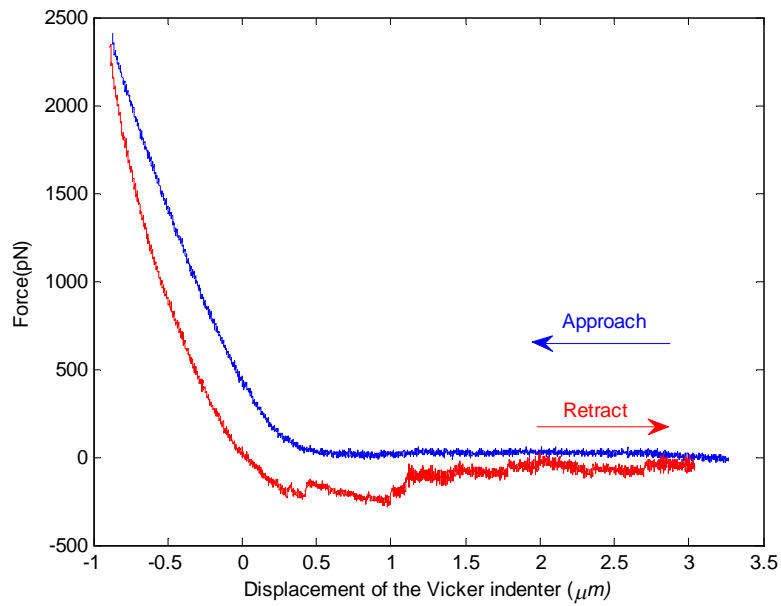


Fig 7.15 $F-d$ curve with considerable force discontinuity during the retraction fraction was discarded for statistics

This chapter explores two ways of fitting the unloading part of $F-d$ curve as detailed below. The first way is fitting from beginning of retraction to the place where the indentation force exhibits severe discontinuities as shown by the big plot in Fig 7.13, which is termed “global fitting”. The second method is fitting the fraction of $F-d$ curve from the point where indentation force decreases to null to where force is significantly discontinuous (this “swale” area corresponds to low indentation depth), as shown by the zoom box area in Fig 7.13, which is termed “local fitting”. The R -square value in the zoom box corresponds to the fit goodness when the extracted parameters produced by “global fitting” are used to describe the “swale” area. It is suggested that when the R -square value in the zoom box is around 0.5 or even higher, there are no significant difference between the fitting results by the two approaches as illustrated by Fig 7.13 (a)-(c). However, when this value is fairly small, significant variation of extracted parameters is observed between the two methods as shown by Fig 7.13(d).

Therefore, it can be concluded that in this “swale” area, adhesion force plays a dominant role for fitting result and has a considerable effect on the extracted parameters.

Table 7.3 Extracted parameters from one cell C2

time	1 st	2nd	3rd	4th	Average	Std
Point	E (kPa)	E (kPa)	E (kPa)	E (kPa)	(kPa)	(kPa)
1	2.99	3.12	2.99	3.64	3.19	0.31
2	3.74	4.05	4.38	-	4.06	0.32
3	2.8	3.74	3.53	-	3.36	0.49
4	3.64	4.99	4.73	-	4.45	0.72
5	2.2	2.33	2.99	2.88	2.6	0.39
time	1 st	2nd	3rd	4th	Average	Std
Point	$\Delta\gamma$ (mJ/m ²)	$\Delta\gamma$ (mJ/m ²)	$\Delta\gamma$ (mJ/m ²)	$\Delta\gamma$ (mJ/m ²)	(mJ/m ²)	(mJ/m ²)
1	0.789	0.592	1	0.48	0.715	0.229
2	1	0.758	0.572	-	0.777	0.215
3	0.744	0.699	0.796	-	0.746	0.049
4	0.733	0.789	0.655	-	0.726	0.067
5	0.558	0.423	0.482	0.556	0.505	0.065

Table 7.4 Extracted parameters from one cell D2

time	1st	2nd	3rd	4th	Average	Std
Point	E (kPa)	E (kPa)	E (kPa)	E (kPa)	(kPa)	(kPa)
1	1.15	1.11	0.925	0.84	1.01	0.15
2	1.01	0.92	1.09	1.16	1.05	0.10
3	1.08	0.96	1.05	0.97	1.02	0.06
4	0.93	0.97	0.83	0.98	0.93	0.07
5	0.83	0.8	0.84	0.88	0.84	0.03
time	1st	2nd	3rd	4th	Average	Std
Point	$\Delta\gamma$ (mJ/m ²)	$\Delta\gamma$ (mJ/m ²)	$\Delta\gamma$ (mJ/m ²)	$\Delta\gamma$ (mJ/m ²)	(mJ/m ²)	(mJ/m ²)
1	0.234	0.252	0.339	0.275	0.275	0.046
2	0.305	0.227	0.358	0.244	0.284	0.06
3	0.338	0.319	0.345	0.267	0.317	0.035
4	0.199	0.361	0.308	0.148	0.254	0.098
5	0.294	0.362	0.273	0.308	0.309	0.038

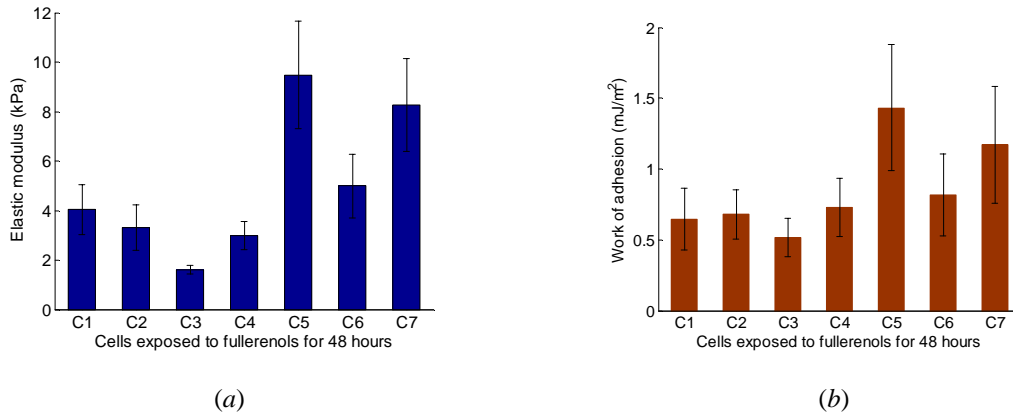


Fig 7.16 Histograms showing the determined (a) Young's modulus and (b) work of adhesion for each cell *C* subject.

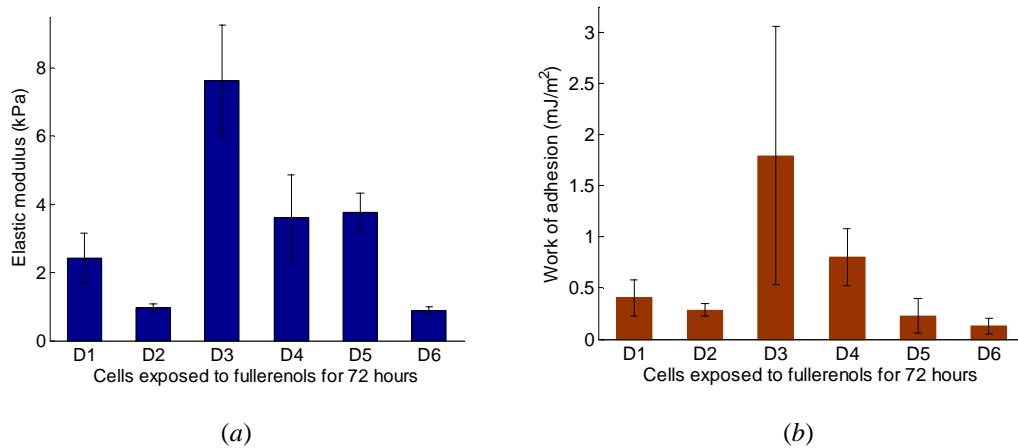


Fig 7.17 Results of the determined (a) Young's modulus and (b) work of adhesion for each cell *D* subject.

Tables 7.3 and 7.4 list the extracted Young's modulus and work of adhesion corresponding to one cell group (cell *C* or *D*) by the "global fitting" method. This indicates that these two parameters do not exhibit significant differences within one cell in adhesion circumstance. Likewise, one performed statistical analysis on $F-d$ curve corresponding to each cell, and the extracted Young's modulus and work of adhesion are shown in Fig 7.16 and Fig 7.17. The average value of the two parameters varies from one cell to another cell, and cells with larger

Young's modulus exhibits larger work of adhesion approximately. For cell *C*, the Young's modulus and work of adhesion mostly range between 3 to 5 kPa and 0.5 to 0.8 mJ/m², respectively. For cell *D*, the Young's modulus and work of adhesion mostly range between 1 to 4 kPa and 0.1 to 0.4 mJ/m², respectively. Fig 7.18 shows the statistics results (average value) taking all cells into consideration. For cell *C* Young's modulus and work of adhesion have an average of 4.88kPa and 0.825 mJ/m² respectively, while for cell *D* Young's modulus and work of adhesion have an average of 2.32kPa and 0.365 mJ/m² respectively. The determined value of work of adhesion in our procedure can almost coincide with the value in a former study^[151] in order of magnitude which in turn justifies this procedure. The difference between the heights of histograms suggests that both cell stiffness and adhesion effect is decreased by fullereneol treatment during the last 24 hours.

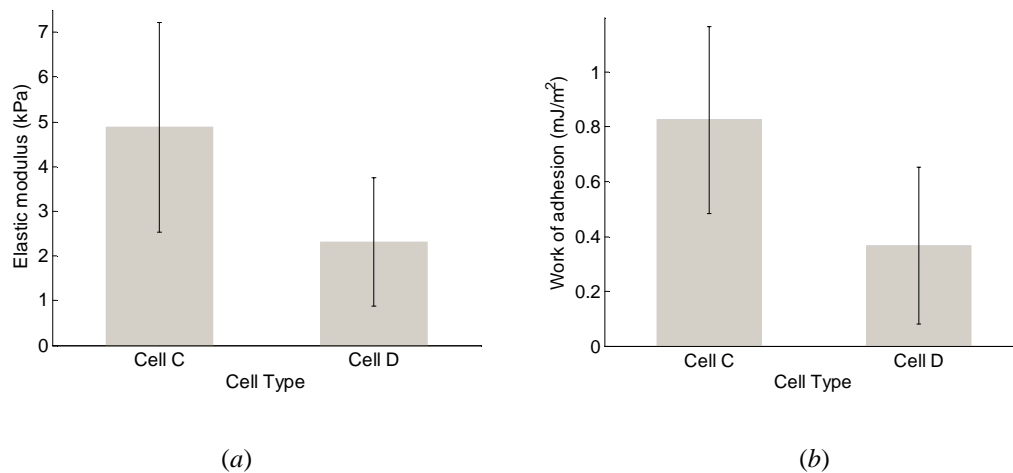


Fig 7.18 The comparison of determined (a) Young's modulus and (b) work of adhesion between cell *C* and *D*.

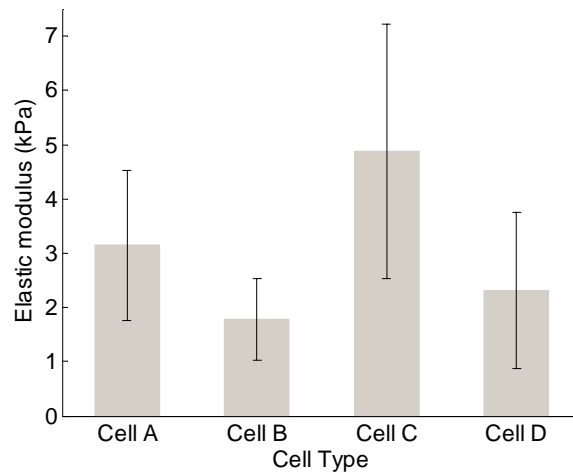


Fig 7.19 Results of Young's moduli of the four group cells by using the JKR model.

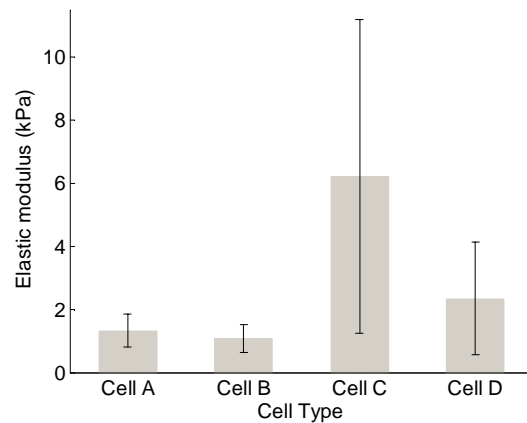


Fig 7.20 Results of Young's moduli of the four group cells, by using Hertzian contact model to fit the loading parts of $F-d$ curves.

Fig 7.19 is the combination of Fig 7.12 and Fig 7.18(a). The effect of duration of fullerenols treatment on extracted modulus seems different from that reported by a former study^[167]. In general, the Young's modulus is derived from the loading curve of the $F-d$ curves by Hertzian contact model. In order to make a comparison, we have tried to apply the Hertzian contact model to fit the loading part of the $F-d$ curves of the four groups of cells. The results (average \pm std) are plotted in Fig 7.20. It can be seen that the pattern of the calculated Young's

modulus values of the four group cells are almost the same as that in Fig 7.19. Therefore, the difference is more likely due to the variation of different batch of cells and the fullerenols treatment.

7.5 Summary

In this chapter, AFM was employed to investigate the adhesion between the *AFM* indenter and the cells treated by fullerenol with different durations. *F-d* curves corresponding to cell *A* and *B* were fitted by Hertz contact model because most of the curves do not exhibit significant adhesion force. On the other hand, there are adhesion force in the *F-d* curves corresponding to cells *C* and *D*, and hence JKR model was employed for fitting those data accordingly. The summary is listed as follows:

- The results show that both Hertz and *JKR* contact model can describe very well the behavior of retraction curves.
- In non-adhesion case, fitting by Hertz model indicates 24 hours treatment of fullerenol may make the treated cells more compliant.
- In adhesion case, “global” fitting by the JKR model suggested both stiffness and adhesion of the treated cells were decreased by a large margin during the last 24 hours treatment of fullerenol.
- The results suggest that the experimental study of cell-tip adhesion may also provide some insights into potential cancer progression in addition to cell stiffness.

8 Conclusions and Future work

8.1 Research Highlights and Conclusions

In this work, a sufficient analysis of surface adhesion in nanoindentation is made from two main aspects, i.e.

- Effect of surface adhesion on shakedown behavior of repetitive microcontact of elastoplastic materials (hard materials).
- Quantitative characterization of surface adhesion in on soft materials subjected to AFM indentation, i.e. biological cells, and its potential application in biomedical diagnostics.

First, an intrinsic physical mechanism accounting for surface adhesion was introduced, and interaction forces between different geometrical bodies were formulated. Several classic adhesive contact models based on contact mechanics were discussed in terms of their characteristics, among which JKR model, DMT model and M-D model were emphasized. The application fields of these adhesive contact models were schematically interpreted. Since surface adhesion is somehow brought up by nanoindentation, nanoindentation, viewed as “carrier” for surface adhesion, was conducted. Based on relevant theoretical models, several mechanical properties of materials were quantitatively investigated, and compared with their typical values for justification. It is worth noting that although nanoindentation is not the focus of this work, it plays as a role of breeding ground for surface adhesion, and thus a routine experimental review of nanoindentation was of significant importance. Following this, the effect of surface adhesion was manifested in repetitive microcontact of elastoplastic

materials (hard materials) in terms of shakedown behavior. A finite element method was employed to simulate surface adhesion force which obeys Lennard-Jones potential and was incorporated into ANSYS as a user defined subroutine. Finally, this work provides a method to quantitatively characterize surface adhesion of soft materials in terms of a new parameter, i.e. work of adhesion. The soft materials include two types of biological living cells, i.e. pancreatic MIN6 cell and human hepatocellular carcinoma together with their medicine treated counterparts. MIN6 cells were treated by +R568 for 48 hours, while hepatocellular carcinoma were treated by fulleranol for 24, 48 and 72 hours (marked as Cell B, Cell C and Cell D, respectively). AFM indentation was performed to quantify the mechanical behavior of biological cells, i.e. force-displacement curve. For MIN6 cells, the AFM tip indenter is a polystyrene sphere, while the cancer cells were indented by a Vickers indenter. JKR contact model, as expert for adhesion circumstance of soft materials, was used to fit the obtained force-displacement curves, resulting in the above mentioned new parameter besides elastic modulus. For MIN6 cell, the original JKR model, its “generalized” form (i.e. with consideration of cell thickness) and finite element simulation were used for fitting the retraction part of $F-d$ curve. For the cancer cell, the original JKR model was modified to adapt itself for Vickers indenter, and this adapted JKR model was utilized for fitting. Hertz model was fitted to the retraction part of $F-d$ curves of control cell and Cell B while the adapted JKR model was fitted to the unloading part of $F-d$ curves of Cell C and Cell D. On the other hand, the loading part of $F-d$ curves of these four type cells were fitted by Hertz model. The difference between the above mentioned biological cells and their medicine treated counterparts were verified in terms of magnitude of this new parameter and together with

Young's modulus. Towards the objectives presented in Chapter 1, conclusions are made as follows.

In terms of the first issue, the following conclusions are established:

- i. FEM can simulate instability jumps in adhesive contact. The jump in and jump off phenomena are manifested by vertical $F-d$ lines which resemble to "brittle" jump.
- ii. In adhesive contact, the indentation depth of rigid indenter corresponding to first yield of substrate material is lower than its non-adhesive counterpart, regardless of the strain hardening manner (i.e. whether isotropic hardening or kinematic hardening). For a larger plasticity parameter S , first yield strain can be observed at the contact periphery even before the two materials contact with each other which can never occur in its non-adhesive counterpart. This means that surface adhesion force alone can alter the mechanical response of substrate material subjected to indentation, in terms of plasticity.
- iii. In terms of cyclic loading-unloading of non-adhesive contact, regardless of strain hardening manner (i.e. whether isotropic hardening or kinematic hardening), plastic deformation can only occur during the first loading half of the first cycle, followed by elastic deformation in subsequent cycles, i.e. the indenter-substrate system shakes down to wholly elastic behavior. However, with the presence of surface adhesion force, by adjusting relevant governing parameters appropriately, closed-cycle plasticity could be observed not only in the first cycle but also in subsequent cycles (i.e. plastic shakedown), regardless of strain hardening manner of substrate materials. Moreover, kinematic hardening material shakes down to plastic behavior more quickly than its isotropic hardening counterpart. By comparing to the non-adhesive circumstance, this

phenomenon means the occurrence of plastic shakedown is due to surface adhesion force. Since structures exhibiting plastic shakedown will fail after a finite number of load cycles due to low-cycle fatigue, it is of guiding significance for future work to consider surface adhesion force in contact.

In terms of the second issue, the following conclusions may be drawn:

- i. Surface adhesion force manifests itself by the negative force monitored in force-displacement curve of biological cells subjected to AFM indentation. When the AFM tip probe detaches the cell, stepwise jumps were observed due to adhesion forces. Because the separation is continuous, it resembles “ductile” separation.
- ii. For MIN6 cells, the fitting curve by JKR model coincided well with the retraction part of $F-d$ curve, except some discontinuity part. The discontinuity part consists of many stepwise jumps, which is due to sudden detachment, and thus it is inappropriate to let this part join in the fitting process. The resulted elastic modulus and work of adhesion agreed with that reported by former studies in order of magnitude. Although the values of these two parameters calculated by original JKR model were higher in comparison to “generalized” JKR model fitting, the tendency of these two parameters between control and treated cells was the same, i.e. Young’s moduli of treated cells were lower than their control counterparts, while work of adhesion of the latter cells was higher than that of former cells.
- iii. For hepatocellular carcinoma, surface adhesion was insignificant in control cell and Cell B but significant in Cell C and Cell D, in terms of negative force monitored in $F-d$ curve.

The stepwise jumps were also observed in Cell C and Cell D, but not significant in control cell and Cell B. The adapted JKR model proved to fit well with the unloading part of $F-d$ curves corresponding to Cell C and Cell D, except some discontinuity segments which was analyzed by analogy to ii. The extracted elastic moduli and work of adhesion were also in their normal range reported by previous studies. A considerable difference was observed between different types of cells in terms of elastic moduli and work of adhesion.

8.2 Future work

In terms of the objectives in this work, future work can be summarized as follows:

- i. The elastoplastic material in this work is homogeneous. Since inhomogeneous materials have been emerging as function-aimed materials, more detailed work is required to achieve a good understanding of shakedown behavior of inhomogeneous materials subjected to repetitive adhesive contact. Functionally graded materials and laminated materials are two common inhomogeneous materials, and there are already some studies focusing on the adhesive contact of these materials which are the footstone of future work.
- ii. This work mainly focuses on the effect of surface adhesion on normal contact. However, in practice, miniaturized devices are subjected to a complicated situation, e.g. both normal and tangential relative movements. Therefore, it is essential to consider the effect of surface adhesion on the tangential behavior. In other words, friction and stiction would be affected by surface adhesion.

- iii. The cell is treated as homogeneous in this work, whereas inhomogeneity prevails with in cell which consists of cytoplasm, cytomembrane and cell nucleus. Hence it is appropriate to develop a more realistic model which takes cell inhomogeneity into consideration. On the other hand, although this work considers the shape diversity of cell, i.e. regarding the cell as a plate with finite thickness, it still conforms to homogeneity assumption. In this regard, it is advisable to treat the plate as laminated materials.
- iv. The JKR model was adopted to fit the force-displacement curve which implies the interaction force between AFM probe surface and cytomembrane is a short range force. However, in practice this interaction force may take a more complicated form, and there is a need to provide a more accurate simulation in terms of interaction force.

Reference

- [¹] Butt, H., Cappella, B., Kappl, M., 2005. Force measurements with the atomic force microscope: technique, interpretation and applications. *Surface Science Report*. 59, 1–152.
- [²] Jalili, N., Laxminarayana, K., 2004. A review of atomic force microscopy imaging systems: Application to molecular metrology and biological sciences. *Mechatronics*. 14, 907–945.
- [³] Garcia, R., R. Perez, R., 2002. Dynamic atomic force microscopy methods. *Surface Science Report*. 47, 197–301.
- [⁴] Wikipedia, https://simple.wikipedia.org/wiki/Atomic_force_microscope
- [⁵] Costa, K.D., 2003. Single-cell elastography: Probing for disease with the atomic force microscope. *Disease Markers*. 19, 139–154.
- [⁶] Jena, B.P., Horber, J.H.K, 2002. Atomic Force Microscopy in Cell Biology. In *Methods in Cell Biology* Volume 68. Academic Press. pp. 67
- [⁷] Lekka, M., Laidler, P., Gil, D., Lekki, J., Stachura, Z., Hryniewicz, A.Z., 1999. Elasticity of normal and cancerous human bladder cells studied by scanning force microscopy. *European Biophysics Journal*. 28 (4), 312–316.
- [⁸] Lekka, M., Laidler, P., Ignacak, J., Labeledz, M., Lekki, J., Struszczyk, H., Stachura, Z., Hryniewicz, A.Z., 2001. The effect of chitosan on stiffness and glycolytic activity of human bladder cells. *Biochimica et Biophysica Acta (BBA)–Molecular Cell Research*. 1540 (2), 127–136.
- [⁹] Mukherjee, S., Ghosh, R.N., Maxfield, F.R., 1997. Endocytic Sorting of Lipid Analogues Differing Solely in the Chemistry of Their Hydrophobic Tails. *The Journal of Cell Biology*. 144, 1271–1284.
- [¹⁰] Peppas, N.A., Langer, R., 1994. New challenges in biomaterials. *Science* 263, 1715–1720.
- [¹¹] Saltzman, W.M., 2001. *Drug Delivery: Engineering Principles for Drug Therapy*. Oxford University Press, Oxford.

- [12] Cho, S.-S., Park, S., 2004. Finite element modeling of adhesive contact using molecular potential. *Tribology International*. 37, 763–769.
- [13] Zhao, Y.P., Wang, L.S., Yu, T.X., 2003. Mechanics of adhesion in MEMS—a review. *Journal of Adhesion Science and Technology*. 17 (4), 519–546.
- [14] Tambe, N.S., Bhushan, B., 2004. Scale dependence of micro/nano-friction and adhesion of MEMS/NEMS materials, coatings and lubricants. *Nanotechnology*. 15, 1561–1570.
- [15] Muller, D.J., Helenius, J., Alsteens, D. D., Nat, Y.F., 2009. Force probing surfaces of living cells to molecular resolution. *Nature Chemical Biology*. 5, 383–390.
- [16] Leite, F. L., Bueno, C. C., Ziemath, E. C., Oliveira, O. N., 2012. Theoretical models for surface forces and adhesion and their measurement using atomic force microscopy. *International Journal of Molecular Sciences*. 13(10), 12773–12856.
- [17] Siamantouras, E., Hills, C.E., Squires, P.E., Liu, K.K., 2015. Nanomechanical Investigation of Soft Biological Cell Adhesion using Atomic Force Microscopy. *Cellular and Molecular Bioengineerin*. 8 (1), 22–31.
- [18] Maugis, D., Pollock, H., 1984. Surface forces, deformation, and adherence. *Acta Metallurgica*. 32 (9), 1323–1334.
- [19] Hertz, H., 1881. Über die Berührung fester elastischer Körper. *Journal für die reine und angewandte Mathematik*. 92, 156–171.
- [20] Bradley, R.S., 1932. The cohesive force between solid surface and the surface energy of solids. *The London, Edinburgh, and Dublin Philosophical Magazine and Journal of Science: Series 7*. 13, 853–862.
- [21] Johnson, K.L., Kendall, K., Roberts, A.D., 1971. Surface energy and the contact of elastic solids. *Proceedings of the Royal Society of London A*. 324, 301–313.
- [22] Derjaguin, B.V., Muller, V.M., Toporov, Y.P., 1975. Effect of contact deformations on the adhesion of particle. *Journal of Colloid and Interface Science*. 53, 314–326.
- [23] Maugis, D., 1992. Adhesion of spheres: the JKR-DMT transition using Dugdale model.

Journal of Colloid and Interface Science. 150, 243–269.

- [24] Israelachvili, J.N., 1992. Intermolecular and Surface Forces, second ed., Academic Press, San Diego, CA.
- [25] Shull, K.R., Ahn, D., Chen, W.L., Flanigan, C.M., Crosby, A.J., 1998. Axisymmetric adhesion tests of soft materials. *Macromolecular Chemistry and Physics*. 199, 2769–2784.
- [26] Shull, K.R., 2002. Contact mechanics and the adhesion of soft solids. *Materials Science and Engineering: R: Reports*. 36 (1), 1–45.
- [27] Brinell, J. A., 1900. Ein Verfahren zur Härtebestimmung nebst einigen Anwendungen desselben. *Baumaterialienkunde*. 5, 276–80, 294–97, 317–20, 364–67, 392–94, 412–16.
- [28] Meyer, E., 1908. Investigations of hardness testing and hardness. *Physikalische Zeitschrift*. 9, 66–74.
- [29] Shore, A. F., 1910. The scleroscope. Proceedings of the American Society for Testing. *Materials*. 10, 490–517.
- [30] Howe, H. M., Levy, A. G., 1916. Notes on the Shore scleroscope test. *Proceedings of the American Society for Testing Materials*. 16, 36–52.
- [31] Rockwell, H. M., Rockwell, S. P., 1919, Hardness tester. US Patent 1,294,171.
- [32] Rockwell, S. P., 1924. Hardness testing machine. US Patent 1,516,207.
- [33] Smith, R. L., Sandland, G. E., 1925. Some notes on the use of a diamond pyramid for hardness testing. *Journal of the Iron and Steel Institute*. 111, 285–304.
- [34] Knoop, F., Peters, C. G., Emerson, W. B., 1939. A sensitive pyramidal diamond tool for indentation measurements. *Journal of Research of the National Bureau of Standards*. 23, 39–61.
- [35] Berkovich, E. S., 1951. Three-faceted diamond pyramid for microhardness testing. *Industrial Diamond Review*. 11, 129–132.
- [36] Newey, D., Wilkins, M. A., Pollock, H. M., 1982. An ultra-low-load penetration hardness tester. *Journal of Physics E: Scientific Instruments*. 15, 119–122.

- [37] Hardness Conversion. Gordon England 2008 [cited; Available from: http://www.gordonengland.co.uk/hardness/hardness_conversion_1c.htm.
- [38] Mott, B.W., 1956. Micro-indentation hardness testing. London: Butterworth's Scientific Publications.
- [39] Wheeler, J.M., 2009. Nanoindentation under Dynamic Conditions, in Department of Materials Science and Metallurgy. *University of Cambridge*: Cambridge.
- [40] Oliver, W.C., Pharr, G.M., 1992. An Improved Technique for Determining Hardness and Elastic Modulus Using Load and Displacement Sensing Indentation Experiments. *Journal of Materials Research*. 7(6), 1564–1583.
- [41] Nili, H., Kalantar-zadeh, K., Bhaskaran, M., Sriram, S., 2013. In situ nanoindentation: probing nanoscale multifunctionality. *Progress in Materials Science*. 58, 1–29.
- [42] Oliver, W.C., Pharr, G.M., 2004. Measurement of hardness and elastic modulus by instrumented indentation: Advances in understanding and refinements to methodology. *Journal of Materials Research*. 19, 3–20.
- [43] Fischer-Cripps, A.C., 2001. Simulation of sub-micron indentation tests with spherical and Berkovich indenters. *Journal of Materials Research*. 16(7), 2149–2157.
- [44] Barber, J.R., Billings, D.A., 1990. An approximation solution for the contact area and elastic compliance of a smooth punch of arbitrary shape. *International Journal of Mechanical Sciences*. 32 (12), 991–997.
- [45] Bilodeau, G.G., 1992. Regular pyramid punch problem. *Journal of Applied Mechanics*. 59, 519–523.
- [46] Bolshakov, A., Pharr, G.M., 1998. Influences of pileup on the measurement of mechanical properties by load and depth sensing indentation. *Journal of Materials Research*. 13(4), 1049–1058.
- [47] Liu, X.D., Bhushan, B., 2002. A review of nanoindentation continuous stiffness measurement technique and its applications. *Materials Characterization*. 48, 11–36.

- [48] Pharr, G.M., 1998. Measurement of mechanical properties by ultra-low load indentation. *Materials Science and Engineering: A*. 253, 151–159.
- [49] Sakai, M., 1993. Energy principle of the indentation-induced inelastic surface deformation and hardness of brittle materials. *Acta Metallurgica et Materialia*. 41 (6), 1751–1758.
- [50] Field, J.S., Swain, M.V., 1993. A simple predictive model for spherical indentation. *Journal of Materials Research*. 8 (2), 297–306.
- [51] Fischer-Cripps, A. C., 2004. Nanoindentation. *Springer*, New York.
- [52] King, R.B., 1987. Elastic analysis of some punch problems for layered medium. *International Journal of Solids and Structures*. 23, 1657–1664.
- [53] Kim, M.T., 1996. Influence of substrates on the elastic reaction of films for microindentation tests. *Thin Solid Films*. 283, 12–16.
- [54] Yu, H.Y., Sanday, S.C., Rath, R.R., 1990. The effect of substrate on the elastic properties of films determined by the indentation test-axisymmetric Boussinesq problem. *Journal of Mechanics and Physics of Solids*. 38, 745–764.
- [55] Mencik, J., Munz, D., Quandt, E., Weppelmann, E.R., Swain, M.V., 1997. Determination of elastic modulus of thin layers using nanoindentation. *Journal of Materials Research*. 12 (9), 2475–2484.
- [56] Page, T.F., Pharr, G.M., Hay, J.C., Oliver, W.C., Lucas, B.N., Herbert, E., Riester, L., 1998. Nanoindentation characterization of coated systems: P/S^2 —a new approach using the continuous stiffness technique. *Materials Research Society Symposium Proceedings*. 522, 53–64.
- [57] Saha, R., Xue, Z.Y., Huang, Y., Nix, W., 2001. Indentation of a soft metal film on a hard substrate: strain gradient hardening effects. *Journal of the Mechanics and Physics of Solids*. 49 (9), 1997–2014.
- [58] Westbrook, J.H., Conrad, H., 1971. The science of hardness testing and its research applications. *American Society for Metals, Metals Park, Ohio*.
- [59] Cabibil, H., Celio, H., Lozano, J., White, J.M., Winter, R.M., 2001. Nanomechanical

- properties of polysiloxane-oxide interphases measured by interfacial force microscopy. *Langmuir*. 17, 2160–2166.
- [60] Fischer-Cripps, A.C., 2000. A review of analysis methods for sub-micro indentation testing. *Vacuum*. 58, 569–585.
- [61] Fisher-Cripps, A.C., 2000. Introduction to contact mechanics. *Springer*, Berlin.
- [62] Palmqvist, S., 1957. A method to determine the toughness of brittle materials, especially hard materials. *Jernkontorets Ann.* 141, 303–307.
- [63] Marshall, D.B., Lawn, B.R., 1979. Residual stress effects in sharp contact cracking. *Journal of Materials Science*. 14, 2001–2012.
- [64] Anstis, G.R., Chantikul, P., Lawn, B.R., Marshall, D.B., 1981. A critical evaluation of indentation techniques for measuring fracture toughness: I , direct crack measurements. *Journal of the American Ceramic Society*. 64 (9), 533–538.
- [65] Laugier, M.T., 1987. Palmqvist indentation toughness in WC-Co composites. *Journal of materials science letters*. 6, 897–900.
- [66] Dukino, R., Swain, M.V., 1992. Comparative measurement of indentation fracture toughness with Berkovich and Vickers indenters. *Journal of the American Ceramic Society*. 75 (12), 3299–3304.
- [67] Li, W.B., Warren, R., 1993. A model for nano-indentation creep. *Acta Metallurgica et Materialia*. 41 (10), 3065–3069.
- [68] Boussinesq, J., 1885. Application des potentiels a l'étude de l'équilibre et du mouvement des solides élastiques. *Gauthier-Villar*, Paris.
- [69] Lee, E.H., Radok, J.R.M., 1960. The contact problem for viscoelastic bodies. *Journal of Applied Mechanics*. 27, 438–444.
- [70] Ting, T.C.T., 1966. The contact stresses between a rigid indenter and a viscoelastic half-space. *Journal of Applied Mechanics*. 33, 845–854.
- [71] Greenwood, J.A., 2010. Contact between an axisymmetric indenter and a viscoelastic half-space. *International Journal of Mechanical Sciences*. 52, 829–835.

- [72] Shinohara, K., Yasuda, K., Yamada, M., Kinoshita, C., 1994. Universal method for evaluating work-hardening exponent of metals using ultra-microhardness tests. *Acta Metallurgica et Materialia*. 42 (11), 3909–3915.
- [73] Ahn, J.H., Kwon, D., 2001. Derivation of plastic stress-strain relationship from ball indentations: Examination of strain definition and pileup effect. *Journal of Materials Research*. 16 (11), 3170–3178.
- [74] Tabor, D., 1976. Surface forces and surfaces interactions. *Journal of Colloid and Interface Science*. 58, 2–23.
- [75] Greenwood, J.A., 1997. Adhesion of elastic spheres. *Proceedings: Mathematical, Physical and Engineering Sciences*. 453, 1277–1297.
- [76] Johnson, K.L., Greenwood, J.A., 1997. An adhesion map for the contact of elastic spheres. *Journal of Colloid and Interface Science*. 192, 326–333.
- [77] Carpick, R.W., Ogletree, D.F., Salmeron, M., 1999. A general equation for fitting contact area and friction vs load measurements. *Journal of Colloid and Interface Science*. 211,395–400.
- [78] Pietrement, O., Troyon, M., 2000. General equations describing elastic indentation depth and normal contact stiffness versus load. *Journal of Colloid and Interface Science*. 226, 166–171.
- [79] Greenwood, J.A., Johnson, K.L., 1998. An alternative to the Maugis model of adhesion between elastic spheres. *Journal of Physics D: Applied Physics*. 31, 3279–3290.
- [80] Shi, Xi., A.Polycarpou, A., 2005. Adhesive transition from noncontacting to contacting elastic spheres: extension of the Maugis–Dugdale model. *Journal of Colloid and Interface Science*. 281, 449–457.
- [81] Schwarz, U.D., 2003. A generalized analytical model for the elastic deformation of an adhesive contact between a sphere and a flat surface. *Journal of Colloid and Interface Science*. 261, 99–106.
- [82] Derjaguin, B.V., Muller, V.M., Toporov, Y. P., 1978. On the role of molecular forces in

contact deformations (critical remarks concerning Dr Tabor's report). *Journal of Colloid and Interface Science*. 67 (2), 378 – 379.

[83] Tabor, D., 1978. On the role of molecular forces in contact deformations (critical remarks concerning Dr Tabor's report). *Journal of Colloid and Interface Science*. 67 (2), 380–395.

[84] Derjaguin, B.V., Muller, V.M., Toporov, Y. P., 1980. On different approaches to the contact mechanics. *Journal of Colloid and Interface Science*. 73 (1), 293–302.

[85] Muller, V.M., Yushchenko, V.S., Derjaguin, B.V., 1980. On the influence of molecular forces on the deformation of an elastic sphere and its sticking to a rigid plane. *Journal of Colloid and Interface Science*. 77 (1), 91 – 101.

[86] Muller, V.M., Yushchenko, V.S., Derjaguin, B.V., 1983. General theoretical consideration of the influence of surface forces on contact deformations and the reciprocal adhesion of elastic spherical particles. *Journal of Colloid and Interface Science*. 92 (1), 92 – 101.

[87] Attard, P., Parker, J.L., 1992. Deformation and adhesion of elastic bodies in contact. *Physical Review A*. 46 (12), 7959 – 7971.

[88] Feng, J. Q., 2000. Contact behavior of spherical elastic particles: a computational study of particle adhesion and deformations. *Colloids and Surfaces A: Physicochemical and Engineering Aspects*. 172(1–3), 175–198.

[89] Radhakrishnan, H., Mesarovic, S.Dj., 2009. Adhesive contact of elastic spheres revisited: numerical models and scaling. *Proceedings of the Royal Society of London A*. 465, 2231–2249.

[90] Lin, Y.Y., Chen, H.Y., 2006. Effect of large deformation and material non-linearity on the JKR test of soft elastic materials. *Journal of Polymer Science Part B: Polymer Physics*. 44, 2912–2922.

[91] Jin, F., Guo, X., Gao, H., 2013. Adhesive contact on power-law graded elastic solids: the JKR–DMT transition using a double-Hertz model. *Journal of Mechanics and Physics of Solids*. 61(12), 2473–2492.

[92] Pashley, M.D., Pethica, J.B., Tabor, D., 1984. Adhesion and micromechanical properties of

- metal surfaces. *Wear*. 100, 7–31.
- [93] Chowdhury, R.S.K., Pollock, H.M., 1981. Adhesion between metal surfaces: The effect of surface roughness. *Wear*. 66, 307–321.
- [94] Chang, W.R., Etsion, I., Bogy, D.B., 1987. An elastic-plastic model for the contact of rough surfaces. *Journal of Tribology*. 109, 257–263.
- [95] Mesarovic, S.D., Johnson, K.L., 2000. Adhesive contact of elastic–plastic spheres. *Journal of Mechanics and Physics of Solids*. 48 (10), 2009–2033.
- [96] Gu, J.Z., Lee, L.Y., 2010. Adhesive contacts of a rigid sphere and an elastic–perfectly plastic half-space. *Computational Materials Science*. 48, 848–853.
- [97] Kogut, L., Etsion, I., 2003. Elastic-Plastic Contact Analysis of a Sphere and a Rigid Flat. *Journal of Colloid and Interface Science*. 261, 372–378.
- [98] Du, Y., Chen, L., McGruer, N.E., Adams, G.G., Etsion, I., 2007. A finite element model of loading and unloading of an asperity contact with adhesion and plasticity. *Journal of Colloid and Interface Science*. 312, 522–528.
- [99] Kadin, Y., Kligerman, Y., Etsion, I., 2008. Loading-unloading of an elastic-plastic adhesive spherical microcontact. *Journal of Colloid and Interface Science*. 321, 242–250.
- [100] Kadin, Y., Kligerman, Y., Etsion, I., 2008. Cyclic loading of an elastic-plastic adhesive spherical microcontact. *Journal of Applied Physics*. 104 (7), Paper 073522.
- [101] Landman, U., Luedtke, W.D., Burnham, N.A., Colton, R.J., 1990. Atomistic Mechanisms and Dynamics of Adhesion, Nanoindentation, and Fracture. *Science*. 248, 454–461.
- [102] Leng, Y.S., Hu, Y.Z., Zheng, L.Q., 1999. Adhesive contact of flattened wedges: theory and computer experiments. *Journal of Tribology*. 121, 128–132.
- [103] Zhu, S.J., Liu, G., Liu, T.X., 2007. Molecular dynamics simulation on adhesive contact between nano-pillar and plane. *Journal of Northwestern Polytechnical University*. 25 (3), 461–466.
- [104] Bao, G., Suresh, S., 2003. Cell and molecular mechanics of biological materials. *Nature Materials*. 2(11), 715–725.

- [105] Van Vliet, K. J., Bao, G., Suresh, S., 2003. The biomechanics toolbox: experimental approaches for living cells and biomolecules. *Acta Materialia*. 51(19), 5881–5905.
- [106] Lim, C. T., Zhou, E. H., Quek, S. T., 2006. Mechanical models for living cells: a review. *Journal of Biomechanics*. 39(2), 195–216.
- [107] Binnig, G., Quate, C.F., Gerber, C., 1986. Atomic resolution with atomic force microscope. *Physical Review Letters*. 56, 930–934.
- [108] Martin, Y., Wickramasinghe, H.K., 1987. Magnetic imaging by “force microscopy” with 1000 Å resolution. *Applied Physics Letters*. 50, 1455–1457.
- [109] Tao, N.J., Lindsay, S.M., Lees, S., 1992. Measuring the microelastic properties of biological material. *Biophysical Journal*. 63, 1165–1169.
- [110] Radmacher, M., 2002. Measuring the elastic properties of living cells by the atomic force microscope. *Methods in Cell Biology*. 68, 67–90.
- [111] Ohashi, T., Ishii, Y., Ishikawa, Y., Matsumoto, T., Sato, M., 2002. Experimental and numerical analyses of local mechanical properties measured by atomic force microscopy for sheared endothelial cells. *Bio-Medical Materials and Engineering*. 12(3), 319–327.
- [112] Kuznetsova, T.G., Starodubtseva, M.N., Yegorenkov, N.I., Chizhik, S.A., Zhdanov, R.I., 2007. Atomic force microscopy probing of cell elasticity. *Micron*. 38, 824–833.
- [113] Li, Q. S., Lee, G. Y. H., Ong, C. N., Lim, C. T., 2008. AFM indentation study of breast cancer cells. *Biochemical and Biophysical Research Communications*. 374(4), 609–13.
- [114] Cross, S. E., Jin, Y. S., Rao, J., Gimzewski, J. K., 2007. Nanomechanical analysis of cells from cancer patients. *Nature Nanotechnology*. 2, 780–783.
- [115] Dammer, U., Popescu, O., Wagner, P., Anselmetti, D., Guntherodt, H.J., Misevic, G.N., 1995. Binding strength between cell adhesion proteoglycans measured by atomic force microscopy. *Science*. 267, 1173–1175.
- [116] Lee, I.S., Marchant, R.E., 2001. Force measurements on the molecular interactions between ligand (RGD) and human platelet $\alpha_{IIb}\beta_3$ receptor system. *Surface Science*. 491 (3),

433–443.

[117] Puech, P.-H., Poole, K., Knebel, D., Muller, D.J., 2006. A new technical approach to quantify cell-cell adhesion forces by AFM. *Ultramicroscopy*. 106(8-9), 637–644.

[118] Friedrichs, J., Helenius, J., Muller, D. J., 2010. Quantifying cellular adhesion to extracellular matrix components by single-cell force spectroscopy. *Nature protocols*. 5(7), 1353–1361.

[119] Jones, J.E., 1924. On the determination of molecular fields. II. From the equation of state of a gas. *Proceedings of the Royal Society of London A*. 106, 463–477.

[120] Derjaguin, B.V., 1934. Theorie des anhaftens kleiner teilchen. *Koll. Z.* 69, 155–164.

[121] Harmaker, H.C., 1937. The London - van der Waals attraction between spherical particles. *Physica*. 4, 1058–1072.

[122] Dugdale, D.S., 1960. Yielding of steel sheets containing slits. *Journal of Mechanics and Physics of Solids*. 8, 100–108.

[123] Maugis, D., 1995. Extension of the Johnson-Kendall-Roberts theory of the elastic contact of spheres to large contact radii. *Langmuir*. 11 (2), 679–682.

[124] Yao, H., Ciavarella, M., Gao, H., 2007. Adhesion maps of spheres corrected for strength limit. *Journal of Colloid and Interface Science*. 315, 786-790.

[125] Sun, W. F., Zeng, Q. H., Yu, A. B., 2013. Calculation of Normal Contact Forces between Silica Nanospheres. *Langmuir*. 29, 2175–2184.

[126] Pharr, G.M., Oliver, W.C., Brotzen, F.R., 1992. On the generality of the relationship among contact stiffness, contact area and the elastic modulus during indentation. *Journal of Materials Research*. 7 (3), 613–617.

[127] Doerner, M.F., Nix, W.D., 1986. A method for interpreting the data from depth-sensing indentation instruments. *Journal of Materials Research*. 1 (4), 601–609.

[128] Lawn, B.R., Evans, A.G., 1980. Elastic/Plastic indentation damage in ceramics: the median/radial crack system. *Journal of the American Ceramic Society*. 63, 574–581.

[129] Lawn, B.R., Wilshaw, T.R., 1975. Fracture of brittle solids. *Cambridge University Press*,

London.

[130] VanLandingham, M.R., 2003. Review of Instrumented Indentation. *Journal of Research of the National Institute of Standards and Technology*. 108, 249–265.

[131] Li, W.Z., Siegmund, T., 2004. An analysis of the indentation test to determine the interface toughness in a weakly bonded thin film coating – substrate system. *Acta Materialia*. 52 (10), 2989–2999.

[132] Fused Silica, SiO₂ Glass Properties.

[cited; available from <http://accuratus.com/fused.html>].

[133] Properties of silicon and silicon wafers.

[cited; Available from: <https://www.el-cat.com/silicon-properties.htm>].

[134] Properties of Silicon.

[cited; Available from: <http://www.design.caltech.edu/Research/MEMS/siliconprop.html>].

[135] Nix, W.D., Gao, H., 1998. Indentation size effects in crystalline materials: a law for strain gradient plasticity. *Journal of the Mechanics and Physics of Solids*. 46, 411–425.

[136] Fischer-Cripps, A.C.K., Veprek, S.P., 2006. On the measurement of hardness of super-hard coatings. *Surface and Coatings Technology*. 200, 5645–5654.

[137] Soifer, Y.M.V., Rapoport, A., Nanoindentation, L., 2002. Nanoindentation size effect in alkali-halide single crystals. *Materials Letters*. 56, 127–130.

[138] Pharra, G.M., Olivera, W.C., Hardinga, D.S., 1991. New evidence for a pressure-induced phase transformation during the indentation of silicon. *Journal of Materials Research*. 6 (6), 1129–1131.

[139] Komvopoulos, K., 1996.

Surface Engineering and Microtribology for Microelectromechanical Systems. *Wear*. 200, 305–327.

[140] Komvopoulos, K., 2003. Adhesion and friction forces in microelectromechanical systems: mechanisms, measurement, surface modification techniques, and adhesion theory.

- Journal of adhesion science and technology*. 17, 477–517.
- [141] Komvopoulos, K., 2000. Head-Disk Interface Contact Mechanics for Ultrahigh Density Magnetic Recording. *Wear*. 238, 1–11.
- [142] Abdel-Karim M., 2005. Shakedown of complex structures according to various hardening rules. *International Journal of Pressure Vessels and Piping*. 82, 427–458.
- [143] Song, Z., Komvopoulos, K., 2011. Adhesion-induced instabilities in elastic and elastic–plastic contacts during single and repetitive normal loading. *Journal of the Mechanics and Physics of Solids*. 59, 884–897.
- [144] Hill, R., 1998. The Mathematical Theory of Plasticity. *Oxford University Press*, London.
- [145] Degarmo, E. P., Black, J.T., Kohser, R.A., 2003. *Materials and Processes in Manufacturing (9th ed.)*, Wiley.
- [146] Dulińska, I., Targosza, M., Strojny, W., Lekka, M., Czuba, P., Balwiercz, W., Szymońska, M., 2006. Stiffness of normal and pathological erythrocytes studied by means of atomic force microscopy. *Journal of Biochemical and Biophysical Methods*. 66, 1–11.
- [147] Ikai, A., Xu, X.M., Mitsui, K., 1997. Measurements of mechanical parameters of biological structures with atomic force microscope. *Scanning Microsc.* 12, 585–596.
- [148] Nowakowski, R., Luckham, P., Winlove, P., 2001. Imaging erythrocytes under physiological conditions by atomic force microscopy. *Biochimica et Biophysica Acta (BBA) – Biomembranes*. 1514, 170–176.
- [149] Alessandrini, A., Facci, P., 2005. AFM: a versatile tool in biophysics. *Measurement Science and Technol.* 16, R65–R92.
- [150] Maciaszek, J.L., Partola, K., Zhang, J., Andemariam, B., Lykotrafitis, G., 2014. Single-cell force spectroscopy as a technique to quantify human red blood cell adhesion to

- subendothelial laminin. *Journal of Biomechanics*. 47, 3855–3861.
- [151] Sirghi, L., Ponti, J., Broggi, F., Rossi, F., 2008. Probing elasticity and adhesion of live cells by atomic force microscopy indentation. *European Biophysics Journal*. J. 37, 935–945.
- [152] Hills, C.E., Younis, M.Y.G., Bennett, J., Siamantouras, E., Liu, K.K., Squires, P.E., 2012. Calcium-Sensing Receptor Activation Increases Cell-Cell Adhesion and β -Cell Function. *Cellular Physiology and Biochemistry*. 30(3), 575–586.
- [153] Ladjal, H., Hanus, J.L., Pillarisetti, A., Keefer, C., Ferreira, A., Desai, J.P., 2009. Atomic force microscopy-based single-cell indentation: Experimentation and finite element simulation. *IEEE/RSJ International Conference on Intelligent Robots and Systems*. 1326–1332.
- [154] ISO/CD 14577–4, 2007 Metallic materials – Instrumented indentation test for hardness and materials parameters – Part 4: Test method for metallic and non-metallic coatings.
- [155] Dimitriadis, E.K., Horkay, F., Maresca, J., Kachar, B., Chadwick, R.S., 2002. Determination of elastic moduli of thin layers of soft material using the atomic force microscope. *Biophysical Journal*. 82, 2798–2810.
- [156] Jung, Y.G., Lawn, B.R., Martyniuk, M., Huang, H., Hu, X.Z., 2004. Evaluation of elastic modulus and hardness of thin films by nanoindentation. *Journal of Materials Research*. 19, 3076–3080.
- [157] Alcaraz, J., Buscemi, L., Grabulosa, M., Trepas, X., Fabry, B., Farree, R., Navajas, D., 2003. Microrheology of human lung epithelial cells measured by atomic force microscopy. *Biophysical Journal*. 84, 2071–2079.

- [158] Koay, E.J., Shieh, A.C., Athanasiou, K.A., 2003. Creep Indentation of Single Cells. *Journal of Biomechanical Engineering*. 125(3), 334–341.
- [159] Rosenbluth, M.J., Lam, W.A., Fletcher, D.A., 2006. Force microscopy of nonadherent cells: a comparison of leukemia cell deformability. *Biophysical Journal*. 90, 2994–3003.
- [160] A-Hassan, E., Heinz, W.F., Antonik, M.D., D’Costa, N.P., Nageswaran, S., Schoenenberger, C.A., Hoh, J.H., 1998. Relative microelastic mapping of living cells by atomic force microscopy. *Biophysical Journal*. 74, 1564–1578.
- [161] Sun, M., Graham, J.S., Hagedus, B., Marga, F., Zhang, Y., Forgacs, G., Grandbois, M., 2005. Multiple membrane tethers probed by atomic force microscopy. *Biophysical Journal*. 89, 4320–4329.
- [162] Chen.Z., Ma, L., Liu, Y., Chen, C., 2012. Applications of functionalized fullerenes in tumor theranostics. *Theranostics*. 2, 238–250.
- [163] Chen, Z., Mao, R., Liu, Y., 2012. Fullerenes for cancer diagnosis and therapy: Preparation, Biological and Clinical Perspectives. *Current Drug Metabolism*. 13, 1035–1045.
- [164] Partha, R., Conyers, J.L., 2009. Biomedical applications of functionalized fullerene-based nanomaterials. *International Journal of Nanomedicine*. 4, 261–275.
- [165] Johnson-Lyles, D.N., Peifley, K., Lockett, S., Neun, B.W., Hansen, M., Clogston, J., Stern, S.T., McNeil, S.E., 2010. Fullerenol cytotoxicity in kidney cells is associated with cytoskeleton disruption, autophagic vacuole accumulation, and mitochondrial dysfunction. *Toxicology and Applied Pharmacology*. 248, 249–258.
- [166] Plodinec, M., Loparic, M., Monnier, C.A., Obermann, E.C., ZanettiDallenbach, R., Oertle, P., Hyotyla, J.T., Aebi, U., Bentires-Alj, M., Lim, M.R., Schoenenberger, C.A., 2012. The nanomechanical signature of breast cancer. *Nature Nanotechnology*. 7, 757–765.
- [167] Liu, Y, Wang, Z.B., Wang, X.Y., 2015. AFM-Based Study of Fullerenol (C₆₀(OH)₂₄)-Induced Changes of Elasticity in Living SMCC-7721 Cells. *Journal of the*

Mechanical Behavior of Biomedical Materials.45, 65–74.

[168] Simon, A., Durrieu, M.C., 2006. Review. Strategies and results of atomic force microscopy in the study of cellular adhesion. *Micron*. 37, 1–13.

[169] Yoo, L., Reed, J., Shin, A., Demer, J.L., 2014. Atomic force microscopy determination of Young's modulus of bovine extra-ocular tendon fiber bundles. *Journal of Biomechanics*. 47 (8), 1899–1903.

[170] Afrin, R., Yamada, T., Ikai, A., 2004. Analysis of force curves obtained on the live cell membrane using chemically modified AFM probes. *Ultramicroscopy*. 100, 187–195.

[171] McNamee, C.E., Pyo, N., Tanaka, S., Vakarelski, I.U., Kanda, Y., Higashitani, K., 2006. Parameters affecting the adhesion strength between a living cell and a colloid probe when measured by the atomic force microscope. *Colloids and Surfaces B: Biointerfaces*. 48, 176–182.

[172] Elter, P., Weihe, T., Lange, R., Gimsa, J., Beck, U., 2011. The influence of topographic microstructures on the initial adhesion of L929 fibroblasts studied by single-cell force spectroscopy. *European Biophysics Journal*. 40(3), 317–327.

[173] Thiery, J.P., 2003. Comptes rendus de l'Academie des Sciences. *Physique*. 4(2), 289-302.

[174] Sneddon, I.N., 1965. The relation between load and penetration in the axisymmetric Boussinesq problem for a punch of arbitrary profile. *International Journal of Engineering Science*. 3, 47–57.

[175] King, R.B., 1987. Elastic analysis of some punch problems for a layered medium. *International Journal of Solids and Structures*. 23, 1657–1664.

[176] Antunes, J.M., Menezes, L.F., Fernandes, J.V., 2006. Three-dimensional numerical simulation of Vickers indentation tests. *International Journal of Solids and Structures*. 43, 784–806.

[177] Siamantouras, E., 2014. Nanomechanical investigation of soft biological cell adhesion using atomic force microscopy. PhD Thesis. *University of Warwick*, p. 91.